Biomimetic Peroxo- and Oxo-manganese Complexes: Insights into Structure and Reactivity through Kinetic, Spectroscopic, and Computational Studies

By

Domenick F. Leto

Submitted to the graduate degree program in Chemistry and the Graduate Faculty of the University of Kansas in partial fulfillment of the requirements for the degree of Doctor of Philosophy

_____

Chairperson: Dr. Timothy A. Jackson

_____

Dr. Mikhail Barybin

_____

Dr. Kristin Bowman-James

_____

Dr. Shenqiang Ren

_____

Dr. Aaron Scurto

Date Defended: May 29, 2014

The Dissertation Committee for Domenick F. Leto certifies that this is the approved version of the following thesis:

Biomimetic Peroxo- and Oxo-manganese Complexes: Insights into Structure and Reactivity through Kinetic, Spectroscopic, and Computational Studies

_____

Chairperson: Dr. Timothy A. Jackson

Date approved: June 6, 2014

Abstract.

Manganese centers that react with O_2 and its reduced derivatives mediate a diverse array of biologically important reactions including the detoxification of superoxide, the conversion of nucleotides to deoxynucleotides, and the generation of O_2 from H_2O. Peroxo-, oxo-, and hydroxo-manganese motifs are frequently invoked in the catalytic cycles of Mn enzymes. To that end, biomimetic complexes featuring peroxo-, oxo-, and hydroxo-manganese adducts were synthesized and studied using spectroscopic techniques, including variable-temperature electronic absorption, electron paramagnetic resonance (EPR), X-ray absorption (XAS), and magnetic circular dichroism (MCD) spectroscopies along with computational methods, such as density functional theory (DFT) and time-dependent DFT. The structural and spectroscopic properties of these species were investigated in order to better understand how the geometric and electronic structure of these complexes affects reactivity.

A novel mononuclear Mn^{II} complex, $[Mn^{II}(N4py)(OTf)](OTf)$, supported by a neutral N_5 aminopyridyl ligand, was synthesized and its chemical reactivity with superoxide, hydrogen peroxide, and iodosylbenzene were explored. Notably, a peroxomanganese(III) adduct was generated upon treatment of $[Mn^{II}(N4py)(OTf)](OTf)$ with excess superoxide at low-temperatures (-40 ^{o}C). This peroxomanganese(III) adduct reacts with $[Mn^{II}(N4py)(OTf)]^{+}$ to form a bis(μ-oxo)manganese(III,IV) compound. This overall reaction mimics the observed chemistry of Mn-ribonucleotide reductase, as it features the conversion of two Mn^{II} species to an oxo-bridged dimanganese(III,IV) compound using superoxide as oxidant. The bis(μ-oxo)manganese(III,IV) compound could be independently prepared through treatment of $[Mn^{II}(N4py)(OTf)](OTf)$ with H_2O_2 and base at −40 °C, and its structure was established using X-ray diffraction. A mononuclear oxomanganese(IV) complex, also supported by the N4py

ligand, was generated at room temperature from the addition of iodosylbenzene to $[Mn^{II}(N4py)(OTf)](OTf)$ and was characterized by spectroscopic methods. The Mn^{IV}=O adduct is capable of activating C–H bonds by a H-atom transfer mechanism and is more reactive in this regard than most Mn^{IV}=O species.

Mn K-edge X-ray absorption spectroscopy was used to gain insights into the geometric and electronic structures of $[Mn^{II}(Cl)_2(Me_2EBC)]$, $[Mn^{IV}(OH)_2(Me_2EBC)]^{2+}$ and $[Mn^{IV}(O)(OH)(Me_2EBC)]^{+}$, which are all supported by the tetradentate, macrocyclic Me_2EBC ligand. Analysis of extended X-ray absorption fine structure (EXAFS) data for $[Mn^{IV}(O)(OH)(Me_2EBC)]^{+}$ revealed Mn–O scatterers at 1.71 and 1.84 Å and Mn–N scatterers at 2.11 Å, providing the first unambiguous support for the formulation of this species as an oxohydroxomanganese(IV) adduct. X-ray absorption near edge structure (XANES) of these complexes was examined within the context of data previously reported for other oxo- and hydroxomanganese(IV) adducts. Time-dependent density functional theory (TD-DFT) computations were used to predict XANES properties for all compounds considered. This combined experimental and computational analysis revealed a correlation between the Mn–O(H) distances and pre-edge peak areas of Mn^{IV}=O and Mn^{IV}–OH complexes, but this trend was strongly modulated by the Mn^{IV} coordination geometry. X- and Q-band EPR spectroscopy, along with computer simulations, were applied to investigate the zero-field splitting parameters $[Mn^{IV}(OH)_2(Me_2EBC)]^{2+}$ and $[Mn^{IV}(O)(OH)(Me_2EBC)]^{+}$, adding to the limited spectroscopic information available for oxo- and hydroxomanganese(IV) complexes.

Acknowledgements.

First and foremost, I would like to thank my research advisor and mentor. None of this would have been possible without his unwavering support and encouragement. Professor Jackson, thank you for instilling in me the fundamentals of being a great researcher. Your drive for excellence and willingness to go above and beyond for your students have truly inspired me, and I wish you and the group continued success in the future.

Misha, thank you for all of your support and guidance over the years. You have been a great second mentor to me. I also want to thank Dr. Bowman-James, Dr. Heather Desaire, and Dr. Aaron Scurto for agreeing to serve on my committee. Your support is greatly appreciated. To Dr. Justin Douglas, thank you for all of your help with the EPR spectrometer and for cleaning out the cavity whenever I broke an EPR sample. I also need to thank Dr. Victor Day for solving my crystal structures and Dr. Erik Farquhar at Brookhaven National Laboratory for all of his assistance during our X-ray absorption trips.

Swarup, thank you for taking me under your wing when I was an undergraduate and first-year graduate student and for teaching me all of the subtleties of inorganic synthesis. You gave me a great foundation for my research. Robert and James… you two definitely made lab interesting and fun (… and loud). Thank you for all of your help and all of the laughs along the way. I have learned so much from both of you and am glad we have remained such good friends. I owe Robert for sharing with me all of his 'tricks' in lab and for making graduate school fun. Amanda, thank you for all of your help along the way and for all of the treats. To my friends from the Barybin group (John, Andy, and Dave) thank you for the friendship, fun, and laughs.

Thank you to all of the current Jackson group members (Hannah, Derek, Allyssa, and Manoj) for putting up with me during my two-year writing spree and for your support and

friendship. Gayan, my buddy, thank you for helping to keep lab fun and for being a great friend. The X-ray absorption trips would not have been the same without you. I will never forget staying up for 48 hours straight with you trying to collect as much data as we could before Hurricane Sandy hit. (Are you going to pay for both cups of coffee? Haha.)

To my family; words cannot express my gratitude for your support, patience, guidance, and love. Without you, I could not be here today. Mom and Dad, thank you for always pushing me to succeed and stressing the importance of education. You taught me to always believe in myself and that there is no substitute for hard work and perseverance. And thank you for all of the delicious Sunday dinners. I will miss those when I am in California. To my soon-to-be in-laws, thank you for the support, encouragement, and love you have shown me over the years. To my dogs, Charlie and Lady, thank you for staying up with me through every all-nighter, you were the best study-buddies I could ask for.

And above all, thank you to my fiancée, Elena. Your companionship, support, patience, and love are what inspired me to keep going even when things seemed overwhelming. You have always offered a shoulder to lean on and have gone above and beyond to support me. Thank you for always believing in me. I love you so much and look forward to embarking on all of life's adventures together.

Rock Chalk!

TABLE OF CONTENTS page

Abbreviations and Acronyms.

Abs	absorption
BDE	bond-dissociation enthalpy
CAN	cerium ammonium nitrate
CCA	cyclohexanecarboxaldehyde
CT	charge-transfer
DFT	density functional theory
DHA	9,10-dihydroanthracene
DPH	diphenylhydrazine
DPM	diphenylmethane
EPR	electron paramagnetic resonance
ESI-MS	electrospray ionization mass spectrometry
EtBz	ethylbenzene
EXAFS	extended X-ray absorption fine-structure
FWHM	full-width at half-maximum
GOF	goodness-of-fit
HF	Hartree-Fock
HPCA	homoprotocatechuate
KIE	kinetic isotope effect
MCD	magnetic circular dichroism
MeCN	acetonitrile
MLCT	metal-to-ligand charge-transfer
MnCAT	manganese catalase

MnHPCD	manganese homoprotocatechuate 2,3-dioxygenase
MnRNR	manganese ribonucleotide reductases
MnSOD	manganese superoxide dismutase
MO	molecular orbital
NSLS	National Synchrotron Light Source
OEC	oxygen evolving complex
PhIO	iodosylbenzene
NIR	near-infrared
NMR	nuclear magnetic resonance
rR	resonance Raman
SOD	superoxide dismutase
TD-DFT	time-dependent density functional theory
Tol	toluene
UV	ultraviolet
VTVH	variable temperature, variable field
XANES	X-ray absorption near-edge structure
XAS	X-ray absorption spectroscopy
XRD	X-ray diffraction
ZFS	zero-field splitting

Chapter 1

Peroxo- and Oxo-manganese Complexes as an Aid to Understanding Redox-Active Manganese Enzymes

This work has been reproduced in part from: D. F. Leto and T. A. Jackson, *J. Biol. Inorg. Chem.*, 2014, **19**, 1 - 15, with kind permission from Springer Science and Business Media

1.1. Introduction.

There are examples of redox-active manganese enzymes that react with dioxygen and all its reduced derivatives (superoxide, peroxide, and water). These enzymes catalyze transformations critical to health and the environment, including the detoxification of reactive oxygen species (superoxide and hydrogen peroxide);[1-3] the catabolism of aromatic molecules by soil bacteria;[4] the breakdown of the toxin oxalate in fungi, plants, and bacteria;[5] the generation of deoxynucleotides in certain bacteria and pathogens;[6] and the oxidation of water to dioxygen in algae, cyanobacteria, and plants.[7,8] Table 1.1 lists the specific reactions and active-site properties of redox-active manganese enzymes.

Table 1.1. Representative redox-active manganese enzymes.

Name	Occurrence	Biological reaction	Resting state
Mn superoxide dismutase	eukaryotes; bacteria; fungi	O_2^- disproportionation	$[Mn^{II}(Asp)(His)_2(OH_2)]$
Mn extradiol dioxygenase	soil bacteria	cleave 2,3-bond of catechols	$[Mn^{II}(Glu)(His)_2(OH_2)_3]$
Mn catalase	bacteria	H_2O_2 disproportionation	$[Mn^{III}_2(Glu)_3(His)_2]$
Mn ribonucleotide reductase	bacteria; pathogens	generates tyrosine radical using O_2^-	$[Mn^{II}_2(Glu)_3(Asp)(His)_2(OH_2)_2]$
oxalate oxidase	bacteria; fungi; plants	oxalate oxidation using O_2	$[Mn^{II}(Glu)(His)_3OH_2)_2]$
oxalate decarboxylase	bacteria; fungi	oxalate decarboxylation using O_2	$[Mn^{II}(Glu)(His)_3(OH_2)_2]$
photosystem II (oxygen evolving complex)	algae; plants; cyanobacteria	H_2O splitting	$[Mn_4CaO_5(Glu)_3(Asp)_2(Ala)(His)]$

Despite the diversity in active-site function and structures, the proposed mechanisms of redox-active manganese enzymes commonly feature peroxo-level intermediates. For manganese superoxide dismutase (Mn-SOD)[9,10] and manganese homoprotocatechuate 2,3-dioxygenase (Mn-HPCD),[4] there is spectroscopic evidence for such intermediates (*vide infra*). However, in most cases peroxomanganese intermediates are inferred on the basis of the reaction chemistry and/or supported by computational investigations. For example, peroxomanganese species are proposed to precede formation of a spectroscopically characterized bis(μ-oxo)dimanganese(III,IV)

intermediate in manganese ribonucleotide reductase (Mn-RNR)[11] and are proposed to be involved in water oxidation by the oxygen evolving complex (OEC).[7,12,13]

Investigations of redox-active manganese enzymes have long benefitted from complementary studies of synthetic models that mimic structural, spectroscopic, and/or reactivity properties.[7,14] In this chapter we describe progress, primarily within the past decade, towards understanding the structure and reactivity of peroxo- and oxomanganese adducts using model systems. Peroxo- and alkylperoxomanganese(III) adducts and oxomanganese(IV) adducts are emphasized, as there has been a surge of activity in the generation and characterization of these complexes. Before discussing these synthetic models, we describe evidence for peroxo-level intermediates in Mn-SOD and Mn-HPCD.

1.1.1. Peroxomanganese(III) Intermediate in Mn-SOD. The Mn-SOD active site contains a trigonal bipyramidal manganese center with three histidines, an aspartate, and a solvent ligand (Figure 1.1A).[15] Superoxide is oxidized to O_2 and reduced to H_2O_2 in separate half-reactions, with the manganese ion shuttling between the Mn^{III} and Mn^{II} states.[16,17] Mn-SODs are unusual among the SOD family in that their activity diminishes at higher superoxide concentrations due to the formation of a product-inhibited complex, long presumed to be a peroxomanganese(III) adduct, that slowly re-enters the catalytic cycle.[9] Thus, superoxide reduction occurs by a gated mechanism involving either a “prompt protonation” or an “inner-sphere” pathway (Figure 1.1B).

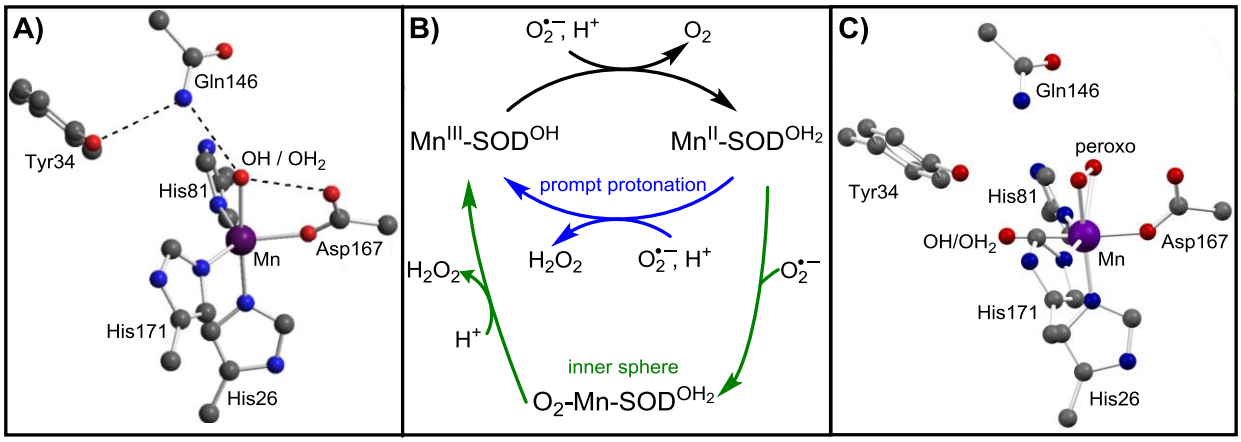

Figure 1.1. A) Active-site of *E. coli* Mn-SOD from 1VEW[13] with hydrogen-bonding network marked with dashes. B) Catalytic cycle of Mn-SOD showing "prompt protonation" and "inner-sphere" pathways for superoxide reduction. The "inner-sphere" pathway occurs under high superoxide concentration and features the formation of a Mn-peroxo adduct. C) Peroxo-Mn-SOD adduct from 3K9S (chain D).[18]

The only spectroscopic data available for the product-inhibited complex is its electronic absorption spectrum, which shows maxima at 410 and 650 nm ($\varepsilon \approx 700$ and 230 $M^{-1}cm^{-1}$),[9,10] consistent with a Mn^{III} center. The structure of this intermediate remains controversial. Several variants of end-on (η^1) hydroperoxomanganese(III)[18,19] and asymmetric side-on (η^2) peroxomanganese(III) adducts[18,20] have been proposed on the basis of density functional theory (DFT) investigations. In all computational models, the peroxo ligand is bound in the cleft flanked by the equatorial histidines. In contrast, a 1.55 Å resolution crystal structure of cryotrapped *E. coli* Mn-SOD treated with peroxide showed an η^2-peroxo occupying the position typical of axial solvent in three of four active sites of the tetramer (Figure 1.1C).[21] An equatorial solvent ligand was observed in two of the three peroxo-Mn-SOD structures. The Mn–O(peroxo) distances, which range from 2.09 – 2.58 Å, are exceptionally long for a peroxomanganese(III) species (*vide infra*). Regardless of whether or not this species corresponds to the product-inhibited complex, it represents the only structurally characterized peroxomanganese adduct in biology.

1.1.2 Peroxo Intermediate in Mn-containing Extradiol Catechol Dioxygenases. Extradiol catechol dioxygenases feature a metal ion (typically Fe^{II}) ligated by the 2-His-1-carboxylate facial triad common for O_2-activating nonheme iron enzymes (Scheme 1.1).[22] Some enzymes in this class have comparable activity with Fe^{II} or Mn^{II} active-site ions. Elegant rapid-freeze-quench EPR investigations on Mn-HPCD from *Brevibacterium fuscum* by Hendrich and co-workers detected two intermediates upon the introduction of O_2-saturated buffer to the Mn-HPCD-HPCA (HPCA = homoprotocatechuate) complex (Scheme 1.1).[4] The first intermediate (**I1**), which maximized to 5% of total Mn at 15 ms and then disappeared, displayed a six-line EPR signal at g = 4.29, with a hyperfine splitting of 60 G and an axial zero-field splitting (ZFS) parameter D of +2.5 cm^{-1} (S = 5/2). Although the S = 5/2 spin state is consistent with high-spin Mn^{II}, the D value and hyperfine splitting are incompatible with this conclusion. Instead, these data indicate that **I1** contains a high-spin Mn^{III} center (S = 2) ferromagnetically coupled to a ligand radical (S = 1/2). Although either a Mn^{III}-peroxo-HPCA radical or a Mn^{III}-superoxo could be possible, the ferromagnetic coupling is more consistent with the latter formulation. The second intermediate (**I2**), which maximized at 75% of total Mn at 34 ms, showed a D value (0.24 cm^{-1}) consistent with high-spin Mn^{II}, and was formulated as a Mn^{II}-alkylperoxo adduct.

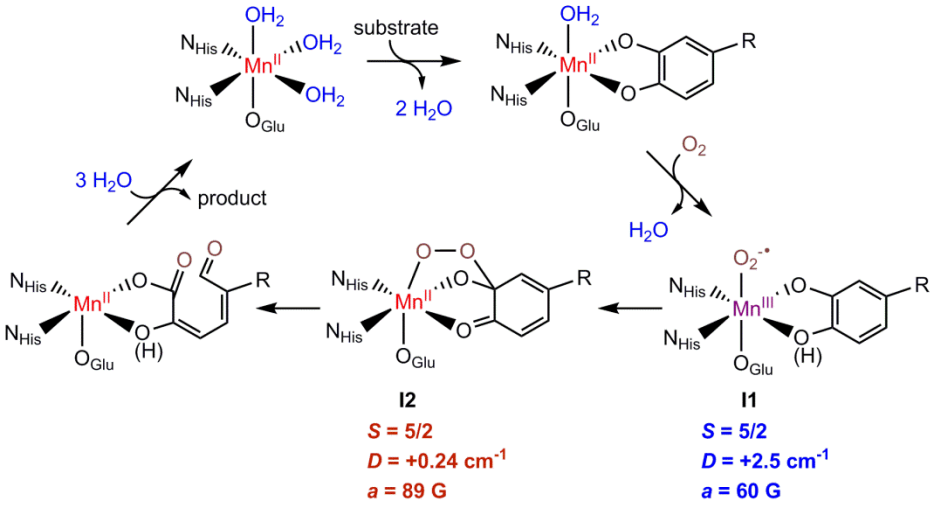

Scheme 1.1. Catalytic cycle of Mn-HPCD, as proposed in Ref 4.

1.2. Formation of Peroxomanganese(III) Complexes.

In 1987, the first crystallographically characterized peroxomanganese(III) complex, $[Mn^{III}(O_2)(TPP)]^-$, was reported by Valentine and co-workers (Scheme 1.2 shows ligands described in this chapter).[23] In the 26 years since that report, only six peroxomanganese(III) complexes have been structurally characterized (Figure 1.2),[24-29] though there are additional compounds whose formulations are supported by spectroscopic, mass spectral, and/or computational studies (Figure 1.3).[30-36] Our discussion of these complexes will begin with methods and strategies used to generate peroxomanganese(III) complexes and then focus on structural and physical properties. Finally, we will describe recent investigations of chemical reactivity.

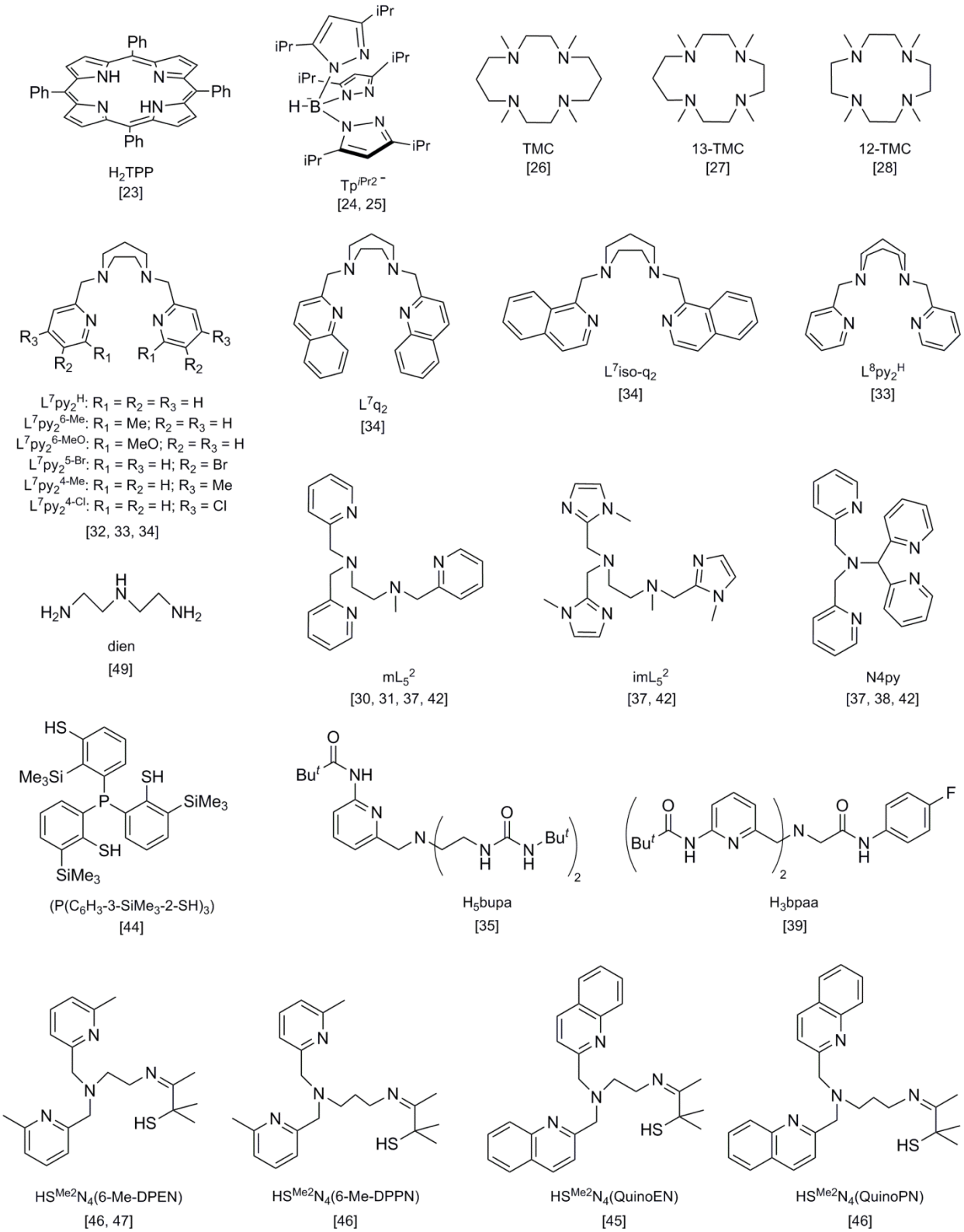

Scheme 1.2. Ligands used to support peroxo- and alkylperoxomanganese complexes. Corresponding literature references to peroxomanganese complexes supported by these ligands are provided.

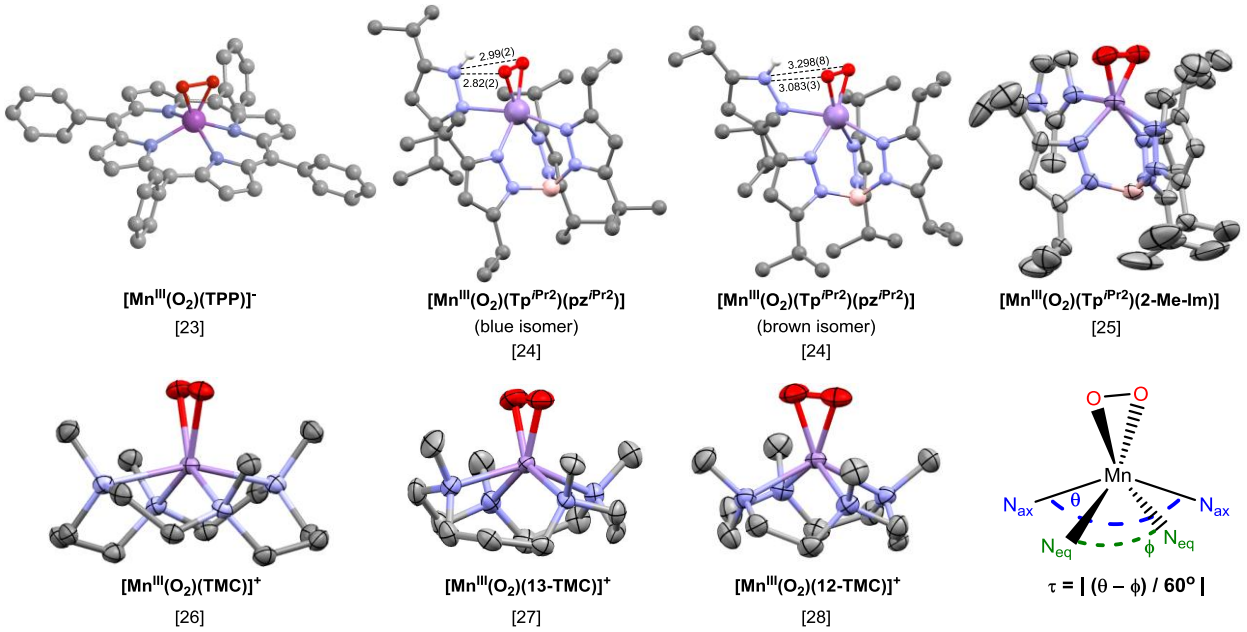

Figure 1.2. X-ray crystal structures of η^2-peroxomanganese(III) complexes. Corresponding literature references are provided beneath the molecular formula.

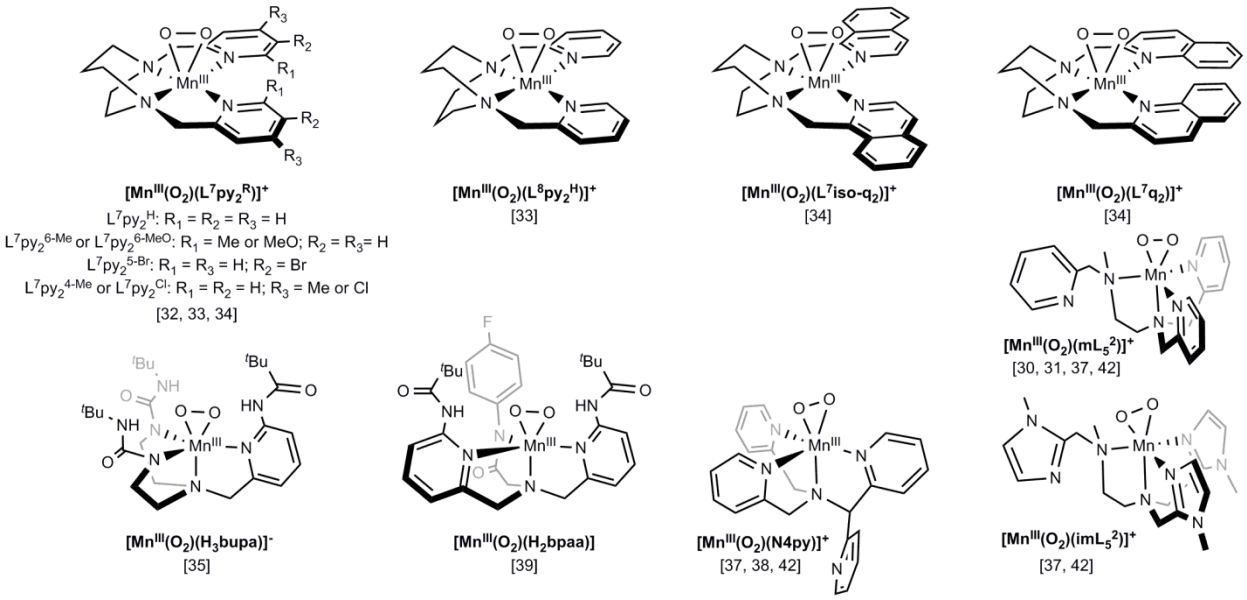

Figure 1.3. Schematic structures of η^2-peroxomanganese(III) compounds. Corresponding literature references are provided beneath the molecular formula.

Potassium superoxide was used to form $[Mn^{III}(O_2)(TPP)]^-$,[23] and it has been employed to generate a number of peroxomanganese(III) adducts from manganese(II) precursors supported by pentadentate N_5 (N4py and mL_5^2)[30,37] and tetradentate N_4 ($L^7py_2^R$ and related)[32-34] ligands. Superoxide presumably acts as a one-electron oxidant of the Mn^{II} center, mimicking the formation of the product inhibited complex in Mn-SOD (Figure 1.1B). This reaction can be complicated by the superoxide scavenging activity of manganese(II) complexes.[38] Alternatively, aqueous H_2O_2 has been used to generate a number of peroxomanganese(III) complexes, including those of the Tp^{iPr}[24,25] and TMC-derived ligands.[26,27] The mechanism for formation of Mn^{III}-O_2 adducts using H_2O_2 has not been established. In some cases, addition of a base such as Et_3N was required,[26-28,32-34,37] while in other cases, only a large excess of H_2O_2[24,25,31,39] or anhydrous H_2O_2-urea was needed.[28,31,37] Notably, the $[Mn^{III}(O_2)(TMC)]^+$ complex can also be generated by peroxo-transfer from Ni^{II}-O_2 and Co^{III}-O_2 adducts supported by *n*-TMC (*n* = 13 and 12) ligands.[40] Low temperatures (less than 0 ^oC) are often,[30-34,37,41] but not always,[24-27] required to trap Mn^{III}-O_2 adducts. In many cases, the yield of the peroxomanganese(III) complex is low to moderate, which has prevented structural characterization using Mn K-edge X-ray absorption spectroscopy (XAS). Significantly increased yields of peroxomanganese(III) adducts from Mn^{II} precursors supported by N_5 ligands were recently achieved using electrochemically generated superoxide, which could enable future XAS and other studies.[42]

Two peroxomanganese(III) complexes have been generated using dioxygen.[35,39,43] Treatment of $[Mn^{II}(H_2bupa)]^-$ with O_2 at room temperature yielded $[Mn^{III}(O_2)(H_3bupa)]^-$ in 50% yield (H_2bupa is a trianionic tripodal ligand with a hydrogen-bonding cavity around the O_2-binding site; the ligand is protonated upon formation of the peroxomanganese(III) species[35]). When oxygenation was carried out in the presence of 0.5 equivalents diphenylhydrazine (DPH),

the rate of formation and yield of $[Mn^{III}(O_2)(H_3bupa)]^-$ was increased. The related $[Mn^{II}(Hbpaa)]$ complex likewise reacts with O_2 in the presence of hydrogen-atom donors (DPH, indene, and fluorene) to form $[Mn^{III}(O_2)(H_2bpaa)]$.[39] Presumably, these Mn^{II} centers react with O_2 to form superoxomanganese(III) adducts that abstract a hydrogen-atom to yield hydroperoxomanganese(III) species. Subsequent deprotonation, or intramolecular proton transfer, would give the observed η^2-peroxomanganese(III) complexes.[35,39]

1.3. Structural Properties of Peroxo- and Alkylperoxomanganese(III) Complexes.

The crystal structures of peroxomanganese(III) complexes supported by TPP,[23] Tp^{iPr2},[24,25] and N_4 macrocylic (TMC, 13-TMC, and 12-TMC)[26-28] ligands reveal six-coordinate Mn^{III} centers with η^2-peroxo ligands (Figure 1.2), with Mn–O and O–O bond lengths ranging from 1.838 to 1.901 Å and 1.402 to 1.43 Å, respectively (Table 1.2). The Mn–O distances of an η^2-peroxomanganese(IV) adduct supported by a tripodal $P(ArS^-)_3$ ligand (1.873 and 1.883 Å) fall within the same range as the η^2-peroxomanganese(III) species, but the O–O distance is shorter (1.379 Å).[44] For most η^2-peroxomanganese(III) complexes, the Mn–O distances are symmetric and differ by less than 0.015 Å. The more asymmetric Mn–O bonds in $[Mn(O_2)(Tp^{iPr2})(Me\text{-}Im)]$ (1.838 and 1.872 Å) are due to intermolecular hydrogen-bonds between Me-Im and peroxo ligands of adjacent molecules.[25] Asymmetric Mn–O bonds in the blue form of $[Mn(O_2)(Tp^{iPr2})(pz^{iPr2})]$ distinguish it from its brown isomer (Table 1.2 and Figure 1.2). These isomers reflect the thermochromism of $[Mn(O_2)(Tp^{iPr2})(pz^{iPr2})]$, with the brown to blue conversion observed upon cooling from -20 to -78 ºC. Short $N(pz^{iPr2})$ to O(peroxo) separations of 2.82(2) and 2.99(2) Å in the blue isomer (compared to corresponding distances of 3.298(8) and 3.083(3) Å in the brown form), suggest that intramolecular hydrogen-bonds are responsible for

the slight asymmetry in the Mn^{III}-O_2 unit. In support, the pz^{iPr2} N–H stretching vibration (ν_{N-H}) of the blue isomer appears as a broad signal at 3325 cm^{-1}, while ν_{N-H} for the brown isomer is a sharp feature at 3374 cm^{-1}. Unexpectedly, the peroxo O–O stretching vibrations (ν_{O-O}) are observed at 892 cm^{-1} for both isomers.

The coordination geometries of η^2-peroxomanganese(III) complexes can be further distinguished if the peroxo is viewed as a monoligand.[24] In this case the τ parameter, as defined in Figure 1.2, is used to classify the Mn^{III} coordination geometries along a continuum from square pyramidal ($\tau = 0$) to trigonal bipyramidal ($\tau = 1$). Using this formalism, $[Mn(O_2)(TPP)]^-$ is nearly square pyramidal ($\tau = 0.15$), with the rigid porphyrin preventing large differences in Mn–N bond lengths and N–Mn–N angles. In contrast, the facially-coordinating Tp^{iPr2} ligand supports η^2-peroxomanganese(III) complexes closest to trigonal bipyramidal ($\tau > 1$), with very large axial bond elongations. For the TMC-derived macrocycles, the geometries vary, but become closer to square pyramidal as the ring size decreases.

Table 1.2. Selected Bond Lengths (Å) for Peroxo- and Alkylperoxomanganese(III) Complexes from X-ray Crystallography

	Mn-O	O-O	Mn-N_{ax} [a]	Mn-N_{eq} [b]	τ [c]	ref.
η^2-peroxomanganese(III) adducts						
$[Mn(O_2)(TPP)]^-$	1.888, 1.901	1.421	2.199, 2.202	2.151, 2.184	0.15	23
$[Mn(O_2)(Tp^{iPr2})(pz^{iPr2})]$ (brown)	1.850, 1.851	1.428	2.270, 2.406	2.066, 2.067	1.1	24
$[Mn(O_2)(Tp^{iPr2})(pz^{iPr2})]$ (blue)	1.841, 1.878	1.43	2.24, 2.41	2.04, 2.09	1.2	24
$[Mn(O_2)(Tp^{iPr2})$(Me-Im)]	1.838, 1.872	1.42	2.272, 2.275	2.034, 2.068	1.2	25
$[Mn(O_2)(TMC)]^+$	1.884, 1.884	1.402	2.315, 2.315	2.215, 2.215	0.52	26
$[Mn(O_2)$(13-TMC)$]^+$	1.855, 1.863	1.410	2.283, 2.291	2.191, 2.200	0.28	27
$[Mn(O_2)$(12-TMC)$]^+$ [d]	1.853	1.408	2.245	2.245	0	28
η^1-alkylperoxomanganese(III) adducts						
	Mn-O	O-O	Mn-N_{HA}	Mn-N_{cis}	Mn-N_{trans}	Mn-S	ref.
$[Mn^{III}(OO^tBu)(S^{Me2}N_4$(QuinoEN))$]^+$	1.861	1.457	2.349, 2.522	2.173	2.034	2.270	45
$[Mn^{III}(OOCm)(S^{Me2}N_4$(QuinoEN))$]^+$	1.84	1.51	2.48, 2.45	2.17	2.01	2.276	45
$[Mn^{III}(OO^tBu)(S^{Me2}N_4$(QuinoPN))$]^+$	1.840	1.438	2.518, 2.450	2.182	2.046	2.269	46
$[Mn^{III}(OO^tBu)(S^{Me2}N_4$(6-Me-DPEN))$]^+$	1.853	1.468	2.471, 2.354	2.163	2.015	2.241	46
$[Mn^{III}(OOCm)(S^{Me2}N_4$(6-Me-DPEN))$]^+$	1.848	1.457	2.389, 2.499	2.145	2.018	2.268	46
$[Mn^{III}(OO^tBu)(S^{Me2}N_4$(6-Me-DPPN))$]^+$	1.843	1.431	2.504, 2.517	2.178	2.061	2.260	46
peroxo-bridged dimanganese(III) adduct							
$[Mn^{III}_2$(*trans*-μ-1,2-$O_2)(S^{Me2}N_4$(6-Me-DPEN))$_2]^{2+}$	1.832	1.452	2.501, 2.581	2.203	2.040	2.475	47

[a] The axial positions are perpendicular to the O–O vector. [b] The equatorial positions are in the same plane as the O–O vector. [c] The parameter τ is defined as the absolute value of the difference between the N_{ax}–Mn–N_{ax} and N_{eq}–Mn–N_{eq} bond angles divided by 60º (see Figure 1.2). [d] The peroxo of $[Mn^{III}(O_2)$(12-TMC)$]^+$ is disordered, making moot the distinction between equatorial and axial nitrogens. Consequently, an average Mn–N distance is provided for both Mn–N_{ax} and Mn–N_{eq}. When considering *trans* nitrogens, the N–Mn–N angles differ by less than 1º, making τ = 0.

Structural information on alkylperoxomanganese(III) adducts has come exclusively from the Kovacs lab.[45,46] Using pentadentate, N_4S^- ligands, a series of six η^1-alkylperoxomanganese(III) complexes were generated by treating the corresponding Mn^{II} complexes with *tert*-butyl- or cumyl-peroxide ($^-OO^{tBu}$ and $^-$OOCm, respectively). The crystal structure of $[Mn^{III}(OO^tBu)(S^{Me2}N_4$(QuinoEN))$]^+$ is shown in Figure 1.4 (left). In all structures, the η^1-alkylperoxo ligand is *cis* to the thiolate, two heterocyclic amines (quinolines or 6-methyl-pyridines), and the tertiary amine. The Mn–O distance is, on average, shorter than that observed for η^2-peroxomanganese(III) analogues, consistent with some Mn=OOR character, while the O–O distances are notably longer (Table 1.2). A crystallographically characterized η^1-

alkylperoxomanganese(II) complex, [Mn^{II}(OOCm)($Tp^{iPr,tBu}$)], shows a significantly longer Mn–O distance of 1.964(3) Å.[48] The greatest structural variation among the η^1-alkylperoxomanganese(III) complexes is the distance between the Mn^{III} center and the nitrogen atoms of the heterocyclic amines (N_{HA}), which range from 2.349 to 2.522 Å. These weak interactions tune the Lewis acidity of Mn^{III} center, resulting in an inverse correlation between the Mn^{III}–N_{HA} and O–O bond lengths (Figure 1.4, right).[46] More Lewis acidic Mn^{III} centers strengthen the O–O bond through greater peroxo-to-Mn^{III} charger transfer. [Mn^{III}(OOCm)($S^{Me2}N_4$(QuinoEn))]$^+$ is an outlier to this trend (Table 1.2), but its lower resolution structure has less reliable metric parameters.[45]

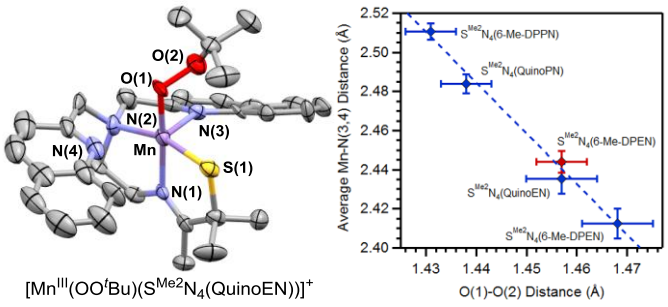

Figure 1.4. X-ray structure of [Mn^{III}(OO^{t}Bu)($S^{Me2}N_4$(QuinoEN))]$^+$ (left) and O(1)–O(2) bond length versus average Mn–N(3,4) distance for η^1-alkylperoxomanganese(III) complexes (right). *Tert*-butylperoxo- and cumylperoxomanganese(III) adducts are indicated in blue and red, respectively. Standard deviations in O(1)–O(2) and average Mn–N(3,4) distances are indicated.

The first structure of a peroxo-bridged Mn^{III} species was that of [Mn^{III}_3(*cis*-μ-1,2-O_2)(μ$_3$-O)(μ-OAc)$_2$(dien)$_3$]$^{3+}$, which was formed by refluxing $Mn^{II}(OAc)_2$ and dien in MeOH and cooling under air.[49] The high symmetry of this compound hampered refinement, leading to large uncertainties in metric parameters. The recently reported [Mn^{III}_2(*trans*-μ-1,2-O_2)($S^{Me2}N_4$(6-Me-DPEN))$_2$]$^{2+}$ complex provides the only high-resolution structure for a peroxo-bridged-

dimanganese(III,III) species (Table 1.2 and Figure 1.5).[47] In this complex, the peroxo has a *trans*-μ-1,2-geometry, with an unusually long O–O distance of 1.452(5) Å and short Mn–O distances of 1.832(3). A dimanganese(IV,IV) complex with a *cis*-μ-1,2-peroxo bridge, as well as two oxo bridges, has comparable O–O and Mn–O bond lengths (1.46(3) and 1.83(2) Å, respectively).[41c] Peroxo-bridged-diiron(III,III) species have shorter O–O bond lengths than $[Mn^{III}_2(\textit{trans}\text{-}\mu\text{-}1,2\text{-}O_2)(S^{Me2}N_4(6\text{-Me-DPEN}))_2]^{2+}$ (~1.41 Å),[50] while peroxo-bridged-dicopper(II,II) species show O–O distances varying greatly from 1.368(9) to 1.540(5) Å.[51,52] The $[Mn^{III}_2(\textit{trans}\text{-}\mu\text{-}1,2\text{-}O_2)(S^{Me2}N_4(6\text{-Me-DPEN}))_2]^{2+}$ complex was formed by reaction of $[Mn^{II}(S^{Me2}N_4(6\text{-Me-DPEN}))]^{+}$ with O_2 at low temperatures. Stopped-flow experiments between -10 and -40 ºC provided evidence for an intermediate (λ_{max} of 515 nm) that appears milliseconds after O_2 addition to $[Mn^{II}(S^{Me2}N_4(6\text{-Me-DPEN}))]^{+}$. This intermediate was formulated as the η^1-superoxo adduct, $[Mn^{III}(O_2)(S^{Me2}N_4(6\text{-Me-DPEN}))]^{+}$.[47] Eventually, $[Mn^{III}_2(\textit{trans}\text{-}\mu\text{-}1,2\text{-}O_2)(S^{Me2}N_4(6\text{-Me-DPEN}))_2]^{2+}$ converts to the oxo-bridged dimanganese(III,III) complex $[Mn^{III}_2(\mu\text{-}O)(S^{Me2}N_4(6\text{-Me-DPEN}))_2]^{2+}$, where the oxo is derived from O_2 (Figure 1.5, right).

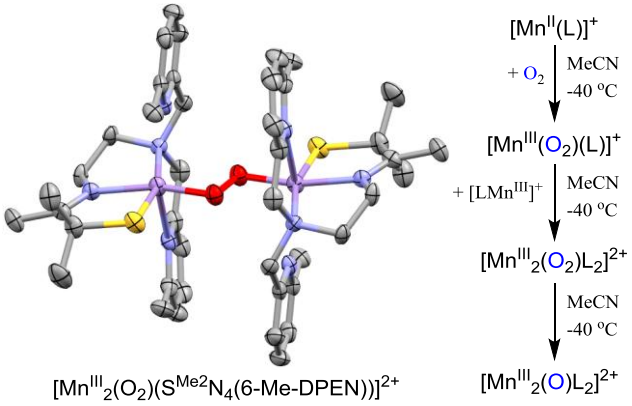

Figure 1.5. X-ray structure of $[Mn^{III}_2(\textit{trans}\text{-}\mu\text{-}1,2\text{-}O_2)(S^{Me2}N_4(6\text{-Me-DPEN}))_2]^{2+}$ (left) and scheme showing the O_2 reactivity of $[Mn^{II}(S^{Me2}N_4(6\text{-Me-DPEN}))]^{+}$ (right).

1.4. Spectroscopic Properties of Peroxo- and Alkylperoxomanganese(III) Complexes.

1.4.1. Vibrational Properties. To date, resonance Raman (rR) experiments of mononuclear η^2-peroxomanganese(III) adducts have been thwarted due to sample degradation upon laser irradiation.[26,30] Thus, vibrational data is scarce, $\nu_{O\text{-}O}$ having been observed for only six complexes (Table 1.3). No frequencies for Mn–O stretching vibrations ($\nu_{Mn\text{-}O}$) are available. The lack of vibrational data is an important challenge that has engendered exploration of new vibrational spectroscopies.[53] The situation is better for η^1-alkylperoxomanganese(III) adducts, where $\nu_{O\text{-}O}$ have been obtained for the majority of compounds (Table 1.3). For both η^2-peroxo- and η^1-alkylperoxo-manganese(III) complexes, $\nu_{O\text{-}O}$ are within the narrow range of 875 – 896 cm^{-1} (Table 1.3). In contrast, the resonance Raman spectrum of $[Mn^{III}_2(\textit{trans}\text{-}\mu\text{-}1,2\text{-}O_2)(S^{Me2}N_4(6\text{-Me-DPEN}))_2]^{2+}$ shows a lower-energy $\nu_{O\text{-}O}$ at 819 cm^{-1}.

The $^{16}O/^{18}O$ isotopic shifts observed for $\nu_{O\text{-}O}$ of η^1-alkylperoxomanganese(III) complexes are larger than expected on the basis of a diatomic harmonic oscillator, which suggests vibrational coupling between $\nu_{O\text{-}O}$ and $\nu_{Mn\text{-}O}$. Consequently, it is ill-advised to relate the $\nu_{O\text{-}O}$ frequencies to the extent of peroxo bond activation. Instead, the O–O force constants, which are obtained from a normal coordinate analysis, must be used to understand O–O activation. Such an analysis has only been achieved for $[Mn^{III}_2(\textit{trans}\text{-}\mu\text{-}1,2\text{-}O_2)(S^{Me2}N_4(6\text{-Me-DPEN}))_2]^{2+}$.[47] This revealed an O–O force constant comparable to those of dicopper(II,II) complexes with *trans*-1,2-bridging peroxo moieties, consistent with a fairly large degree of O–O activation.

Table 1.3. Experimental $\nu_{O\text{-}O}$ Frequencies (cm^{-1}); Mn^{III} Zero-field Splitting Parameters D (cm^{-1}) and E/D and Hyperfine Parameter A (mT); and Electronic Absorption Maxima (λ_{max} nm) and Extinction Coefficients (ε; $M^{-1}cm^{-1}$) for Peroxo- and Alkylperoxomanganese Complexes.

Complex	$\nu_{O\text{-}O}$ ($\Delta^{18}O$)	D	E/D	A	λ_{max} (ε)	ref.
η^2-peroxomanganese(III) adducts						
$[Mn(O_2)(Tp^{iPr2})(pz^{iPr2})]$ (brown)	892 (51)	ND[a]	ND[a]	ND[a]	561 (~50)[b]	24
$[Mn(O_2)(Tp^{iPr2})(pz^{iPr2})]$ (blue)	892 (51)	ND[a]	ND[a]	ND[a]	583 (~60)[b]	24
$[Mn(O_2)(Tp^{iPr2})(Me\text{-}Im)]$	896	ND[a]	ND[a]	ND[a]	381 (314), 478 (173)	25
$[Mn^{III}(O_2)(H_3bupa)]^-$	885 (48)	-2.0(5)	0.13(3)	5.7	660 (300), 490 (ND[a])	35
$[Mn^{III}(O_2)(H_2bpaa)]$	891 (52)	-2.03(3)	0.13	5.77	590 (58)	39
$[Mn^{III}(O_2)(mL_5^2)]^+$	ND[a]	-2.9	0.075	6.9	585 (335)	30,31
$[Mn^{III}(O_2)(imL_5^2)]^+$	ND[a]	-2	0.25-0.3	ND[a]	542 (484)	37
$[Mn^{III}(O_2)(N4py)]^+$	ND[a]	-1.5	0.15-0.3	6.8	617 (280)	37,38
$[Mn^{III}(O_2)(L^7py_2^H)]^{2+}$	ND[a]	-2	0.13	ND[a]	445 (280), 590 (120)	32
$[Mn^{III}(O_2)(L^7py_2^{6\text{-}Me})]^{2+}$	ND[a]	-3	0.05	ND[a]	415 (280)	32
$[Mn^{III}(O_2)(L^7py_2^{4\text{-}Me})]^{2+}$	ND[a]	-1.0	0.3	ND[a]	445 (260), ~588 (100)	33
$[Mn^{III}(O_2)(L^7py_2^{4\text{-}Cl})]^{2+}$	ND[a]	-1.0	0.2	ND[a]	442 (262), 568 (102)	34
$[Mn^{III}(O_2)(L^7iso\text{-}q_2)]^{2+}$	ND[a]	-1.0	0.2	ND[a]	446 (291), 587 (112)	34
$[Mn^{III}(O_2)(L^7py_2^{6\text{-}MeO})]^{2+}$	ND[a]	ND[a]	ND[a]	ND[a]	416 (250)	32
$[Mn^{III}(O_2)(L^7py_2^{5\text{-}Br})]^{2+}$	ND[a]	ND[a]	ND[a]	ND[a]	445 (220)	32
$[Mn^{III}(O_2)(L^7q_2)]^{2+}$	ND[a]	ND[a]	ND[a]	ND[a]	416 (305)	34
$[Mn^{III}(O_2)(L^8py_2^H)]^{2+}$	ND[a]	ND[a]	ND[a]	ND[a]	464 (280), 599 (120)	33
$[Mn^{III}(O_2)(TMC)]^+$	ND[a]	ND[a]	ND[a]	ND[a]	453 (490), 630 (120)	26
$[Mn^{III}(O_2)(13\text{-}TMC)]^+$	ND[a]	ND[a]	ND[a]	ND[a]	452 (390), 615 (190)	27
$[Mn^{III}(O_2)(12\text{-}TMC)]^+$	ND[a]	ND[a]	ND[a]	ND[a]	455 (250), 620 (200)	28
η^2-peroxomanganese(IV) adducts						
$[Mn^{IV}(O_2)(P(C_6H_3\text{-}3\text{-}SiMe_3\text{-}2\text{-}S)_3)]^-$	903 (42)	0.42-0.68	ND[a]	ND[a]	550 (1750), 755 (1000)[b]	44
$[Mn^{IV}(O_2)(TPP)]$	983 (50)	ND[a]	ND[a]	ND[a]	ND[a]	54
η^1-alkylperoxomanganese(IV) adducts						
$[Mn^{III}(OO^tBu)(S^{Me2}N_4(QuinoEN))]^+$	888 (57)	ND[a]	ND[a]	ND[a]	385 (640), 590 (465)	45
$[Mn^{III}(OOCm)(S^{Me2}N_4(QuinoEN))]^+$	ND[a]	ND[a]	ND[a]	ND[a]	596 (679)	45
$[Mn^{III}(OO^tBu)(S^{Me2}N_4(QuinoPN))]^+$	895 (64)	ND[a]	ND[a]	ND[a]	415 (510), 590 (465)	46
$[Mn^{III}(OO^tBu)(S^{Me2}N_4(6\text{-}Me\text{-}DPEN))]^+$	875 (59)	ND[a]	ND[a]	ND[a]	355 (1060), 600 (575)	46
$[Mn^{III}(OO^tBu)(S^{Me2}N_4(6\text{-}Me\text{-}DPPN))]^+$	893 (58)	ND[a]	ND[a]	ND[a]	420 (240), 585 (320)	46
$[Mn^{III}(OOCm)(S^{Me2}N_4(6\text{-}Me\text{-}DPEN)]^+$	ND[a]	ND[a]	ND[a]	ND[a]	590 (ND)[a]	46
peroxo-bridged dimanganese(III) adduct						
$[Mn^{III}_2(trans\text{-}\mu\text{-}1,2\text{-}O_2)(S^{Me2}N_4(6\text{-}Me\text{-}DPEN))_2]^{2+}$	819 (47)	-1.6	0		640 (830)	47

[a] Not determined. [b] Estimated from figure.

1.4.2. Ground-State Properties. The determination of ground-state spin Hamiltonian parameters, such as ZFS and hyperfine parameters, for well-defined manganese model complexes has long aided in the characterization of enzymatic intermediates.[14] Parallel-mode X-band EPR experiments for several η^2-peroxomanganese(III) adducts have shown a six-line signal centered at ~80 mT with a hyperfine splitting of ~6 – 7 mT (Table 1.3).[30,31,42] The ZFS parameters of η^2-peroxomanganese(III) and peroxo-bridged dimanganese(III,III) complexes are typical of axially elongated $S = 2$ Mn^{III} centers, with $D \approx -1$ to -2 cm^{-1} (Table 1.3). ZFS parameters have not yet been reported for η^1-alkylperoxomanganese(III) adducts.

1.4.3. Electronic Structure and Excited-state Properties of η^2-Peroxomanganese(III) Complexes. Combined spectroscopic and computational studies of η^2-peroxomanganese(III) complexes have afforded the experimentally validated bonding description schematically represented in Figure 1.6.[32,34] The Mn^{III} ligand field is dominated by strong interactions with the peroxo π^b and π^* frontier MOs that are fully occupied in the O_2^{2-} fragment. This results in the peroxo serving exclusively as a donor ligand. The peroxo π^b and π^* orbitals are classified as in-plane (π_{ip}) or out-of-plane (π_{op}) with respect to the η^2-Mn^{III}-O_2 unit. Using *D*-tensor coordinates from DFT computations, where the z-axis is along the elongated axis perpendicular to the O–O bond and the x-axis originates at Mn and bisects the O–O bond (Figure 1.6), the π_{ip}^* and π_{ip}^b sets participate in σ-interactions with the Mn d_{xy} and d_{z^2} orbitals, respectively. The π_{ip}^b orbital also has the proper symmetry to have a σ-interaction with the $d_{x^2-y^2}$ orbital. However, due to poor orbital orientations and the low energy of the peroxo π_{ip}^b orbital relative to the Mn 3d manifold, the $d_{x^2-y^2}$-π_{ip}^b and d_{z^2}-π_{ip}^b interactions are fairly weak. Better overlap is achieved between the Mn d_{xy} and π_{ip}^* orbitals, and this represents the dominant bonding interaction for η^2-

peroxomanganese(III) species. Because the Mn d_{xy}-based MO is unoccupied, the admixture of peroxo π_{ip}* character into this MO strengthens the O–O bond relative to the O_2^{2-} fragment. This is only slightly offset by a weakening of the O–O bond through the modest d_{z^2}-π_{ip}^{b} and $d_{x^2-y^2}$-π_{ip}^{b} interactions that mix peroxo bonding character into singly-occupied Mn d orbitals.

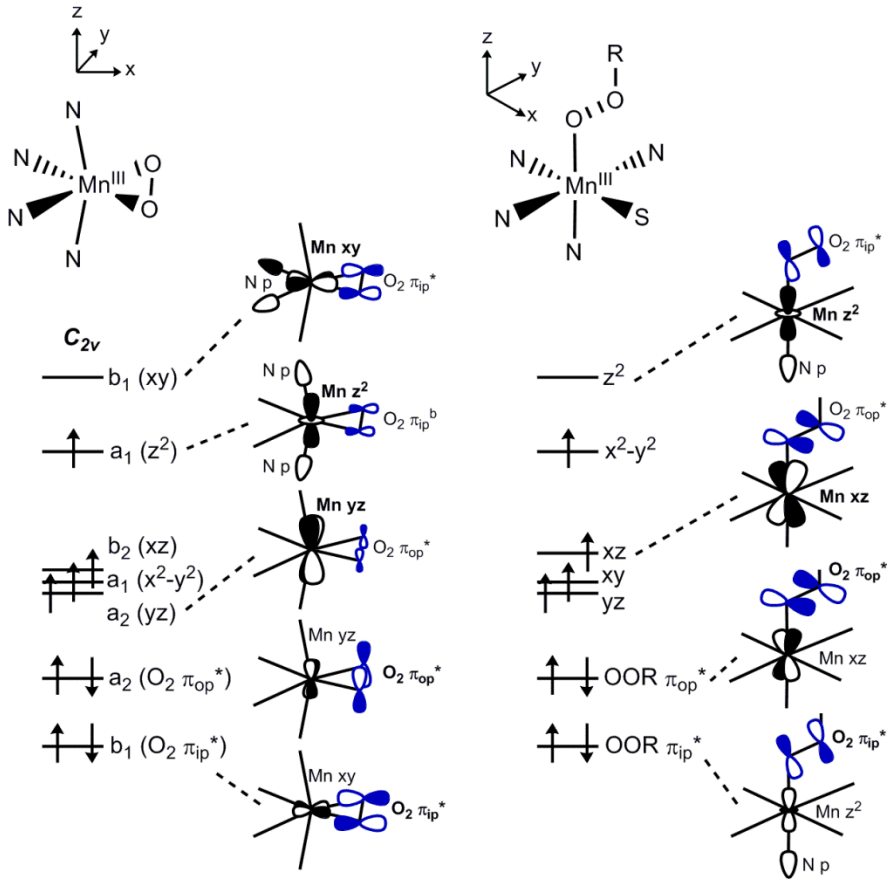

Figure 1.6. Qualitative representation of frontier molecular orbital splitting patterns for a six-coordinate η^2-peroxomanganese(III) complex with C_{2v} symmetry (left) and a six-coordinate η^1-alkylperoxomanganese(III) complex (right). Important Mn-OO(R) bonding interactions are indicated with schematic MO plots.

η^2-peroxomanganese(III) bonding is quite similar to that of η^2-peroxoiron(III) adducts. In both cases, the relatively high effective nuclear charge of the metal and the strong exchange stabilization of the respective $3d^4$ and $3d^5$ ions places the metal 3d manifolds at too low an

energy to interact strongly with the unoccupied peroxo σ* MO. Thus, there is virtually no metal-peroxo back-bonding. This stands in contrast to Cu^{II}-peroxo complexes, most prominently μ:η^2:η^2-peroxodicopper(II,II) systems such as oxyhemocyanin, where strong back-bonding interactions between the Cu^{II} $3d_{xy}$ orbital and the unoccupied peroxo σ* orbital weakens the O–O bond considerably.[51]

An important difference between the η^2-peroxomanganese(III) and η^2-peroxoiron(III) systems is that the metal-peroxo σ* MO (*i.e.* the $3d_{xy}$-based MO) is singly-occupied in the latter. All else being equal, partial occupancy of the metal-peroxo σ* MO is expected to lead to longer Fe^{III}–O bonds in η^2-Fe^{III}-O_2 systems. Though comparative studies of η^2-peroxomanganese(III) and η^2-peroxoiron(III) adducts are scarce, investigations using neutral N_5 ligands (mL_5^2 and N4py) provide evidence for differences in coordination preferences. For the η^2-peroxoiron(III) systems, the mL_5^2 and N4py ligands likely coordinate in a pentadentate mode, albeit with one long Fe–N distance *trans* to the peroxo moiety (Figure 1.7, left).[37,55] In contrast, spectroscopic and computational studies of $[Mn^{III}(O_2)(mL_5^2)]^+$ and $[Mn^{III}(O_2)(N4py)]^+$ indicate that the supporting ligands bind in a tetradentate fashion with noncoordinating pyridine moieties (Figure 1.7, right).[37] Presumably the shorter Mn^{III}–O bonds, and strong preference for η^2-peroxo coordination, forces the unusual tetradentate binding of the N_5 ligands.[37] A tetradentate N4py ligand was recently observed in a crystal structure of $[Mn^{III}Mn^{IV}(\mu\text{-}O)_2(N4py)_2]^{3+}$.[38] Notably, the Mn-SOD and Mn-HPCD-HPCA active sites (Figure 1.1 and Scheme 1.1) show only one coordination site available for an oxygen species, which could disfavor the formation of η^2-peroxomanganese adducts.

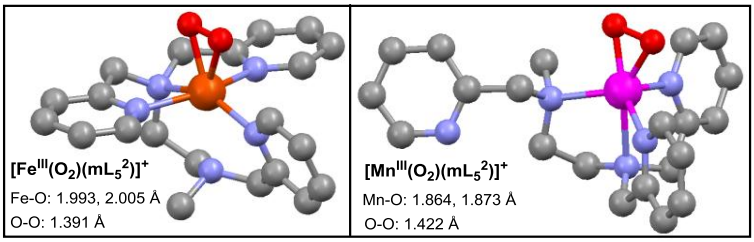

Figure 1.7. DFT-derived molecular structures of $[Fe^{III}(O_2)(mL_5{}^2)]^+$ (left) and $[Mn^{III}(O_2)(mL_5{}^2)]^+$ (right) complexes. The M–O and O–O distances are adjacent to the corresponding structures. For $[Fe^{III}(O_2)(mL_5{}^2)]^+$ the nitrogen *trans* to the peroxo unit is a distance of 2.479 Å from the Fe^{III} center.

η^2-Peroxomanganese(III) complexes show weak (ε = 60 - 490 $M^{-1}cm^{-1}$) bands in the visible region (λ_{max} = 670 – 415 nm; 14 925 – 24 096 cm^{-1}) that arise from a combination of Mn^{III} ligand-field and peroxo-to-Mn^{III} charge-transfer (CT) transitions.[32] On the basis of combined electronic absorption, magnetic circular dichroism (MCD), and TD-DFT investigations, detailed spectral assignments were developed for $[Mn^{III}(O_2)(L^7py_2{}^H)]^+$.[32] The dominant electronic absorption band of $[Mn^{III}(O_2)(L^7py_2{}^H)]^+$ (Figure 1.8, left) at 445 nm (22 472 cm^{-1}) was assigned as the peroxo $\pi_{op}^* \rightarrow Mn^{III}$ d_{yz} CT transition (see Figure 1.6).[32] The low intensity of this CT feature (ε = 280 $M^{-1}cm^{-1}$) is a consequence of the small peroxo character in the acceptor MO. The weaker absorption feature at 590 nm (16 950 cm^{-1}) was attributed to an electronic transition originating from a Mn^{III} $d_z{}^2 \rightarrow d_{xy}$ one-electron excitation. The corresponding transition energy for a "typical" six-coordinate Mn^{III} center is ~10 000 cm^{-1}.[56] The blue-shift for the peroxomanganese(III) complex results from strong peroxo-to-manganese(III) covalency significantly destabilizing the $3d_{xy}$ acceptor orbital (Figure 1.6). Variations in the strength of Mn^{III}-O_2 interactions among a series of structurally related complexes cause a shift in the Mn^{III} $d_z{}^2 \rightarrow d_{xy}$ transition.[34] Specifically, the ~3 000 cm^{-1} blue-shift of this transition energy for $[Mn^{III}(O_2)(L^7py_2{}^{6\text{-}Me})]^+$ relative to $[Mn^{III}(O_2)(L^7py_2{}^H)]^+$ (Figure 1.8) is consistent with weaker

Mn-O_2 interactions in the former complex. A DFT structure of $[Mn^{III}(O_2)(L^7py_2{}^{6\text{-}Me})]^+$ showed that the 6-Me-pyridine moieties crowd the peroxo binding pocket, causing a slightly elongated Mn–O bond relative to that of $[Mn^{III}(O_2)(L^7py_2{}^{H})]^+$. This minor change in bond length is magnified in the excited state energies because of the high covalency of the Mn^{III}-O_2 σ-interaction. Extension of this model to a series of peroxomanganese(III) complexes revealed a correlation between the Mn^{III} $d_z{}^2 \rightarrow d_{xy}$ transition energy and the DFT-calculated Mn–O distances (Figure 1.8, right).[34]

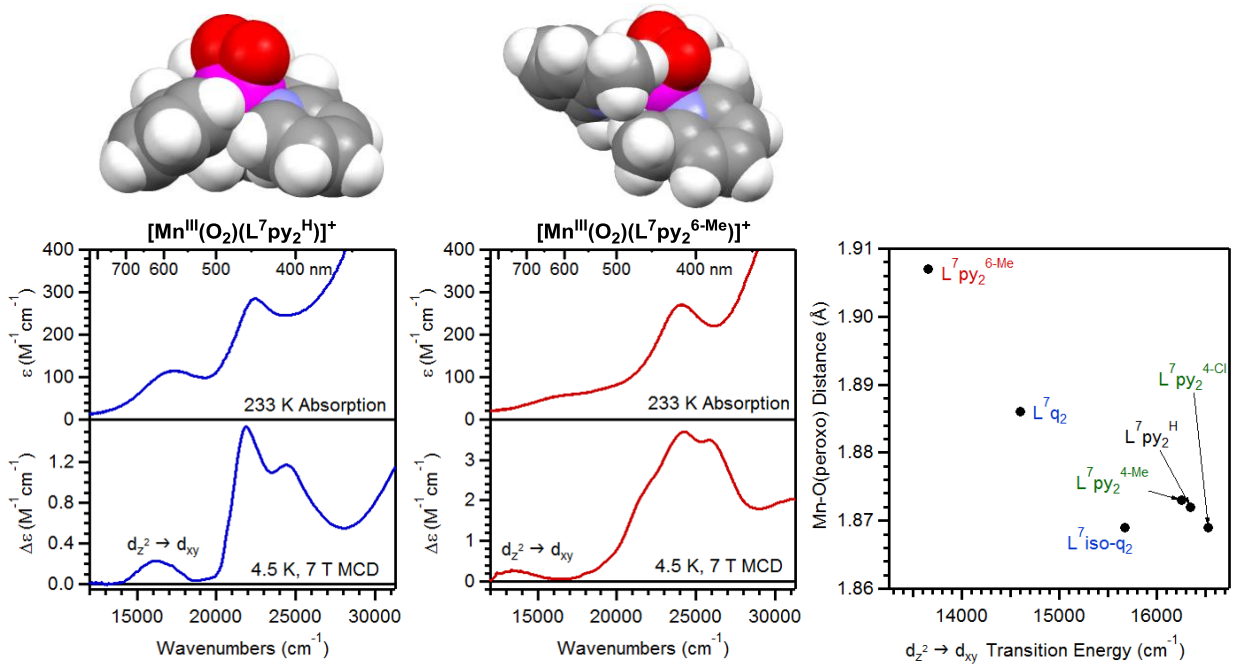

Figure 1.8. Electronic absorption and MCD spectra of $[Mn^{III}(O_2)(L^7py_2{}^{H})]^+$ (left) and $[Mn^{III}(O_2)(L^7py_2{}^{6\text{-}Me})]^+$ (center) with corresponding space-filling diagrams (top); relationship between the experimental Mn^{III} $d_z{}^2 \rightarrow d_{xy}$ transition energy and the longest DFT-computed Mn–O(peroxo) distance for a series of η^2-peroxomanganese(III) complexes supported by neutral N_4 ligands (right).

1.4.4. Electronic Structure and Excited-state Properties of η^1-Alkylperoxomanganese(III) Complexes. A schematic bonding description for an η^1-

alkylperoxomanganese(III) complex, which is modeled on that reported for a high-spin Fe^{III}-OOR system,[57] is shown in Figure 1.6 (right). The Mn^{III}-OOR unit consists of a σ-bond between the alkylperoxo π_{ip}* and Mn^{III} $3d_{z^2}$ orbitals and a π-bond between the alkylperoxo π_{op}* and Mn^{III} $3d_{xz}$ orbitals. The strength of the Mn–OOR π-bond is modulated by the Lewis acidity of the Mn^{III} center.[46] More Lewis acidic Mn^{III} centers have greater Mn d_{xz} character in the Mn–OOR π-bonding MO, which strengthens the O–O bond.[46] For the σ-interaction, admixture of alkylperoxo π_{ip}* character into the Mn^{III} $3d_{z^2}$-based MO should also strengthen the O–O bond. However, the alkylperoxo π_{ip}^{b} and σ^{b} orbitals could also contribute to Mn^{III}-OOR σ-interactions, as observed for a low-spin Fe^{III}-OOR complex.[58] These interactions would further strengthen the Mn–O bond but weaken the O–O bond. Considering that both low-spin Fe^{III}-OOR and Mn^{III}-OOR adducts decay by O-O homolysis, similarities in bonding might be expected (*vide infra*). The nature and relative contributions of σ- and π-bonding in Mn^{III}-OOR moieties are under investigation.

The electronic absorption spectra of η^1-alkylperoxomanganese(III) complexes show two bands at ~400 and 600 nm (Table 1.3) that have been assigned as Mn^{III} ligand-field and alkylperoxo-to-manganese(III) CT transitions, respectively.[46] The O–O bond length is correlated with the CT transition energy; longer bonds mark higher-energy transitions. Elongation of the O–O bond stabilizes the alkylperoxo π_{op}* donor MO relative to the Mn 3d manifold, causing the blue-shift of the CT transition energy. The intensity of the higher-energy alkylperoxo-to-manganese(III) CT transition varies considerably among the complexes (ε = 240 – 1060 $M^{-1}cm^{-1}$). This was attributed to modulation of Mn–OOR π-interactions caused by the range of Mn–O–O–R dihedral angles (126.6 – 163.6º).[46] The CT transition intensities of Mn^{III}-OOR

adducts fall on the low-end of first-row metal-peroxo CT intensities. For example, both high-spin and low-spin Fe^{III}-OOR systems show alklyperoxo π_{op}* to Fe^{III} d_{xz} CT transitions of moderate intensity ($\varepsilon \approx 1000 - 2000$ $M^{-1}cm^{-1}$), which has been associated with π-interactions that are, generally, weaker than those of copper-peroxo systems.[57,58] Thus, one could extrapolate from these data sets that π-interactions in Mn^{III}-OOR species are quite weak. However, care must be made in this comparison, as the supporting ligands for the Mn^{III} and Fe^{III} complexes are not equivalent and spectral deconvolutions are required to permit comparison of transition oscillator strengths.

1.5. Chemical Reactivity of Peroxo- and Alkylperoxomanganese(III) Adducts.

1.5.1. η^2-Peroxomanganese(III) Adducts. η^2-peroxomanganese(III) complexes are nucleophilic, reacting with aldehydes, protons, acid chlorides and anhydrides, and other metal centers. For example, treatment of η^2-peroxomanganese(III)-porphyrin complexes with benzoyl chloride or benzoyl anhydride yields acylperoxomanganese(III) species that undergo O–O heterolysis to produce the corresponding oxomanganese(V) complexes (Scheme 1.3A).[59-61] More recently, the hydroxo-hydroperoxo-manganese(III) complex, [Mn(OH)(OOH)(TDMImP)] (TDMImP = 5,10,15,20-tetrakis-(1,3-dimethylimidazolium-2-yl)porphyrin), which features an electron-deficient porphyrin, was shown to decay to a *trans*-dioxomanganese(V) species.[62] In this reaction O–O heterolysis is coupled to deprotonation of the *trans* OH^- ligand, mimicking the "push-pull" mechanism of P450 enzymes.

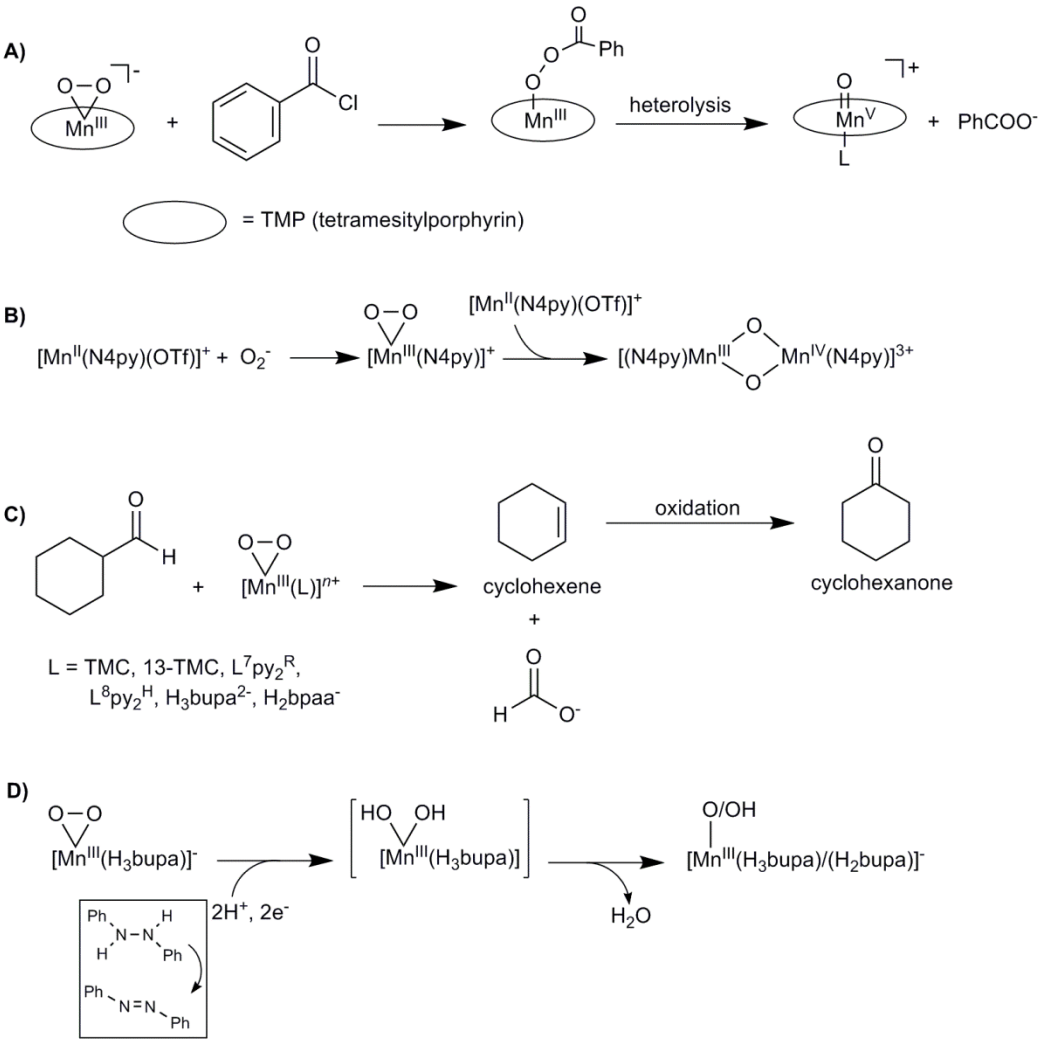

Scheme 1.3. Chemical reactivity of peroxomanganese(III) adducts.

The conversion of non-porphyrin η^2-peroxomanganese(III) complexes to high-valent oxomanganese species is less common. The $[Mn^{III}(O_2)(mL_5^2)]^+$ complex reacts with acid to generate 2-pyridinecarboxylate by oxidative degradation of mL_5^2, implying acid-assisted formation of a strong oxidant.[31] The related $[Mn^{III}(O_2)(N4py)]^+$ complex, which is generated from $[Mn^{II}(N4py)(OTf)]^+$ and superoxide, reacts with $[Mn^{II}(N4py)(OTf)]^+$ to generate the bis(μ-oxo)dimanganese(III,IV) complex $[Mn^{III}Mn^{IV}(\mu\text{-}O)_2(N4py)_2]^{3+}$ (Scheme 1.3B).[38] Presumably, the nucleophilic peroxo of $[Mn^{III}(O_2)(N4py)]^+$ attacks $[Mn^{II}(N4py)(OTf)]^+$ to form a dinuclear,

peroxo-bridged intermediate prior to the formation of $[Mn^{III}Mn^{IV}(\mu\text{-}O)_2(N4py)_2]^{3+}$. The conversion of two Mn^{II} species to an oxo-bridged $Mn^{III}Mn^{IV}$ compound using superoxide mimics the currently proposed mechanism for assembly of the $Mn^{III}Mn^{IV}$ cofactor in Mn-RNR.[11] Moreover, this general reactivity is similar to that of mononuclear Cu^{II}-O_2 and Ni^{III}-O_2 adducts, which can react with a second metal complex to form homo- and hetero-dinuclear complexes with bis-(μ-oxo) or μ-peroxo cores.[63-65]

The nucleophilicity of η^2-peroxomanganese(III) complexes is most commonly on display in aldehyde deformylation reactions (Scheme 1.3C). Such reactivity has been reported for η^2-peroxomanganese(III) complexes featuring H_3bupa^{2-},[35] H_2bpaa^-,[39] TMC-derived,[26-28] and $L^7py_2^R$-derived[33] ligands. Using a series of $[Mn^{III}(O_2)(13\text{-}TMC)(X)]$ complexes (where X = CN^-, NCS^-, $CF_3CO_2^-$, and N_3^-), it was found that the rate of cyclohexanecarboxaldehyde (CCA) deformylation increases with the electron-donating ability of the axial ligand *trans* to the peroxo.[27] Specifically, the second-order rate constant for CCA deformylation by $[Mn^{III}(O_2)(13\text{-}TMC)(N_3)]$ was 10^4 larger than that of $[Mn^{III}(O_2)(13\text{-}TMC)]^+$. Binding of a strongly electron-donating ligand clearly enhances the nucleophilicity of the Mn^{III}-O_2 unit, perhaps by favoring a more end-on structure.[27] The TMC ligand was also used to compare the deformylation activity of $[M^{III}(O_2)(TMC)]^+$ complexes (M = Fe, Mn, and Co).[66] $[Mn^{III}(O_2)(TMC)]^+$ and $[Co^{III}(O_2)(TMC)]^+$ showed similar rates, but were an order of magnitude faster than $[Fe^{III}(O_2)(TMC)]^+$.[66] This contrasts with the reactivity of $[Mn^{III}(O_2)(TMP)]^-$ and $[Fe^{III}(O_2)(TMP)]^-$ (TMP = tetramesitylporphyrin), where the Fe^{III}-O_2 species shows significantly more nucleophilicity towards a range of substrates.[67] The factors accounting for these disparate results are unclear.

While there has been limited success in activating non-porphyrin η^2-peroxomanganese(III) adducts using electrophilic substrates, activation of the O–O bond in

$[Mn^{III}(O_2)(H_3bupa)]^-$ was achieved by treatment with a hydrogen-atom donor. This intriguing chemistry was employed in the catalytic reduction of O_2 to H_2O by $[Mn^{II}(H_2bupa)]^-$, with DPH or hydrazine as the reductant.[36] In the first step of the catalytic cycle, $[Mn^{III}(O_2)(H_3bupa)]^-$ is generated from $[Mn^{II}H_2bupa]^-$, O_2, and 0.5 equivalents DPH. The Mn^{III}-O_2 unit then accepts two hydrogen atoms from an additional equivalent of DPH, and the resulting species undergoes O–O cleavage to give H_2O and a new manganese(III) intermediate described as a Mn^{III}–O and Mn^{III}–OH hybrid, with strong hydrogen bonding to the supporting ligand.[36] This intermediate reacts with half an equivalent DPH to produce a second H_2O molecule and regenerate $[Mn^{II}(H_2bupa)]^-$.[36] The reactivity of $[Mn^{III}(O_2)(H_3bupa)]^-$ with reductants is initially surprising, considering that the η^2-Fe^{III}-O_2 adduct $[Fe^{III}(O_2)(EDTA)]^{3-}$ is unreactive towards strong one- and two-electron reductants such as $Na_2S_2O_4$ and $NaBH_4$.[68] This reactivity difference is presumably a consequence of the intrinsically lower potential of the $Fe^{II/III}$ couple relative to $Mn^{II/III}$ (the reduction potentials for hexaaqua $Fe^{II/III}$ and $Mn^{II/III}$ are 0.77 and 1.51 V versus NHE). In support, very recent work has shown that the binding of Lewis acids to an η^2-peroxoiron(III) complex promotes reaction with reductants, leading to the formation of an oxoiron(IV) species.[69]

1.5.2. η^1-Alkylperoxomanganese(III) Adducts. η^1-alkylperoxomanganese(III) complexes show a lack of reactivity with electrophilic or nucleophilic organic substrates. However, there is strong evidence that these complexes decay in the absence of substrates by rate-determining O–O homolysis.[45,46] Activation parameters ($\Delta H^{\ddagger}$ and $\Delta S^{\ddagger}$) for thermal decay are correlated with O–O bond length, with shorter bonds associated with higher activation barriers. Only a small correlation was observed between activation parameters and the Mn–O bond lengths. Support for O–O homolysis was offered by a product analysis of the anaerobic decay of

cumylperoxomanganese(III) complexes, which revealed exclusive formation of acetophenone rather than cumenol.[46]

It is interesting to consider these results in light of the decay pathways of high- and low-spin Fe^{III}–OOR centers, which, generally, are primed for Fe–O and O–O homolysis, respectively.[57,58] The preference for O–O homolysis in the low-spin system was attributed to the following factors: i) electron transfer from the Fe^{III} center to the peroxo ligand is facilitated by an allowed orbital interaction between the donor and acceptor MOs, leading to a low activation barrier for O–O cleavage; ii) the lack of electrons in the Fe^{III}-peroxo σ* MO allows for the gradual formation of a strong Fe–O σ-bond as the O–O bond is elongated.[57,58] Although the specific orbital pathways for O–O homolysis in η^1-alkylperoxomanganese(III) systems have not yet been defined, the d^4 electron configuration of the η^1-alkylperoxomanganese(III) adducts leads to an unoccupied metal(III)-peroxo σ* MO (the Mn^{III} d_z^2 MO in Figure 1.6), similar to low-spin Fe^{III}-OOR systems. Thus, a strong Mn–O bond is expected to form as the O–O coordinate is elongated. It is unclear at present how specific aspects of the supporting ligand tune the decay pathway of the η^1-alkylperoxomanganese(III) unit. For low-spin Fe^{III}-OOR adducts, thiolate ligation is known to strongly modulate reactivity.[70]

1.6. Oxomanganese(IV) Complexes.

High-valent oxomanganese centers have been invoked as key intermediates in a variety of biological and synthetic processes, ranging from water splitting in the oxygen-evolving complex of photosystem II to olefin epoxidation in synthetic manganese catalysts.[7,71-77] In particular, synthetic oxomanganese(V)- and manganese(IV) adducts have attracted much interest over the past 30 years, and their reactivities have been investigated in oxidation reactions such as

C–H bond activation, olefin epoxidation, halogenation, and hydride- and electron-transfer reactions.[73,78-83] In synthetic oxidation reactions catalyzed by manganese, it has been proposed that monomeric oxomanganese adducts, generated with oxygen-atom transfer agents such as iodosobenzene, peroxy acids, or NaOCl, participate as reactive electrophiles.[75,77,80-82] Oxomanganese(IV) complexes are emphasized in this dissertation, and our discussion of these complexes will begin with methods used to generate oxomanganese(IV) adducts and then focus on structural and physical properties.

1.6.1. Formation and Characterization of Oxomanganese(IV) Complexes. Monomeric oxomanganese(IV) complexes supported by dianionic, tetradentate (N4) porphyrin ligands were first isolated and spectroscopically characterized in the 1980's.[73,84-88] A variety of oxidizing agents, such as *m*-chloroperoxybenzoic acid (under basic conditions),[73,85,86,89] peroxoycarbonate,[87,90] and hypochlorite,[84] have been employed to generate Mn^{IV}=O porphyrin complexes from manganese(III)-porphyrin precursors (Table 1.4). In addition, a number of Mn^{IV}=O porphyrins have been prepared by electrochemical,[73,85,86] photochemical,[83] and aerobic[73] oxidation of manganese(III)-porphyrin precursors (Table 1.4). Depending on the method used to prepare these Mn^{IV}=O porphyrins, five- and six-coordinate species have been isolated.

Table 1.4. Oxidants Used to Generate Oxomanganese(IV) Adducts from Manganese(II) and Manganese(III) Precursors; Experimental (EXAFS) and DFT-computed Mn–O Distances (Å); Experimental $\nu_{Mn\text{-}O}$ Frequencies (cm^{-1}); Mn^{IV} Zero-field Splitting Parameters *D* (cm^{-1}) and *E/D*; and *g*-values for Oxomanganese(IV) Complexes.

Complex	oxidant	Mn–O	$\nu_{(Mn\text{-}O)}$	*D*	*E/D*	*g*-value	ref.
oxomanganese(IV) porphyrins							
$[Mn^{IV}(O)(OH_2)(TPP)]$	NaOCl	1.84	ND[a]	ND[a]	ND[a]	ND[a]	84
$[Mn^{IV}(O)(TPP)]$	CO_2OO^{2-}	ND[a]	ND[a]	>0.31	ND[a]	~4.4, ~2	85,87
$[Mn^{IV}(O)(TPFPP)]$	CO_2OO^{2-}	1.67	ND[a]	>0.31	ND[a]	~4.4, ~2	87
$[Mn^{IV}(O)(T_{piv}PP)]$	CO_2OO^{2-}	1.69	ND[a]	>0.31	ND[a]	~4.4, ~2	84,87,90
$[Mn^{IV}(O)(TMP)]$	*m*-cpba[b,c]	ND[a]	754	ND[a]	ND[a]	~4, ~2	85,91
$[Mn^{IV}(O)(OH)(TMP)]^-$	*m*-cpba[b,c]	ND[a]	712	ND[a]	ND[a]	~4, ~2	91
$[Mn^{IV}(O)(X)(TMP)]^-$	O_2	ND[a]	752	ND[a]	ND[a]	~4, ~2	91
$[Mn^{IV}(O)(Cl_8TPP)]$	*m*-cpba	ND[a]	728	ND[a]	ND[a]	ND[a]	89
non-porphyrin oxomanganese(IV)							
$[Mn^{IV}(O)(salen)]$	*m*-cpba[b] *or* O_3	1.58 (1.67)[d]	ND[a]	>0	~0.05	4.2, 3.5, 1.95	92
$[Mn^{IV}(O)(Bn\text{-}TPEN)]^{2+}$	PhIO[e]	1.69 (1.68)[d]	ND[a]	ND[a]	ND[a]	5.5, 2.76, 1.76	82
$[Mn^{IV}(O)(N4py)]^{2+}$	PhIO[e]	1.69 (1.67)[d]	ND[a]	ND[a]	ND[a]	~5.76	79
$[Mn^{IV}(O)(OH_2)(BQCN)]^{2+}$	CAN/H_2O[f] *or* PhIO[e]	(1.67)[d]	707	2	0	~4	93
$[Mn^{IV}(O)(H_3buea)]^-$	$[Cp_2Fe]BF_4$	(1.706)[d]	737	3.0	0.26	5.15, 2.44, 1.63	94
$[Mn^{IV}(O)(OH)(Me_2EBC)]^+$	NaOH	1.68 (1.71)[d]	ND[a]	+1.0(5)	0.22(1)	4.99, 2.62, 1.69	95
$[Mn^{IV}(O)(OH)(^{H,Me}Pytacn)]^+$	^{t}BuOK	ND[a]	712	ND[a]	ND[a]	~4, ~2	96

[a] Not determined. [b] *m*-chloroperoxybenzoic acid. [c] can also be formed by electrochemical oxidation. [d] DFT-computed Mn–O distance. [e] iodosylbenzene. [f] cerium ammonium nitrate.

Non-porphyrin oxomanganese(IV) complexes have been more elusive and were not isolated until the mid-2000's.[80,92,97] Five-coordinate $[Mn^{IV}(O)(salen)]$, supported by a dianionic tetradentate ligand ($[salen]^{2-}$ = bis(3,5-dimesitylsalicylidene)-1,2-dimesitylethylenediamine), has a structure most similar to that of the Mn^{IV}=O porphyrins (Figure 1.9) and can be generated by oxidation of the manganese(III) precursor with either *m*-chloroperoxybenzoic acid or ozone.[92,98] The oxygen-atom transfer agent iodosylbenzene has been used to form three six-coordinate oxomanganese(IV) species from manganese(II) complexes supported by neutral aminopyridinyl pentadentate N5 (N4py, Bn-TPEN)[79,82] and aminoquinyl tetradentate N4 (BQCN)[93] ligands. Notably, $[Mn^{IV}(O)(OH_2)(BQCN)]^{2+}$ (BQCN = *N,N'*-dimethyl-*N,N'*-bis(8-

quinolyl)cyclohexanediamine) can also be generated from $[Mn^{II}(BQCN)](CF_3SO_3)_2$ using water as an oxygen source and cerium ammonium nitrate (CAN) as a one-electron oxidant.[93] Similarly, Borovik *et al.* prepared an oxomanganese(IV) complex upon oxidation of $[Mn^{III}(O)(H_3buea)]^{2-}$ ($[H_3buea]^{3-}$ = tris[(*N*'-*tert*-butylureaylato)-*N*-ethylene]aminato), a Mn^{III}–oxo complex in which the oxo ligand is derived from water,[99] with $[Cp_2Fe]BF_4$, a mild, one-electron oxidant.[80] Two oxo(hydroxo)manganese(IV) complexes, $[Mn^{IV}(O)(OH)(Me_2EBC)]^+$ and $[Mn^{IV}(O)(OH)(^{H,Me}Pytacn)]^+$ (Me_2EBC = 4,11-dimethyl-1,4,8,11-tetraazabicyclo[6.6.2]hexadecane and $^{H,Me}Pytacn$ = 1-(2-pyridylmethyl)-4,7-dimethyl-1,4,7-triazacyclononane), have been formed by deprotonation of a hydroxo ligand of the corresponding bis(hydroxo)manganese(IV) complexes using NaOH and ^{t}BuOK, respectively.[95,97,100]

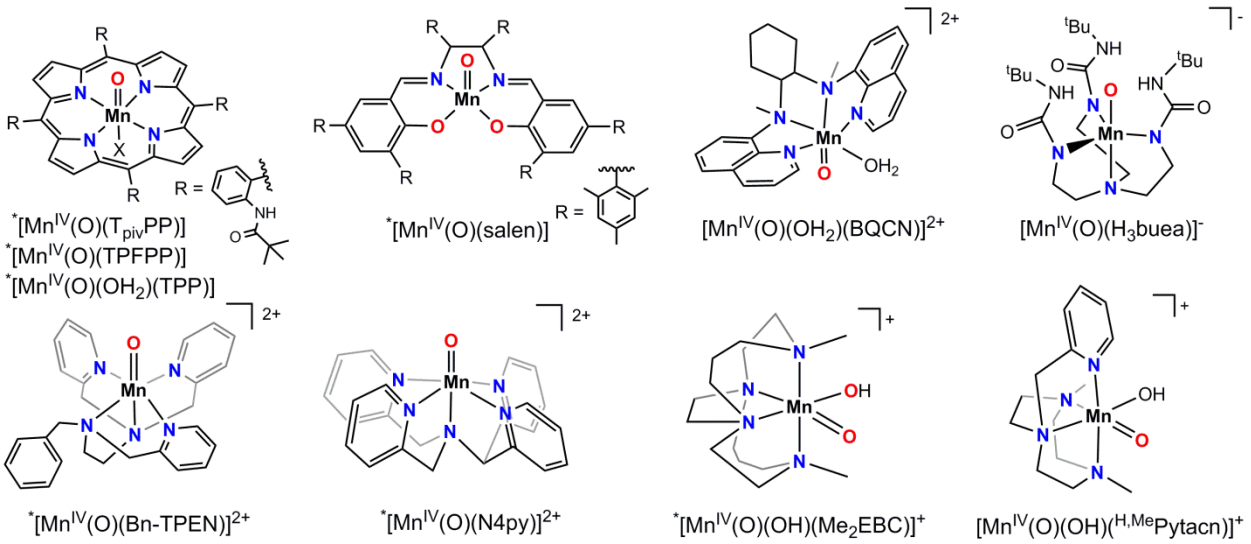

Figure 1.9. Molecular structures of oxomanganese(IV) complexes. These structures are inferred on the basis of spectroscopic data and, in some cases, from models developed using DFT methods. Complexes of this set that have been structurally characterized by Mn K-edge X-ray absorption spectroscopy are marked with an asterisk.

Although none of these oxomanganese(IV) complexes have been characterized by X-ray diffraction, their formulations and structures are inferred on the basis of spectroscopic, mass spectral, and/or computational studies. Nearly all of the isolated Mn^{IV}=O compounds have been characterized, at least in part, using perpendicular-mode X-band EPR spectroscopy. The EPR spectra of Mn^{IV}=O porphyrins have invariably shown strong, broad resonances centered at $g_{\perp} \approx 4$ and weak resonances at $g_{\parallel} \approx 2$. This set of signals is characteristic of high-spin (S = 3/2) Mn^{IV} centers in which the axial zero-field splitting parameter D is larger than the energy of the incident microwave photon (0.3 cm^{-1}; see Table 1.4).[101-104] The EPR spectra of some non-porphyrin Mn^{IV}=O complexes show resonances similar to those of the porphyrin species ($g_{\perp} \approx 4$ and $g_{\parallel} \approx 2$), while some show signals that are more rhombic, with three resonances at $g \approx 5.1$, 2.5, and 1.6. Values for the ZFS parameters, however, have only been reported for $[Mn^{IV}(O)(OH_2)(BQCN)]^{2+}$ (D = 2, E/D = 0) and $[Mn^{IV}(O)(H_3buea)]^{-}$ (D = 3.0, E/D = 0.26), which display axial and rhombic EPR signals, respectively (Table 1.4).[80,93]

Direct evidence for Mn–oxo bonds in oxomanganese(IV) complexes comes from resonance Raman and infrared spectroscopy, where the Mn–O stretching vibration can be determined from $^{16}O/^{18}O$ labelling experiments. Vibrational data have been reported for approximately half the Mn^{IV}=O complexes, and in those cases Mn–O stretching vibrations (ν_{Mn-O}) have been observed in the range of 712 – 754 cm^{-1} (Table 1.4).[73,80,85,89,93,100] The position of ν_{Mn-O} varies with coordination environment. For example, ν_{Mn-O} was located at 754 cm^{-1} for five-coordinate $[Mn^{IV}(O)(TMP)]$ and at 712 cm^{-1} for six-coordinate $[Mn^{IV}(O)(OH)(TMP)]^{-}$ (Table 1.4).[85] The lower ν_{Mn-O} of $[Mn^{IV}(O)(OH)(TMP)]^{-}$ is attributed to vibrational coupling of the Mn=O stretch with the Mn–O–H bend of the axial hydroxide ligand.[85] The Mn^{IV}–oxo bond in $[Mn^{IV}(O)(TMP)]$ is much weaker than the corresponding Fe^{IV}–oxo bond in the related

$[Fe^{IV}(O)(TMP)]^+$, as evident by the metal-oxo force constants obtained from normal coordinate analyses, where the Mn^{IV}=O force constant is significantly lower than that of Fe^{IV}=O (4.15 and 5.21 mdyn/Å, respectively).[85] The Fe^{IV}=O force constant is higher due to the greater effective nuclear charge of Fe^{IV} relative to that of Mn^{IV}.

Mn K-edge XAS has played a critical role in defining manganese-ligand distances for oxomanganese(IV) complexes that have thus far eluded characterization by X-ray crystallography.[79,82,87,90,92] Only a handful of monomeric oxomanganese(IV) complexes have been characterized by XAS.[79,82,90,92] The structures of these complexes are denoted by an asterisk in Figure 1.9. The oxomanganese(IV) complexes fall into three classes: i) six-coordinate oxomanganese(IV) complexes supported by neutral N5 ligands ($[Mn^{IV}(O)(N4py)]^{2+}$ and $[Mn^{IV}(O)(Bn\text{-}TPEN)]^{2+}$);[79,82] ii) six-coordinate complexes with an N_4O^- coordination sphere ($[Mn^{IV}(O)(OH)(Me_2EBC)]^+$); and iii) five-coordinate, square pyramidal complexes supported by dianionic ligands ($[Mn^{IV}(O)(salen)]$, $[Mn^{IV}(O)(T_{piv}PP)]$, and $[Mn^{IV}(O)(TPFPP)]$ where $T_{piv}PP$ = *meso*-tetra(*α,α,α,α*-pivalamidophenyl-porphyrinato) dianion and TPFPP = 5,10,15,20-tetrakis(pentafluorophenyl) porphyrinato dianion).[87,90,92] The EXAFS-determined Mn^{IV}=O bond lengths fall within the range of 1.67 – 1.71 Å, where $[Mn^{IV}(O)(OH)(Me_2EBC)]^+$ features the longest Mn^{IV}=O bond, possibly due to the presence of a strong σ-donor (hydroxide) *cis* to the oxo (Table 1.4). With one exception, the experimentally determined Mn^{IV}=O distances are in excellent agreement with the DFT-computed metric parameters, as well as for models of other Mn(IV) centers with terminal oxo ligands (1.673 – 1.706 Å by DFT computations).[79,80,82,87,90,92,93,95,98] The only exception is $[Mn^{IV}(O)(salen)]$, where the EXAFS-determined Mn–O bond length (1.58 Å) is much shorter than both the computational result (1.67 Å) and the range of EXAFS distances observed for other oxomanganese(IV) species. This

exceptionally short bond length is more consistent with an oxomanganese(V) unit (1.55 – 1.56 Å).[105-109]

Notes and References.

1. Miller, A.-F., *Curr. Opin. Chem. Biol.* **2004,** *8*, 162-168.
2. Wu, A. J.; Penner-Hahn, J. E.; Pecoraro, V. L., *Chem. Rev.* **2004,** *104*, 903-938.
3. Grove, L. E.; Brunold, T. C., *Comments Inorg. Chem.* **2008,** *29*, 134-168.
4. Gunderson, W. A.; Zatsman, A. I.; Emerson, J. P.; Farquhar, E. R.; Que, L.; Lipscomb, J. D.; Hendrich, M. P., *J. Am. Chem. Soc.* **2008,** *130*, 14465-14467.
5. Svedružic, D.; Jónsoon, S.; Toyota, C. G.; Reinhardt, L. A.; Ricagno, S.; Lindqvist, Y.; Richards, N. G. J., *Arch. Biochem. Biophys.* **2005,** *433*, 176-192.
6. Cotruvo, J. J. A.; Stubbe, J., *Metallomics* **2012,** *4*, 1020-1036.
7. McEvoy, J. P.; Brudvig, G. W., *Chem. Rev.* **2006,** *106*, 4455-4483.
8. Cox, N.; Pantazis, D. A.; Neese, F.; Lubitz, W., *Acc. Chem. Res.* **2013,** *46*, 1588-1596.
9. Bull, C.; Niederhoffer, E. C.; Yoshida, T.; Fee, J. A., *J. Am. Chem. Soc.* **1991,** *113*, 4069-4076.
10. Hearn, A. S.; Tu, C. K.; Nick, H. S.; Silverman, D. N., *J. Biol. Chem.* **1999,** *274*, 24457-24460.
11. Cotruvo, J. A.; Stich, T. A.; Britt, R. D.; Stubbe, J., *J. Am. Chem. Soc.* **2013**.
12. Messinger, J.; Badger, M.; Wydrzynski, T., *Proceedings of the National Academy of Sciences* **1995,** *92*, 3209-3213.
13. Pecoraro, V. L.; Baldwin, M., J.; Caudle, M. T.; Hsieh, W.-Y.; Law, N., A., *Pure Appl. Chem.* **1998,** *70*, 925-929.
14. Pecoraro, V. L.; Baldwin, M. J.; Gelasco, A., *Chem. Rev.* **1994,** *94*, 807-826.
15. Edwards, R. A.; Baker, H. M.; Whittaker, M. M.; Whittaker, J. W.; Jameson, G. B.; Baker, E. N., *J. Biol. Inorg. Chem.* **1998,** *3*, 161-171.
16. Pick, M.; Rabani, J.; Yost, F.; Fridovich, I., *J. Am. Chem. Soc.* **1974,** *96*, 7329-7333.
17. Hsu, J. L.; Hsieh, Y. S.; Tu, C. K.; Oconnor, D.; Nick, H. S.; Silverman, D. N., *J. Biol. Chem.* **1996,** *271*, 17687-17691.
18. Carrasco, R.; Morgenstern-Badarau, I.; Cano, J., *Inorg. Chim. Acta* **2007,** *360*, 91-101.
19. Abreu, I. A.; Rodriguez, J. A.; Cabelli, D. E., *The Journal of Physical Chemistry B* **2005,** *109*, 24502-24509.
20. Jackson, T. A.; Karapetian, A.; Miller, A.-F.; Brunold, T. C., *Biochemistry* **2005,** *44*, 1504-1520.
21. Porta, J.; Vahedi-Faridi, A.; Borgstahl, G. E. O., *J. Mol. Biol.* **2010,** *399*, 377-384.
22. Koehntop, K. D.; Emerson, J. P.; Que, L., Jr., *J. Biol. Inorg. Chem.* **2005,** *10*, 87-93.
23. VanAtta, R. B.; Strouse, C. E.; Hanson, L. K.; Valentine, J. S., *J. Am. Chem. Soc.* **1987,** *109*, 1425-1434.
24. Kitajima, N.; Komatsuzaki, H.; Hikichi, S.; Osawa, M.; Moro-oka, Y., *J. Am. Chem. Soc.* **1994,** *116*, 11596-11597.
25. Singh, U. P.; Sharma, A. K.; Hikichi, S.; Komatsuzaki, H.; Moro-oka, Y.; Akita, M., *Inorg. Chim. Acta* **2006,** *359*, 4407-4411.

26. Seo, M. S.; Kim, J. Y.; Annaraj, J.; Kim, Y.; Lee, Y.-M.; Kim, S.-J.; Kim, J.; Nam, W., *Angew. Chem., Int. Ed. Engl.* **2007,** *46*, 377-380.
27. Annaraj, J.; Cho, J.; Lee, Y.-M.; Kim, S. Y.; Latifi, R.; de Visser, S. P.; Nam, W., *Angew. Chem., Int. Ed. Engl.* **2009,** *48*, 4150-4153.
28. Kang, H.; Cho, J.; Cho, K.-B.; Nomura, T.; Ogura, T.; Nam, W., *Chem. Eur. J.* **2013,** *19*, 14119-14125.
29. Cho, J.; Sarangi, R.; Nam, W., *Acc. Chem. Res.* **2012,** *45*, 1321-1330.
30. Groni, S.; Blain, G.; Guillot, R.; Policar, C.; Anxolabéhère-Mallart, E., *Inorg. Chem.* **2007,** *46*, 1951-1953.
31. Groni, S.; Dorlet, P.; Blain, G.; Bourcier, S.; Guillot, R.; Anxolabéhère-Mallart, E., *Inorg. Chem.* **2008,** *47*, 3166-3172.
32. Geiger, R. A.; Chattopadhyay, S.; Day, V. W.; Jackson, T. A., *J. Am. Chem. Soc.* **2010,** *132*, 2821-2831.
33. Geiger, R. A.; Chattopadhyay, S.; Day, V. W.; Jackson, T. A., *Dalton Trans.* **2011,** *40*, 1707-1715.
34. Geiger, R. A.; Wijeratne, G.; Day, V. W.; Jackson, T. A., *Eur. J. Inorg. Chem.* **2012**, 1598-1608.
35. Shook, R. L.; Gunderson, W. A.; Greaves, J.; Ziller, J. W.; Hendrich, M. P.; Borovik, A. S., *J. Am. Chem. Soc.* **2008,** *130*, 8888-8889.
36. Shook, R. L.; Peterson, S. M.; Greaves, J.; Moore, C.; Rheingold, A. L.; Borovik, A. S., *J. Am. Chem. Soc.* **2011,** *133*, 5810-5817.
37. Geiger, R. A.; Leto, D. F.; Chattopadhyay, S.; Dorlet, P.; Anxolabéhère-Mallart, E.; Jackson, T. A., *Inorg. Chem.* **2011,** *50*, 10190-10203.
38. Leto, D. F.; Chattopadhyay, S.; Day, V. W.; Jackson, T. A., *Dalton Trans.* **2013,** *42*, 13014-13025.
39. Shook, R. L.; Borovik, A. S., *Inorg. Chem.* **2010,** *49*, 3646-3660.
40. Cho, J.; Sarangi, R.; Kang, H. Y.; Lee, J. Y.; Kubo, M.; Ogura, T.; Solomon, E. I.; Nam, W., *J. Am. Chem. Soc.* **2010,** *132*, 16977-16986.
41. Beinert, H.; Kennedy, M. C.; Stout, C. D., *Chem. Rev.* **1996,** *96*, 2335-2373.
42. El Ghachtouli, S.; Vincent Ching, H. Y.; Lassalle-Kaiser, B.; Guillot, R.; Leto, D. F.; Chattopadhyay, S.; Jackson, T. A.; Dorlet, P.; Anxolabehere-Mallart, E., *Chem. Commun.* **2013,** *49*, 5696-5698.
43. There are also a limited number of peroxomanganese(IV) species derived from dioxygen: (a) Weschler CJ, Hoffman BM, Basolo F (1975) J. Am. Chem. Soc. 97:5278-5280. (b) Hoffman BM, Weschler CJ, Basolo F (1976) J. Am. Chem. Soc. 98:5473-5482. (c) Bossek U, Weyhermuller T, Wieghardt K, Nuber B, Weiss J (1990) J. Am. Chem. Soc. 112:6387-6388.
44. Lee, C.-M.; Chuo, C.-H.; Chen, C.-H.; Hu, C.-C.; Chiang, M.-H.; Tseng, Y.-J.; Hu, C.-H.; Lee, G.-H., *Angewandte Chemie International Edition* **2012,** *51*, 5427-5430.
45. Coggins, M. K.; Kovacs, J. A., *J. Am. Chem. Soc.* **2011,** *133*, 12470-12473.
46. Coggins, M. K.; Martin-Diaconescu, V.; DeBeer, S.; Kovacs, J. A., *J. Am. Chem. Soc.* **2013,** *135*, 4260-4272.
47. Coggins, M. K.; Sun, X.; Kwak, Y.; Solomon, E. I.; Rybak-Akimova, E. V.; Kovacs, J. A., *J. Am. Chem. Soc.* **2013,** *135*, 5631-5640.
48. Komatsuzaki, H.; Sakamoto, N.; Satoh, M.; Hikichi, S.; Akita, M.; Moro-oka, Y., *Inorg. Chem.* **1998,** *37*, 6554-6555.

49. Bhula, R.; Gainsford, G. J.; Weatherburn, D. C., *J. Am. Chem. Soc.* **1988,** *110*, 7550-7552.
50. Costas, M.; Mehn, M. P.; Jensen, M. P.; Que, L., Jr., *Chem. Rev.* **2004,** *104*, 939-986.
51. Mirica, L. M.; Ottenwaelder, X.; Stack, T. D. P., *Chem. Rev.* **2004,** *104*, 1013-1046.
52. Park, G. Y.; Qayyum, M. F.; Woertink, J.; Hodgson, K. O.; Hedman, B.; Narducci Sarjeant, A. A.; Solomon, E. I.; Karlin, K. D., *J. Am. Chem. Soc.* **2012,** *134*, 8513-8524.
53. Wolk, A. B.; Leavitt, C. M.; Fournier, J. A.; Kamrath, M. Z.; Wijeratne, G. B.; Jackson, T. A.; Johnson, M. A., *Int. J. Mass Spectrom.*
54. Urban, M. W.; Nakamoto, K.; Basolo, F., *Inorg. Chem.* **1982,** *21*, 3406-3408.
55. Roelfes, G.; Vrajmasu, V.; Chen, K.; Ho, R. Y. N.; Rohde, J.-U.; Zondervan, C.; la Crois, R. M.; Schudde, E. P.; Lutz, M.; Spek, A. L.; Hage, R.; Feringa, B. L.; Münck, E.; Que, L. J., *Inorg. Chem.* **2003,** *42*, 2639-2653.
56. Lever, A. B. P., *Inorganic Electronic Spectroscopy*. 2nd ed.; Elsevier: Amsterdam; New York, 1984; p xvi, 863.
57. Lehnert, N.; Ho, R. Y. N.; Que, L. J.; Solomon, E. I., *J. Am. Chem. Soc.* **2001,** *123*, 12802-12816.
58. Lehnert, N.; Ho, R. Y. N.; Que, L. J.; Solomon, E. I., *J. Am. Chem. Soc.* **2001,** *123*, 8271-8290.
59. Groves, J. T.; Watanabe, Y.; McMurry, T. J., *J. Am. Chem. Soc.* **1983,** *105*, 4489-4490.
60. Creager, S. E.; Murray, R. W., *Inorg. Chem.* **1987,** *26*, 2612-2618.
61. Creager, S. E.; Raybuck, S. A.; Murray, R. W., *J. Am. Chem. Soc.* **1986,** *108*, 4225-4227.
62. Jin, N.; Lahaye, D. e. E.; Groves, J. T., *Inorg. Chem.* **2010,** *49*, 11516-11524.
63. Aboelella, N. W.; York, J. T.; Reynolds, A. M.; Fujita, K.; Kinsinger, C. R.; Cramer, C. J.; Riordan, C. G.; Tolman, W. B., *Chem. Commun.* **2004**, 1716-1717.
64. Kieber-Emmons, M. T.; Riordan, C. G., *Acc. Chem. Res.* **2007,** *40*, 618-625.
65. Cramer, C. J.; Tolman, W. B., *Acc. Chem. Res.* **2007,** *40*, 601-608.
66. Jo, Y.; Annaraj, J.; Seo, M. S.; Lee, Y.-M.; Kim, S. Y.; Cho, J.; Nam, W., *J. Inorg. Biochem.* **2008,** *102*, 2155-2159.
67. Sisemore, M. F.; Selke, M.; Burstyn, J. N.; Valentine, J. S., *Inorg. Chem.* **1997,** *36*, 979-984.
68. Neese, F.; Solomon, E. I., *J. Am. Chem. Soc.* **1998,** *120*, 12829-12848.
69. Lee, Y.-M.; Bang, S.; Kim, Y. M.; Cho, J.; Hong, S.; Nomura, T.; Ogura, T.; Troeppner, O.; Ivanovic-Burmazovic, I.; Sarangi, R.; Fukuzumi, S.; Nam, W., *Chemical Science* **2013,** *4*, 3917-3923.
70. Stasser, J.; Namuswe, F.; Kasper, G. D.; Jiang, Y.; Krest, C. M.; Green, M. T.; Penner-Hahn, J.; Goldberg, D. P., *Inorg. Chem.* **2010,** *49*, 9178-9190.
71. Abu-Omar, M. M., *Dalton Trans.* **2011,** *40*, 3435-3444.
72. Adam, W.; Mock-Knoblauch, C.; Saha-Möller, C. R.; Herderich, M., *J. Am. Chem. Soc.* **2000,** *122*, 9685-9691.
73. Groves, J. T.; Stern, M. K., *J. Am. Chem. Soc.* **1988,** *110*, 8628-8638.
74. Hage, R.; Lienke, A., *J. Mol. Catal. A: Chem.* **2006,** *251*, 150-158.
75. Hage, R.; Lienke, A., *Angew. Chem., Int. Ed. Engl.* **2006,** *45*, 206-222.
76. Pecoraro, V. L.; Hsieh, W.-Y., *Inorg. Chem.* **2008,** *47*, 1765-1778.
77. Zhang, R.; Newcomb, M., *Acc. Chem. Res.* **2008,** *41*, 468-477.
78. Jin, N.; Bourassa, J. L.; Tizio, S. C.; Groves, J. T., *Angewandte Chemie International Edition* **2000,** *39*, 3849-3851.
79. Leto, D. F.; Ingram, R.; Day, V. W.; Jackson, T. A., *Chem. Commun.* **2013,** *49*, 5378-5380.

80. Parsell, T. H.; Behan, R. K.; Green, M. T.; Hendrich, M. P.; Borovik, A. S., *J. Am. Chem. Soc.* **2006,** *128*, 8728-8729.
81. Parsell, T. H.; Yang, M.-Y.; Borovik, A. S., *J. Am. Chem. Soc.* **2009,** *131*, 2762-2763.
82. Wu, X.; Seo, M. S.; Davis, K. M.; Lee, Y.-M.; Chen, J.; Cho, K.-B.; Pushkar, Y. N.; Nam, W., *J. Am. Chem. Soc.* **2011,** *133*, 20088-20091.
83. Zhang, R.; Horner, J. H.; Newcomb, M., *J. Am. Chem. Soc.* **2005,** *127*, 6573-6582.
84. Bortolini, O., *Nouv. J. Chim.* **1986,** *10*, 39 - 49.
85. Czernuszewicz, R. S.; Su, Y. O.; Stern, M. K.; Macor, K. A.; Kim, D.; Groves, J. T.; Spiro, T. G., *J. Am. Chem. Soc.* **1988,** *110*, 4158-4165.
86. Groves, J. T.; Stern, M. K., *J. Am. Chem. Soc.* **1987,** *109*, 3812-3814.
87. Schappacher, M.; Weiss, R., *Inorg. Chem.* **1987,** *26*, 1189-1190.
88. Willner, I.; Otvos, J. W.; Calvin, M., *J. Chem. Soc., Chem. Commun.* **1980**, 964-965.
89. Arasasingham, R. D.; He, G. X.; Bruice, T. C., *J. Am. Chem. Soc.* **1993,** *115*, 7985-7991.
90. Ayougou, K.; Bill, E.; Charnock, J. M.; Garner, C. D.; Mandon, D.; Trautwein, A. X.; Weiss, R.; Winkler, H., *Angew. Chem., Int. Ed. Engl.* **1995,** *34*, 343-346.
91. Groves, J. T.; Stern, M. K., *Journal of the American Chemical Society* **1988,** *110*, 8628-8638.
92. Kurahashi, T.; Kikuchi, A.; Tosha, T.; Shiro, Y.; Kitagawa, T.; Fujii, H., *Inorg. Chem.* **2008,** *47*, 1674-1686.
93. Sawant, S. C.; Wu, X.; Cho, J.; Cho, K.-B.; Kim, S. H.; Seo, M. S.; Lee, Y.-M.; Kubo, M.; Ogura, T.; Shaik, S.; Nam, W., *Angew. Chem., Int. Ed. Engl.* **2010,** *49*, 8190-8194.
94. Parsell, T. H.; Behan, R. K.; Green, M. T.; Hendrich, M. P.; Borovik, A. S., *J. Am. Chem. Soc.* **2006,** *128*, 8728-8729.
95. Chattopadhyay, S.; Geiger, R. A.; Yin, G.; Busch, D. H.; Jackson, T. A., *Inorg. Chem.* **2010,** *49*, 7530-7535.
96. Garcia-Bosch, I.; Company, A.; Cady, C. W.; Styring, S.; Browne, W. R.; Ribas, X.; Costas, M., *Angewandte Chemie International Edition* **2011,** *50*, 5648-5653.
97. Yin, G.; Danby, A. M.; Kitko, D.; Carter, J. D.; Scheper, W. M.; Busch, D. H., *J. Am. Chem. Soc.* **2008,** *130*, 16245-16253.
98. Kurahashi, T.; Kikuchi, A.; Shiro, Y.; Hada, M.; Fujii, H., *Inorg. Chem.* **2010,** *49*, 6664-6672.
99. Gupta, R.; MacBeth, C. E.; Young, V. G.; Borovik, A. S., *J. Am. Chem. Soc.* **2002,** *124*, 1136-1137.
100. Garcia-Bosch, I.; Company, A.; Cady, C. W.; Styring, S.; Browne, W. R.; Ribas, X.; Costas, M., *Angew. Chem., Int. Ed. Engl.* **2011,** *50*, 5648-5653.
101. Bane, K.; Geiger, R. A.; Chabolla, S. A.; Jackson, T. A., *Inorg. Chim. Acta* **2012,** *380*, 135-140.
102. Camenzind, M. J.; Hollander, F. J.; Hill, C. L., *Inorg. Chem.* **1983,** *22*, 3776-3784.
103. Kessissoglou, D. P.; Li, X.; Butler, W. M.; Pecoraro, V. L., *Inorg. Chem.* **1987,** *26*, 2487-2492.
104. Rajendiran, T. M.; Kampf, J. W.; Pecoraro, V. L., *Inorg. Chim. Acta* **2002,** *339*, 497-502.
105. Collins, T. J.; Gordon-Wylie, S. W., *J. Am. Chem. Soc.* **1989,** *111*, 4511-4513.
106. Collins, T. J.; Powell, R. D.; Slebodnick, C.; Uffelman, E. S., *J. Am. Chem. Soc.* **1990,** *112*, 899-901.

107. Lansky, D. E.; Mandimutsira, B.; Ramdhanie, B.; Clausén, M.; Penner-Hahn, J.; Zvyagin, S. A.; Telser, J.; Zhan, R.; Ou, Z.; Kadish, K. M.; Zakharov, L.; Rheingold, A. L.; Goldberg, D. P., *Inorg. Chem.* **2005,** *44*, 4485-4498.
108. MacDonnell, F. M.; Fackler, N. L. P.; Stern, C.; O'Halloran, T. V., *J. Am. Chem. Soc.* **1994,** *116*, 7431-7432.
109. Miller, C. G.; Gordon-Wylie, S. W.; Horwitz, C. P.; Strazisar, S. A.; Peraino, D. K.; Clark, G. R.; Weintraub, S. T.; Collins, T. J., *J. Am. Chem. Soc.* **1998,** *120*, 11540-11541.

Chapter 2

Geometric and Electronic Structures of Peroxomanganese(III) Complexes Supported by Pentadentate Amino-pyridine and -imidazole Ligands

This work has been reproduced in part from: R. A. Geiger, D. F. Leto, S. Chattopadhyay, P. Dorlet, E. Anxolabéhère-Mallart, and T. A. Jackson, *Inorg. Chem.*, 2011, **50**, 10190-10203, with permission from the American Chemical Society; and S. El Ghachtouli, H. Y. V. Ching, B. Lassalle-Kaiser, R. Guillot, D. F. Leto, S. Chattopadhyay, T. A. Jackson, P. Dorlet and E. Anxolabéhère-Mallart, *Chem. Commun.*, 2013, **49**, 5696-5698, with permission from The Royal Society of Chemistry.

2.1. Introduction.

Mononuclear superoxo- and peroxomanganese(III) species have been proposed to form in a number of redox-active manganese enzymes, including manganese superoxide dismutase (MnSOD),[1-6] manganese-dependent homoprotocatechuate 2,3-dioxygenase (MndD),[7,8] and the oxalate-degrading enzymes oxalate oxidase[9,10] and oxalate decarboxylase.[11-13] In addition, manganese-peroxide interactions are relevant to the dinuclear enzymes manganese catalase[14] and manganese ribonucleotide reductase.[15] Experimental evidence for a peroxomanganese(III) adduct has been obtained for MnSOD. Under high superoxide concentrations, a product-inhibited complex is formed, and this species displays absorption features consistent with a peroxomanganese(III) adduct.[4,6] Notably, the kinetics associated with formation and decay of this intermediate are affected by substitution of outer-sphere amino acid residues.[6,16-19] Rapid freeze-quench electron paramagnetic resonance (EPR) experiments on MndD under single-turnover conditions identified an $S = 5/2$ intermediate with an axial zero-field splitting parameter too large for a Mn^{II} species ($D = 2.5$ cm^{-1}).[7] This intermediate was formulated as a superoxomanganese(III) adduct, although a peroxomanganese(III)-(homoprotocatechuate radical) is an alternative possibility.[7] Because these biological peroxo- and superoxomanganese(III) species are highly unstable, relatively little is known concerning their structural, electronic, and reactivity properties.

In contrast, a variety of mononuclear peroxomanganese(III) model complexes have been described (Figure 2.1),[20-29] and some of these have been structurally characterized using X-ray diffraction (XRD).[20-24] Although the properties of these supporting ligands are rather diverse, in all cases the peroxide is bound to the Mn^{III} ions in a side-on (η^2) fashion, and the coordination sphere is completed by four other donors, leading to six-coordinate manganese(III) centers

(Figure 2.1). Nam and co-workers have reported that the Mn^{III} center of the $[Mn^{III}(O_2)(13\text{-}TMC)]^+$ complex can be bound by exogenous anions X^- ($X^- = N_3^-$, NCS^-, CN^-, and $CF_3CO_2^-$).[23] On the basis of the greater nucleophilicity of the resulting $[Mn^{III}(O_2)(13\text{-}TMC)(X)]$ complexes, they have suggested that anion binding may convert the peroxo from side-on to end-on, thereby retaining a six-coordinate Mn^{III} center.[23] Density functional theory (DFT) computations predict the end-on peroxo ligand to bear significantly more negative charge, in keeping with the increase in nucleophilicity observed experimentally.[23] However, there is no structural data to support this proposal, and, to date, resonance Raman experiments on Mn^{III}-O_2 have proved fruitless,[24,26] likely due to photo-induced sample degradation.

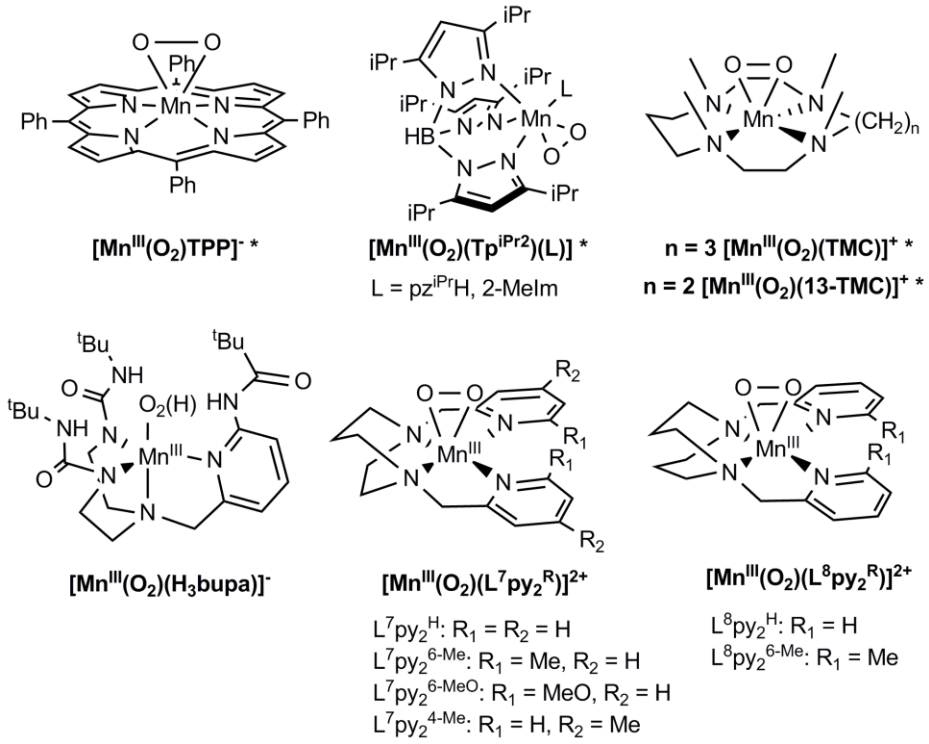

Figure 2.1. Mononuclear peroxomanganese(III) adducts. Complexes marked with an asterisk have been structurally characterized by X-ray diffraction.

Peroxomanganese(III) adducts with seven-coordination geometries, or with end-on peroxo ligands, could bear greater relevance to analogous enzymatic intermediates. For example, the product-inhibited form of MnSOD is generated by reaction of a five-coordinate Mn^{II} center with superoxide (Figure 2.2, left). Thus, formation of a side-on peroxomanganese(III) adduct would result in a seven-coordinate Mn^{III} complex, assuming none of the native ligands dissociate. Alternatively, an end-on peroxo ligand would result in a six-coordinate center. A model of the product-inhibited complex of MnSOD developed using DFT computations shows a Mn^{III}-O_2 unit with a more end-on structure, with Mn-O_{peroxo} distances of 1.80 and 2.22 Å.[3] The active-site Mn^{II} ion of MndD is bound by three exogenous ligands and reacts with dioxygen in the presence of homoprotocatechuate (HPCA) substrate.[7,8,30] With substrate bound in the expected bidentate fashion and assuming that none of the three proteinaceous ligands dissociate, only one coordination site is available for interaction with oxygen. This site is occupied by water in an X-ray crystal structure (Figure 2.2, right).[8] Thus, the putative superoxomanganese(III) adduct observed experimentally is likely either an end-on bound six-coordinate species or a side-on bound seven-coordinate species.

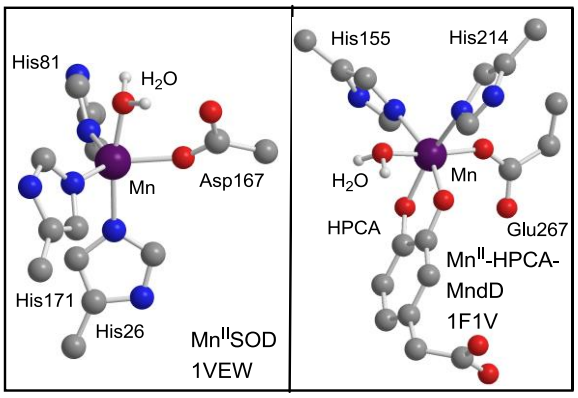

Figure 2.2. Active sites of Mn^{II}SOD (left) and the HPCA adduct of Mn^{II}MndD (right) derived from PDB files 1VEW and 1F1V, respectively. For clarity, only H-atoms on coordinated solvent ligands are shown.

In this chapter we have examined the geometric and electronic structures of peroxomanganese(III) adducts supported by three pentadentate ligands (Scheme 2.1): mL_5^2 (*N*-methyl-*N*,*N*',*N*''-tris(2-pyridylmethyl)ethane-1,2-diamine), imL_5^2 (*N*-methyl-*N*,*N*',*N*''-tris((1-methyl-4-imidazolyl)methyl)ethane-1,2-diamine), and N4py (*N*,*N*-bis(2-pyridylmethyl)-*N*-bis(2-pyridyl)methylamine). Previous spectroscopic and reactivity studies of $[Mn^{III}(O_2)(mL_5^2)]^+$ have clearly established the formulation of this species,[26,27] although the coordination geometry of this species is ill-defined (Scheme 2.1). Results reported herein support the formulation of the new $[Mn^{III}(O_2)(imL_5^2)]^+$ and $[Mn^{III}(O_2)(N4py)]^+$ complexes. This current study seeks to answer two important questions: Are the peroxomanganese(III) complexes supported by these pentadentate ligands six- or seven-coordinate? If the complexes are six-coordinate, which donor group is dissociating? On the basis of electronic absorption (Abs), magnetic circular dichroism (MCD), variable-temperature, variable-field (VTVH) MCD spectroscopies, as well as density functional theory (DFT) computations, we conclude that all three complexes contain a six-coordinate Mn^{III} center with a side-on peroxo ligand and a dissociated pyridine (or imidazole). Thus, there is a strong preference for six-coordinate geometry for peroxomanganese(III) species, and end-on peroxomanganese(III) units are predicted to be unstable and, potentially, highly reactive. The relevance of these findings with respect to biological manganese centers is discussed.

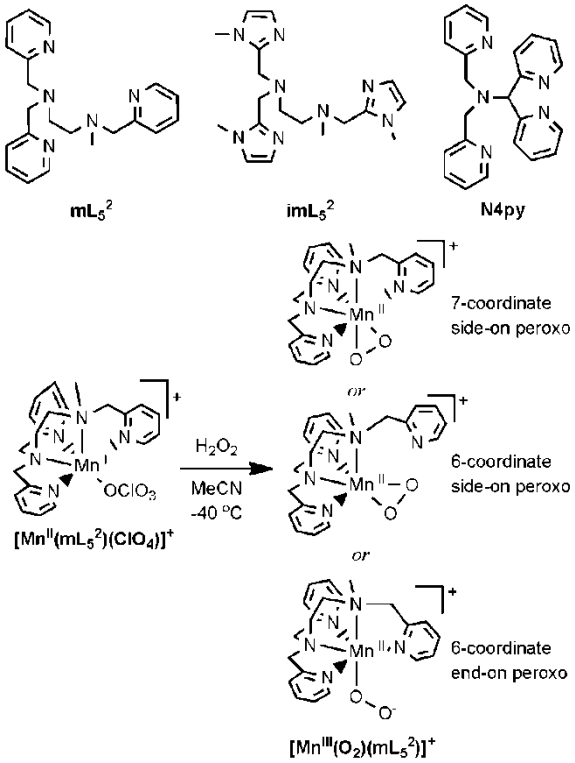

Scheme 2.1. Structure of Pentadentate Ligands and Possible Coordination Modes of Peroxo Ligand.

2.2. Experimental and Computational Methods.

2.2.1. Materials and Instrumentation. All chemicals and solvents were obtained from commercial vendors and were ACS grade or better and used as received except for cyclohexanecarboxaldehyde. Fractional distillation at 43 ^{o}C was performed under reduced pressure (10 torr) to remove acid impurities from cyclohexanecarboxaldehyde. ^{1}H-NMR spectra were collected on a Bruker DRZ 400 MHz spectrometer and a Bruker DPX 300 MHz spectrometer with an ONP probe. All ^{1}H-NMR experiments were performed at room temperature in $CDCl_3$ (δ = 7.24 ppm). Mass spectrometry experiments were performed using an LCT Primers MicroMass electrospray time-of-flight instrument. Elemental analysis was performed by Columbia Analytical Services, Tucson AZ. Electronic absorption spectra were obtained on a

Varian Cary 50 Bio spectrophotometer that was interfaced with a Unisoku cryostat (USP-203-A) capable of maintaining temperatures between 150 and 373 K. MCD spectra were collected on a Jasco circular dichroism spectrometer (J-815) interfaced with an Oxford Instruments magnetocryostat (SM-4000-8) capable of a horizontal field up to 8 T and a temperature range of 1.5 to 300 K.

2.2.2. Synthesis of N4py Ligand. The synthesis of N4py was performed according to a previously described procedure.[31,32] Di-2-pyridylmethanamine was first synthesized from the reduction of di-2-pyridyl ketone oxime.[31] N4py was then prepared in 40% yield from the reaction of di-2-pyridylmethanamine with 2 equivalents picolyl chloride HCl, followed by treatment with concentrated $HClO_4$ and extraction with dichloromethane.[32] ^1H NMR data (400 MHz) for N4py ($CDCl_3$, δ) 3.97 (s, 4H), 5.35(s, 1H), 7.13 (m, 4H), 7.63 (m, 8H), 8.51 (d, 2H), 8.57 (d, 2H) ppm.

2.2.3. Synthesis of [Mn^{II}(N4py)(OTf)](OTf). The [Mn^{II}(N4py)(OTf)](OTf) complex (OTf^- = $CF_3SO_3^-$) was synthesized in excellent yield (~90%) by reacting N4py ligand with $Mn^{II}(OTf)_2$ in acetonitrile (MeCN) solution in a 1:1 molar ratio. $Mn(OTf)_2$ was prepared using a previously reported procedure, where equimolar amounts of $(CH_3)_3Si(OTf)$ and anhydrous $MnCl_2$ are reacted.[24] Details of a representative preparation for a metal complex are as follows. To a stirred solution of 1.84 g (5.223 mmol) of $Mn(OTf)_2$ in 10 mL of MeCN was added N4py (1.92 g, 5.223 mmol) in 10 mL of MeCN. The red solution was stirred overnight and evaporated under reduced pressure. The solid thus obtained was dried in vacuo. Recrystallization of the crude solid from MeCN–diethyl ether afforded nearly colorless crystals of [Mn^{II}(N4py)(OTf)](OTf) (3.27 g, 87%). Elemental analysis [Mn^{II}(N4py)(OTf)](OTf)•0.5CH_3CH_2OH: $MnC_{26}H_{24}N_5O_{6.5}F_6S_2$ calcd (%): C 42.00, H 3.25, N

9.42; found (%): C 42.16, H 3.61, N 9.68. The minor ethanol contaminant resulted from insufficiently dried ligand. ESI-MS data are as follows: {[Mn(N4py)](Cl)$^+$} *m/z* = 457.0876 (calc. 457.0866), where a chloride ion was exchanged for a triflate ion in the mass spectrometer.

2.2.4. Preparation of MCD Sample. Two equivalents of KO_2, in the form of a solution prepared from 14.2 mg KO_2 and 200 mg 18-crown-6 dissolved in 2 mL butyronitrile, was added to the 5 mM butyronitrile solution of [Mn^{II}(N4py)(OTf)](OTf). Once formation of [$Mn^{III}(O_2)$(N4py)]$^+$ was judged complete by absorption spectroscopy, the sample was further cooled to -80 ^{o}C, transferred to a pre-cooled MCD cell at -80 ^{o}C, and flash-frozen in liquid N_2.

2.2.5. Aldehyde Deformylation Reactivity Studies. Kinetic analyses of aldehyde deformylation were carried out by adding excess CCA or benzaldehyde to 5 or 2.5 mM acetonitrile solutions of [$Mn^{III}(O_2)$(N4py)]$^+$ and monitoring the time-dependent decay of the band at 16 200 cm^{-1}, a characteristic feature of the Mn^{III}–O_2 intermediate, at -40 °C.

2.2.6. Computations. All calculations utilized the *ORCA* 2.8.0 software package developed by F. Neese (University of Bonn, Germany).[33] Crystal structure coordinates of [Mn^{II}(N4py)(OTf)](OTf) were modified to include peroxo ligands and served as the starting points for geometry optimizations. Geometry optimizations and surface scans were performed at the spin-unrestricted level using the Becke-Perdew (BP) functional[34,35] and TZVP (for Mn, O, and N) and SVP (for C and H) basis sets.[36,37] These calculations employed the resolution of the identity (RI) approximation[38] that employed the TZV/J and SV/J auxiliary basis sets.[38] Frequency calculations were used to verify that all energy-minimized models showed no imaginary frequencies. Single-point calculations to obtain energies for the optimized structures employed the B3LYP functional[39-41] and def2-TZVPP basis sets for all atoms.[36,37,42] The effects of acetonitrile solvation on the total energies of these systems were evaluated using the COSMO

method as implemented in *ORCA*. Cartesian coordinates for all geometry optimized models can be found in Appendix A.2 (Tables A.2.5 – A.2.13).

Electronic transition energies and intensities were computed for select models using the time-dependent DFT (TD-DFT).[43-46] TD-DFT calculations were performed within the Tamm-Dancoff approximation and utilized the TZVP (for Mn, N, and O) and SVP (for C and H) basis sets. For each calculation, 40 excited states were calculated by including all one-electron excitations within a ±3 Hartree energy window with respect to the highest occupied and lowest unoccupied MOs.

2.3. Results and Analysis.

2.3.1. Formation and Mass Spectral Characterization of $[Mn^{III}(O_2)(N4py)]^+$ and $[Mn^{III}(O_2)(imL_5^2)]^+$. It was previously reported that the $[Mn^{II}(mL_5^2)]^{2+}$ complex can be converted to the peroxomanganese(III) (Mn^{III}-O_2) adduct $[Mn^{III}(O_2)(mL_5^2)]^+$ by reaction with either KO_2 or H_2O_2.[26,27] The $[Mn^{II}(imL_5^2)(ClO_4)](ClO_4)$ and $[Mn^{II}(N4py)(OTf)](OTf)$ complexes are structurally similar to $[Mn^{II}(mL_5^2)(ClO_4)](ClO_4)$, both having the supporting ligands bound in the expected pentadentate fashion, with a counter ion (perchlorate and triflate, respectively) completing the coordination sphere.[47,48] When a 5 mM solution of the $[Mn^{II}(N4py)(OTf)](OTf)$ complex is treated with two equivalents KO_2 in acetonitrile at -40 °C, the initially colorless solution turns blue within minutes, and the electronic absorption (Abs) spectrum of this solution is very similar to that of $[Mn^{III}(O_2)(mL_5^2)]^+$ (Figure 2.3, *vide infra*). Electrospray ionization mass spectrometry (ESI-MS) experiments on the resulting solution revealed a major ion peak at *m/z* 454.1097, supporting the assignment of the blue species as $[Mn^{III}(O_2)(N4py)]^+$ (calc. *m/z* = 454.1076). Furthermore, when $K^{18}O_2$ is used as oxidant the major ion peak shifts +4 *m/z* (*m/z* =

458.1), indicating that the O_2^{2-} ligand in $[Mn(O_2)(N4py)]^+$ derives from the oxidant. Similarly, addition of 10 equivalents H_2O_2 and $(Et)_3N$ to a 1:1 butyronitrile:ethanol solution of $[Mn^{II}(imL_5^2)(ClO_4)](ClO_4)$ at -20 ^oC results in the formation of a purple solution that displays a prominent peak at *m/z* 443.1697 in an ESI-MS experiment, consistent with its formulation as $[Mn^{III}(O_2)(imL_5^2)]^+$ (calc. *m/z* = 443.1716).

Additionally, our collaborators Dr. Anxolabéhère-Mallart and co-workers developed a method to form these peroxomanganese(III) species using electrochemically generated superoxide as the oxidant.[47] Higher yields of $[Mn^{III}(O_2)(mL_5^2)]^+$, $[Mn^{III}(O_2)(imL_5^2)]^+$, and $[Mn^{III}(O_2)(N4py)]^+$ are observed when these peroxomanganese(III) adducts are prepared electrochemically, as compared to when prepared using H_2O_2 or KO_2. Electrochemical generation of these peroxomanganese(III) complexes minimizes the formation of side-products (*e.g.* dinuclear $[Mn_2O_2(ligand)_2]$), as determined by electron paramagnetic spectroscopy (Figure A.2.1).

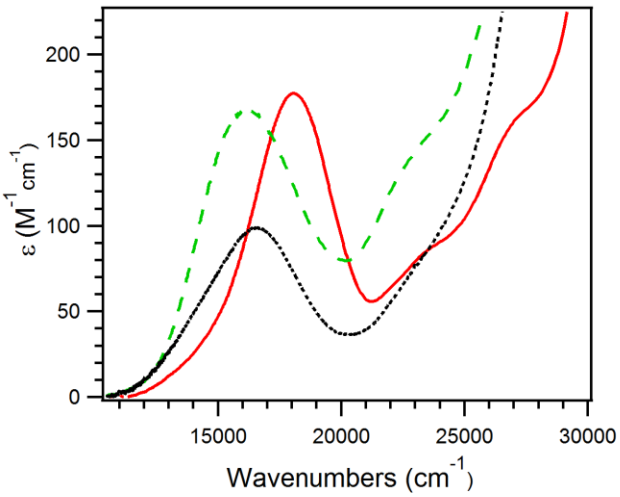

Figure 2.3. 233 K electronic absorption spectra of $[Mn^{III}(O_2)(mL_5^2)]^+$ (dotted black line), $[Mn^{III}(O_2)(imL_5^2)]^+$ (solid red line), and $[Mn^{III}(O_2)(N4py)]^+$ (dashed green line) in acetonitrile generated using either H_2O_2 or KO_2. The extinction coefficients for $[Mn^{III}(O_2)(imL_5^2)]^+$ and $[Mn^{III}(O_2)(N4py)]^+$ were determined under the assumption that 100% of Mn^{II} is converted to the corresponding peroxomanganese(III) species. Because it has been reported that the reaction of $[Mn^{II}(mL_5^2)]^{2+}$ with hydrogen peroxide results in some unreacted Mn^{II}, the extinction coefficients should be viewed as a lower limit.[49]

2.3.2. Comparison of Electronic Absorption Spectra. Figure 2.3 shows an overlay plot of the Abs spectra of the three peroxomanganese(III) complexes, $[Mn^{III}(O_2)(mL_5^2)]^+$, $[Mn^{III}(O_2)(imL_5^2)]^+$, and $[Mn^{III}(O_2)(N4py)]^+$, generated using chemical oxidants (either H_2O_2 or KO_2). As previously described,[26,27] the Abs spectrum of $[Mn^{III}(O_2)(mL_5^2)]^+$ displays a prominent band at ~17 200 cm^{-1} and a shoulder at ~23 500 cm^{-1} (ε = 335 and 290 $M^{-1}cm^{-1}$, respectively). The Abs spectrum of $[Mn^{III}(O_2)(N4py)]^+$ is very similar, with $\lambda_{max} \approx$ 16 200 and 22 800 cm^{-1} (ε = 278 and 228 M^{-1} cm^{-1}, respectively). These similarities suggest common coordination environments for the manganese(III) centers. For all three compounds, no other absorption features are observed down to 9 100 cm^{-1}.

The lowest-energy Abs feature observed for $[Mn^{III}(O_2)(imL_5^2)]^+$ is at ~18 000 cm^{-1}, and the intensity of this band is roughly twice that of the low-energy band of $[Mn^{III}(O_2)(mL_5^2)]^+$ but

is comparable to that of $[Mn^{III}(O_2)(N4py)]^+$ (Figure 2.3). Two well-resolved shoulders are observed for $[Mn^{III}(O_2)(imL_5^2)]^+$ at ~23 200 and 27 000 cm^1. Notably $[Mn^{III}(O_2)(mL_5^2)]^+$ and $[Mn^{III}(O_2)(N4py)]^+$ show a single shoulder at 23 000 cm^{-1} and the onset of more intense features at >25 000 cm^{-1}. We attribute this difference to the presence of pyridines in the mL_5^2 and N4py ligands, which likely give rise to charge-transfer transitions involving π^* pyridine orbitals and intra-ligand transitions in the near-UV and UV regions that will obscure weaker Abs bands.

Table 2.1 summarizes the extinction coefficients determined for all three complexes prepared chemically (by H_2O_2 or KO_2) and electrochemically. Based on the extinction coefficient of the low-energy Abs band, over a two-fold increase in yield is observed for electrochemically prepared $[Mn^{III}(O_2)(mL_5^2)]^+$ and $[Mn^{III}(O_2)(imL_5^2)]^+$ as compared to samples prepared by chemical oxidation, while a 60% increase in yield is observed for $[Mn^{III}(O_2)(N4py)]^+$ (Table 2.1). The ability to form these peroxomanganese(III) species in high yields using electrochemically generated superoxide is promising and could allow for future structural characterization using Mn K-edge X-ray absorption spectroscopy. In the past, X-ray absorption experiments on $[Mn^{III}(O_2)(N4py)]^+$ were not successful due to the low yields obtained using chemical oxidants.

Table 2.1. Wavelengths (cm^{-1}) and Extinction Coefficients ($M^{-1}cm^{-1}$) Obtained from Electronic Absorption Spectra of $[Mn^{III}(O_2)(mL_5^2)]^+$, $[Mn^{III}(O_2)(N4py)]^+$, and $[Mn^{III}(O_2)(imL_5^2)]^+$ Generated by either Chemical Oxidation (using H_2O_2 or KO_2) or Upon Reduction at E = -1.2 V (versus SCE) in the Presence of O_2.

Complex	Oxidant	λ_1, ε_1	λ_2, ε_2	ref
$[Mn^{III}(O_2)(mL_5^2)]^+$	H_2O_2 [a]	17 200, 89	23 500, 90	26
	$O_2^{\bullet-}$ [b]	17 200, 335	23 500, 290	47
$[Mn^{III}(O_2)(N4py)]^+$	KO_2 [c]	16 200, 168	22 800, 139	50
	$O_2^{\bullet-}$ [b]	16 200, 278	22 800, 228	47
$[Mn^{III}(O_2)(imL_5^2)]^+$	H_2O_2 [d]	18 000, 180	23 200, 170	50
	$O_2^{\bullet-}$ [b]	18 000, 484	23 200, 427	47

[a] 5 equiv H_2O_2 and 2 equiv $(Et)_3N$; 5 mM $[Mn^{II}(mL_5^2)]^{2+}$ in 1:1 butyronitrile:ethanol at 233 K. [b] $[Mn^{III}(O_2)(mL_5^2)]^+$, $[Mn^{III}(O_2)(N4py)]^+$, or $[Mn^{III}(O_2)(imL_5^2)]^+$ (1 mM in DMF and 0.2 M $TBAPF_6$) in a thin spectroelectrochemical cell (path length l = 0.5 mm, Pt working electrode) at 243 K. [c] 2 equiv of KO_2; 5 mM $[Mn^{II}(N4py)]^{2+}$ in acetonitrile at 233 K. [d] 10 equiv H_2O_2 and $(Et)_3N$; 5 mM $[Mn^{II}(imL_5^2)]^{2+}$ in 1:1 butyronitrile:ethanol at 233 K.

2.3.3. MCD Spectroscopy and Spectral Deconvolution. To compare the $[Mn^{III}(O_2)(mL_5^2)]^+$, $[Mn^{III}(O_2)(imL_5^2)]^+$, and $[Mn^{III}(O_2)(N4py)]^+$ complexes in more detail, low-temperature magnetic circular dichroism (MCD) data were collected (Figure 2.4). For all complexes, the intensities of the MCD features between 11 000 and 34 000 cm^{-1} show an inverse temperature dependence (*C*-term behavior), consistent with the paramagnetic ground states of these compounds. The MCD spectrum of $[Mn^{III}(O_2)(imL_5^2)]^+$ is considerably simpler than that of $[Mn^{III}(O_2)(mL_5^2)]^+$ and $[Mn^{III}(O_2)(N4py)]^+$, showing only three maxima (Figure 2.4). We attribute this to the lack of pyridines in the imL_5^2 ligand, which results in fewer excited states with energies in the visible to near-UV region.

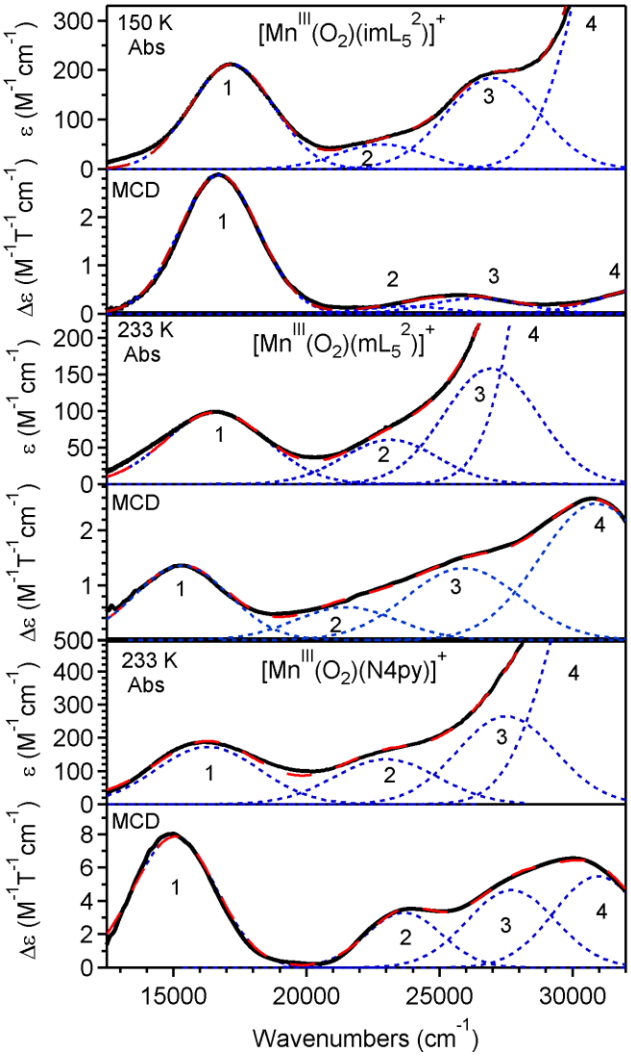

Figure 2.4. Abs and 4.5 K, 7 T MCD spectra of $[Mn^{III}(O_2)(imL_5^2)]^+$ (top two panels), $[Mn^{III}(O_2)(mL_5^2)]^+$ (middle two panels), and $[Mn^{III}(O_2)(N4py)]^+$ (bottom two panels). Individual transitions (blue dotted lines) and their sums (red dashed lines) obtained from an iterative Gaussian fit of the data sets, are displayed on their respective spectra. Complete fit parameters are included in Table A.2.1. Conditions: Abs data for $[Mn^{III}(O_2)(mL_5^2)]^+$ (233 K) and $[Mn^{III}(O_2)(N4py)]^+$ (233 K) from MeCN solutions. Corresponding data for $[Mn^{III}(O_2)(imL_5^2)]^+$ was collected for a frozen solution in butyronitrile at 150 K. MCD data for $[Mn^{III}(O_2)(imL_5^2)]^+$ and $[Mn^{III}(O_2)(N4py)]^+$ were collected for frozen butyronitrile solutions; MCD data for $[Mn^{III}(O_2)(mL_5^2)]^+$ was of a 50:50 vol:vol ethanol:butyronitrile mixture.

Iterative Gaussian deconvolutions of the Abs and MCD data shown in Figure 2.4 were performed to determine the minimum number of electronic transitions responsible for the spectral features of $[Mn^{III}(O_2)(mL_5^2)]^+$, $[Mn^{III}(O_2)(imL_5^2)]^+$, and $[Mn^{III}(O_2)(N4py)]^+$. Because the

Abs and MCD data were collected at different temperatures, the positions of the Gaussian bands were allowed to shift by up to 1 000 cm^{-1}, but in most cases shifts were significantly smaller. The energies obtained from deconvolution of these data sets are collected in Table 2.2, along with oscillator strengths for the Abs bands. Complete information regarding Abs and MCD deconvolution are in Appendix A.2 (Table A.2.1). Because of the apparent simplicity of the Abs and MCD data for $[Mn^{III}(O_2)(imL_5^2)]^+$, the spectral analysis of this complex will be discussed first.

Table 2.2. Energies (cm^{-1}) and Oscillator Strengths ($f_{exp} \times 10^3$) of Electronic Transitions for $[Mn^{III}(O_2)(imL_5^2)]^+$, $[Mn^{III}(O_2)(mL_5^2)]^+$, and $[Mn^{III}(O_2)(N4py)]^+$ Obtained from Gaussian Deconvolution of Experimental Absorption and MCD Spectra

$[Mn^{III}(O_2)(imL_5^2)]^+$			$[Mn^{III}(O_2)(mL_5^2)]^+$			$[Mn^{III}(O_2)(N4py)]^+$		
band	energy	$f_{exp} \times 10^3$	band	energy	$f_{exp} \times 10^3$	band	energy	$f_{exp} \times 10^3$
1	Abs: 17 200	3.58	1	Abs: 16 600	2.03	1	Abs: 16 300	3.64
	MCD: 16 720			MCD: 15 325			MCD: 15 064	
2	Abs: 22 800	0.883	2	Abs: 23 155	1.25	2	Abs: 23 000	2.85
	MCD: 23 800			MCD: 21 500			MCD: 23 670	
3	Abs: 27 000	3.53	3	Abs: 26 940	3.02	3	Abs: 27 510	5.28
	MCD: 26 400			MCD: 25 900			MCD: 27 710	
4	Abs: 32 200	13.8	4	Abs: 30 770	20.20	4	Abs: 31 040	16.38
	MCD: 32 800			MCD: 30 900			MCD: 30 960	

(A) $[Mn^{III}(O_2)(imL_5^2)]^+$. Spectral deconvolution for $[Mn^{III}(O_2)(imL_5^2)]^+$ reveals at least four bands from 13 000 to 33 000 cm^{-1}. Band 1 gives rise to the prominent Abs and MCD feature at ~16 700 cm^{-1}, that shows a strong blue-shift as temperature is increased. Bands 2 and 3 are responsible for the other two Abs features at ~23 200 and 27 000 cm^{-1}, and contribute to a weak MCD feature centered at ~26 000 cm^{-1}. Band 4 accounts in part for the rising Abs intensity at ~30 000 cm^{-1}, but is responsible for a weak MCD feature. Because of the expected low symmetry of the Mn^{III} center in $[Mn^{III}(O_2)(imL_5^2)]^+$, four *d-d* transitions are anticipated for this high-spin d^4 metal. Band 1 is the lowest energy feature observed for $[Mn^{III}(O_2)(imL_5^2)]^+$, and, considering its relatively large MCD intensity as well as its temperature-dependent Abs intensity,

this band is assigned as the lowest energy *d-d* transition, which, using symmetry labels of the parent octahedral point group, involves excitation within the ^5E_g ground state that is split in the low-symmetry ligand field. For this d^4 system, the transition corresponds to a one-electron excitation within the e_g-derived orbitals. For peroxomanganese(III) complexes, the splitting of these orbitals arises because of the stronger σ-interactions with the peroxo ligands relative to the N-donor ligands.[29] The low oscillator strengths of bands 2 and 3 (Table 2.2) lead us to tentatively attribute these bands to Mn^{III} *d-d* transitions as well, although these transitions, especially band 2 which carries almost negligible MCD intensity, could also be weak peroxo-to-manganese(III) charge-transfer (CT) bands.[29] Given its considerably larger Abs intensity, band 4 is assigned as a peroxo-to-manganese(III) CT transition.

(B) $[Mn^{III}(O_2)(mL_5^2)]^+$ and $[Mn^{III}(O_2)(N4py)]^+$. The Abs and MCD spectra of $[Mn^{III}(O_2)(mL_5^2)]^+$ and $[Mn^{III}(O_2)(N4py)]^+$ are both well fit with a minimum of four Gaussian bands between 12 000 and 32 000 cm^{-1} (Figure 2.4). In most cases, the energies of these bands are within ~2 000 cm^{-1} to those of $[Mn^{III}(O_2)(imL_5^2)]^+$ (Table 2.2), firmly establishing the geometric and electronic similarities of these complexes. Thus, the tentative band assignments discussed above for $[Mn^{III}(O_2)(imL_5^2)]^+$ are expected to apply to the $[Mn^{III}(O_2)(mL_5^2)]^+$ and $[Mn^{III}(O_2)(N4py)]^+$ complexes as well. Overall, the Gaussian analyses of Abs and MCD data collected for these three peroxomanganese(III) adducts provide strong evidence that the Mn^{III} centers in these three complexes share a common geometry.

2.3.4. VTVH MCD Spectroscopy. Variable-temperature, variable-field (VTVH) MCD spectroscopy was used to determine ground-state zero-field splitting (ZFS) parameters and transition polarizations for the three peroxomanganese(III) complexes. In these experiments, the intensity of an MCD signal at a given wavelength is monitored as a function of magnetic field at

various fixed temperatures. For $S > ½$ systems, the saturation behavior of these curves reflect the ground-state *g*-values and axial (*D*) and rhombic (*E/D*) ZFS parameters as well as transition polarization.[51,52] VTVH MCD curves collected at several wavelengths for the same sample are thus useful for evaluating the polarizations of different transitions. For example, VTVH MCD data collected for bands 1 and 4 of $[Mn^{III}(O_2)(mL_5^2)]^+$ (16 700 and 30 800 cm^{-1}) show distinct saturation behavior (Figure 2.5, A and B), with the MCD signal saturating more rapidly for band 1. Fits of these data sets using ZFS parameters and *g*-values obtained by EPR experiments (g_{iso} = 2.0, D = -2.9 cm^{-1} and E/D = 0.075)[27] reveal that band 1 is predominantly *y*-polarized with a minor *x*-component (5% *x*-, 89% *y*-, and 6% *z*-polarization), whereas band 4 is nearly 100% *z*-polarized (<1% *x*, <1% *y*-, and 99% *z*-polarization). VTVH MCD data collected for band 3 (26 700 cm^{-1}) appear almost identical to those of band 4, indicating that this band is also *z*-polarized (Figure A.2.2 and Table A.2.2).

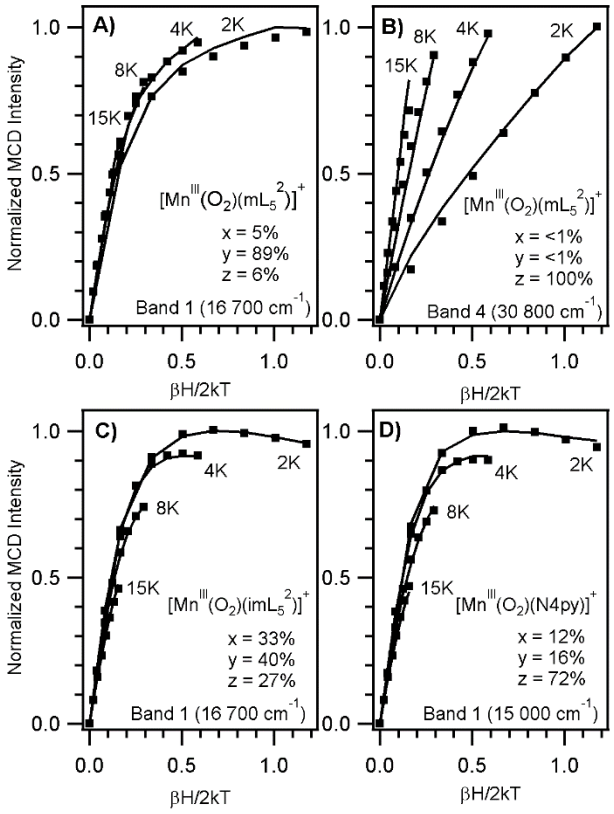

Figure 2.5. VTVH MCD data (dots) collected for $[Mn^{III}(O_2)(mL_5^2)]^+$ (A and B), $[Mn^{III}(O_2)(imL_5^2)]^+$ (C), and $[Mn^{III}(O_2)(N4py)]^+$ (D) at the energies indicted in the insets. Fits (solid lines) of these data sets used g_{iso} = 2.0, the polarizations listed in the insets, and the following ZFS parameters: $[Mn^{III}(O_2)(mL_5^2)]^+$: D = -2.9 cm^{-1}, E/D = 0.075; $[Mn^{III}(O_2)(imL_5^2)]^+$: D = -2 cm^{-1}, E/D = 0.3; $[Mn^{III}(O_2)(N4py)]^+$: D = -1.5 cm^{-1}, E/D = 0.15.

Because ZFS parameters have not been previously determined for $[Mn^{III}(O_2)(imL_5^2)]^+$ and $[Mn^{III}(O_2)(N4py)]^+$, VTVH MCD data for these complexes were systematically fit to extract both ZFS parameters and transition polarizations. In this protocol, D and E/D were respectively varied from -3 to 3 cm^{-1} and 0 to 0.3 in increments of 0.5 and 0.05 cm^{-1}.[3] Transition-moment products were optimized to fit the experimental data for a given set of D and E/D values. The goodness of fit was assessed by the χ^2 value, which is the sum of the squares of the differences between experimental and fit data sets. All data sets were best fit assuming an S = 2 ground state. To evaluate the accuracy of this protocol in determining ZFS parameters for these

peroxomanganese(III) complexes, it was first applied to $[Mn^{III}(O_2)(mL_5^2)]^+$. Figure A.2.3 shows contours plots of χ^2 as a function of *D* and *E/D* for VTVH MCD data collected at bands 3 and 4 (26 700 and 30 800 cm^{-1}, respectively). In both cases, excellent fits are obtained for $|D| = 2.5 – 3$ cm^{-1} and $E/D = 0.05 – 0.30$. Thus, for this system, the goodness of fit is strongly dependent on the magnitude of *D*, but insensitive to the sign of *D* and to the rhombicity. Importantly, the ZFS parameters determined by EPR spectroscopy ($D = -2.9$ cm^{-1} and $E/D = 0.075$) fall within this range.[26,27] We thus conclude that this protocol will yield accurate values for the magnitude of *D* for $[Mn^{III}(O_2)(imL_5^2)]^+$ and $[Mn^{III}(O_2)(N4py)]^+$.

VTVH MCD data collected for $[Mn^{III}(O_2)(imL_5^2)]^+$ at 16 700 cm^{-1} (Figure 2.5C) were well fit ($\chi^2 < 0.02$) within the two ranges $D = -1.5 – -2$ cm^{-1}, $E/D = 0.1 – 0.3$ and $D = +2$, $E/D = 0.1 – 0.25$ (Figure A.2.4, left). However, the acceptable range for $D < 0$ cm^{-1} can be narrowed to $D = -2$ cm^{-1}, $E/D = 0.25 – 0.30$ when data collected at 25 600 cm^{-1} are also considered (Figure A.2.4, right). Likewise, data collected for $[Mn^{III}(O_2)(N4py)]^+$ at 14 700 cm^{-1} (Figure 2.5D) are well fit with $D = -1.5$ cm^{-1}, $E/D = 0.15 – 0.30$ and $D = +1.5 – +2.0$ cm^{-1}, $E/D = 0 – 0.33$ (Figure A.2.5).[53] Thus, in both cases the magnitude of *D* is reduced relative to that of $[Mn^{III}(O_2)(mL_5^2)]^+$, but the sign of *D* cannot be unambiguously assigned. Given the strong similarities between the absorption and MCD data of these three complexes, as well as the fact that all ZFS parameters determined for peroxomanganese(III) adducts to date show $D < 0$,[26-29] we conclude that $[Mn^{III}(O_2)(imL_5^2)]^+$ and $[Mn^{III}(O_2)(N4py)]^+$ likewise have negative *D* values (Table 2.3). Under this assumption, and using ZFS parameters giving optimal χ^2 values, transition polarizations were determined for the different MCD features of $[Mn^{III}(O_2)(imL_5^2)]^+$ and $[Mn^{III}(O_2)(N4py)]^+$ (Table A.2.2).

Table 2.3. Axial (*D*) and Rhombic (*E/D*) Zero-Field Splitting Parameters for Peroxomanganese(III) Complexes

	D (cm^{-1})	*E/D*	reference
$[Mn^{III}(O_2)(mL_5^2)]^+$	-2.9	0.075	26,27
$[Mn^{III}(O_2)(imL_5^2)]^+$	-2.0	0.25 – 0.30	50
$[Mn^{III}(O_2)(N4py)]^+$	-1.5	0.15 – 0.30	50
$[Mn^{III}(O_2)(L^7py_2^H)]^{+\,b}$	-2	0.13	29
$[Mn^{III}(O_2)(L^7py_2^{Me})]^{+\,c}$	-3	0.05	29
$[Mn^{III}(O_2)(H_3bupa)]^{-\,d}$	-2.0	0.13	28

Taken together, the results of the MCD and VTVH MCD experiments reveal that the ground- and excited-state properties of these complexes are similar with one another, which requires that these three complexes have very similar coordination geometries. Importantly, these spectroscopic data can also provide a basis for evaluating a variety of hypothetical models developed using DFT computations through comparison of computed and experimental spectroscopic parameters.

2.3.5. Density Functional Theory Computations. (A) Hypothetical Structures for $[Mn^{III}(O_2)(mL_5^2)]^+$. Several structures were considered as hypothetical models of $[Mn^{III}(O_2)(mL_5^2)]^+$ (Scheme 2.1): i) a seven-coordinate Mn^{III} center with a side-on peroxo ligand and mL_5^2 bound in a pentadentate fashion, ii) a six-coordinate complex with an end-on peroxo ligand and mL_5^2 bound in a pentadentate fashion, and iii) a six-coordinate complex with a side-on peroxo ligand and mL_5^2 bound in a tetradentate fashion (*i.e.*, with a dissociated amine or pyridine group). Notably, dissociation of a pyridine arm for mL_5^2 was previously observed in the X-ray crystal structure of $[Fe_2(\mu\text{-}O)(Cl)_2(mL_5^2)_2](NEt_4)_2$.[54] Two recently crystallized bis(μ-oxo)dimanganese(IV,IV) species supported by ligands similar to mL_5^2, but with a carboxylate replacing one of the pyridine groups (bpmg and mcbpen),[55] also showed dissociation of a pyridine arm.[56] We first examined the possibility of side-on versus end-on peroxo coordination with the mL_5^2 ligand bound in its commonly observed pentadentate binding mode. Starting

geometries were obtained by modifying the crystal structure coordinates of $[Mn^{II}(mL_5^2)(ClO_4)]^+$ by replacing perchlorate with a peroxo ligand in either a side-on or end-on geometry. In both cases, these starting geometries yielded the same structure upon convergence (referred to as $[Mn^{III}(O_2)(mL_5^2)\text{-}N(1)]^+$; see Figure 2.6): a side-on Mn^{III}-O_2 adduct with Mn–O_{peroxo} distances of 1.899 and 1.894 Å (Table 2.4). In this structure, the amine nitrogen *trans* to the peroxo unit, N(1), displays a long Mn–N(1) distance of 2.61 Å. To evaluate the energetic and structural consequences associated with conversion from the $[Mn^{III}(O_2)(mL_5^2)\text{-}N(1)]^+$ geometry to a Mn^{III}-O_2 complex with an end-on peroxo, we performed a relaxed surface scan where one Mn–O_{peroxo} distance was elongated from 1.85 to 2.60 Å in 0.1 Å increments. As shown in Figure A.2.6 (top), elongation of the Mn–O_{peroxo} distance leads to a substantial increase in energy, indicating that the side-on peroxo binding mode is strongly favored. The O–O bond length decreases from 1.413 to 1.363 Å as one Mn–O_{peroxo} distance is elongated (Figure A.2.6, center). The shortest O–O distance is midway between common ranges observed for peroxo and superoxo ligands (1.50 – 1.40 and 1.30 – 1.20 Å, respectively). Notably the elongation in one Mn–O_{peroxo} distance is associated with a shortening of the Mn–N(1) bond length by 0.3 Å over the course of the surface scan (Figure A.2.6, bottom). A complementary surface scan of Mn–N(1) distance showed a similar inverse correlation between the Mn–N(1) distance and one Mn–O_{peroxo} bond length (Figure A.2.7), which is taken to indicate the preference for hexacoordination for the Mn^{III} center. In either case, elongation of one Mn–O_{peroxo} bond by more than ~0.3 Å results in models with significantly higher energies (>7 kcal/mol) relative to $[Mn^{III}(O_2)(mL_5^2)\text{-}N(1)]^+$.

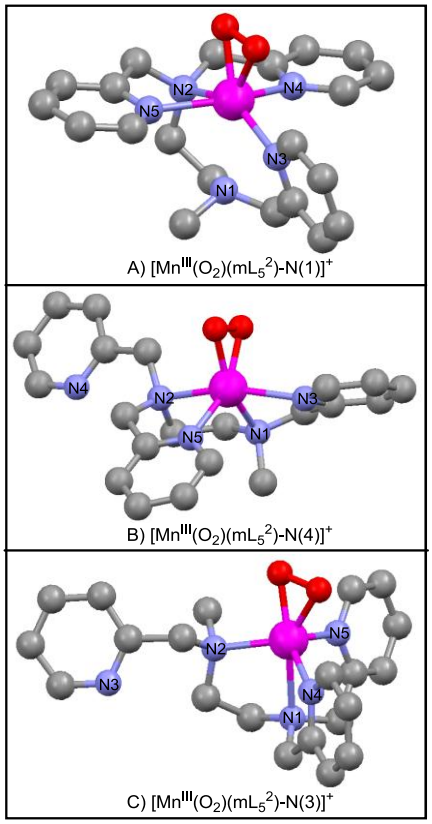

Figure 2.6. Hypothetical structures of $[Mn^{III}(O_2)(mL_5^2)]^+$ complexes developed using DFT computations.

Table 2.4. Relative Energies (kcal/mol) and Mn-Ligand Bond Lengths (Å) for Four Hypothetical Models of $[Mn^{III}(O_2)(mL_5^2)]^+$ Developed using DFT Computations.

	Relative Energy	Mn-O	O-O	Mn-N(1)	Mn-N(2)	Mn-N(3)	Mn-N(4)	Mn-N(5)
$[Mn^{III}(O_2)(mL_5^2)\text{-}N(1)]^+$	17.9	1.899	1.427	2.610	2.349	2.187	2.275	2.272
	19.3[a]	1.894						
	21.3[b]							
$[Mn^{III}(O_2)(mL_5^2)\text{-}N(4)]^+$	0	1.850	1.433	2.204	2.368	2.285	5.209	2.095
	0[a]	1.848						
	0[b]							
$[Mn^{III}(O_2)(mL_5^2)\text{-}N(3)]^+$	6.5	1.873	1.422	2.444	2.226	5.137	2.167	2.244
	7.6[a]	1.864						
	8.0[b]							
$[Mn^{III}(O_2)(imL_5^2)\text{-}N(1)]^+$	20.3	1.873	1.420	2.805	2.529	2.096	2.240	2.236
	21.4[a]	1.869						
$[Mn^{III}(O_2)(imL_5^2)\text{-}N(4)]^+$	8.4	1.861	1.434	2.240	2.447	2.247	5.345	2.067
	9.2[a]	1.847						
$[Mn^{III}(O_2)(imL_5^2)\text{-}N(3)]^+$	0	1.860	1.431	2.723	2.359	5.408	2.088	2.088
	0[a]	1.857						
$[Mn^{III}(O_2)(N4py)\text{-}N(1)]^+$	24.9	1.870	1.417	2.510	2.274	2.240	2.293	2.278
	26.6[a]	1.862						
$[Mn^{III}(O_2)(N4py)\text{-}N(2)]^+$	0	1.869	1.425	2.419	5.335	2.209	2.076	2.206
	0[a]	1.845						
$[Mn^{III}(O_2)(N4py)\text{-}N(3)]^+$	6.5	1.867	1.421	2.453	2.230	5.078	2.166	2.126
	4.6[a]	1.862						

[a] Total-energy calculated for gas-phase optimized geometry included solvation effects associated with acetonitrile that were incorporated using the COSMO method. [b] Both the geometry optimization and total-energy calculations included acetonitrile solvation effects using COSMO.

Given the clear preference for both side-on peroxo binding and a six-coordinate Mn^{III} center, we next evaluated the possibility of dissociation of one of the pyridine arms of mL_5^2 through two relaxed surface scans. In these calculations the Mn–N(4) and Mn–N(3) distances (see Figure 2.6 for atom labeling) were elongated through rotation of the appropriate pyridylmethyl arms. In both scans, local minima were found that correspond to six-coordinate complexes with side-on peroxo ligands and dissociated pyridines. These structures were subjected to full geometry optimization, with no structural parameters fixed, to provide an even comparison with $[Mn^{III}(O_2)(mL_5^2)\text{-}N(1)]^+$. These fully optimized structures, referred to as $[Mn^{III}(O_2)(mL_5^2)\text{-}N(3)]^+$ and $[Mn^{III}(O_2)(mL_5^2)\text{-}N(4)]^+$ for dissociated N(3) and N(4) atoms, respectively, are lower in energy than $[Mn^{III}(O_2)(mL_5^2)\text{-}N(1)]^+$ by ~20 and 14 kcal/mol (Table

2.4). Thus, pyridine dissociation is strongly favored for $[Mn^{III}(O_2)(mL_5^2)]^+$. The relative energies show a very small dependence on solvation effects, which were incorporated using the COSMO method (Table 2.4). Given the expected accuracy of total energies obtained by B3LYP DFT calculations for transition metal systems (~5 kcal/mol),[57] both $[Mn^{III}(O_2)(mL_5^2)\text{-}N(4)]^+$ and $[Mn^{III}(O_2)(mL_5^2)\text{-}N(3)]^+$ appear to be reasonable models.

The optimized structures of $[Mn^{III}(O_2)(mL_5^2)\text{-}N(4)]^+$ and $[Mn^{III}(O_2)(mL_5^2)\text{-}N(3)]^+$ reveal the coordinative flexibility of the mL_5^2 ligand (Figure 2.6 and Table 2.4). The Mn^{III} center of $[Mn^{III}(O_2)(mL_5^2)\text{-}N(4)]^+$ is in a distorted octahedral geometry, with N(2)–Mn–N(3) and N(1)–Mn–N(5) angles of 156° and 101°. With regards to the Mn^{III} coordination geometry, $[Mn^{III}(O_2)(mL_5^2)\text{-}N(4)]^+$ is very similar to the XRD structures of $[Mn^{III}(O_2)(TMC)]^+$ and $[Mn^{III}(O_2)(13\text{-}TMC)]^+$,[23,24] as well as the DFT-computed structures of $[Mn^{III}(O_2)(L^7py_2^R)]^+$ complexes (Figure 2.1).[29,58] In all these structures, the peroxo sits above four nitrogen atoms in a tetragonal arrangement. In contrast, the N ligands in $[Mn^{III}(O_2)(mL_5^2)\text{-}N(3)]^+$ are bound in a tripodal fashion, with N(1) occupying the basal position and N(2), N(4), and N(5) defining a trigonal plane. In this case, the coordination geometry around the Mn^{III} center is very similar to that proposed for $[Mn^{III}(O_2)(H_2bupa)]^-$, although the latter complex contains a dianionic ligand and likely possesses second-sphere H-bonding interactions with the peroxo moiety (Figure 2.1).[28,59]

(B) Spectroscopic Properties of $[Mn^{III}(O_2)(mL_5^2)\text{-}N(4)]^+$ and $[Mn^{III}(O_2)(mL_5^2)\text{-}N(3)]^+$. To evaluate the validity of the $[Mn^{III}(O_2)(mL_5^2)\text{-}N(4)]^+$ and $[Mn^{III}(O_2)(mL_5^2)\text{-}N(3)]^+$ models, the TD-DFT method was used to determine electronic transition energies and oscillator strengths. The Abs spectra obtained from these computations are shown in Figure 2.7, and the experimental spectrum is included for comparison. The TD-DFT-computed Abs spectra of

$[Mn^{III}(O_2)(mL_5^2)\text{-}N(4)]^+$ and $[Mn^{III}(O_2)(mL_5^2)\text{-}N(3)]^+$ both contain sets of bands at ~18 000 and 23 500 cm^{-1} (bands *i* and *ii*) that are in good agreement with the experimental Abs spectrum of $[Mn^{III}(O_2)(mL_5^2)]^+$, which shows a band at ~17 300 cm^{-1}, a shoulder at ~23 500 cm^{-1}, and more intense features at higher energy. However, the intensity ratios of bands *i* and *ii* are dramatically different for $[Mn^{III}(O_2)(mL_5^2)\text{-}N(4)]^+$ and $[Mn^{III}(O_2)(mL_5^2)\text{-}N(3)]^+$ (0.06:1 and 0.80:1, respectively). Only the latter is in reasonable agreement with the ~1:1 ratio of experimental Abs intensities at 15 000 and 26 000 cm^{-1}. Band *i* of $[Mn^{III}(O_2)(mL_5^2)\text{-}N(3)]^+$ is predominantly *y*-polarized with a slight *x*-component (14% *x*-, 85% *y*-, and <1% *z*-polarization), in excellent agreement with analysis of VTVH MCD data collected for band 1 (5% *x*-, 89% *y*-, and 6% *z*-polarization; see Figure 2.5).[60] In contrast, band *i* of $[Mn^{III}(O_2)(mL_5^2)\text{-}N(4)]^+$ is significantly more *z*-polarized (4% *x*-, 67% *y*-, and 29% *z*-polarization), inconsistent with experimental data. On the basis of the agreement between experimental and TD-DFT-computed electronic transition energies, oscillator strengths, and polarizations $[Mn^{III}(O_2)(mL_5^2)\text{-}N(3)]^+$ is a better model for $[Mn^{III}(O_2)(mL_5^2)]^+$.

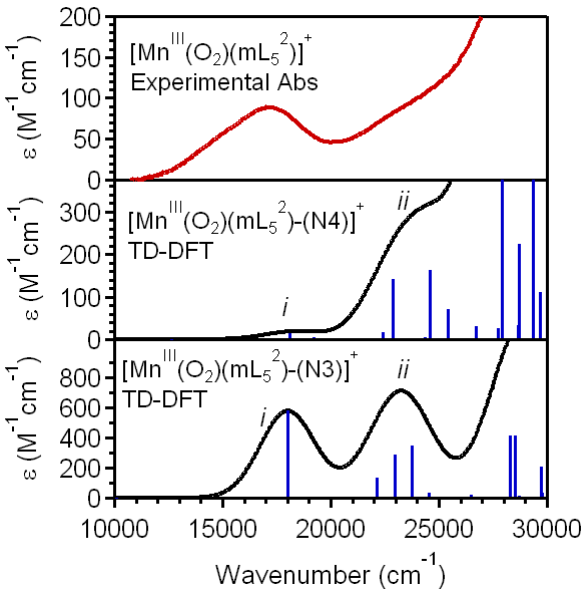

Figure 2.7. Experimental electronic absorption spectrum of $[Mn^{III}(O_2)(mL_5^2)]^+$ (top) and TD-DFT-computed absorption spectra for $[Mn^{III}(O_2)(mL_5^2)\text{-}N(4)]^+$ (center) and $[Mn^{III}(O_2)(mL_5^2)\text{-}N(3)]^+$ (bottom). The vertical sticks represent individual electronic transitions.

Given the success of the TD-DFT computations for $[Mn^{III}(O_2)(mL_5^2)\text{-}N(3)]^+$ in reproducing the major spectral features of $[Mn^{III}(O_2)(mL_5^2)]^+$, it is warranted to discuss similarities and differences in the bonding descriptions provided by these methods and make spectral assignments. The Mn^{III} 3d splitting pattern afforded by the DFT computations is shown in Figure 2.8. The compositions of the spin-up Mn 3d-based Kohn-Sham MOs are in Table 2.5, and more complete information is provided in Appendix 2.2 (Table A.2.2). Because of the trigonal arrangement of the equatorial nitrogen donors, the Mn 3d-based MOs are mixtures of the canonical 3d orbitals, and are labeled according to the dominant contributor. For example, MO 120β is labeled as x^2-y^2, but this orbital contains significant contributions from x^2-y^2 (33%), *xy* (19%), z^2 (10%) and *xz* (10%). Because of this mixing, the surface contour plot of this MO only slightly resembles a canonical x^2-y^2 orbital (Figure 2.8). The lowest-energy Mn d-based MOs (*xz* and *yz*), which are both singly-occupied, are involved in π-antibonding interactions with the

peroxo ligand, as evidenced by the ~17% peroxo character in the spin-up MOs (MOs 105α and 109α in Table 2.5). The greater contributions from the mL_5^2 ligand in the *yz* MO shift it to higher energy relative to *xz*. The singly-occupied z^2 and x^2-y^2 MOs are predominantly involved in σ-antibonding interactions with the mL_5^2 ligand, with the x^2-y^2 MO carrying more peroxo character than z^2 (11 versus 5%, respectively). The highest-energy Mn d-based MO (*xy*) is unoccupied and is the dominant Mn–O_2 σ-antibonding MO, containing similar contributions from Mn 3d and peroxo in-plane π* MOs (π_{ip}*).[61] This electronic structure description of a high-spin (S = 2) Mn^{III} center and a peroxo (O_2^{2-}) ligand is best described as a peroxomanganese(III) species.

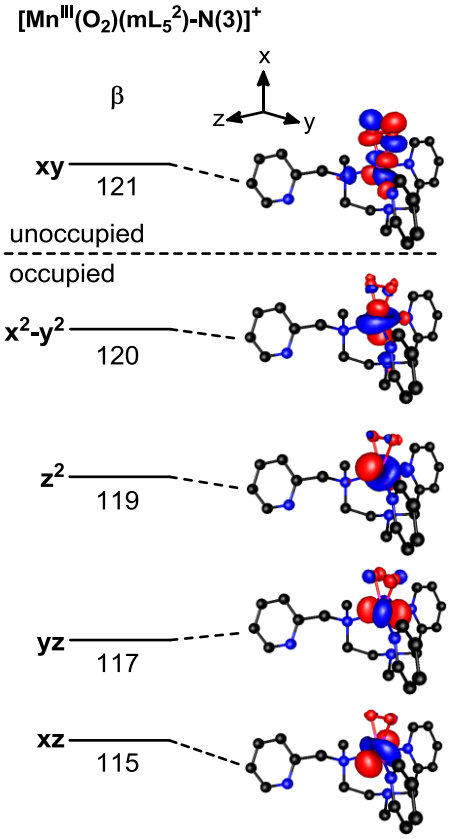

Figure 2.8. Schematic molecular orbital splitting diagram for $[Mn^{III}(O_2)(mL_5^2)\text{-}N(3)]^+$ and surface contour plots of quasi-restricted orbitals based on DFT computations.

Table 2.5. Energies (eV) and Compositions of the Spin-Up (α) Mn 3d-based MOs from B3LYP Spin-Unrestricted DFT Computations for $[Mn^{III}(O_2)(mL_5^2)]^+$.

	xz (105α)	*yz* (109α)	z^2 (110α)	x^2-y^2 (113α)	*xy* (115α)
Energy	-10.855	-10.221	-9.836	-9.014	-4.842
Mn 3d	57.3	33.0	24.9	39.2	30.7
z^2	5.9	1.1	13.3	12	0.3
x^2-y^2	39.5	1.1	8.6	1.9	0.1
xy	0.4	25.8	0.5	0.3	1.7
xz	9.9	2.2	1.1	14.5	9.8
yz	1.6	2.8	1.4	10.5	18.8
O_2 2p	16.5	17.3	5.1	11.3	48.3
mL_5^2 (N 2p)	7.3	24.5	38.9	32.8	5.9

According to the TD-DFT calculations, the lowest-energy *d-d* transition involves excitation from x^2-y^2 to *xy*, which is predicted at 18 015 cm^{-1} (band *i* in Figure 2.7, bottom), in good agreement with the experimental energy of band 1 (Table 2.2). At higher-energy, the TD-DFT method predicts an Abs band centered at ~23 000 – 25 000 cm^{-1} that contains contributions from a cluster of transitions, including peroxo-to-manganese(III) charge transfer bands, of which the O_2 $\pi_{op}^* \rightarrow yz$ is predicted as the most intense by both methods, and two *d-d* transitions ($z^2 \rightarrow xy$ and $yz \rightarrow xy$). Thus, this computational method is in good agreement with our Gaussian analysis of Abs and MCD data collected for $[Mn^{III}(O_2)(mL_5^2)]^+$.

(C) Hypothetical Structures for $[Mn^{III}(O_2)(imL_5^2)]^+$ and $[Mn^{III}(O_2)(N4py)]^+$. The spectroscopic similarities of $[Mn^{III}(O_2)(mL_5^2)]^+$ with $[Mn^{III}(O_2)(imL_5^2)]^+$ and $[Mn^{III}(O_2)(N4py)]^+$ require that these three complexes have similar geometries. DFT geometry optimizations of hypothetical models of $[Mn^{III}(O_2)(imL_5^2)]^+$ and $[Mn^{III}(O_2)(N4py)]^+$ provide compelling evidence that ligand dissociation, resulting in the formation of six-coordinate Mn^{III} centers with side-on peroxo ligands, is energetically feasible for these systems as well (Table 2.4 and Figure 2.9). For $[Mn^{III}(O_2)(imL_5^2)]^+$, dissociation of an imidazole arm in models $[Mn^{III}(O_2)(imL_5^2)\text{-}N(4)]^+$ and $[Mn^{III}(O_2)(imL_5^2)\text{-}N(3)]^+$ leads to significantly lower energies (~10 – 20 kcal/mol) relative to a

model with a dissociated amine nitrogen *trans* to the peroxo group ($[Mn^{III}(O_2)(imL_5^2)\text{-}N(1)]^+$). The structure of $[Mn^{III}(O_2)(imL_5^2)\text{-}N(3)]^+$ is virtually identical to that of $[Mn^{III}(O_2)(mL_5^2)\text{-}N(3)]^+$, consisting of an amine nitrogen *trans* to the peroxo unit and three equatorial nitrogen donors (cf. Figure 2.9, top and Figure 2.6, bottom), and it is lower in energy than the $[Mn^{III}(O_2)(imL_5^2)\text{-}N(4)]^+$ model by nearly 10 kcal/mol. While the Mn-N(1) distance is quite long in $[Mn^{III}(O_2)(imL_5^2)\text{-}N(3)]^+$ (2.72 Å; see Table 2.4), shortening this bond to 2.40 Å is associated with an increase in energy of only 2.6 kcal/mol (Table A.2.4 and Figure A.2.7, top). Consequently, the long Mn–N(1) distance might be exaggerated in the energy-minimized structure. In the TD-DFT-computed Abs spectra, shortening the Mn-N(1) distance leads to a red-shift of the lowest-energy Abs band (Figure A.2.7, bottom), lending credence to our proposal that the temperature-dependence of the experimental Abs spectrum of $[Mn^{III}(O_2)(imL_5^2)]^+$ is due to small, temperature-dependent changes in metal-ligand distances. For $[Mn^{III}(O_2)(N4py)]^+$, pyridine dissociation is also favored by ~20 – 25 kcal/mol (Table 2.4). The lowest-energy conformer, $[Mn^{III}(O_2)(N4py)\text{-}N(2)]^+$ (Figure 2.9, bottom), is structurally similar to $[Mn^{III}(O_2)(mL_5^2)\text{-}N(3)]^+$ and $[Mn^{III}(O_2)(imL_5^2)\text{-}N(3)]^+$, and the TD-DFT-computed Abs spectrum of this model is fully consistent with experimental data (Figure 2.10).

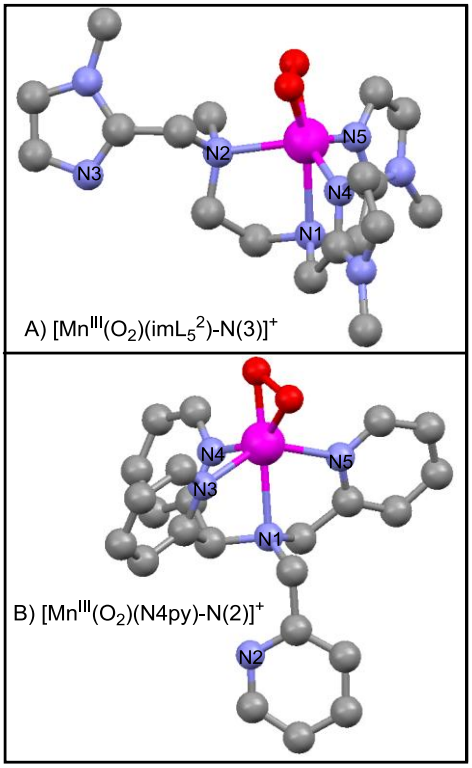

Figure 2.9. Molecular structures of $[Mn^{III}(O_2)(imL_5^2)\text{-}N(3)]^+$ and $[Mn^{III}(O_2)(N4py)\text{-}N(2)]^+$ developed using DFT computations.

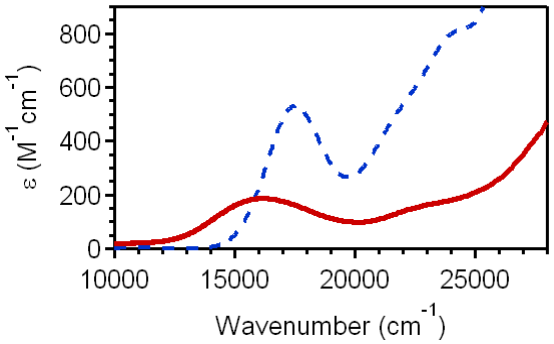

Figure 2.10. TD-DFT-computed electronic absorption spectrum of $[Mn^{III}(O_2)(N4py)\text{-}N(2)]^+$ (dashed line) and corresponding experimental spectra for $[Mn^{III}(O_2)(N4py)]^+$ at 248 K (solid line).

2.3.6. Aldehyde Deformylation Activity of $[Mn^{III}(O_2)(N4py)]^+$. Due to the nucleophilic nature of the peroxo ligand in synthetic peroxomanganese(III) complexes, these species often

take part in aldehyde deformylation reactions.[62] A common substrate that has been used to compare relative reactivities of peroxomanganese(III) complexes supported by different supporting ligands is cyclohexanecarboxaldehyde (CCA).[23,24,58,59,63,64] The addition of excess CCA (10 – 100 equivalents) to the blue acetonitrile solution of $[Mn^{III}(O_2)(N4py)]^+$ at -40 ºC results in the disappearance of the characteristic visible band at 16 200 cm^{-1}, which indicates the decay of the peroxomanganese(III) complex (Figure 2.11). As the band at 16 200 cm^{-1} decays, two new bands at ~15 200 and 17 500 cm^{-1} become resolved (Figure 2.11). These absorption features, although quite weak, are reminiscent of those of $[Mn^{III}Mn^{IV}(\mu\text{-}O)_2(N4py)_2]^{3+}$ and indicate that ~20% of $[Mn^{III}(O_2)(N4py)]^+$ (0.006 mmol) converts to $[Mn^{III}Mn^{IV}(\mu\text{-}O)_2(N4py)_2]^{3+}$ (~0.0013 mmol) during the course of the reaction with CCA.[65] Because the bands at ~15 200 and 17 500 cm^{-1} overlap with the band at 16 200 cm^{-1}, the time course for decay of the 16 200 cm^{-1} band does not follow pseudo-first-order kinetic behavior (Figure 2.11, inset), which severely complicates the kinetic analysis. Consequently, we are unable to extract reasonable rate data from these reactions to permit a comparison of the CCA deformylation reactivity of $[Mn^{III}(O_2)(N4py)]^+$ with that of other peroxomanganese(III) complexes. We note that similarly complex kinetic behavior is observed when $[Mn^{III}(O_2)(N4py)]^+$ is treated with excess benzaldehyde (20 – 60 equivalents), another substrate often used to explore peroxometal deformylation reactivity.

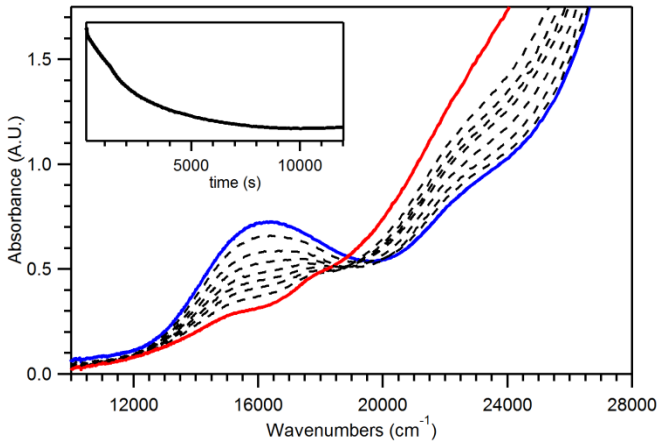

Figure 2.11. Electronic absorption spectra of $[Mn^{III}(O_2)(N4py)]^+$ (blue solid trace), formed by adding 2 equiv. KO_2 to 5 mM $[Mn^{II}(N4py)(OTf)]^+$ in MeCN at -40 ^oC, and spectral changes upon addition of cyclohexanecarboxaldehyde (10 equivalents, 50 mM) at -40 ^oC in MeCN. The inset shows the time course of the absorbance at 16 200 cm^{-1}.

2.4. Discussion.

While pentadentate ligands are often used to support peroxometal intermediates, including manganese[26,27] and iron[66-69] species, the molecular structures of these species have remained elusive. For example, while there are several crystallographically characterized peroxomanganese(III) adducts supported by tetradentate[20,23,24] and tridentate[21,22] ligands, corresponding adducts featuring pentadentate ligands are comparatively scarce and structural data are lacking for these species.[26,27] This is despite the fact that such pentadentate frameworks may provide higher fidelity to the first coordination spheres of Mn enzymes that react with oxygen and its reduced derivatives, as these often consist of five, tightly bound ligands (see Figure 2.1).[2,8,70] In this study, we have used a variety of spectroscopic and computational methods to demonstrate that the peroxomanganese(III) adducts supported by the pentadentate mL_5^2, imL_5^2, and N4py ligands feature six-coordinate Mn^{III} centers with side-on peroxo ligands, which requires the ligands convert from a pentadentate binding mode in the Mn^{II} complexes to a

tetradentate mode for the Mn^{III}-O_2 species. Specifically, on the basis of DFT-computed energies and the agreement between experimental and calculated spectroscopic data, we conclude that these six-coordinate, side-on peroxomanganese(III) complexes feature pyridine (or imidazole) arms that are dissociated. The implications of these studies for biological Mn enzymes are discussed below.

Dissociation of a pyridine or imidazole arm for the mL_5^2, imL_5^2, and N4py ligands is possible in the peroxomanganese(III) complexes because these ligands can adopt a variety of metal-binding modes, some of which are of comparable energy. This is illustrated in the three hypothetical structures developed for $[Mn^{III}(O_2)(mL_5^2)]^+$ (Figure 2.6). In contrast to these apparently flexible pentadentate ligands, metalloenzyme active sites, such as those of MnSOD and MndD (Figure 2.1), typically feature amino acid ligands whose positions are greatly constrained by the protein matrix. In these systems ligand dissociation would presumably be disfavored energetically. By limiting the coordination sites available for peroxo (or superoxo) binding, these sites may inhibit the formation of more thermodynamically stable side-on peroxomanganese(III) centers.[3] Surface scans evaluating the conversion from side-on to end-on peroxo binding for $[Mn^{III}(O_2)(mL_5^2)]^+$ revealed an inverse correlation between one $Mn–O_{peroxo}$ distance and the Mn–N(1) distance, where the N(1) ligand is *trans* to the peroxo unit. On the basis of this correlation, a short, strong Mn–L bond *trans* to the peroxo unit would favor end-on peroxo binding. In the case of $[Mn^{III}(O_2)(mL_5^2)]^+$, shorter Mn–N(1) and longer $Mn–O_{peroxo}$ distances led to a thermodynamic destabilization, because strengthening the Mn–N(1) bond could not compensate for weakening the $Mn–O_{peroxo}$ bond. However, it is speculated that a stronger *trans* ligand (*e.g.*, a carboxylate) could make side-on and end-on peroxo binding modes comparable in energy. This model is consistent with the proposal by Nam and co-workers that

anionic *trans* ligands in $[Mn^{III}(O_2)(13\text{-TMC})(X)]$ could elongate one $Mn–O_{peroxo}$ bond, thus leading to the observed increase in reactivity upon X^- binding.[23] In addition, according to this model, the presence of a carboxylate ligand *trans* to the expected superoxide and dioxygen binding sites in MnSOD and MndD, respectively, would further disfavor side-on binding in these active sites.[3]

The proposal that pyridine and imidazole dissociation is possible for the mL_5^2, imL_5^2, and N4py ligands also has relevance for metal-catalyzed transformations that utilize these types of pentadentate ligands. Such ligands are employed in catalytic reactions including textile and wood pulp bleaching, a variety of substrate oxygenation reactions, and atom transfer radical polymerizations.[71-76] On the basis of our results, it may not be well-founded to assume that such ligands remain bound in a pentadentate mode during catalysis.

Notes and References.

1. Grove, L. E.; Brunold, T. C., *Comments Inorg. Chem.* **2008,** *29*, 134-168.
2. Miller, A.-F., *Curr. Opin. Chem. Biol.* **2004,** *8*, 162-168.
3. Jackson, T. A.; Karapetian, A.; Miller, A.-F.; Brunold, T. C., *Biochemistry* **2005,** *44*, 1504-1520.
4. Bull, C.; Niederhoffer, E. C.; Yoshida, T.; Fee, J. A., *J. Am. Chem. Soc.* **1991,** *113*, 4069-4076.
5. Hearn, A. S.; Stroupe, M. E.; Cabelli, D. E.; Lepock, J. R.; Tainer, J. A.; Nick, H. S.; Silverman, D. N., *Biochemistry* **2001,** *40*, 12051-12058.
6. Hearn, A. S.; Tu, C. K.; Nick, H. S.; Silverman, D. N., *J. Biol. Chem.* **1999,** *274*, 24457-24460.
7. Gunderson, W. A.; Zatsman, A. I.; Emerson, J. P.; Farquhar, E. R.; Que, L.; Lipscomb, J. D.; Hendrich, M. P., *J. Am. Chem. Soc.* **2008,** *130*, 14465-14467.
8. Vetting, M. W.; Wackett, L. P.; Que, L., Jr.; Lipscomb, J. D.; Ohlendorf, D. H., *J. Bacteriol.* **2004,** *186*, 1945-1958.
9. Opaleye, O.; Rose, R.-S.; Whittaker, M. M.; Woo, E.-J.; Whittaker, J. W.; Pickersgill, R. W., *J. Biol. Chem.* **2006,** *281*, 6428-6433.
10. Borowski, T.; Bassan, A.; Richards, N. G. J.; Siegbahn, P. E. M., *J. Chem. Theory Comput.* **2005,** *1*, 686-693.
11. Reinhardt, L. A.; Svedruzic, D.; Chang, C. H.; Cleland, W. W.; Richards, N. G. J., *J. Am. Chem. Soc.* **2003,** *125*, 1244-1252.

12. Svedružic, D.; Jónsoon, S.; Toyota, C. G.; Reinhardt, L. A.; Ricagno, S.; Lindqvist, Y.; Richards, N. G. J., *Arch. Biochem. Biophys.* **2005,** *433*, 176-192.
13. Tanner, A.; Bowater, L.; Fairhurst, S. A.; Bornemann, S., *J. Biol. Chem.* **2001,** *276*, 43627-43634.
14. Wu, A. J.; Penner-Hahn, J. E.; Pecoraro, V. L., *Chem. Rev.* **2004,** *104*, 903-938.
15. Cotruvo, J. A.; Stubbe, J., *Biochemistry* **2010,** *49*, 1297-1309.
16. Hearn, A. S.; Stroupe, M. E.; Cabelli, D. E.; Ramilo, C. A.; Luba, J. P.; Tainer, J. A.; Nick, H. S.; Silverman, D. N., *Biochemistry* **2003,** *42*, 2781-2789.
17. Guan, Y.; Hickey, M. J.; Borgstahl, G. E. O.; Hallewell, R. A.; Lepock, J. R.; O'Connor, D.; Hsieh, Y. S.; Nick, H. S.; Silverman, D. N.; Tainer, J. A., *Biochemistry* **1998,** *37*, 4722-4730.
18. Hsieh, Y. S.; Guan, Y.; Tu, C. K.; Bratt, P. J.; Angerhofer, A.; Lepock, J. R.; Hickey, M. J.; Tainer, J. A.; Nick, H. S.; Silverman, D. N., *Biochemistry* **1998,** *37*, 4731-4739.
19. Lévêque, V. J.-P.; Stroupe, M. E.; Lepock, J. R.; Cabelli, D. E.; Tainer, J. A.; Nick, H. S.; Silverman, D. N., *Biochemistry* **2000,** *39*, 7131-7137.
20. VanAtta, R. B.; Strouse, C. E.; Hanson, L. K.; Valentine, J. S., *J. Am. Chem. Soc.* **1987,** *109*, 1425-1434.
21. Kitajima, N.; Komatsuzaki, H.; Hikichi, S.; Osawa, M.; Moro-oka, Y., *J. Am. Chem. Soc.* **1994,** *116*, 11596-11597.
22. Singh, U. P.; Sharma, A. K.; Hikichi, S.; Komatsuzaki, H.; Moro-oka, Y.; Akita, M., *Inorg. Chim. Acta* **2006,** *359*, 4407-4411.
23. Annaraj, J.; Cho, J.; Lee, Y.-M.; Kim, S. Y.; Latifi, R.; de Visser, S. P.; Nam, W., *Angew. Chem., Int. Ed. Engl.* **2009,** *48*, 4150-4153.
24. Seo, M. S.; Kim, J. Y.; Annaraj, J.; Kim, Y.; Lee, Y.-M.; Kim, S.-J.; Kim, J.; Nam, W., *Angew. Chem., Int. Ed. Engl.* **2007,** *46*, 377-380.
25. Grapperhaus, C. A.; Mienert, B.; Bill, E.; Weyhermuller, T.; Wieghardt, K., *Inorg. Chem.* **2000,** *39*, 5306-5317.
26. Groni, S.; Blain, G.; Guillot, R.; Policar, C.; Anxolabéhère-Mallart, E., *Inorg. Chem.* **2007,** *46*, 1951-1953.
27. Groni, S.; Dorlet, P.; Blain, G.; Bourcier, S.; Guillot, R.; Anxolabéhère-Mallart, E., *Inorg. Chem.* **2008,** *47*, 3166-3172.
28. Shook, R. L.; Gunderson, W. A.; Greaves, J.; Ziller, J. W.; Hendrich, M. P.; Borovik, A. S., *J. Am. Chem. Soc.* **2008,** *130*, 8888-8889.
29. Geiger, R. A.; Chattopadhyay, S.; Day, V. W.; Jackson, T. A., *J. Am. Chem. Soc.* **2010,** *132*, 2821-2831.
30. Emerson, J. P.; Kovaleva, E. G.; Farquhar, E. R.; Lipscomb, J. D.; Que, L., Jr., *Proc. Natl. Acad. Sci. USA* **2008,** *105*, 7347-7352.
31. Chang, J.; Plummer, S.; Berman, E. S. F.; Striplin, D.; Blauch, D., *Inorg. Chem.* **2004,** *43*, 1735-1742.
32. Lubben, M.; Meetsma, A.; Wilkinson, E. C.; Feringa, B.; Que, L., Jr., *Angew. Chem., Int. Ed. Engl.* **1995,** *34*, 1512-1514.
33. Neese, F., *ORCA - an ab initio, Density Functional and Semiempirical Program Package, Version 2.8*, University of Bonn, 2011. *ORCA - an ab initio, Density Functional and Semiempirical Program Package, Version 2.8, University of Bonn, 2009.*
34. Becke, A. D., *J. Chem. Phys.* **1986,** *84*, 4524-4529.
35. Perdew, J. P., *Phys. Rev. B* **1986,** *33*, 8822-8824.

36. Schäfer, A.; Horn, H.; Ahlrichs, R., *J. Chem. Phys.* **1992,** *97*, 2571-2577.
37. Schäfer, A.; Huber, C.; Ahlrichs, R., *J. Chem. Phys.* **1994,** *100*, 5829-5835.
38. Neese, F., *J. Comput. Chem.* **2003,** *24*, 1740-1747.
39. Becke, A. D., *J. Chem. Phys.* **1993,** *98*, 1372-1377.
40. Becke, A. D., *J. Chem. Phys.* **1993,** *98*, 5648-5652.
41. Lee, C.; Yang, W.; Parr, R. G., *Phys. Rev. B* **1988,** *37*, 785-789.
42. Weigend, F.; Ahlrichs, R., *Phys. Chem. Chem. Phys.* **2005,** *7*, 3297-3305.
43. Bauernschmitt, R.; Ahlrichs, R., *Chem. Phys. Lett.* **1996,** *256*, 454-464.
44. Casida, E. M.; Jamorski, C.; Casida, K. C.; Salahub, D. R., *J. Chem. Phys.* **1998,** *108*, 4439-4449.
45. Stratman, R. E.; Scuseria, G. E.; Frisch, M. J., *J. Chem. Phys.* **1998,** *109*, 8218-8224.
46. Neese, F.; Olbrich, G., *Chem. Phys. Lett.* **2002,** *362*, 170-178.
47. El Ghachtouli, S.; Vincent Ching, H. Y.; Lassalle-Kaiser, B.; Guillot, R.; Leto, D. F.; Chattopadhyay, S.; Jackson, T. A.; Dorlet, P.; Anxolabéhère-Mallart, E., *Chem. Commun.* **2013,** *49*, 5696-5698.
48. Leto, D. F.; Ingram, R.; Day, V. W.; Jackson, T. A., *Chem. Commun.* **2013,** *49*, 5378-5380.
49. With these ligand sets, any Mn^{II} species present in solution will not contribute to the absorption or MCD spectra in the visible and near-UV regions. Thus, these experiments selectively probe the Mn^{III} complexes.
50. Geiger, R. A.; Leto, D. F.; Chattopadhyay, S.; Dorlet, P.; Anxolabéhère-Mallart, E.; Jackson, T. A., *Inorg. Chem.* **2011,** *50*, 10190-10203.
51. Kirk, M. L.; Peariso, K., *Curr. Opin. Chem. Biol.* **2003,** *7*, 220-227.
52. Neese, F.; Solomon, E. I., *Inorg. Chem.* **1999,** *38*, 1847-1865.
53. Despite numerous attempts, we were unable to acceptably fit VTVH MCD data collected for $[Mn^{III}(O_2)(N4py)]^+$ at higher energies. We presume this is due to the overlap of electronic transitions with different polarizations at higher energies. Alternatively, larger MCD B-term contributions could also affect the quality of VTVH MCD data collected at these wavelengths.
54. Nivorozhkin, A. L.; Anxolabéhère-Mallart, E.; Mialane, P.; Davydov, R.; Guilhem, J.; Cesario, M.; Audière, J.-P.; Girerd, J.-J.; Styring, S.; Schussler, L.; Seris, J.-L., *Inorg. Chem.* **1997,** *36*, 846-853.
55. bpmg = 2-[[2-[bis(pyridin-2-ylmethyl)amino]-ethyl](methyl)amino]acetic acid and mcbpen = N-methyl-N'-carboxymethyl-N,N'-bis(pyridylmethyl)ethane-1,2-diamine.
56. Berggren, G.; Thapper, A.; Huang, P.; Eriksson, L.; Styring, S. r.; Anderlund, M. F., *Inorg. Chem.* **2011,** *50*, 3425-3430.
57. Neese, F., *J. Biol. Inorg. Chem.* **2006,** *11*, 702-711.
58. Geiger, R. A.; Chattopadhyay, S.; Day, V. W.; Jackson, T. A., *Dalton Trans.* **2011,** *40*, 1707-1715.
59. Shook, R. L.; Borovik, A. S., *Inorg. Chem.* **2010,** *49*, 3646-3660.
60. The TD-DFT-computed transition polarizations are relative to the principal axes of the D-tensor, as determined by coupled-perturbed DFT computations.
61. The peroxo frontier orbitals, which are O–O π-antibonding, are conventionally classified as in-plane (πip*) or out-of-plane (πop*) depending on their orientation with respect to the metal-peroxo bond vectors.
62. Leto, D. F.; Jackson, T. A., *J. Biol. Inorg. Chem.* **2014,** *19*, 1-15.

63. Kang, H.; Cho, J.; Cho, K.-B.; Nomura, T.; Ogura, T.; Nam, W., *Chem. Eur. J.* **2013,** *19*, 14119-14125.
64. Shook, R. L.; Gunderson, W. A.; Greaves, J.; W., Z.; Hendrich, M. P.; Borovik, A. S., *J. Am. Chem. Soc.* **2008,** *130*, 8888-8889.
65. Leto, D. F.; Chattopadhyay, S.; Day, V. W.; Jackson, T. A., *Dalton Trans.* **2013,** *42*, 13014-13025.
66. Costas, M.; Mehn, M. P.; Jensen, M. P.; Que, L., Jr., *Chem. Rev.* **2004,** *104*, 939-986.
67. Girerd, J.-J.; Banse, F.; Simaan, A. J., *Struc. Bonding* **2000,** *97*, 143-177.
68. Koehntop, K. D.; Rohde, J.-U.; Costas, M.; Que Jr, L., *Dalton Trans.* **2004**, 3191-3198.
69. Roelfes, G.; Vrajmasu, V.; Chen, K.; Ho, R. Y. N.; Rohde, J.-U.; Zondervan, C.; la Crois, R. M.; Schudde, E. P.; Lutz, M.; Spek, A. L.; Hage, R.; Feringa, B. L.; Münck, E.; Que, L. J., *Inorg. Chem.* **2003,** *42*, 2639-2653.
70. Miller, A.-F., Superoxide processing. In *Comprehensive Coordination Chemistry II*, McCleverty, J. A.; Meyer, T. J., Eds. Elsevier Ltd.: Oxford, UK, 2004; Vol. 8, pp 479-506.
71. Klopstra, M.; Hage, R.; Kellogg, R. M.; Feringa, B. L., *Tetrahedron Lett.* **2003,** *44*, 4581-4584.
72. Roelfes, G.; Lubben, M.; Hage, R.; Que, J. L.; Feringa, B. L., *Chem. Eur. J.* **2000,** *6*, 2152-2159.
73. Roelfes, G.; Lubben, M.; Leppard, S. W.; Schudde, E. P.; Hermant, R. M.; Hage, R.; Wilkinson, E. C.; Que, L.; Feringa, B. L., *J. Mol. Catal. A: Chem.* **1997,** *117*, 223-227.
74. van den Berg, T. A.; de Boer, J. W.; Browne, W. R.; Roelfes, G.; Feringa, B. L., *Chem. Commun.* **2004**, 2550-2551.
75. Zhang, L.; Tang, H.; Tang, J.; Shen, Y.; Meng, L.; Radosz, M.; Arulsamy, N., *Macromolecules* **2009,** *42*, 4531-4538.
76. Hage, R.; Lienke, A., *Angew. Chem., Int. Ed. Engl.* **2006,** *45*, 206-222.

Chapter 3

Reaction Landscape of a Pentadentate N5-Ligated Mn^{II} Complex with $O_2^{\bullet-}$ and H_2O_2 Includes Conversion of a Peroxomanganese(III) Adduct to a Bis(μ-oxo)dimanganese(III,IV) Species

This work has been reproduced from: D. F. Leto, S. Chattopadhyay, V. W. Day and T. A. Jackson, *Dalton Trans.*, 2013, **42**, 13014 - 13025, with permission from The Royal Society of Chemistry.

3.1. Introduction.

The diverse chemistry of manganese-dependent enzymes commonly features the reaction of a redox-active manganese ion with molecular oxygen or one of its reduced derivatives (*i.e.*, superoxide, hydrogen peroxide, and water).[1-3] For example, Mn-dependent dioxygenases[4,5] and oxalate oxidase[6,7] react with molecular oxygen to perform substrate oxidations. Manganese superoxide dismutase[3,8,9] and manganese catalase[2] react with superoxide and hydrogen peroxide, respectively, as defense against reactive oxygen species. The tetramanganese cofactor in the oxygen-evolving complex of photosystem II converts water to O_2.[10,11] Finally, it was recently established that Mn-ribonucleotide reducatase (Mn-RNR) from *Bacillus subtilis* requires superoxide for the assembly of an oxo-bridged dimanganese(III,IV) species.[12] The $Mn^{III}Mn^{IV}$ form of Mn-RNR rapidly converts to a Mn^{III}_2-$Y^{\bullet}$ cofactor that itself generates a cysteine radical to initiate the conversion of nucleotides to deoxynucleotides.[13-15] The molecular mechanism by which the $Mn^{III}Mn^{IV}$ form of Mn-RNR is assembled is unknown, although a (hydro)-peroxomanganese(III) species was proposed as an intermediate.[12]

Examination of the spectroscopic properties and reactivity of Mn-containing model complexes has played a prominent role in advancing our understanding of Mn enzymes.[1,2,11,16-18] With respect to Mn-RNR, for example, there are numerous model complexes featuring bis(μ-oxo)dimanganese(III,IV) cores that serve as potential mimics of the $Mn^{III}Mn^{IV}$ form of the enzyme.[11,19] These model complexes, which are often observed upon treatment of manganese(II) complexes with H_2O_2 at room temperature,[2,19] are generally very stable thermodynamically. Crystal structures of these complexes reveal typical Mn---Mn separations of ~2.7 Å.[11,19-23] Some of these bis(μ-oxo)dimanganese(III,IV) complexes have been shown to oxidize substrates by a H-atom transfer mechanism, thus mimicking tyrosine oxidation by the $Mn^{III}Mn^{IV}$ form of Mn-

RNR.[24,25]

Mononculear side-on peroxomanganese(III)[26-38] and end-on alkylperoxomanganese(III)[39-41] intermediates have also been reported and characterized. These intermediates can be generated from their corresponding manganese(II) precursors using a variety of oxidants, including superoxide, hydrogen (or alkyl) peroxide, and molecular oxygen. They often, but not always,[30-32] are thermally unstable and must be formed and characterized at low temperatures. Reactivity studies of peroxomanganese(III) adducts have shown that the peroxo group is nucleophilic and attacks aldehydes to initiate a deformylation reaction.[27,30,31,34,42] Notably, although several examples of oxo-bridged dimanganese(III,IV) and (alkyl)peroxomanganese(III) species exist, there is, to the best of our knowledge, limited evidence that (alkyl)peroxomanganese(III) adducts can serve as intermediates in the generation oxo-bridged dimanganese(III,IV) complexes.[39-41]

To better understand the relationship of peroxomanganese(III) and bis(μ-oxo)dimanganese(III,IV) species, we have explored the chemical reactivity of the mononuclear $[Mn^{II}(N4py)(OTf)](OTf)$ complex with superoxide and hydrogen peroxide. In a previous, collaborative study with Dorlet and Anxolabéhère-Mallart, we established that the $[Mn^{II}(N4py)(OTf)](OTf)$ complex converts to a Mn^{III}-O_2 adduct upon treatment with excess superoxide (Scheme 1).[28] On the basis of detailed spectroscopic and computational studies of $[Mn^{III}(O_2)(N4py)]^+$, as well as the closely related $[Mn^{III}(O_2)(mL_5^2)]^+$ and $[Mn^{III}(O_2)(imL_5^2)]^+$ complexes (mL_5^2 = *N*-methyl-*N*,*N*′,*N*′′,-tris(2-pyridylmethyl)ethane-1,2-diamine and imL_5^2 = *N*-methyl-*N*,*N*′,*N*′′,-tris((1-methyl-4-imidazolyl)methyl)ethane-1,2-diamine), we concluded that the N4py ligand in $[Mn^{III}(O_2)(N4py)]^+$ is bound in an unusual tetradentate fashion (termed herein κ^4-N4py), whereas the peroxo is coordinated in a side-on (*i.e.*, η^2-O_2) mode. Because tetradentate binding of the N4py ligand could be achieved by either dissociation of a methylenepyridine or a

dipyridinylmethane moiety, two isomers of $[Mn^{III}(O_2)(\kappa^4\text{-N4py})]^+$ are possible. Molecular structures of these isomers, which were previously developed using density functional theory (DFT) computations, are shown in Scheme 3.1.[28] While the DFT-optimized structures are very similar, the $[Mn^{III}(O_2)(\kappa^4\text{-N4py})]^+$ isomer with a dissociated methylenepyridine arm was lower in total energy by ~6 kcal/mol, and TD-DFT-computed spectroscopic properties for this isomer were more consistent with the available spectroscopic data. Thus, we favored this isomer, but were unable to make a definitive conclusion on the basis of the available data.[43]

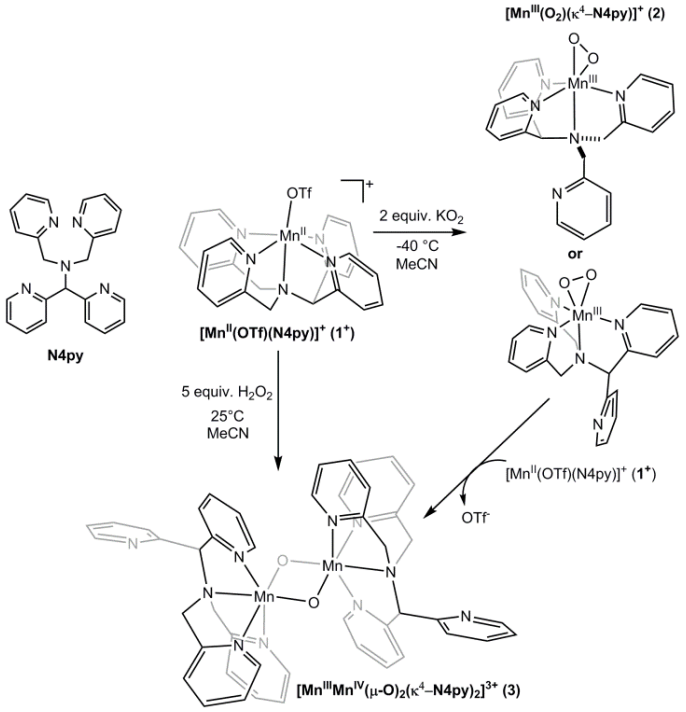

Scheme 3.1.

In this chapter, we extend our understanding of the reactivity of $[Mn^{II}(N4py)(OTf)](OTf)$ by showing that this complex converts to $[Mn^{III}Mn^{IV}(\mu\text{-O})_2(\kappa^4\text{-N4py})_2]^{3+}$ upon treatment with H_2O_2 and base even at -40 °C. Intriguingly, the $[Mn^{III}Mn^{IV}(\mu\text{-O})_2(\kappa^4\text{-N4py})_2]^{3+}$ complex can be formed in ~90% yield by reaction of the peroxomanganese(III) complex $[Mn^{III}(O_2)(\kappa^4\text{-N4py})]^+$

with $[Mn^{II}(N4py)(OTf)](OTf)$. As this reaction features the conversion of two Mn^{II} species to a $Mn^{III}Mn^{IV}$ compound using O_2^- as oxidant, it mimics formation of the $Mn^{III}Mn^{IV}$ form of Mn-RNR.

3.2. Experimental Methods.

3.2.1. Materials and Methods. All chemicals and solvents were obtained from commercial vendors and were ACS reagent-grade or better and used as received. Electronic absorption spectra were obtained on either a Varian Cary 50 Bio or an Agilent 8453 spectrophotometer, both of which were interfaced with a Unisoku cryostat (USP-203-A) capable of maintaining temperatures between 150 and 373 K. Mass spectrometry experiments were performed using an LCT Primers MicroMass electrospray time-of-flight instrument.

3.2.2. Synthesis. The synthesis of N4py ligand was performed according to a previously described procedure.[44,45] **1** was synthesized by reacting N4py ligand with $Mn^{II}(OTf)_2$ in an acetonitrile (MeCN) solution in a 1:1 molar ratio as previously reported.[28] **3** was synthesized as follows. Five equiv. H_2O_2 (30% aqueous) and 0.5 equiv. triethylamine (Et_3N) were slowly added to a 36 mM aqueous solution of $[Mn^{II}(N4py)(OTf)](OTf)$ (**1**) at 5 ^oC while stirring. The solution instantly changed from colorless to dark forest green and gas evolution was observed. After stirring for one hour, the water was removed in vacuo. The solid was redissolved in cold MeCN and a precipitate was formed from the solution by layering with cold ether. The solvent was decanted and the precipitate was washed with cold ether and dried (yield 95%). ESI-MS data were as follows: $\{[Mn^{III}Mn^{IV}(\mu\text{-}O)_2(N4py)_2](OTf)_2\}^+$ m/z = 1174.1285 (calc 1174.1305). To grow X-ray diffraction quality crystals, an aqueous solution of **3** (25 mM) was treated with a saturated aqueous solution of tetrabutylammonium hexafluorophosphate (NBu_4PF_6) dropwise at

5 ^{o}C and was stirred for 30 minutes. The green precipitate that formed was isolated by filtration, rinsed with ether, and dried in vacuo. Recrystallization of the crude solid from butyronitrile (PrCN)-diethyl ether afforded dark green crystals of $[Mn^{III}Mn^{IV}(\mu\text{-}O)_2(N4py)_2](PF_6)_3$. Elemental analysis $[Mn^{III}Mn^{IV}(\mu\text{-}O)_2(N4py)_2](PF_6)_3 \bullet C_4H_7N \bullet C_4H_{10}O$: $C_{54}H_{59}F_{18}Mn_2N_{11}O_3P_3$ calc (%): C 44.58, H 4.09, N 10.59; found (%): C 44.46, H 4.07, N 10.49.

The average oxidation state of the Mn in **3** was determined using an iodometric technique.[46] A 2.5 mM solution of recrystallized **3** was prepared in CH_2Cl_2 and a 0.25 mL aliquot of this solution was transferred to a 10 mL volumetric flask containing 0.25 mL glacial acetic acid and 4.8 mg tetrabutylammonium iodide. The volume was then adjusted to 10 mL with CH_2Cl_2. The bright yellow solution was mixed and the absorbance was measured in a 0.5 cm cuvette at 25 ^{o}C immediately after mixing. The triiodide produced was quantified by measuring the absorbance of the solution at 295 and 365 nm and the final oxidation state of the manganese was determined by the ratio of the triiodide liberated and the Mn consumed.[46] The average oxidation state of the Mn in recrystallized **3** was 3.4 ± 0.3 (average of four separate experiments).

A similar method was followed to determine the average oxidation state of the Mn in solution following the reaction of **1** with one equiv. KO_2 at -40 ^{o}C. For this reaction, a 5 mM MeCN solution of **1** was treated with one equiv. KO_2 at -40 ^{o}C. The reaction was monitored by electronic absorption and after six hours, the formation of **3** was complete. A 0.25 mL aliquot was quickly transferred to a 10 mL volumetric flask containing 0.25 mL glacial acetic acid and 4.8 mg tetrabutylammonium iodide. The volume was then adjusted to 10 mL with CH_2Cl_2. The bright yellow solution was mixed and the absorbance was measured in a 0.5 cm cuvette at 25 ^{o}C

immediately after mixing. The average oxidation state of the Mn in the reaction mixture was 2.48 ± 0.02 (average of two separate experiments).

3.2.3. X-Ray Diffraction Experiments. (A) $[Mn(O)(C_{23}H_{21}N_5)]_2$•2.8 CF_3SO_3•0.2 PF_6•2 CH_3CN (3a). Green single crystals of the CH_3CN solvated mixed salt, $[Mn(O)(C_{23}H_{21}N_5)]_2 \bullet 2.8\ CF_3SO_3 \bullet 0.2\ PF_6$ (**3a**), obtained from slow diffusion of diethyl ether into an acetonitrile solution of **3** at -20 ^oC, are, at 100(2) K, triclinic, space group P $\bar{1}$ – C_i^1 (No. 2). All entities appear to be disordered, however, a difference Fourier clearly revealed all of the hydrogen atoms bonded to carbon atoms in the dimer. This permitted identification of the non-coordinated nitrogen atom N(5) since it had no significant residual electron density near it but carbon atom C(20) did.

(B) $[Mn(O)(C_{23}H_{21}N_5)]_2 \bullet 3\ PF_6 \bullet 0.5\ H_2O$ (3b). Green single crystals of the hydrated salt, $[Mn(O)(C_{23}H_{21}N_5)]_2 \bullet 3\ PF_6 \bullet 0.5\ H_2O$ (**3b**), obtained from slow diffusion of diethyl ether into butyronitrile solution of **3** at -20 ^oC, are, at 100(2) K, monoclinic, space group P21/c – C_{2h}^5 (No. 2). Although the PF_6^- anions are severely disordered, **3b** clearly shows the anticipated effects of different Mn oxidation states, allowing for the axially elongated Mn^{III} center to be distinguished from the Mn^{IV} center.

Crystal structure, data collection, and refinement parameters for all crystal structures are provided in Appendix A.1.1 and summarized in Table A.1.1. CCDC-936496 contains the supplementary crystallographic data for $[Mn(O)(C_{23}H_{21}N_5)]_2$ - 2.8 CF_3SO_3 - 0.2 PF_6 (**3a**) and CCDC-936497 contains the supplementary crystallographic data for $[Mn(O)(C_{23}H_{21}N_5)]_2$ - 3 PF_6 (**3b**). This data can be obtained free of charge from the Cambridge Crystallographic Data Centre via www.cccdc.cam.ac/data_request/cif.

3.2.4. EPR Spectroscopy. Samples of **2** were prepared as follows. Two equiv. KO_2, in the form of a solution prepared from 14.2 mg KO_2 and 200 mg 18-crown-6 dissolved in 2 mL butyronitrile, were added to a 5 mM solution of $[Mn^{II}(N4py)(OTf)_2]$ (**1**) in butyronitrile at -40 ^oC. Once formation of $[Mn^{III}(O_2)(N4py)]^+$ (**2**) was judged complete by electronic absorption spectroscopy, the sample was further cooled to -80 ^oC, and ~250 μL were transferred to a pre-cooled 4 mm quartz EPR tube maintained at -80 ^oC using a cold ethanol bath. The sample was then flash-frozen in liquid N_2. An EPR sample of **3** was prepared by transferring 250 μL of a 0.5 mM solution of **3** in butyronitrile to a 4 mm quartz EPR tube, and flash-frozen in liquid N_2. All EPR spectra were collected on an X-band (9 GHz) Bruker EMXPlus spectrometer equipped with an Oxford ESR900 continuous-flow liquid helium cryostat and an Oxford ITC503 temperature system to monitor and regulate the temperature. A dual mode cavity (Bruker ER4116DM) was used for perpendicular and parallel mode detection. Spectra were recorded under non-saturating conditions using 100 kHz field modulation. Other parameters (microwave frequency, modulation amplitude, microwave power, time constant, conversion time, sweep rate, and field resolution) are given in the captions of the appropriate figures. The baseline contribution was insignificant and so, a blank spectrum was not subtracted from the spectra.

3.2.5. Mn K-edge X-ray Absorption Spectroscopy. (A) General Considerations. An XAS sample of **3** was prepared from a 30 mM aqueous solution of the complex. Approximately 150 μL of this solution were transferred to a sample holder covered with Kapton tape and the sample was flash-frozen in liquid N_2.

(B) XAS Data Collection. XAS spectra were recorded on beamline X3B at the National Synchrotron Light Source (NSLS), Brookhaven National Lab (storage ring conditions, 2.8 GeV, 100 - 300 mA). Mn K-edge X-ray absorption spectra were recorded on frozen solutions

maintained at 25 K with a helium Displex closed-cycle cryostat over the energy range 6.4 – 7.4 keV (Si(111) monochromater). Data were obtained as fluorescence excitation spectra using either a solid-state 13-element germanium detector (Canberra). Contamination of higher harmonics radiation was minimized by using a harmonic rejection mirror. Background fluorescence signal was reduced by use of a 6 μm chromium filter. A manganese foil spectrum was recorded concomitantly for internal energy calibration and the first inflection point of the K-edge energy was assigned to 6539.0 eV. Spectra were measured with 5 eV steps below the edge, 0.3 eV steps in the edge region, and steps equivalent to 0.05 $Å^{-1}$ increments above the edge (region borders were 6354, 6529, and 6554 eV). The XAS spectrum of complex **3** (30 mM in H_2O) represents the average of 9 scans.

(C) XAS Data Analysis. XAS data reduction and averaging were treated entirely using the program EXAFSPAK.[50] Pre-edge background intensity was removed by fitting a Gaussian function to the pre-edge background and subtracting this function from the whole spectrum. The spectrum was then fit with a three-segment spline with fourth-order polynomial components to remove low-frequency background. EXAFS refinement was carried out on $k^3\chi(k)$ data, using phase and amplitude functions obtained from *FEFF*, version 6.[51] The *k*-space used for data analysis of **3** was k = 2 - 14.3 $Å^{-1}$ (resolution 0.128 Å). For each fit, the parameters r (average distance between Mn and scattering atom) and σ^2 (Debye-Waller factor) were optimized, while n, the number of atoms in the shell, was kept fixed. n was varied by integer steps systematically. The goodness-of-fit (GOF) was evaluated by the parameter F, where $F = \Sigma\,(\chi_{calcd} - \chi_{expt})^2$ / N, and N is the number of data points. The threshold energy, E_0, in electronvolts (k = 0 point) was kept at a common, variable value for every shell of a given fit.

3.2.6. Magnetic Circular Dichroism Spectroscopy. The MCD sample of **3** was 2.5 mM in butyronitrile. MCD spectra were collected on a Jasco circular dichroism spectrometer (J-815) interfaced with an Oxford Instruments magnetocryostat (SM-4000-8) capable of a horizontal field up to 8 T and a temperature range of 1.5 to 300 K. Low-temperature absorption samples were prepared in acetonitrile and MCD samples were prepared in the glassy solvent butyronitrile (PrCN). VTVH MCD data were fit using software developed by Neese and Solomon.[52]

3.3. Results and Analysis.

3.3.1. Formation and Decay of $[Mn^{III}(O_2)(\kappa^4\text{-N4py})]^+$. The molecular structure of $[Mn^{II}(OTf)(N4py)](OTf)$ (**1**) has been previously determined by X-ray crystallography.[53,54] In the structure, the N4py ligand is coordinated in a pentadentate fashion, with the four pyridine nitrogen ligands defining the equatorial plane. The amino group of the N4py ligand is in an axial position *trans* to the monodentate triflate anion (see Scheme 2.1). When **1** is treated with KO_2 in MeCN at -40 ºC, it converts to the peroxomanganese(III) complex $[Mn^{III}(O_2)(\kappa^4\text{-N4py})]^+$ (**2**), as previously reported.[28] Figure 3.1 (left) shows the electronic absorption spectrum of the formation of **2** from the addition of one equiv. KO_2 and four equiv. 18-crown-6 ether at -40 ^oC. The electronic absorption spectrum of **2** displays a prominent band at 16 200 cm^{-1} (617 nm) and a shoulder at 22 800 cm^{-1} (438 nm). Although formation of **2** is observed using one equiv. KO_2, it is not maximally formed under these conditions. In recent work, Anxolabéhère-Mallart and co-workers have shown that **2** is formed in high yield using electrochemically generated O_2^{-}.[55] In contrast, the chemical method employing one equiv. KO_2 affords **2** in only a ~30% yield (this yield is estimated assuming 100% formation of **2** by the electrochemical method of Anxolabéhère-Mallart and co-workers).

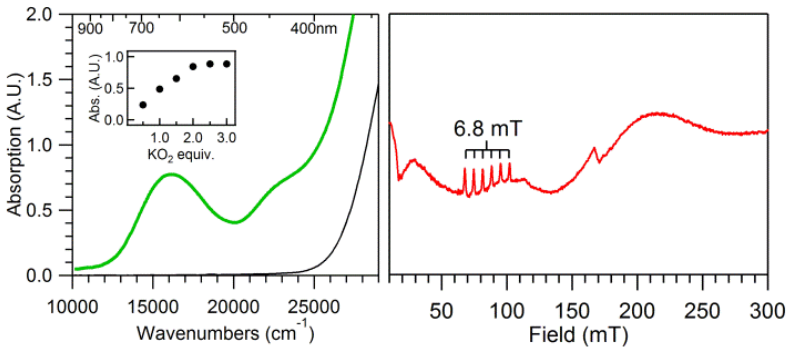

Figure 3.1. Left: Electronic absorption spectrum of **1** (black trace) and **2** (green trace), the latter of which was formed by adding 1 equiv. KO_2 to 7.5 mM **1** in MeCN at -40 °C. Inset: Maximum intensity at 16 200 cm^{-1} as a function of KO_2 equiv. added to 5 mM **1** in MeCN at -40 °C. **Right:** Parallel-mode X-band EPR spectrum of **2** in butyronitrile, formed using 2 equiv. KO_2. Recording conditions: 5 K, 9.3918 GHz microwave frequency, 2.0 mW microwave power, 0.4 mT modulation amplitude, 100 kHz modulation frequency, 81.92 ms time constant, and 15 000 point resolution.

The conditions under which **2** is maximally formed by chemical oxidation were determined by performing a KO_2 titration on a 5 mM acetonitrile solution of **1**. The intensity of the band at 16 200 cm^{-1} maximizes at two equiv. KO_2 (Figure 3.1, left inset). The use of three equiv. KO_2 does not noticeably increase the yield. We attribute the increased formation of **2** under these conditions to the instability of KO_2 and not to a two-electron oxidation of **1**. MCD[28] and EPR experiments[55] firmly establish **2** as a high-spin Mn^{III} complex.[56] For example, the parallel-mode X-band EPR spectrum of **2** displays a six-line signal centered at 84.5 mT with a hyperfine splitting of 6.8 mT (Figure 3.1, right), indicative of high-spin Mn^{III}.[37,38] The intensity of this signal decreases with increasing temperature (Figure A.3.1), consistent with a negative axial zero-field splitting parameter (*i.e.*, $D < 0$ cm^{-1}).

Given that **2** is metastable even at low temperatures, we used electronic absorption and EPR spectroscopies to investigate the products formed upon thermal decay. Notably, the identity of the decay products depends on the amount of KO_2 used to form **2**. When **2** is generated in high

yields (~60%) using 2 equiv. KO_2, the peroxomanganese(III) complex decays over the course of three hours to give a solution with an ill-defined absorption spectrum (Figure A.3.2). The perpendicular-mode EPR spectrum of the decayed solution of **2** in butyronitrile reveals the presence of Mn^{II} species. The Mn^{III} signal at 84.5 mT, is no longer observed in the corresponding parallel-mode spectrum (Figure A.3.3). We note that the Mn^{II} species observed under these conditions display EPR signals distinct from those of butyronitrile samples of $[Mn^{II}(N4py)(OTf)](OTf)$ and $Mn^{II}(OTf)_2$ (Figure A.3.4).[57]

In contrast, when **2** is formed using 1 equiv. KO_2, it decays to yield a new chromophore (**3**) with electronic absorption maxima at 15 000 and 17 700 cm^{-1} (667 and 565 nm; see Figure 3.2, left). This spectral pattern is similar to those of bis(μ-oxo)dimanganese(III,IV) complexes.[58-60] Indeed, independent preparation of **3** from **1** and H_2O_2 (*vide infra*) establishes its identity as $[Mn^{III}Mn^{IV}(\mu\text{-}O_2)(\kappa^4\text{-}N4py)_2]^{3+}$. The rate of formation of **3** increases linearly as the initial concentration of **1** increases, with a rate constant (k) of 2.12×10^{-3} M^{-1} min^{-1} at -40 ^oC (Figure A.3.5). On the basis of the extinction coefficients of authentic samples of **3**, the decay of **2** affords only a 33% conversion to **3** (based on total Mn concentration). With ~30% formation of **2** under these conditions, the conversion of **2** to **3** is nearly quantitative. Two lines of evidence suggest the balance of Mn is present in the Mn^{II} oxidation state. First, the perpendicular-mode EPR spectrum of the solution following the decay of **2** shows a sixteen-line signal typical of bis(μ-oxo)dimanganese(III,IV) complexes,[60-62] but also present are broader features from Mn^{II} species (Figure 3.2, right). Second, we determined the average oxidation state of the manganese species in the decay solution through an iodometric analysis.[46] In this procedure, the decay solution, which has a known manganese concentration, was treated with excess tetrabutylammonium iodide and glacial acetic acid. The triiodide produced upon reaction with

the manganese species was quantified using the electronic absorbance bands of triiodide at 295 and 365 nm; this gave an average oxidation state of manganese in solution of 2.48 ± 0.02. This average oxidation state can be well accounted for considering 33% $Mn^{III}Mn^{IV}$ from **3** and 67% Mn^{II}, which gives an average oxidation state of 2.49.

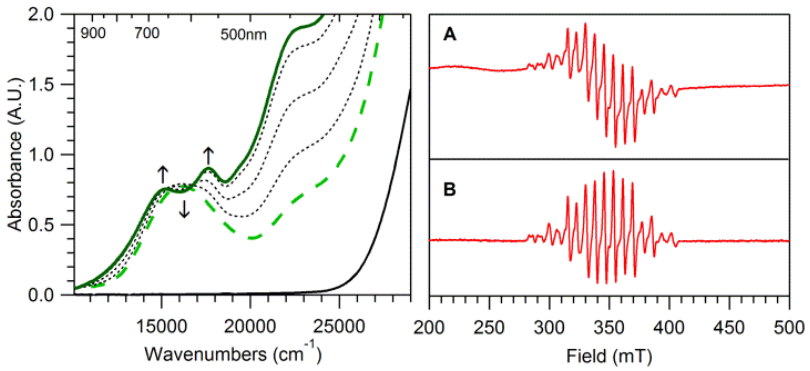

Figure 3.2. Left: Electronic absorption spectra of a 7.5 mM acetonitrile solution of **1** (solid black line) treated with 1 equiv. KO_2 at -40 ^oC in MeCN. The black dashed traces shows the conversion of **2** (green dashed trace) to **3** (solid green trace). **Right:** A) Perpendicular-mode X-band EPR spectrum of a 5 mM butyronitrile solution of **1** six hours after treatment with 1 equiv. KO_2 at -40 ^oC (complex **3**). Recording conditions: 5 K, 9.6374 GHz microwave frequency, 5.02 mW microwave power, 0.4 mT modulation amplitude, 100 kHz modulation frequency, 81.92 ms time constant, and 15 000 point resolution. B) Perpendicular-mode X-band EPR spectrum of a 0.54 mM frozen solution of recrystallized **3** in butyronitrile. Recording conditions: 20 K, 9.6386 GHz microwave frequency, 5.02 mW microwave power, 0.4 mT modulation amplitude, 100 kHz modulation frequency, 81.92 ms time constant, and 15 000 point resolution.

When the peroxomanganese(III) complex **2** is formed using 2 equiv. KO_2, it can be converted to **3** by treatment with the Mn^{II} starting material **1**. In this reaction, **2** was initially formed in ~60% yield (0.006 mmol) by adding 2 equiv. KO_2 to a 5 mM solution (0.010 mmol) of **1**. When 0.010 mmol **1** were added to the solution containing **2**, 0.0027(3) mmol (1.2 ± 0.1 mM) of **3** were rapidly produced (Figure A.3.6). Thus, approximately 90% of the Mn in the form of **2** is converted to the dimeric complex **3**. The same quantity of **3** is formed when 0.5 equiv. **1** was added to **2**, indicating that the formation of **3** is dependent on the amount of complex **2** formed

by the chemical oxidation of **1**. No spectral changes were observed when five equiv. **1** were added to an acetonitrile solution of **3** at 25 ^{o}C.

3.3.2. Formation of 3 using H_2O_2. The oxo-bridged dimanganese(III,IV) complex **3** can be independently prepared in high yield by treatment of **1** with H_2O_2. Specifically, when 5 equiv. 30% H_2O_2 and 0.5 equiv. Et_3N are added to an aqueous solution of **1** at 5 ^{o}C, complex **3** is formed quantitatively. Under these conditions, **3** is stable in solution at 25^{o} C for at least 15 hours (we have not monitored the solution stability of **3** past 15 hours). The molar extinction coefficients, determined by dissolving isolated **3** in MeCN, are 830 M^{-1} cm^{-1} and 680 M^{-1} cm^{-1} for the electronic absorption bands at 17 700 and 15 000 cm^{-1}, respectively. The perpendicular-mode EPR spectrum of isolated **3** in butyronitrile reveals the same 16-line signal as the EPR spectrum of **3** from the conversion of **2**; however, no broad signals from Mn^{II} species are observed for the isolated sample of **3** (Figure 3.2A and 3.2B). Complex **3** can also be formed in an analogous reaction in MeCN, albeit with ~50% yield. Without the addition of Et_3N, **3** is formed in ~30% yield in MeCN over the course of 12 hours, although a large excess of H_2O_2 (250 equiv.) and lower temperatures (-25 ^{o}C) are required. The average oxidation state of the manganese centers in a CH_2Cl_2 solution of recrystallized **3** was determined to be 3.4 ± 0.3 using an iodometric technique.[46]

Because urea-H_2O_2, which serves as an anhydrous source of H_2O_2, was previously used to generated a peroxomanganese(III) adduct using the closely related, pentadentate mL_5^2 ligand,[28] we investigated the reactivity of **1** with this oxidant. Treatment of a 7.5 mM acetonitrile solution of **1** at -18 ^{o}C with 50 equiv. urea-H_2O_2 changed the originally colorless solution to green. After the solution was filtered into a pre-cooled UV-Vis cuvette at -20 ^{o}C, electronic absorption spectroscopy was used to monitor the course of the reaction. The electronic

absorption data showed an initial broad feature at ~16 200 cm^{-1}, with a small shoulder around ~17 700 cm^{-1}. The intensity of the band at ~16 200 cm^{-1} is indicative of formation of **2** in ~3% yield relative to **1**. This spectrum resembled a mixture of complexes **2** and **3** (Figure 3.3, top). As time progressed, the visible feature at ~16 200 cm^{-1} lost intensity while the visible features at ~15 000 and ~17 700 cm^{-1} gained intensity (Figure 3.3, bottom). After four hours, the formation of **3** was completed, with a conversion of ~42%. To explore the effect of a stronger base on this process, **1** was incubated with 0.5 equiv Et_3N and then treated with an excess of urea-H_2O_2. In this reaction, the formation of **3** was completed in 10 minutes, and **3** was formed in higher yield (~57%).

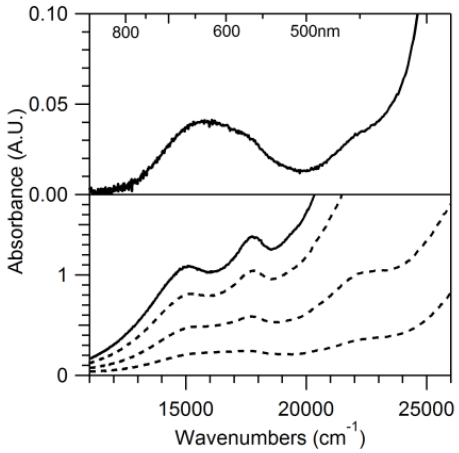

Figure 3.3. Electronic absorption spectra showing the reaction of a 7.5 mM acetonitrile solution of **1** with 50 equiv. anhydrous H_2O_2-urea at -18 ^oC. The solution was filtered into a pre-cooled cuvette (-20 ^oC) prior to collecting the first absorption spectrum (top). After four hours at -20 ^oC, the final absorption spectrum was obtained (bottom; solid line).

The effect of water on the formation of **2** and its conversion to **3** using H_2O_2-urea was investigated by treating the initial solution of **1** with 50 μL H_2O (55 equiv.) before the addition of solid H_2O_2-urea. Initially a small amount of **2** formed in ~4% yield relative to **1** with a final conversion to **3** of ~32%, relative to the total Mn concentration. The formation of a small amount

of **2** with and without excess water in solution using H_2O_2-urea as the oxidant was surprising because the formation of **2** was not observed when aqueous H_2O_2 (with Et_3N) was used as the oxidant.

3.3.3. Characterization of 3 by MCD Spectroscopy. Low-temperature MCD and variable-temperature, variable-field (VTVH) MCD data were collected on a 2.5 mM frozen solution of **3** in butyronitrile. Figure 3.4 shows both the 295 K electronic absorption and 7 T, VT MCD spectra of **3** (top and bottom, respectively). Whereas the electronic absorption spectrum consists of two maxima at 15 000 and 17 700 cm^{-1}, the 7 T MCD spectra display a series of five features from 11 000 – 28 000 cm^{-1}. VTVH MCD data collected at 16 500 cm^{-1} (Figure 3.4, bottom inset) were best fit with an $S = 1/2$ spin state, consistent with the EPR data. Moreover, the MCD spectrum is very similar to those reported for other bis(μ-oxo)dimanganese(III,IV) complexes.[59] Specifically, the MCD spectrum of complex **3** exhibits a pseudo-*A* term centered at 16 000 cm^{-1}, characteristic of bis(μ-oxo)dimanganese(III,IV) complexes. A Gaussian deconvolution of the MCD spectrum of **3** revealed 10 bands below 28 000 cm^{-1} (Figure A.3.7 and Table A.3.1). In an analysis of the MCD spectra of the bis(μ-oxo)dimanganese(III,IV) complexes $[Mn_2O_2(cyclam)_2]^{3+}$ (cyclam = 1,4,8,1 l-tetraazacyclotetradecane), $[Mn_2O_2(bipy)_4]^{3+}$ (bipy = 2,2'-bipyridine), and $[Mn_2O_2(phen)_4]^{3+}$ (phen = 1,10-phenanthroline), Gamelin *et al.* resolved 13 Gaussian bands.[59] Compared to this previous work, two of the low-energy bands (<12 000 cm^{-1}) and one high-energy band (>28 000 cm^{-1}) are not resolved in the MCD spectrum of **3**. Nonetheless, the energies of the resolved bands are very similar to those of $[Mn_2O_2(cyclam)_2]^{3+}$, further supporting the formulation of **3** as $[Mn^{III}Mn^{IV}(\mu\text{-}O)_2(N4py)_2]^{3+}$.

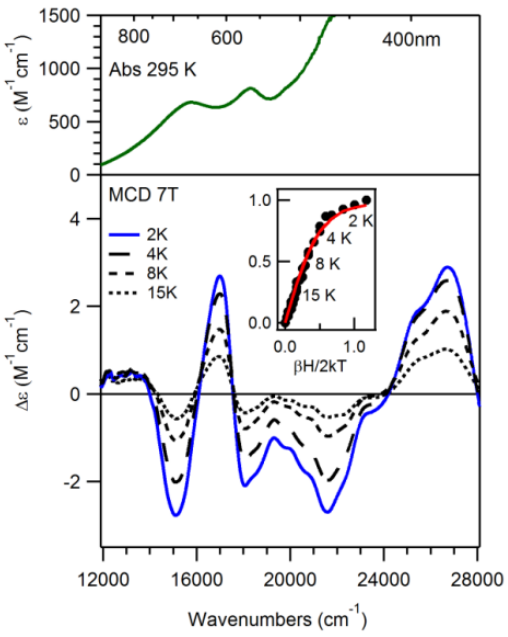

Figure 3.4. Top: 295 K electronic absorption spectrum of a 1.66 mM MeCN solution of recrystallized **3**. **Bottom:** 7 T MCD spectra of a 2.5 mM frozen butyronitrile solution of **3** at 2, 4, 8, and 15 K (bottom). Inset: 16 500 cm^{-1} VTVH MCD data (dots) and fits (solid lines).

3.3.4. Structural Characterization of 3. (A) X-ray Diffraction. The structure of **3** was established using X-ray crystallography (Figure 3.5). Crystals of **3** suitable for such experiments were only obtainable through the addition of a saturated aqueous solution of NBu_4PF_6 to aqueous solutions of **3**. Consequently, solid-state crystal structures were determined for two polymorphic salts of the mixed-oxidation state dimeric cation **3**, obtained from separate batches of complex **3** that differ by the types of counter anions, $[Mn^{III}Mn^{IV}(\mu\text{-}O)_2(\kappa^4\text{-}N4py)_2](OTf)_{2.8}(PF_6)_{0.2}$ (**3a**) and $[Mn^{III}Mn^{IV}(\mu\text{-}O)_2(\kappa^4\text{-}N4py)_2](PF_6)_3$ (**3b**). Only one polymorph of complex **3** has a crystallographic inversion center (**3a**).

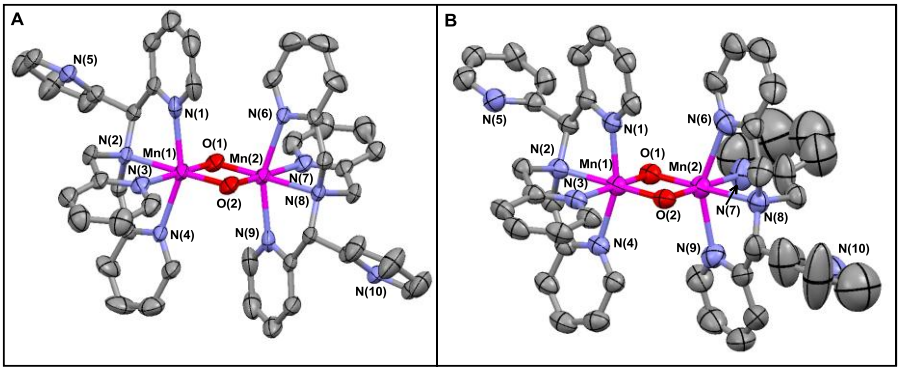

Figure 3.5. ORTEP diagrams (50% probability ellipsoids) of A) $[Mn^{III}Mn^{IV}(\mu\text{-}O)_2(\kappa^4\text{-}N4py)_2](OTf)_{2.8}(PF_6)_{0.2}$ (**3a**) and B) $[Mn^{III}Mn^{IV}(\mu\text{-}O)_2(\kappa^4\text{-}N4py)_2](PF_6)_3$ (**3b**) Hydrogen atoms, counter ions, and solvents of crystallization have been omitted for clarity.

Even though complex **3** is not symmetric, the metrical differences for the two halves of the dimer are expected to be small. The fact that there are small differences in the two similar halves of a rather large molecule might preclude observing them in a crystal structure determination due to packing disorder.[63-65] Both salts contain disordered anions with (heavier) P or S atoms and **3a** also contains a disordered metal dimer. Nonetheless, it was possible to locate hydrogen atoms for the noncoordinating pyridine ligands of **3a**, which permitted an unambiguous identification of carbon and nitrogen atoms. Even with the presence of severely disordered hexafluorophosphate anions and a water solvent molecule of crystallization, the structure of the second polymorphic form **3b** clearly shows the anticipated effects of different metal oxidation states and allows one to distinguish the axially elongated Mn^{III} center Mn(2) from the Mn^{IV} center Mn(1) (Table 3.1). Since the dimer is disordered in **3a**, the Mn^{III}- and Mn^{IV}-ligand bond distances and angles are essentially averaged in the crystal structure and agree well with the metrical parameters determined from the EXAFS data for **3** (*vide infa*), which likewise represent average Mn-ligand interatomic distances. The metrical parameters determined

for **3a** are also in good agreement with the average metal-to-ligand bond lengths and angles for both metals in **3b** (Table 3.1).

Table 3.1. Selected bond distances (Å) and angles (°) for $[Mn^{III}Mn^{IV}(\mu\text{-}O)_2(N4py)_2](OTf)_{2.8}(PF_6)_{0.2}$ (**3a**), $[Mn^{III}Mn^{IV}(\mu\text{-}O)_2(N4py)_2](PF_6)_3$ (**3b**), averaged bond distances and angles for **3b**, and from EXAFS data analysis of **3**.

	3a [a]	**3b** [b]	**EXAFS**
Mn(1)···Mn(2)	2.6483(8)	2.648(2)	2.63
Mn(1)–O(1)	1.815(3)	1.787(5)	
Mn(1)–O(2)	1.812(3)	1.767(6)	1.79
Mn(2)–O(1)	1.815(3)	1.835(6)	
Mn(2)–O(2)	1.812(3)	1.834(5)	
Mn(1)–N(1)	2.116(4)	2.012(6)	
Mn(1)–N(2)	2.096(4)	2.094(7)	
Mn(1)–N(3)	2.055(4)	2.055(5)	
Mn(1)–N(4)	2.143(4)	2.045(7)	2.00
Mn(2)–N(6)	2.143(4)	2.274(8)	2.17
Mn(2)–N(7)	2.055(4)	2.091(5)	
Mn(2)–N(8)	2.096(4)	2.129(6)	
Mn(2)–N(9)	2.116(4)	2.236(8)	
O(1)–Mn(1)–O(2)	86.2(1)	87.4(2)	
O(1)–Mn(2)–O(2)	86.2(1)	84.0(2)	
Mn(1)–O(1)–Mn(2)	93.8(1)	93.9(2)	
Mn(1)–O(2)–Mn(2)	93.8(1)	94.6(2)	
N(1)–Mn(1)–N(4)	155.7(2)	159.3(2)	
N(6)–Mn(2)–N(9)	155.7(2)	149.6(2)	

[a] Average Mn-ligand distances for **3a** are as follows: Mn-O = 1.813 Å; Mn-N = 2.102 Å. [b] Average Mn-ligand distances for **3a** are as follows: Mn-O = 1.806 Å; Mn-N = 2.117 Å.

The XRD structure of **3** clearly establish the κ^4-N4py motif, which was previously proposed for **2**.[28] The dissociation of a pyridine arm in a bis(μ-oxo)dimanganese complex is not unprecedented. Anderlund and co-workers recently described two bis(μ-oxo)dimanganese(IV,IV) complexes supported by the pentadentate N_4O bpmg and mcbpen ligands (bpmg = 2-[[2-[bis(pyridin-2-ylmethyl)amino]ethyl](methyl)amino]acetic acid, and

mcbpen = *N*-methyl-*N'*-carboxymethyl-*N,N'*-bis(2-pyridylmethyl)ethane-1,2-diamine) that likewise feature noncoordinating pyridine arms in the XRD structures.[66]

(B) Mn-K Edge X-ray Absorption Spectroscopy. Further structural characterization of **3** was obtained by X-ray absorption studies at the Mn K-edge. The X-ray absorption near edge spectrum (XANES) of **3** exhibits a single pre-edge feature, presumably from 1*s* – 3*d* transitions, at 6541.4 eV (Figure 3.6). For comparison, the XANES spectra[54] of $[Mn^{II}(N4py)(OTf)]^{+}$ (**1**$^{+}$) and $[Mn^{IV}(O)(N4py)]^{2+}$ are included in Figure 3.6 and discussed below. The edge energy of **3**, fit to the maximum of the first inflection point, was 6550.6 eV, which is in good agreement with the edge energies of other synthetic $Mn^{III}Mn^{IV}$ complexes (~6549.7 eV; see Table 3.2), as well as the superoxidized (*i.e.*, $Mn^{III}Mn^{IV}$) form of Mn-catalase (6549.2 eV).[67] The Fourier transform (*R*′ space) of the extended X-ray absorption fine structure (EXAFS) data for **3** has two principal peaks centered at *R*′ = 1.3 and 2.4 Å (Figure 3.7). These features are well fit with six shells of scatterers (Table 3.3). The short shell of O scatterers at 1.79 Å corresponds to the bridging oxygen atoms observed with average Mn–O distances of 1.81 Å in the XRD structures. The EXAFS shells at 2.00 and 2.17 Å are in good agreement with the average distances of the equatorial and axial nitrogen atoms from the Mn ions in the XRD structures (Table 3.1). The most prominent peak in the Fourier transform at *R*′ = 2.4 Å is due to the strong Mn•••Mn scattering, which requires one Mn at 2.63 Å. The inclusion of two outer-sphere shells of carbon scatterers at 2.81 and 2.96 Å significantly improves the GOF; however, the number of carbon atoms in each shell does not have a large effect on the quality of the fit (Table A.3.2).

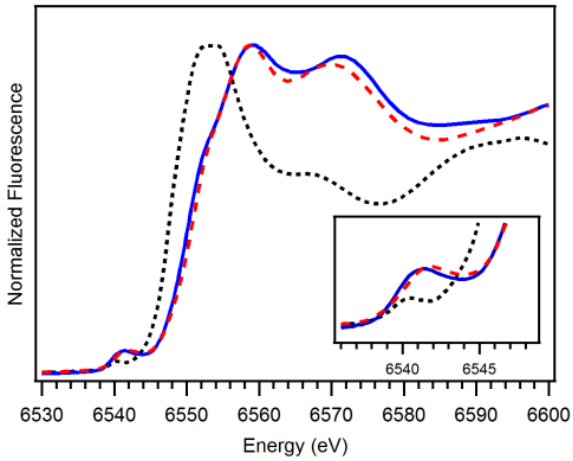

Figure 3.6. Mn K-edge XANES of $[Mn^{III}Mn^{IV}(\mu\text{-}O)_2(N4py)_2]^{3+}$ (blue solid trace), $[Mn^{II}(N4py)(OTf)]^{+}$ (black dotted trace),[54] and $[Mn^{IV}(O)(N4py)]^{2+}$ (red dashed trace)[54] at 20 K.

Table 3.2. Mn K-edge XAS Near-Edge Properties of $[Mn^{III}Mn^{IV}(\mu\text{-}O)_2(N4py)_2]^{3+}$ (**3**), $[Mn^{II}(N4py)(OTf)]^{+}$, $[Mn^{IV}(O)(N4py)]^{2+}$ and other bis(μ-oxo)dimanganese(III,IV) complexes.

complex	edge energy (eV)	pre-edge energy (eV)	pre-edge peak height[a]	reference
$[Mn^{III}Mn^{IV}(\mu\text{-}O)_2(N4py)_2]^{3+}$	6550.6	6541.4	0.074	*b*
Mn-catalase ($Mn^{III}Mn^{IV}$)	6549.2	~6540	NR[c]	67
$[Mn^{III}Mn^{IV}(\mu\text{-}O)_2(phen)_4]^{3+}$	6549.6	6539.6	NR[c]	68
$[Mn^{III}Mn^{IV}(\mu\text{-}O)_2(pda)_2]^{-}$ [d]	6549.8	6540.4	NR[c]	21
$[Mn^{IV}(O)(N4py)]^{2+}$	6550.8	6541.9	0.077	54
$[Mn^{II}(N4py)(OTf)]^{+}$	6547.3	6540.6	0.042	54

[a]To permit comparison of pre-edge peak heights, each XAS spectrum was normalized with respect to the most intense fluorescence peak. [b]This work. [c]Not reported. [d]pda^{2-} = picolyldiacetic acid.[21]

Table 3.3. EXAFS Fitting Results for $[Mn^{III}Mn^{IV}(\mu\text{-}O)_2(N4py)_2]^{3+}$ Complex.[a]

	Mn−O			Mn−N			Mn···C			Mn···Mn		
	n	*r* (Å)	$\sigma^2 \times 10^3$ (Å)^2	*n*	*r* (Å)	$\sigma^2 \times 10^3$ (Å)^2	*n*	*r* (Å)	$\sigma^2 \times 10^3$ (Å)^2	*n*	*r* (Å)	$\sigma^2 \times 10^3$ (Å)^2
$[Mn^{III}Mn^{IV}(\mu\text{-}O)_2(N4py)_2]^{3+}$	2	1.79	4.2	2	2.00	3.6	4	2.81	4.4	1	2.63	1.8
				1	2.17	3.7	5	2.96	4.2			

[a] Fourier transform range for $[Mn^{III}Mn^{IV}(\mu\text{-}O)_2(N4py)_2]^{3+}$: k = 2 – 14.3 Å^{-1} (resolution 0.128 Å).

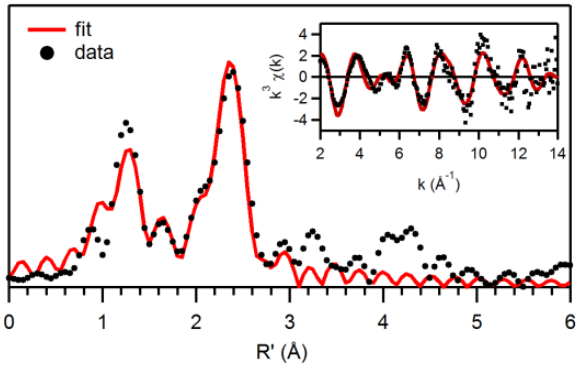

Figure 3.7. Fourier transforms of Mn K-edge EXAFS data [$k^3\chi(k)$] and raw EXAFS spectra (insets), experimental data (···) and fits (−) for $[Mn^{III}Mn^{IV}(\mu\text{-}O)_2(N4py)_2]^{3+}$. Details regarding the EXAFS fits are given in Table 3.1 and Table A.3.2.

3.4. Discussion.

The reactivity of a mononuclear Mn^{II} complex, supported by a pentadentate aminopyridyl ligand, with superoxide and hydrogen peroxide (with base) at low temperatures revealed a reaction landscape that, to the best of our knowledge, is unique amongst synthetic Mn^{II} complexes. A Mn^{III}-O_2 species was generated from the addition of superoxide to a solution of $[Mn^{II}(N4py)(OTf)]^+$ and this species was subsequently shown to react with additional $[Mn^{II}(N4py)(OTf)]^+$ to form a heterovalent bis(μ-oxo)dimanganese(III,IV) complex. This oxo-bridged dimer was also generated by treating $[Mn^{II}(N4py)(OTf)]^+$ with excess hydrogen peroxide and was characterized structurally and spectroscopically. Notably, these chemical conversions require flexibility in the denticity of the N4py ligand, which changes from pentadentate in the Mn^{II} complex to tetradentate in the Mn^{III}-O_2 and oxo-bridged $Mn^{III}Mn^{IV}$ species. Such change in ligand denticity has been termed flexidentate by Stratton and Busch.[69] The tetradentate binding of the N4py ligand in the peroxomanganese(III) complex $[Mn^{III}(O_2)(N4py)]^+$ is supported by previous spectroscopic and computational studies;[28]

however, those studies were unable to definitively establish which type of pyridine group (*i.e.*, methylenepyridine or pyridinylmethane) is dissociated. Given that the XRD structure of **3** shows dissociation of one of the pyridinylmethane moieties, it appears most probable that the same type of pyridine arm is noncoordinating in the corresponding peroxomanganese(III) complex.

While the peroxomanganese(III) complex **2** can be readily generated chemically from **1** using a molar excess of KO_2, the reaction of **1** with either aqueous H_2O_2 in the presence of base or H_2O_2-urea generates **3** even at low temperatures. This is in contrast to a number of Mn^{II} complexes, also supported by aminopyridyl ligands, that react with either KO_2 or H_2O_2 and base, to generate Mn^{III}-O_2 adducts at low temperatures (-20 to -40 ºC).[26-29,31,37,38] Indeed, the closely related complexes $[Mn^{II}(mL_5^2)]^{2+}$ and $[Mn^{II}(imL_5^2)]^{2+}$, which also feature pentadentate N_5 ligands (Figure 3.8), react with H_2O_2 at -20 to -40 ºC to give peroxomanganese(III) adducts.[28,37,38] On the basis of detailed spectroscopic and computational studies of the $[Mn^{III}(O_2)(mL_5^2)]^+$ and $[Mn^{III}(O_2)(imL_5^2)]^+$ complexes, the mL_5^2 and imL_5^2 ligands are bound in a tetradentate fashion.[28] For $[Mn^{II}(mL_5^2)]^{2+}$, formation of the peroxomanganese(III) complex is most effective using H_2O_2-urea as the oxidant.[38] Electronic absorption data provides evidence for the generation of a small amount of **2** within 60 seconds of reaction of **1** with H_2O_2-urea, but this species is quickly overcome by the formation of **3** (Figure 3.3). On the basis of these limited data, it is not clear whether or not the Mn^{III}-O_2 adduct is an intermediate en route to formation of **3** when H_2O_2-urea is the oxidant.

While there are myriad reports on the formation of oxo-bidged dimanganese compounds by reaction of mononuclear Mn^{II} species with H_2O_2,[1,2,11,59] the exact mechanism by which the dimeric species are formed is not well established.[70-72] Given that the Mn^{III}-O_2 adducts of N4py, mL_5^2, and imL_5^2 all feature supporting ligands bound in a tetradentate fashion through

dissociation of a pyridylmethyl or imidazolylmethyl arm, differences in the dissociation rates of these arms would be reasonably expected to impact the formation of the Mn^{III}-O_2 species and thus influence how these complexes react with different oxidants. The N4py ligand, which consists of four pyridyl arms from a central tertiary amine (Scheme 3.1), has a fundamentally different structure than the mL_5^2 and imL_5^2 ligands that feature a central ethylenediamine moiety (Figure 3.8). The different structures of these ligands could impact the dissociation rates of the pyridylmethyl or imidazolylmethyl arms. Any discussion of the specific elementary steps impacted by dissociation of these arms would be overly speculative, however, as the mechanism (or mechanisms) for formation of Mn^{III}-O_2 adducts by reaction of Mn^{II} precursors with H_2O_2 and base is not established.

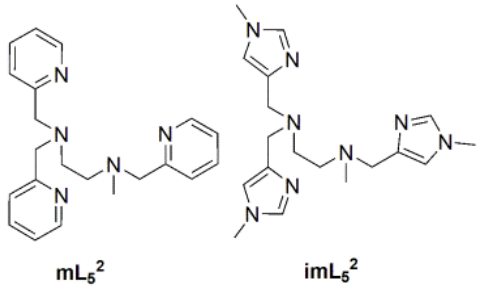

Figure 3.8. Pentadentate ligands mL_5^2 and imL_5^2.

3.4.1. XAS Comparison of Mn^{II}, Oxo-bridged $Mn^{III}Mn^{IV}$, and Terminal Mn^{IV}=O Species. For comparison of this series of complexes supported by the N4py ligand, the XANES spectra of a frozen aqueous sample of **1** and a frozen CF_3CH_2OH sample of $[Mn^{IV}(O)(N4py)]^{2+}$ (**4**) (Figure 3.6) and the EXAFS data and fits (Table A.3.3 and Figure A.3.8) are considered.[54] Relative to **1**, the Mn K-edge energies of **3** and **4** are blue-shifted by over 3 eV, consistent with the higher oxidation state of Mn in the two latter compounds. The pre-edge feature of **4** is at a higher energy and intensity than those of **3** and **1** (Table 3.2). However, the variation in pre-edge

position and height among this series are fairly modest, especially between the **4** and **3**, which is consitent with the XANES of **3** being reflective of an average of the Mn^{III} and Mn^{IV} properties.

3.4.2. Formation of $[Mn^{III}Mn^{IV}(\mu\text{-}O)_2(N4py)_2]^{3+}$ from $[Mn^{II}(N4py)(OTf)]^+$ and Superoxide. In the currently proposed mechanism for cofactor assembly in Mn-RNR, a dinuclear Mn^{II} center reacts with O_2^- to generate a bis(μ-oxo)dimanganese(III,IV) species.[12,14,15] Our observation that **1** converts to **3** upon reaction with a limiting amount of O_2^- mimics this chemistry. In this process, the Mn^{III}-O_2 complex serves as an intermediate. We propose that the nucleophilic peroxo ligand on **2** reacts with the Mn^{II} center in **1** to form **3**. This proposal is consistent with the following observations: i) **2** does not decay to **3** in significant quantities when the former is generated in higher yields, ii) the addition of **1** to **2** leads to the formation of **3** in ~90% yield relative to the amount of **2** generated, and iii) equal amounts of **3** are produced when either 0.5 or 1 equiv. **1** is added to **2** (i.e., the formation of **3** is limited by the amount of **2**).

The reactivity of **1** with superoxide is highly reminiscent of previous work done independently by Dismukes[70] and Perrée-Fauvet[72] using Mn^{II}(TPP) (TPP = tetraphenylporphyrin). In both cases, a $[Mn^{III}Mn^{IV}(\mu\text{-}O)_2(TPP)]^-$ species, formulated on the basis of EPR data, was proposed to form upon reaction of $[Mn^{II}(TPP)]$ with O_2^-. Notably, the formation of the $Mn^{III}Mn^{IV}$ dimer was only observed when the ratio of O_2^- to $[Mn^{II}(TPP)(py)]$ was 0.5:1.[72] When a 1:1 ratio was used, the $[Mn(O_2)(TPP)]^-$ species was presumed to form in high yield and the $Mn^{III}Mn^{IV}$ dimer was not observed. Our current work thus extends this prior base of knowledge to a non-porphyrinoid manganese system and provides further details on these transformations.

It is tempting to speculate that the reaction between **1** and **2** to produce **3** proceeds through a dinuclear peroxo-bridged intermediate $[Mn^{II}Mn^{III}(\mu\text{-}O_2)(\kappa^4\text{-}N4py)_2]^{3+}$ (Scheme

3.2).[70,72] Two electrons are required to convert the peroxo ligand to the two oxo ligands in $[Mn^{III}Mn^{IV}(\mu\text{-}O)_2(\kappa^4\text{-}N4py)_2]^{3+}$. The Mn^{II} and Mn^{III} centers of the peroxo-bridged intermediate could each provide an electron to cleave the peroxo bond, resulting in the formation of **3**. Labelling experiments with $K^{18}O_2$ could, in principle, be used to establish the origin of the bridging oxo ligands in **3**. However, in practice, these experiments were complicated due to the limited solubility of superoxide without excess 18-crown-6 ether present in solution. When 18-crown-6 ether was added to increase the solubility of $K^{18}O_2$, the ESI-MS data were dominated by the 18-crown-6 ether signal.

Groni *et al.* proposed the formation of a homovalent dinuclear peroxo-bridged intermediate, $[Mn^{III}Mn^{III}(\mu\text{-}O_2)(mL_5^2)_2]^{4+}$, en route to the formation of bis(μ-oxo)dimanganese(III,IV) product, $[Mn^{III}Mn^{IV}(\mu\text{-}O_2)(mL_5^2)_2]^{3+}$.[38] They suggested that this peroxo-bridged dimanganese(III,III) intermediate is formed by the reaction of $[Mn^{III}(O_2)(mL_5^2)]^{+}$ with $[Mn^{III}(OH_2)(mL_5^2)]^{3+}$ in a basic aqueous medium.[38] Unsupported peroxo-bridged dimanganese complexes are rather rare. To the best of our knowledge, the only well-characterized example of an unsupported peroxo-bridged dimanganese complex was reported earlier this year by Coggins *et al.*[40] The $\{[Mn^{III}(S^{Me2}N_4(6\text{-Me-DPEN})]_2(\textit{trans}\text{-}\mu\text{-}1,2\text{-}O_2)\}^{2+}$ (6-Me-DPEN = *N*,*N*-Bis(6-methyl-2-pyridilmethyl)ethane-1,2-diamine) complex features a peroxo ligand bridged between two Mn^{III} ions in an end-on *trans*-μ-1,2-fashion.[40] A peroxo-bridged Mn cluster, the trinuclear Mn_2^{III} μ-peroxo complex $[Mn_3(dien)_2(OAc)_2(\mu\text{-}O_2)Cl](ClO_4)_2$ (dien = diethylenetriamine),[73] and a bis(μ-oxo)dimanganese(IV,IV) complex with a *cis*-μ-1,2-peroxo bridge, $[L_2Mn_2(\mu\text{-}O)_2(\mu\text{-}O_2)](ClO_4)_2$ (L = 1,4,7-trimethyl-1,4,7-triazacyclononane),[74] have also been described.

3.5. Summary.

The reactivity of $[Mn^{II}(N4py)(OTf)]^+$ with superoxide and hydrogen peroxide is unique among synthetic mononuclear Mn^{II} complexes as a peroxomanganese(III) intermediate was formed from the reaction of **1** with superoxide, whereas a heterovalent bis(μ-oxo)dimanganese(III,IV) complex was formed in high yields from the reaction of **1** with hydrogen peroxide and base. The Mn^{III}-O_2 intermediate was converted to the heterovalent oxo-bridged manganese(III,IV) dimer by a subsequent reaction with $[Mn^{II}(N4py)(OTf)]^+$. This conversion of two Mn^{II} species to an oxo-bridged $Mn^{III}Mn^{IV}$ compound using O_2^- as oxidant mimics the formation of the $Mn^{III}Mn^{IV}$ form of Mn-RNR. The oxo-bridged dimer was characterized structurally and spectroscopically, which revealed a change in denticity of the N4py ligand from pentadentate in the Mn^{II} complex to tetradentate in the oxo-bridged dimer.

Notes and References

1. Pecoraro, V. L.; Baldwin, M. J.; Gelasco, A., *Chem. Rev.* **1994,** *94*, 807-826.
2. Wu, A. J.; Penner-Hahn, J. E.; Pecoraro, V. L., *Chem. Rev.* **2004,** *104*, 903-938.
3. Grove, L. E.; Brunold, T. C., *Comments Inorg. Chem.* **2008,** *29*, 134-168.
4. Emerson, J. P.; Kovaleva, E. G.; Farquhar, E. R.; Lipscomb, J. D.; Que, L., Jr., *Proc. Natl. Acad. Sci. USA* **2008,** *105*, 7347-7352.
5. Gunderson, W. A.; Zatsman, A. I.; Emerson, J. P.; Farquhar, E. R.; Que, L.; Lipscomb, J. D.; Hendrich, M. P., *J. Am. Chem. Soc.* **2008,** *130*, 14465-14467.
6. Borowski, T.; Bassan, A.; Richards, N. G. J.; Siegbahn, P. E. M., *J. Chem. Theory Comput.* **2005,** *1*, 686-693.
7. Opaleye, O.; Rose, R.-S.; Whittaker, M. M.; Woo, E.-J.; Whittaker, J. W.; Pickersgill, R. W., *J. Biol. Chem.* **2006,** *281*, 6428-6433.
8. Jackson, T. A.; Brunold, T. C., *Acc. Chem. Res.* **2004,** *37*, 461-470.
9. Miller, A.-F., *Curr. Opin. Chem. Biol.* **2004,** *8*, 162-168.
10. McEvoy, J. P.; Brudvig, G. W., *Chem. Rev.* **2006,** *106*, 4455-4483.
11. Mullins, C. S.; Pecoraro, V. L., *Coord. Chem. Rev.* **2008,** *252*, 416-443.
12. Cotruvo, J. A.; Stich, T. A.; Britt, R. D.; Stubbe, J., *J. Am. Chem. Soc.* **2013**.
13. Cotruvo, J. A.; Stubbe, J., *Proc. Natl. Acad. Sci. U.S.A.* **2008,** *105*, 14383-14388.
14. Cotruvo, J. A.; Stubbe, J., *Biochemistry* **2010,** *49*, 1297-1309.
15. Boal, A. K.; Cotruvo, J. A.; Stubbe, J.; Rosenzweig, A. C., *Science* **2010,** *329*, 1526-1530.
16. Pecoraro, V. L.; Hsieh, W.-Y., *Inorg. Chem.* **2008,** *47*, 1765-1778.
17. Shook, R. L.; Borovik, A. S., *Inorg. Chem.* **2010,** *49*, 3646-3660.
18. Stone, K. L.; Borovik, A. S., *Curr. Opin. Chem. Biol.* **2009,** *13*, 114-118.

19. Mukhopadhyay, S.; Mandal, S. K.; Bhaduri, S.; Armstrong, W. H., *Chem. Rev.* **2004,** *104*, 3981-4026.
20. Chen, H. Y.; Tagore, R.; Das, S.; Incarvito, C.; Faller, J. W.; Crabtree, R. H.; Brudvig, G. W., *Inorg. Chem.* **2005,** *44*, 7661-7670.
21. Dubois, L.; Jacquamet, L.; Pecaut, J.; Latour, J.-M., *Chem. Commun.* **2006**, 4521-4523.
22. Hureau, C.; Blondin, G.; Charlot, M.-F.; Philouze, C.; Nierlich, M.; Cesario, M.; Anxolabehere-Mallart, E., *Inorg. Chem.* **2005,** *44*, 3669-3683.
23. Schindler, S.; Walter, O.; Pedersen, J. Z.; Toftlund, H., *Inorg. Chim. Acta* **2000,** *303*, 215-219.
24. Baldwin, M. J.; Pecoraro, V. L., *J. Am. Chem. Soc.* **1996,** *118*, 11325-11326.
25. Wang, K.; Mayer, J. M., *J. Am. Chem. Soc.* **1997,** *119*, 1470-1471.
26. Geiger, R. A.; Chattopadhyay, S.; Day, V. W.; Jackson, T. A., *J. Am. Chem. Soc.* **2010,** *132*, 2821-2831.
27. Geiger, R. A.; Chattopadhyay, S.; Day, V. W.; Jackson, T. A., *Dalton Trans.* **2011,** *40*, 1707-1715.
28. Geiger, R. A.; Leto, D. F.; Chattopadhyay, S.; Dorlet, P.; Anxolabéhère-Mallart, E.; Jackson, T. A., *Inorg. Chem.* **2011,** *50*, 10190-10203.
29. Geiger, R. A.; Wijeratne, G.; Day, V. W.; Jackson, T. A., *Eur. J. Inorg. Chem.* **2012**, 1598-1608.
30. Annaraj, J.; Cho, J.; Lee, Y.-M.; Kim, S. Y.; Latifi, R.; de Visser, S. P.; Nam, W., *Angew. Chem., Int. Ed. Engl.* **2009,** *48*, 4150-4153.
31. Seo, M. S.; Kim, J. Y.; Annaraj, J.; Kim, Y.; Lee, Y.-M.; Kim, S.-J.; Kim, J.; Nam, W., *Angew. Chem., Int. Ed. Engl.* **2007,** *46*, 377-380.
32. Kitajima, N.; Komatsuzaki, H.; Hikichi, S.; Osawa, M.; Moro-oka, Y., *J. Am. Chem. Soc.* **1994,** *116*, 11596-11597.
33. VanAtta, R. B.; Strouse, C. E.; Hanson, L. K.; Valentine, J. S., *J. Am. Chem. Soc.* **1987,** *109*, 1425-1434.
34. Shook, R. L.; Gunderson, W. A.; Greaves, J.; Ziller, J. W.; Hendrich, M. P.; Borovik, A. S., *J. Am. Chem. Soc.* **2008,** *130*, 8888-8889.
35. Shook, R. L.; Peterson, S. M.; Greaves, J.; Moore, C.; Rheingold, A. L.; Borovik, A. S., *J. Am. Chem. Soc.* **2011,** *133*, 5810-5817.
36. Singh, U. P.; Sharma, A. K.; Hikichi, S.; Komatsuzaki, H.; Moro-oka, Y.; Akita, M., *Inorg. Chim. Acta* **2006,** *359*, 4407-4411.
37. Groni, S.; Blain, G.; Guillot, R.; Policar, C.; Anxolabéhère-Mallart, E., *Inorg. Chem.* **2007,** *46*, 1951-1953.
38. Groni, S.; Dorlet, P.; Blain, G.; Bourcier, S.; Guillot, R.; Anxolabéhère-Mallart, E., *Inorg. Chem.* **2008,** *47*, 3166-3172.
39. Coggins, M. K.; Martin-Diaconescu, V.; DeBeer, S.; Kovacs, J. A., *J. Am. Chem. Soc.* **2013,** *135*, 4260-4272.
40. Coggins, M. K.; Sun, X.; Kwak, Y.; Solomon, E. I.; Rybak-Akimova, E.; Kovacs, J. A., *J. Am. Chem. Soc.* **2013,** *135*, 5631-5640.
41. Coggins, M. K.; Toledo, S.; Shaffer, E.; Kaminsky, W.; Shearer, J.; Kovacs, J. A., *Inorg. Chem.* **2012,** *51*, 6633-6644.
42. Sisemore, M. F.; Selke, M.; Burstyn, J. N.; Valentine, J. S., *Inorg. Chem.* **1997,** *36*, 979-984.
43. Magnetic circular dichroism (reference 28) and electron paramagnetic resonance data (vide infra) collected for frozen solutions of $[Mn^{III}(O_2)(N4py)]^+$ indicate only the presence of one peroxomanganese(III) unit, suggesting that a mixture of the two isomers is not present.
44. Chang, J.; Plummer, S.; Berman, E. S. F.; Striplin, D.; Blauch, D., *Inorg. Chem.* **2004,** *43*, 1735-1742.
45. Lubben, M.; Meetsma, A.; Wilkinson, E. C.; Feringa, B.; Que, L., *Angew. Chem., Int. Ed. Engl.* **1995,** *34*, 1512-1514.
46. Perez-Benito, J. F.; Brillas, E.; Arias, C., *Can. J. Chem.* **1990,** *68*, 79-81.

47. *Data Collection: SMART Software Reference Manual.* Bruker-AXS. 5465 E. Cheryl Parkway, Madison, WI 53711-5373 USA, 1998.
48. Data Reduction: SAINT Software Reference Manual (1998). Bruker-AXS, 6300 Enterprise Dr., Madison, WI 53719-1173, USA.
49. G. M. Sheldrick (2000). SHELXTL Version 6.10 Reference Manual. Bruker-AXS, 5465 E. Cheryl Parkway, Madison, WI 53711-5373 USA.
50. George, G. N. *EXAFSPAK; Stanford Synchrotron Radiation Laboratory; Stanford, CA, 1990.*, 1990.
51. Rehr, J. J.; Mustre de Leon, J.; Zabinsky, S. I.; Albers, R. C., *J. Am. Chem. Soc.* **1991,** *113*, 5135-5140.
52. Neese, F.; Solomon, E. I., *Inorg. Chem.* **1999,** *38*, 1847-1865.
53. Chen, J.; Lee, Y.-M.; Davis, K. M.; Wu, X.; Seo, M. S.; Cho, K.-B.; Yoon, H.; Park, Y. J.; Fukuzumi, S.; Pushkar, Y. N.; Nam, W., *J. Am. Chem. Soc.* **2013,** *135*, 6388-6391.
54. Leto, D. F.; Ingram, R.; Day, V. W.; Jackson, T. A., *Chem. Commun.* **2013,** *49*, 5378-5380.
55. El Ghachtouli, S.; Vincent Ching, H. Y.; Lassalle-Kaiser, B.; Guillot, R.; Leto, D. F.; Chattopadhyay, S.; Jackson, T. A.; Dorlet, P.; Anxolabéhère-Mallart, E., *Chem. Commun.* **2013,** *49*, 5696-5698.
56. An alternative explanation for the maximum chemical formation of **2** with two equiv. KO_2 is that **2** is actually formed by the reaction of **1** with peroxide generated by O_2- disproportionation. According to this model, the use of 2 equiv. KO_2 would result in 66% formation of **2**, consistent with the experimental results. However, under this scenario, the formation of **2** would be maximized at 3 equiv. KO_2, which is not observed. It is possible that an excess of KO_2 is required to maximize the formation of **2** because **1** has modest O_2- scavenging activity.
57. The electronic absorption spectrum of the decayed solution shows two weak bands at 15 000 and 17 700 cm^{-1}, indicating that **2** decayed to **3** in no greater than 10% yield, based on the total Mn concentration (vide infra). However, the perpendicular-mode EPR spectrum of this solution reveals that the yield of **3** is likely much lower than 10%, as only a weak, broad multi-line signal is observed at 345 mT, where the 16-line signal of **3** would be expected (Figure A.3.3).
58. Goodson, P. A.; Glerup, J.; Hodgson, D. J.; Michelsen, K.; Weihe, H., *Inorg. Chem.* **1991,** *30*, 4909-4914.
59. Gamelin, D. R.; Kirk, M. L.; Stemmler, T. L.; Pal, S.; Armstrong, W. H.; Pennerhahn, J. E.; Solomon, E. I., *J. Am. Chem. Soc.* **1994,** *116*, 2392-2399.
60. Brewer, K. J.; Calvin, M.; Lumpkin, R. S.; Otvos, J. W.; Spreer, L. O., *Inorg. Chem.* **1989,** *28*, 4446-4451.
61. Goodson, P. A.; Glerup, J.; Hodgson, D. J.; Michelsen, K.; Pedersen, E., *Inorg. Chem.* **1990,** *29*, 503-508.
62. Hureau, C.; Blondin, G.; Charlot, M.-F.; Philouze, C.; Nierlich, M.; Cesario, M.; Anxolabéhère-Mallart, E., *Inorg. Chem.* **2005,** *44*, 3669-3683.
63. Lu, Y.-H.; Fun, H.-K.; Chantrapromma, S.; Razak, I. A.; Shen, Z.; Zuo, J.-L.; You, X.-Z., *Acta Crystallogr., Sect. C: Cryst. Struct. Commun.* **2001,** *57*, 911-913.
64. Manchanda, R.; Brudvig, G. W.; de Gala, S.; Crabtree, R. H., *Inorg. Chem.* **1994,** *33*, 5157-5160.
65. Stebler, M.; Ludi, A.; Buergi, H. B., *Inorg. Chem.* **1986,** *25*, 4743-4750.
66. Berggren, G.; Thapper, A.; Huang, P.; Eriksson, L.; Styring, S. r.; Anderlund, M. F., *Inorg. Chem.* **2011,** *50*, 3425-3430.
67. Stemmler, T. L.; Sturgeon, B. E.; Randall, D. W.; Britt, R. D.; Penner-Hahn, J. E., *J. Am. Chem. Soc.* **1997,** *119*, 9215-9225.
68. Visser, H.; Anxolabéhère-Mallart, E.; Bergmann, U.; Glatzel, P.; Robblee, J. H.; Cramer, S. P.; Girerd, J.-J.; Sauer, K.; Klein, M. P.; Yachandra, V. K., *J. Am. Chem. Soc.* **2001,** *123*, 7031-7039.
69. Stratton, W. J.; Busch, D. H., *J. Am. Chem. Soc.* **1958,** *80*, 3191-3195.

70. Dismukes, G. C.; Sheats, J. E.; Smegal, J. A., *J. Am. Chem. Soc.* **1987,** *109*, 7202-7203.
71. Horwitz, C. P.; Dailey, G. C., *Comments Inorg. Chem.* **1993,** *14*, 283-319.
72. Perree-Fauvet, M.; Gaudemer, A.; Bonvoisin, J.; Girerd, J. J.; Boucly-Goester, C.; Boucly, P., *Inorg. Chem.* **1989,** *28*, 3533-3538.
73. Bhula, R.; Gainsford, G. J.; Weatherburn, D. C., *J. Am. Chem. Soc.* **1988,** *110*, 7550-7552.
74. Bossek, U.; Weyhermueller, T.; Wieghardt, K.; Nuber, B.; Weiss, J., *J. Am. Chem. Soc.* **1990,** *112*, 6387-6388.

Chapter 4

Spectroscopic Properties and Reactivity of a Mononuclear Oxomanganese(IV) Complex

This work has been reproduced in part from: D. F. Leto, R. Ingram, V. W. Day and T. A. Jackson, *Chem. Commun.*, 2013, **49**, 5378-5380 with permission from The Royal Society of Chemistry.

4.1. Introduction.

High-valent oxomanganese adducts are suggested as active oxidants for synthetic and biological manganese catalysts, including those involved in textile and paper bleaching with H_2O_2 and oxygen evolution from water.[1-3] Oxomanganese(V) adducts with $S = 0$ and $S = 1$ spin states have been reported, and these invariably feature strongly electron-donating, anionic ligands.[4-9] Oxomanganese(IV) complexes with neutral, non-porphyrinic ligands are comparatively less common.[10-14] Detailed studies of substrate oxidation exist for a limited number of complexes.[10-12,15-17] In addition, few Mn^{IV}=O complexes have been characterized by Mn K-edge X-ray absorption spectroscopy (XAS),[11,18-20] a technique featuring prominently in the study of Mn enzymes[2] and biominerals.[21] In this chapter, the spectroscopic properties and oxidative reactivity of an oxomanganese(IV) complex supported by the neutral, pentadentate N4py ligand (*N*,*N*-bis(2-pyridylmethyl)-*N*-bis(2-pyridyl)methylamine) are described. This Mn^{IV}=O adduct is capable of activating C–H bonds by a H-atom transfer mechanism and is more reactive in this regard than most Mn^{IV}=O species.

4.2. Experimental and Computational Methods.

4.2.1. Materials. All chemicals and solvents were obtained from commercial vendors and were ACS reagent-grade or better and used as received, except for 9,10-dihydroanthracene (DHA) which was recrystallized from ethanol.[22] All solvents were dried and degassed according to published procedures.[22] $H_2{}^{18}O$ (97% ^{18}O-enriched) was purchased from ICON Services Inc. (Summit, NJ, USA). d_4-DHA was synthesized as previously reported.[23]

4.2.2. Synthesis and Characterization of $[Mn^{II}(N4py)(OTf)](OTf)$ and $[Mn^{IV}(O)(N4py)]^{2+}$. The synthesis of the N4py ligand was performed according to a previously

described procedure.[24-25] The triflate salt of **1**, $[Mn^{II}(N4py)(OTf)](OTf)$, was synthesized by reacting N4py ligand with $Mn^{II}(OTf)_2$ in an acetonitrile (CH_3CN) solution in a 1:1 molar ratio overnight in a dry-box as previously reported.[26] The resulting solution was filtered and purified by recrystallization with diethyl ether. Single crystals suitable for X-ray analysis were obtained by slow diffusion of diethyl ether to a solution of **1** in acetonitrile (overall yield 90%). Elemental analysis for $[Mn^{II}(N4py)(OTf)](OTf)\bullet 0.5CH_3CH_2OH$: $MnC_{26}H_{24}N_5O_{6.5}F_6S_2$ calc. (%): C 42.00, H 3.25, N 9.42; found (%): C 42.16, H 3.61, N 9.68. Elemental analysis was performed by Columbia Analytical Services, Tuscon, Arizona.

The $[Mn^{IV}(O)(N4py)]^{2+}$ complex (**2**) was prepared by adding 2.5 equivalents (2.2 mg, 0.01 mmol) of iodosylbenzene (PhIO) to a 2 mM (2.9 mg, 0.004 mmol) solution of **1**$(OTf)_2$ in 2,2,2-trifluoroethanol (CF_3CH_2OH) at 25 ^oC under an Ar atmosphere. The formation of the new green species **2** was complete in 10 minutes with the formation of a broad electronic absorption band at 950 nm and weak shoulders at 600 and 450 nm. Complex **2** was less stable under an Ar atmosphere ($t_{1/2} \approx 0.5$ h at 25 ^oC) than in air ($t_{1/2} \approx 2.75$ h at 20 ^oC). Electronic absorption spectra were obtained on either a Varian Cary 50 Bio or an Agilent 8453 spectrophotometer, both of which were interfaced with a Unisoku cryostat (USP-203-A) capable of maintaining temperatures between 150 and 373 K.

4.2.3. X-ray Crystallography of $[Mn^{II}(N4py)(OTf)](OTf)$. Yellow crystals of $[Mn(C_{23}H_{21}N_5)(O_3SCF_3)]_2[O_3SCF_3][ClO_4]$ are, at 100(2) K, monoclinic, space group $P2_1 - C_2^2$ (No. 4).[27] Crystal structure, data collection, and refinement parameters for the crystal structure are provided in Appendix A.1.2 and summarized in Table A.1.2. CCDC-885972 contains the supplementary crystallographic data for [Mn(N4py)(OTf)](OTf). This data can be obtained free

of charge from the Cambridge Crystallographic Data Centre via www.cccdc.cam.ac/data_request/cif.

4.2.4. Electrospray-ionization Mass Spectrometry (ESI-MS) Experiments. For ESI-MS experiments, a 2 mM CF_3CH_2OH solution of **2** was prepared under an Ar atmosphere. A 50 µL aliquot of the solution of **2** was diluted into CH_3CN and analyzed by ESI-MS (Figure A.4.1A). (We note that, on the basis of electronic absorption measurements, **2** is less stable in CH_3CN than pure CF_3CH_2OH and begins to decay under these conditions.) A second 50 µL aliquot of **2** was treated with 10 µL of $H_2{}^{18}O$ and then diluted into CH_3CN. The resulting solution was analyzed by ESI-MS five minutes after the addition of the $H_2{}^{18}O$ (Figure A.4.1B). The remaining solution of **2** decayed to **3** after three hours, and a 20 µL aliquot of the solution of **3** was diluted into CH_3CN for ESI-MS analysis (Figure A.4.1C). Electrospray ionization mass spectrometry experiments were performed using an LCT Primers MicroMass electrospray time-of-flight instrument.

4.2.5. X- and Q-band EPR Experiments. 250 µL of a 2 mM CF_3CH_2OH solution of **1** were transferred to a 4 mm quartz EPR tube and flash frozen in liquid N_2. Samples of **2** used for EPR experiments were prepared by adding 2.5 equivalents of PhIO to a 2 mM solution of **1** in CF_3CH_2OH at 25 ^oC under an Ar atmosphere. After the formation of **2** was judged complete by electronic absorption spectroscopy (~10 min.), 250 µL of the solution were transferred to a 4 mm quartz EPR tube flash frozen in liquid N_2 for X-band experiments. Similarly, ~30 µL of the solution were transferred to a 1.1 mM quartz EPR tube for Q-band experiments. The remaining solution of **2** fully decayed to **3** in three hours, as monitored by electronic absorption, and from this solution of **3**, 250 µL were transferred to an EPR tube and flash frozen in liquid N_2.

EPR spectra were collected on an X-band (9 GHz) Bruker EMXPlus spectrometer equipped with an Oxford ESR900 continuous-flow liquid helium cryostat and an Oxford ITC503 temperature system to monitor and regulate the temperature. A dual mode cavity (Bruker ER4116DM) was used for perpendicular and parallel mode detection. Spectra were recorded under non-saturating conditions using 100 kHz field modulation. Other parameters (microwave frequency, modulation amplitude, microwave power, time constant, conversion time, sweep rate, and field resolution) are given in the captions of the corresponding figures. Because the baseline contribution was insignificant, a blank spectrum was not subtracted from the spectra. The Q-band (35 GHz) EPR spectrum was collected by our collaborator Prof. Joshua Telser (Roosevelt University) in Prof. Brian Hoffman's lab at Northwestern University.

4.2.6. Magnetic Circular Dichroism (MCD) Spectroscopy. A 7.5 mM MCD sample of **2** was prepared from a 15 mM CF_3CH_2OH solution of **2** that was diluted to 7.5 mM with ethanol as follows. The solution was diluted with ethanol to form a glassy solvent mixture with CF_3CH_2OH (50:50). A 1.0 mL CF_3CH_2OH suspension containing 2.5 equivalents of PhIO (16.5 mg, 0.3 mmol) was added to a 1.0 mL CF_3CH_2OH solution of **1**$(OTf)_2$ (21.6 mg, 0.012 mmol). The resulting mixture was stirred on the bench at 25 ^oC for 15 minutes. The cloudy green solution of **2** (15 mM) was then filtered through a 0.45 μM syringe to remove unreacted PhIO. Since **2** reacts with ethanol at room temperature, the solution was cooled to -40 ^oC in a freezer and diluted to 7.5 mM with 2.0 mL cold ethanol (-40 ^oC). The sample was then transferred to a pre-cooled MCD cell at -80 ^oC, and flash frozen in liquid N_2. MCD spectra were collected on a Jasco circular dichroism spectrometer (J-815) interfaced with an Oxford Instruments magnetocryostat (SM-4000-8) capable of a horizontal field up to 8 T and a temperature range of 1.5 to 300 K.

4.2.7. Mn K-edge X-ray Absorption (XAS) Experiments. (A) Sample Preparation. The XAS sample of **1** was prepared by transferring approximately 200 µL of a 10 mM aqueous solution of **1**$(OTf)_2$ to an XAS sample holder which was then flash-frozen in liquid N_2. For the XAS sample of **2**, a 14 mM solution of **1**$(OTf)_2$ in CF_3CH_2OH was treated with 2.5 equivalents of PhIO at 25 ^oC under an Ar atmosphere. Once the formation was complete, three samples were prepared by transferring approximately 400 µL of **2** to each XAS sample holder. All samples were immediately flash-frozen in liquid N_2.

(B) XAS Data Collection. XAS spectra were recorded on beamline X3B at the National Synchrotron Light Source (NSLS), Brookhaven National Lab (storage ring conditions, 2.8 GeV, 100 - 300 mA). Mn K-edge X-ray absorption spectra were recorded on frozen solutions maintained at 20 K with a helium Displex closed-cycle cryostat over the energy range 6.4 – 7.4 keV (Si(111) monochromater). The data were obtained as fluorescence excitation spectra using a solid-state 31-element germanium detector (Canberra). Contamination of higher harmonics radiation was minimized by using a harmonic rejection mirror. Background fluorescence signal was reduced by use of a 6 µm chromium filter for sample **1**. A manganese foil spectrum was recorded concomitantly for internal energy calibration and the first inflection point of the K-edge energy was assigned to 6539.0 eV. Spectra were measured with 5 eV steps below the edge, 0.3 eV steps in the edge region, and steps equivalent to 0.05 $Å^{-1}$ increments above the edge (region borders were 6354, 6529, and 6554 eV). Even under conditions of low X-ray flux, it was observed that complex **2** was slightly photoreduced after each scan as the edge energy shifted ~0.3 eV to lower energy in subsequent scans on the same spot. Thus, the effects of photoreduction on the XAS data set were minimized by collecting only one scan per sample spot.

The XAS spectra of complexes **1** (10 mM in H_2O) and **2** (14 mM in CF_3CH_2OH) represent the average of 7 scans (Figure A.4.6).

(C) EXAFS Data Analysis. Extended X-ray absorption fine-structure (EXAFS) data reduction and averaging were treated entirely using the program EXAFSPAK.[28] Pre-edge background intensity was removed by fitting a Gaussian function to the pre-edge background and subtracting this function from the whole spectrum. The spectrum was then fit with a three-segment spline with fourth-order polynomial components to remove low-frequency background. EXAFS refinement was carried out on $k^3\chi(k)$ data, using phase and amplitude functions obtained from *FEFF*, version 6.[29] The EXAFS fitting was also performed using EXAFSPAK. For each fit, the parameters r (average distance between Mn and scattering atom) and σ^2 (Debye-Waller factor) were optimized, while n, the number of atoms in the shell, was kept fixed. n was varied by integer steps systematically. The goodness-of-fit (GOF) was evaluated by the parameter F, where $F = \Sigma\ (\chi_{calcd} - \chi_{expt})^2 / N$, and N is the number of data points. The threshold energy, E_0, in electronvolts (k = 0 point) was kept at a common, variable value for every shell of a given fit.

4.2.8. Density Functional Theory Computations for 2. DFT calculations employed the ORCA program package (version 2.8.0).[30] Initial coordinates for **2** were derived from the X-ray structure of [**1**(OTf)]$^+$, where the coordinated triflate was replaced with an oxo ligand. The nuclear coordinates of this model were subjected to full DFT energy minimization and converged to the S = 3/2 ground state, using the functional[31,32] in conjunction with triple-ζ quality TZVP basis sets on Mn, O, and N and SVP basis sets on C and H.[33,34] The resolution of identity approximation[35] was used to accelerate the calculations using the auxiliary basis set SV/J. The Cartesian coordinates for the geometry-optimized model of **2** are provided in Table A.4.4.

4.2.9. Kinetic Measurements with DHA and d_4-DHA. All kinetic measurements were performed under an Ar atmosphere. 2.9 mg (0.004 mmol) of **1**$(OTf)_2$ and 2.2 mg (2.5 equivalents, 0.01 mmol) of PhIO were each dissolved in 1 mL deoxygenated CF_3CH_2OH. These solutions were combined, stirred for five minutes, and transferred to a UV-Vis cuvette at 25 ^oC. The formation of **2** ([**2**] = 2 mM) was monitored by the growth of the broad absorption band at 950 nm. Once the formation of **2** was complete, 100 µL of dichloromethane (CH_2Cl_2) containing the substrate (DHA or d_4-DHA) was added and the reaction was monitored by following the decay of the band at 950 nm. Under these conditions, and using varying concentrations of substrate ([DHA] = 0.020 – 0.050 M and [d_4-DHA] = 0.020 - 0.040 M) complex **2** showed pseudo-first order decay to at least four half-lives. The second-order reaction rate k_2 was calculated from a linear correlation between the substrate concentration and the observed rate and corrected for the number of reactive C–H bonds to yield k_2' (Table A.4.2). From the k_2 values obtained from these linear plots for DHA (k_2 = 3.6 M^{-1} s^{-1}) and d_4-DHA (k_2 = 0.32 M^{-1} s^{-1}), the kinetic isotope effect (KIE) was calculated to be 11.2.

The effect of solvent on the rate of substrate oxidation by **2** was investigated by forming **2** in a CF_3CH_2OH:CH_2Cl_2 1:1 (volume:volume) solvent mixture under the same conditions as above. Once the formation of **2** was completed, 100 µL of dichloromethane (CH_2Cl_2) containing DHA ([DHA] = 0.020 – 0.050 M) or d_4-DHA ([d_4-DHA] = 0.020 – 0.040 M) were added and the reaction was monitored by following the decay of the band at 950 nm. The second-order reaction rates for DHA (k_2 = 2.61 M^{-1} s^{-1}) and d_4-DHA (k_2 = 0.30 M^{-1} s^{-1}) were calculated from the linear correlation between the substrate concentration and the observed rate (Figure A.4.7). The KIE was determined to be 8.7 (Table 4.4). Formation of **2** in a CF_3CH_2OH:$(CH_3)_2NC(O)H$ (1:1 volume:volume) solvent mixture was unsuccessful. Although it was possible to form **2** in

CF_3CH_2OH:CH_3CN (1:1 volume:volume) and CF_3CH_2OH:$(CH_3)_2CO$ (1:1 volume:volume) solvent mixtures, the stability of **2** was greatly reduced, hampering any kinetic experiments.

The activation parameters of hydrogen-atom abstraction for the reactions of **2** (1 mM) with DHA (0.01 M) and d_4-DHA (0.01 M) were determined from experiments in a CF_3CH_2OH:CH_2Cl_2 (1:1) solvent mixture in the temperature range of 268 – 308 K. The decay of **2** was monitored by electronic absorption and the pseudo-first order rate constant was calculated for each reaction at each temperature (Figure A.4.3; Tables 4.5 and 4.6).

4.2.10. Kinetic Measurements with Other Substrates. The reactions of **2** in a deoxygenated CF_3CH_2OH:CH_3CN 19:1 (volume:volume) mixture with 0.150 mL of CF_3CH_2OH:CH_3CN (19:1) containing the substrate (ethylbenzene, diphenylmethane, and toluene) were also monitored by electronic absorption spectroscopy. Under the conditions of these reactions ([ethylbenzene] = 0.10 – 0.40 M, [diphenylmethane] = 0.10 – 0.22 M, and ([toluene] = 0.40 – 0.70 M), **2** decayed with pseudo-first order behavior to at least four half-lives, and a linear relationship was observed between the substrate concentration and the pseudo-first-order rate constant (Figure A.4.2). The second-order rate constants determined from this relationship were corrected for the number of reactive C–H bonds (Table A.4.2).

4.2.11. Product Analysis and Final Oxidation State of Manganese. 2.9 mg (0.004 mmol) of **1**$(OTf)_2$ and 2.2 mg (0.01 mmol) of PhIO were each dissolved in 1 mL deoxygenated CF_3CH_2OH under an Ar atmosphere and were combined, stirred for ten minutes ([**2**] = 2 mM), and treated with 7.5 mg DHA (10 equivalents) in 100 μL of deoxygenated CH_2Cl_2. After 30 min, the solvent was removed and the organic products were redissolved in 2 mL of cyclohexane. The anthracene produced by the reaction of **2** with DHA was quantified by measuring the absorbance

of the cyclohexane solution of the organic products at 356 nm, yielding 1.1 ± 0.15 mM anthracene (average of 6 different experiments).

The final oxidation state of the manganese was determined using an iodometric titration.[36] 2.9 mg (0.004 mmol) of **1**$(OTf)_2$ and 2.2 mg (0.01 mmol) of PhIO were each dissolved in 1 mL deoxygenated CF_3CH_2OH under an Ar atmosphere and were combined, stirred for ten minutes ([**2**] = 2 mM), and treated with 7.5 mg DHA (10 equivalents) in 100 µL of deoxygenated CH_2Cl_2. After 30 min, the solvent was removed and the organic products were removed from the manganese product (**3**) by rinsing the residue with diethyl ether (3 × 5 mL). The residue was dried and redissolved in 2 mL of CH_2Cl_2 and a 1 mL aliquot was transferred to a 10 mL volumetric flask containing 1 mL glacial acetic acid and 0.019 g tetrabutylammonium iodide, followed by dilution with CH_2Cl_2 up to 10 mL. The bright yellow solution was mixed and the absorbance was measured in a 0.5 cm cuvette at 25 ^oC immediately after mixing. The triiodide produced was quantified by measuring the absorbance of the solution at 295 and 365 nm and the final oxidation state of the manganese was determined by the ratio of the triiodide liberated and the Mn^{IV} consumed.[36] The final oxidation state of **3** was 2.7 ± 0.15 (average of 5 different experiments).

4.2.12. Cyclic voltammetry. The electrochemical properties of a nitrogen-purged CF_3CH_2OH:CH_2Cl_2 solution of **2** (2 mM) were investigated by cyclic voltammetry using an EPSILON (Bioanalytical Systems INC., West Lafayette, IN) electrochemical workstation. Tetrabutylammonium hexafluorophosphate (0.1 M) in CF_3CH_2OH:CH_2Cl_2 was used as a supporting electrolyte. Cyclic voltammograms were recorded at 25 ^oC using a three component system consisting of a platinum working electrode, a platinum wire auxiliary electrode, and a glass-encased non-aqueous silver/silver chloride reference electrode. The reference Ag/Ag^+

electrode was monitored with the external Cp_2Fe/Cp_2Fe^+ couple. Complex **2** exhibits a one-electron redox process at 0.370 V versus Cp_2Fe/Cp_2Fe^+ (0.8 V versus SCE) in CF_3CH_2OH:CH_2Cl_2 (1:1 with 0.1 M NBu_4PF_6), which was assigned to the $Mn^{III}(O)/Mn^{IV}(O)$ couple (Figure A.4.4). The redox wave is partially reversible at 50 and 100 mV s^{-1} scan velocities. An irreversible reduction process is also observed at E_{pc} = -0.260 V versus Cp_2Fe/Cp_2Fe^+, which is attributed to the reduction of excess iodosylbenzene (Figure A.4.4). Complex **2** exhibits a higher reduction potential than $[Mn^{IV}(O)(H_3buea)]^-$ ($E_{1/2}$ = -1.0 V versus Cp_2Fe/Cp_2Fe^+; -0.570 V versus SCE)[15] and $[Mn^{IV}(O)(OH)(^{H,Me}Pytacn)]^+$ ($E_{1/2}$ = -0.38 V versus Cp_2Fe/Cp_2Fe^+; 0.05 V versus SCE).[10]

4.3. Results and Analysis.

4.3.1 Generation and Characterization of $[Mn^{IV}(O)(N4py)]^{2+}$ (2). The manganese(II) complex $[Mn^{II}(N4py)]^{2+}$ (**1**) was generated as the triflate salt. The X-ray diffraction (XRD) structure exhibits a distorted octahedral Mn^{II} center with pentadentate N4py and monodentate triflate ligands (Figure 4.1, left). The Mn−ligand bond lengths are 2.1 to 2.3 Å. The Mn K-edge XAS spectrum of a frozen aqueous sample of **1**$(OTf)_2$ displays a pre-edge feature at 6540.6 eV and an edge at 6547.3 eV. The Fourier transform of the EXAFS spectrum of **1**$(OTf)_2$ exhibits a broad peak at $R' \approx 1.7$ Å with a weak feature at $R' \approx 2.3$ Å (Figure 4.2, top). The EXAFS data are best fit with 1 O at 2.09 Å, 5 N at 2.26 Å, and 3 C at 3.00 Å, in excellent agreement with the XRD structure (Tables 4.1 and 4.2).

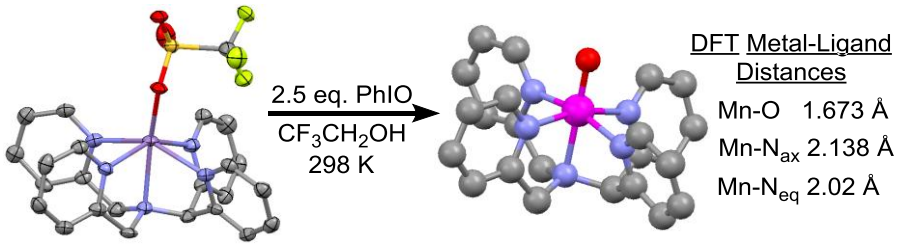

Figure 4.1. XRD structure of $[Mn^{II}(N4py)(OTf)]^+$ (**1**(OTf), left) and DFT (BP/TZVP) structure of $[Mn^{IV}(O)(N4py)]^{2+}$ (**2**, right). Hydrogen atoms are omitted for clarity.

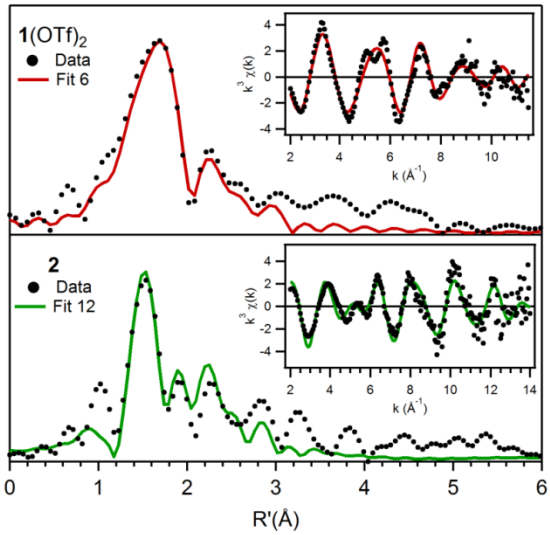

Figure 4.2. Fourier transforms of Mn K-edge EXAFS data [$k^3\chi(k)$] and raw EXAFS spectra (insets), experimental data (···) and fits (−) for $[Mn^{II}(N4py)(OTf)](OTf)$ (**1**$(OTf)_2$, top) and $[Mn^{IV}(O)(N4py)]^{2+}$ (**2**, bottom). Details regarding EXAFS fits are given in Tables 4.1 and A.4.1.

Table 4.1. EXAFS fitting results for $[Mn^{II}(N4py)(OTf)]^+$, and $[Mn^{IV}(O)(N4py)]^{2+}$.

	Mn – O			Mn – N			Mn • • • C			GOF
	n	*r*	σ^2	*n*	*r*	σ^2	*n*	*r*	σ^2	*F*
$[Mn^{II}(N4py)(OTf)]^+$	1	2.09	2.4	5	2.26	5.6	3 3	3.00 3.15	7.1 3.8	39.3
$[Mn^{IV}(O)(N4py)]^{2+}$	1	1.69	4.4	4 1	2.00 2.24	6.0 4.4	3 5	2.82 2.97	3.7 3.9	56.1

Fourier transform range for $[Mn^{II}(N4py)(OTf)]^+$: 2 – 11.5 $Å^{-1}$ (resolution 0.167 Å); $[Mn^{IV}(O)(N4py)]^{2+}$: k = 2 – 14.0 $Å^{-1}$ (resolution 0.131 Å). r is in Å, σ^2 (Debye-Waller factor) in 10^3 $Å^2$, F is a weighted goodness-of-fit parameter x 10^3.

Table 4.2. Manganese−Ligand Bond Lengths (Å) for $[Mn^{II}(N4py)(OTf)](OTf)$ (**1**$(OTf)_2$) and $[Mn^{IV}(O)(N4py)]^{2+}$ (**2**) Obtained from X-ray Diffraction (XRD), Mn K-edge XAS Data (EXAFS), and DFT Geometry Optimization.

	1$(OTf)_2$ (XRD)	**1**$(OTf)_2$ (EXAFS)	**2** (EXAFS)	**2** (DFT)
Mn−O[a]	2.107	2.09	1.69	1.673
$Mn-N_{ax}$	2.258	2.26	2.24	2.138
$Mn-N_{eq}$[b]	2.308	2.26	2.00	2.024

[a] The O atom derives from a triflate and terminal oxo ligand for **1** and **2**, respectively. [b] The average distance of all equatorial Mn−N bond lengths is listed.

The addition of excess PhIO (2.5 equiv) to **1** in CF_3CH_2OH at 298 K led to the formation of a green species (**2**), with a broad electronic absorption band at 950 nm and weaker features at 600 and 450 nm (Figure 4.3). At 298 K, the formation of **2** finished in ~10 minutes, and **2** showed a half-life of 30 minutes. The absorption features of **2** are very similar to those of other non-porphyrinic Mn^{IV}=O complexes in tetragonal, six-coordinate environments, which display broad near-infrared bands from ~1040 – 825 nm and weaker features at higher energies.[10,11,37] The perpendicular mode X-band EPR spectrum of **2** is typical of a mononuclear, S = 3/2 Mn^{IV} ion (Figure 4.4).[10,11,13,38] Hyperfine coupling for the g_{eff} = 5.76 feature is ~76 G, in good agreement with that observed for other Mn^{IV}=O complexes.[13] High-resolution electrospray-ionization mass spectral (ESI-MS) data of **2** reveal a major ion peak at *m/z* 219.0502 (Figure A.4.1, consistent with $[Mn^{IV}(O)(N4py)]^{2+}$ (*m/z* calc. 219.0563). When **2** is spiked with 10 μL $H_2{}^{18}O$ (97% ^{18}O-enriched), a new molecular ion peak is observed at *m/z* 220.0537, indicating incorporation of ^{18}O from $H_2{}^{18}O$ ($[Mn^{IV}(^{18}O)(N4py)]^{2+}$ *m/z* calc. 220.0585). The electronic absorption, EPR, and ESI-MS data together support the formulation of **2** as $[Mn^{IV}(O)(N4py)]^{2+}$.

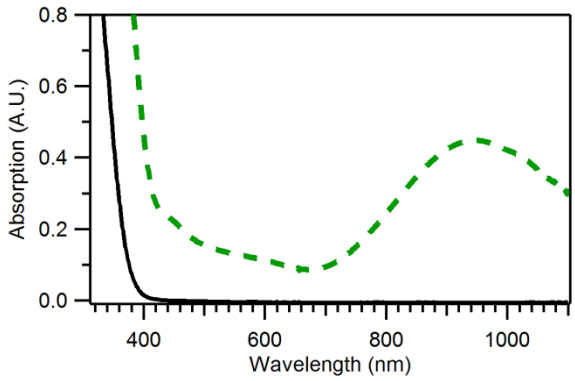

Figure 4.3. 298 K electronic absorption spectra of 2.0 mM CF_3CH_2OH solutions of **1** (black solid trace) and **2** (green dashed trace).

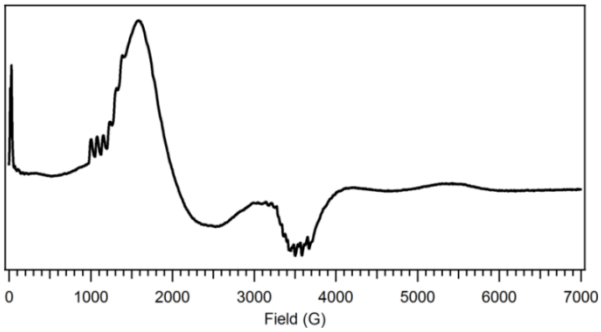

Figure 4.4. X-band, perpendicular-mode EPR spectrum of a frozen 2 mM CF_3CH_2OH solution of **2**. Recording conditions: T = 5 K, 9.637 GHz microwave frequency, 2.000 mW microwave power, 6 G modulation amplitude, 100 kHz modulation frequency, 81.92 ms time constant, and 11 667 point resolution.

The geometric and electronic structure of **2** was further examined using low-temperature MCD spectroscopy. Previous studies in our lab have shown the power of MCD spectroscopy in developing experimentally-validated bonding descriptions for manganese(IV) complexes.[37] The low-temperature MCD spectrum of **2** displays negative near-infrared bands ~11 000 cm^{-1} (~1000 nm) and additional positive features at higher energies (Figure 4.5) All features are temperature-dependent *C*-term signals that arise from the paramagnetic ground-state of **2**. The MCD spectrum of **2** is similar to that of $[Mn^{IV}(O)(OH)(Me_2EBC)]^{2+}$, which also displays transitions in the near-

infrared and visible spectral regions.[37] An iterative Gaussian deconvolution of the MCD and electronic absorption spectra of **2** revealed a total of 9 electronic transitions between 10 000 and 30 000 cm^{-1} (Figure A.4.9 and Table A.4.3). Given that only six *d-d* transitions are expected for a Mn^{IV} center in a low symmetry environment, at least several of these transitions are charge-transfer in nature. Transition polarizations, which can be obtained through fitting variable-temperature, variable-field (VTVH) MCD data,[37] are required in order to rigorously assign the MCD features of **2**. For VTVH MCD experiments, the intensity of an MCD band is monitored as a function of the magnetic field at various temperatures. VTVH MCD curves are also impacted by the ground-state spin Hamiltonian parameters (*i.e.*, *g*-values and zero-field splitting parameters) of the Mn^{IV} center. VTVH MCD curves for the major MCD features of **2** are shown in Figure A.4.10. These curves are only slightly nested (*i.e.*, the isotherms show slightly different field dependencies), indicative of a small zero-field splitting. Detailed fits of these VTVH MCD curves were hampered due to the fact that neither ground-state spin Hamiltonian parameters nor transition polarizations are known. Preliminary simulations of the EPR data collected for **2** (Figure 4.4) were undertaken to determine the ground-state spin Hamiltonian parameters, but satisfactory simulations have, to date, remained elusive.

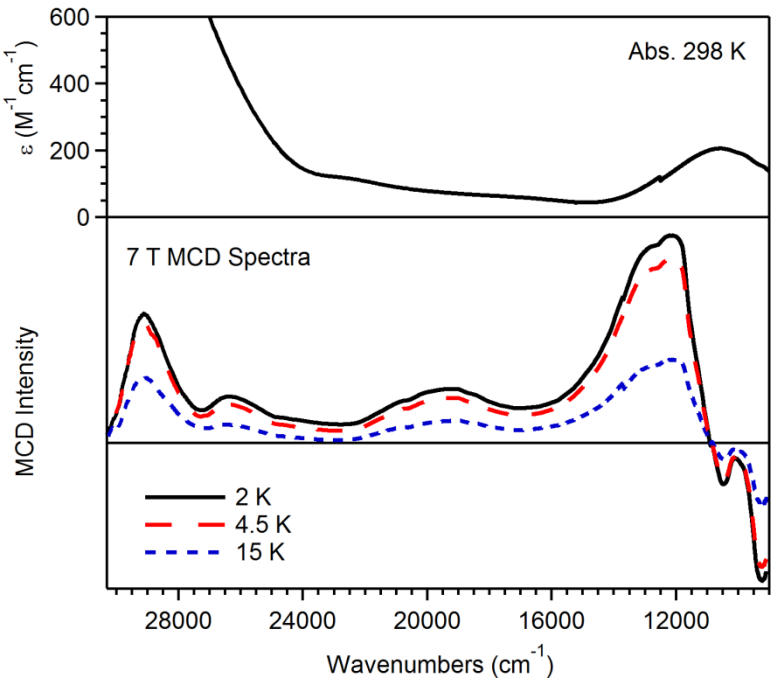

Figure 4.5. Top: 298 K electronic absorption spectrum of a 2.0 mM CF_3CH_2OH solution of **2**. **Bottom:** Variable-temperature MCD spectra of a 7.5 mM frozen CF_3CH_2OH:C_2H_5OH (1:1) solution of **2** collected at 7 T and 2, 4.5, and 15 K.

As we have been unable to grow crystals of **2**, its molecular structure was investigated by Mn K-edge XAS. The edge energy of **2** (6550.8 eV) is blue-shifted over 3 eV relative to that of **1**, as expected for the higher oxidation state of Mn (Figure 4.6). The edge energy of **2** is within 1 eV of those reported for Mn^{IV}=O complexes supported by salen and porphyrin ligands (6549.9 – 6551.2 eV; Table 4.3).[18-20] The pre-edge peak of **2** at 6541.9 eV is significantly more intense than that of **1** (Figure 4.6, inset), consistent with a large deviation from centrosymmetry.

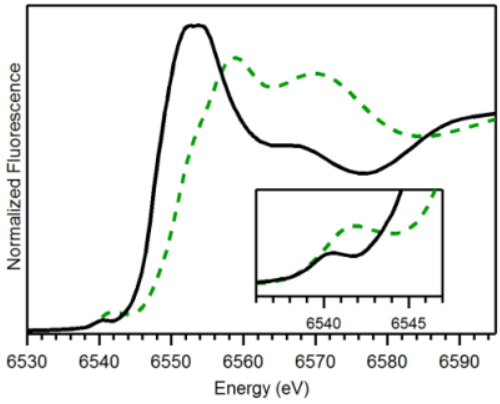

Figure 4.6. 20 K Mn K-edge XAS near-edge region of **1**$(OTf)_2$ (black solid trace) and **2** (green dashed trace) in H_2O and CF_3CH_2OH, respectively.

Table 4.3. Mn K-edge XAS Near-Edge Properties of $[Mn^{II}(N4py)(OTf)]^+$ and $[Mn^{IV}(O)(N4py)]^{2+}$ and other Mn^{IV}=O complexes.

complex	edge energy (eV)	pre-edge energy (eV)	reference
$[Mn^{II}(N4py)(OTf)]^+$	6547.3	6540.6	39
$[Mn^{IV}(O)(N4py)]^{2+}$	6550.8	6541.9	39
$[Mn^{IV}(O)(Bn\text{-}TPEN)]^{2+}$	NR[a]	6541.6	11
$[Mn^{IV}(O)(salen)]$	6549.9	6538.9	19
$[Mn^{IV}(O)(T_{piv}PP)]$	6551.2	~6541[b]	18

[a] Not reported. [b] The pre-edge feature for this complex was reported as being "some 10 eV lower in energy than the edge"; see reference 18.

The Fourier transform (R' space) of the EXAFS data of **2** exhibits a prominent, sharp peak at $R' \approx 1.5$ Å with less prominent peaks at $R' \approx 1.9$, 2.2, and 2.8 Å (Figure 4.2, bottom). The first coordination sphere of **2** is fit well with two or three shells of N/O atoms at distances (r) of 1.69, 2.00, and 2.24 Å (Table 4.1). The shell at 1.69 Å, which corresponds to the oxo ligand, is much shorter than the Mn^{II}–O (solvent H_2O) distance of 2.09 Å observed for **1**. The remaining first coordination sphere can be fit with either a single shell of 5 nitrogen scatterers at 1.99 Å or two shells of nitrogen scatterers at 2.00 Å (4 N atoms) and 2.24 Å (1 N atom), representing the nitrogen atoms of the pentadentate N4py ligand. The fit with two shells of N scatterers affords lower GOF and Debye-Waller values than the fit with just one shell of five N scatterers. Fits

including outer-sphere features reveal two Mn•••C shells at 2.82 and 2.97 Å (3 and 5 C atoms, respectively).

Metric parameters from the EXAFS data of **2** are in good agreement with a DFT-computed structure (Figure 4.1, right). This structure has a Mn=O bond of 1.673 Å (*cf.* the EXAFS distance of 1.69 Å, Table 4.2). The equatorial nitrogen ligands in the DFT-optimized structure have an average Mn–N distance of 2.024 Å, while the *trans* amine has a longer distance of 2.138 Å, consistent with the two shells of Mn–N scatterers at 2.00 and 2.24 Å.

4.3.2 Oxidative Reactivity of $[Mn^{IV}(O)(N4py)]^{2+}$ (2). The ability of **2** to activate C–H bonds was investigated using dihydroanthracene (DHA), diphenylmethane (DPM), ethylbenzene (EtBz), and toluene (Tol), which span a ~10 kcal/mol range of C–H bond strengths. For each substrate, the addition of an excess to **2** at 298 K under an Ar atmosphere led to i) a disappearance in the optical bands of **2**, ii) formation of a new species, **3**, with bands at 460 and 630 nm, and iii) the appearance of an isosbestic point at 714 nm (Figure 4.6A). The decay of **2** and the formation of **3** occurred with the same rate, both following pseudo-first order behavior to at least four half-lives. Second-order rate constants (k_2', corrected for the number of reactive C–H bonds) determined for all substrates revealed a linear relationship between $\log(k_2')$ and substrate bond dissociation enthalpies (BDEs), with a slope of 0.35 (Figures 4.7B and A.4.2; Table A.4.2). Such behavior is highly suggestive of a rate-limiting H-atom transfer.[10]

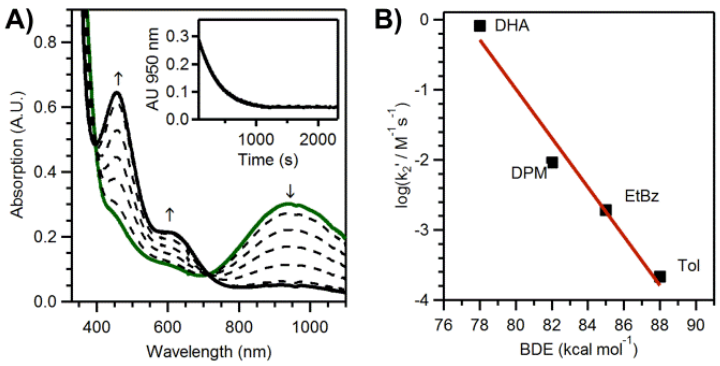

Figure 4.7. A) Electronic absorption spectra of **2** upon addition of 200 equiv EtBz in CF_3CH_2OH at 298 K. Inset: decay of the 950 nm absorption signal. B) Corrected second-order rate constant (k_2') versus bond dissociation enthalpies of organic substrates.

In support of a rate-limiting H-atom transfer, reactions of **2** with deuterated-DHA (d_4-DHA) reveal a kinetic isotope effect (KIE) of 11.2, which is larger than that observed for DHA oxidation by other Mn^{IV}=O adducts (3.1 – 8; Table 4.4).[6,10,15,40] Activation energies (E) and Arrhenius prefactors (A) determined from the reaction of **2** with DHA and d_4-DHA from 35 to -5 °C in 1:1 CF_3CH_2OH:CH_2Cl_2 provide evidence for H-atom tunnelling (Table 4.5 and Figure A.4.3). Specifically, the difference in activation energies for DHA and d_4-DHA ($E_D - E_H$) is greater than the difference in zero-point energies of the C–H and C–D bonds (3.6 and 1.26 kcal/mol, respectively); and the ratio of Arrhenius prefactors (A_H/A_D = 0.02) is much less than 0.7, and comparable to that of $[Fe^{IV}(O)(N4py)]^{2+}$, where a H-atom tunnelling mechanism was also implicated.[41] The reaction of **2** with DHA proceeded with a second-order rate constant (k_2 = 3.6 $M^{-1}s^{-1}$) 2 – 3 orders of magnitude larger than those observed at similar temperatures for nearly all other non-porphyrinic Mn^{IV}=O complexes.[10,15,40,42] Activation parameters, determined from an Eyring analysis of DHA activation from 35 to -5 °C, reveal $\Delta H^{\ddagger}$ and $\Delta S^{\ddagger}$ of 9 ± 0.8 kcal/mol and -35 ± 3 cal/mol K, respectively (Table 4.6). These parameters yield a $\Delta G^{\ddagger}$ (at 25 °C) that is comparable to that of $[Mn^{IV}(O)(H_3buea)]^-$ but 2 kcal/mol smaller than those observed

for other Mn^{IV}=O complexes,[10,15,16] consistent with the greater reactivity of **2**.

Table 4.4. Corrected Second-order Rate Constants (k_2) for Reaction of Mn^{IV}=O Complexes with DHA at the Temperature Indicated.

complex[a] [concentration]	k_2' ($M^{-1}s^{-1}$)	T (*K*)	solvent	KIE	ref
$[Mn^{IV}(O)(OH)(TF_4TMAP)]^{3+}$ [0.01 mM]	1.22	288	H_2O:MeCN (2:1)	8	6
$[Mn^{IV}(O)(N4py)]^{2+}$ [1.9 mM]	0.90	298	CF_3CH_2OH: CH_2Cl_2 (20:1)	11.2	39
$[Mn^{IV}(O)(N4py)]^{2+}$ [1.9 mM]	0.65	298	CF_3CH_2OH: CH_2Cl_2 (1:1)	8.7	39
$[Mn^{IV}(O)(OH_2)(BQCN)]^{2+}$ [2 mM]	0.030	273	MeCN:H_2O (9:1)		12
$[Mn^{IV}(O)(H_3buea)]^{-}$ [0.6 mM]	0.026	293	DMSO	6.8	15
$[Mn^{IV}(O)_2(Me_2EBC)]$ [2 mM]	0.01496	288	$(CH_3)_2CO$:H_2O (4:1)	3.78	40
$[Mn^{IV}(O)(OH)(^{H,Me}Pytacn)]^{+}$ [1 mM]	0.0065	298	MeCN:H_2O (4:1)	3.1	10

[a]Ligand abbreviations: TF_4TMAP = meso-tetrakis(2,3,5,6-tetrafluoro-*N*,*N*,*N*-trimethyl-4-aniliniumyl)porphyrinato dianion; BQCN = *N*,*N*′-dimethyl- *N*,*N*′-bis(8-quinolyl)cyclohexanedimaine; H_3buea = tris[(*N*′-*tert*-butylureaylato)-*N*-ethylene]aminato; Me_2EBC = 4,11-dimethyl-1,4,8,11-tetraazabicyclo[6.6.2]hexadecane; ^{H,Me}Pytacn = 1-(2-pyridylmethyl)-4,7-dimethyl-1,4,7-triazacyclononane.

Table 4.5. Activation Parameters for Reaction of Mn^{IV}=O Complexes with DHA and d_4-DHA.

complex[a] [concentration]	E_H [b]	E_D [b]	A_H [c]	A_D [c]	A_H/A_D	ref
$[Mn^{IV}(O)(N4py)]^{2+}$ [1.0 mM][d]	9.6 ± 0.9	13.2 ± 1.9	2.9×10^5	1.4×10^7	0.021	39
$[Mn^{IV}(O)_2(Me_2EBC)]$ [2 mM][e]	14.3 ± 0.6	20.3 ± 0.5	7.6×10^7	7.3×10^{11}	1.1×10^{-4}	16

[a] Ligand abbreviations are the same as those given for Table 4.4. [b] kcal/mol. [c] s^{-1}. [d] solvent: CF_3CH_2OH:CH_2Cl_2 (1:1). [e] solvent: $(CH_3)_2CO$:H_2O (4:1).

Table 4.6. Kinetic Parameters for Reaction of Mn^{IV}=O Complexes with DHA.

complex[a] [concentration]	$\Delta G^{\ddagger}$ [b]	$\Delta H^{\ddagger}$ [b]	$\Delta S^{\ddagger}$ [c]	$E_{1/2}$ [d]	ref
$[Mn^{IV}(O)(N4py)]^{2+}$ [1.0 mM][e]	19.4 ± 0.8	9 ± 0.8	-35 ± 3	800	39
$[Mn^{IV}(O)(H_3buea)]^{-}$ [0.6 mM] [f]	19.6 ± 1	5 ± 1	-49 ± 4	-570	15
$[Mn^{IV}(O)_2(Me_2EBC)]$ [2 mM][g]	21.0 ± 0.6	13.7 ± 0.6	-24.5 ± 2.2		16
$[Mn^{IV}(O)(OH)(^{H,Me}Pytacn)]^{+}$ [1 mM][h]	21.3 ± 0.7	10.3 ± 0.7	-37 ± 2	50	10

[a] Ligand abbreviations are the same as those given for Table 4.4. [b] kcal/mol (at 25 °C for $\Delta G^{\ddagger}$). [c] cal / mol K. [d] mV vs. SCE. [e] solvent: CF_3CH_2OH:CH_2Cl_2 (1:1). [f]solvent: DMSO. [g] solvent: $(CH_3)_2CO$:H_2O (4:1). [h] solvent: MeCN:H_2O (4:1).

The reaction of **2** with DHA yielded 0.56(8) equiv of anthracene per equiv of **2**. A final Mn oxidation state of 2.7(15) was determined by iodometric titration. This product distribution is consistent with the generation of anthracene by reaction of 1 equiv DHA with 2 equiv Mn^{IV}=O rather than two successive H-atom transfers with a single Mn^{IV}=O center. Thus, **2** acts as a one-electron oxidant, which has been observed for other Mn^{IV}=O compounds.[10,15,17,21] Such reactivity is consistent with DFT studies by Shaik and Nam that have shown a second H-atom transfer between the nascent organic radical and Mn^{III}–OH center to be less favorable than diffusion of the organic radical from the Mn^{III}–OH adduct.[43] To the best of our knowledge, two-electron oxidation of DHA by a Mn^{IV}=O has only been observed for $[Mn^{IV}(O)_2(Me_2EBC)]^+$ and $[Mn^{IV}(O)(OH_2)(BQCN)]^{2+}$.[12,17]

While the iodometric product analysis gives an average Mn oxidation state following the reaction of **2** with DHA, the nature of the Mn-based products can be better defined on the basis of EPR, electronic absorption, and ESI-MS data. Perpendicular-mode EPR spectra of the product solution showed the strong Mn^{IV}=O signals replaced by very weak signals. Broad features over a large field range and a sharp multiline signal at $g \approx 2$ are respectively attributed to mononuclear Mn^{II} and binuclear species (Figure 4.8). Corresponding parallel-mode EPR spectra are silent. This does not preclude the presence of mononuclear Mn^{III} species, as favorable Mn^{III} zero-field splitting parameters and high-quality glasses are often required to observed the weak six-line signals of mononuclear Mn^{III} centers in X-band experiments. The optical absorption features of product **3** are quite similar to those of $[Mn^{III}(OCH_2CF_3)(Bn\text{-}TPEN)]^{2+}$ (Bn-TPEN = *N*-benzyl-*N*,*N*′,*N*′-tris(2-pyridylmethyl)-1,2-diaminoethane), which was the dominant Mn product when $[Mn^{IV}(O)(Bn\text{-}TPEN)]^{2+}$ was reacted with hydrocarbons.[11] In addition, the dominant molecular ion peak in ESI-MS data of **3** is at *m*/*z* 620.1289, consistent with

{[Mn^{III}(OCH_2CF_3)(N4py)](OCH_2CF_3)}$^+$ (*m/z* calc. 620.1293). Thus, we propose a mononuclear Mn^{III} species as the dominant, but not sole, Mn-based product when **2** reacts with DHA.[44]

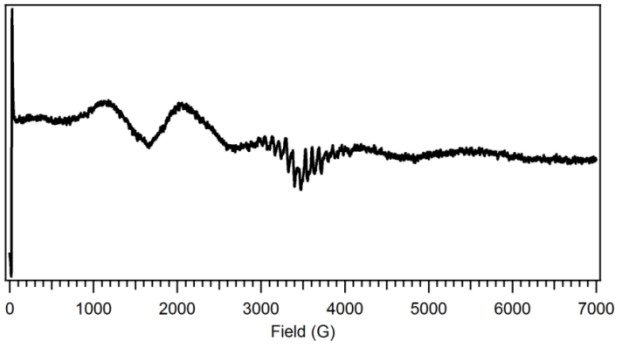

Figure 4.8. X-band, perpendicular-mode EPR spectrum of a frozen 2 mM CF_3CH_2OH solution of **3**. Recording conditions: T = 5 K, 9.637 GHz microwave frequency, 2.000 mW microwave power, 6 G modulation amplitude, 100 kHz modulation frequency, 81.92 ms time constant, and 11 667 point resolution.

4.4. Discussion and Avenues for Future Work.

The chemical reactivity of **2** is similar to that of [Mn^{IV}(O)(Bn-TPEN)]$^{2+}$.[11] Both N4py and Bn-TPEN are N5 aminopyridyl ligands that also support highly reactive Fe^{IV}=O complexes.[41] For the Mn^{IV}=O adducts, previous DFT computations predicted that **2** has a larger barrier for H-atom abstraction from cyclohexane than [Mn^{IV}(O)(Bn-TPEN)]$^{2+}$.[43] Although the addition of a large excess (400 – 600 equiv) of cyclohexane increases the decay rate of **2**, the reaction does not show pseudo-first order behavior. In contrast, [Mn^{IV}(O)(Bn-TPEN)]$^{2+}$ reacts with cyclohexane at 25 °C. Thus, we are unable to determine a k_2 value to provide a quantitative comparison of reactivity using cyclohexane. However, a comparison can be made using EtBz, with which both compounds react at 25 °C in CF_3CH_2OH. In the reaction with EtBz, [Mn^{IV}(O)(Bn-TPEN)]$^{2+}$ (1 mM) shows a second-order rate five-fold larger than that of **2** (2 mM): $k_2 = 2.7 \times 10^{-2}$ and 5.7×10^{-3} $M^{-1}s^{-1}$, respectively.[11] Thus, while **2** is dramatically more

reactive towards C–H bonds than most Mn^{IV}=O adducts, it is less reactive than $[Mn^{IV}(O)(Bn\text{-}TPEN)]^{2+}$. This trend holds for the corresponding Fe^{IV}=O adducts; *i.e.*, $[Fe^{IV}(O)(Bn\text{-}TPEN)]^{2+}$ is more reactive towards C–H bonds.[41]

The origin of the high reactivity of **2** towards C–H bonds is currently unclear. Cyclic voltammetry studies of **2** show a $Mn^{III/IV}$ reduction potential ($E_{1/2}$) ~700 mV higher than those of other Mn^{IV}=O complexes (Figure A.4.4; Table 4.6).[10,15,40] Thus, **2** is a significantly more effective one-electron oxidant. Notably the $E_{1/2}$ of **2** is similar to those of other dicationic Mn^{IV} complexes,[10,40] suggesting that the increase in $E_{1/2}$ is attributed to the +2 total charge of **2** versus the +1 and -1 charges of other Mn^{IV}=O adducts (Table 4.6).[10,15] However, rates of H-atom transfer reactions, which are strongly correlated to thermodynamic driving force, depend not only on the reduction potential of the oxidant, but also on the basicity of the metal-hydroxo product.[45] Both the $Mn^{III/IV}$ reduction potential and the pK_a of the Mn^{III}–OH complex, which for this system is unknown, are necessary for a thermodynamic analysis. While we cannot comment at present on the driving force for C–H bond activation by **2**, we note that many other Mn^{IV}=O adducts have sterically demanding supporting ligands that shield the oxo. In contrast, the oxo ligand in **2** is well-exposed to substrate (Figure 4.1, right). Reduced steric clash with substrate could contribute to the relatively high reactivity of **2**.

Future work is needed to determine the role ligand sterics, solvent effects, and thermodynamic driving force play in influencing the H-atom transfer reactivity of **2**, and to explore further why Mn^{IV}=O adducts such as **2** may eschew standard rebound or desaturation mechanisms for C–H activation. Furthermore, analysis of the MCD and VTVH MCD data can provide insight into the dominant metal-ligand bonding interactions of **2**, which may help to explain the high reactivity of this complex. A similar analysis has been performed for the

$[Mn^{IV}(O)(OH)(Me_2EBC)]^+$ complex, which shows distinct reactivity patterns when compared with **2**. In particular, $[Mn^{IV}(O)(OH)(Me_2EBC)]^+$ is a relatively sluggish oxidant (Table 4.6). Nonetheless, $[Mn^{IV}(O)(OH)(Me_2EBC)]^+$ facilitates two-electron oxidation of hydrocarbons, whereas **2** mediates one-electron oxidations. Two-electron substrate oxidation regenerates the manganese(II) starting complex, and, therefore, is a requisite for efficient catalysis. A detailed comparison of spectroscopically-derived bonding descriptions of $[Mn^{IV}(O)(OH)(Me_2EBC)]^+$ and **2** could provide insights into the subtle, yet important, differences in reactivity between these complexes. Finally, spectral fitting of the X-band and Q-band EPR data collected for **2** can provide information about its ground-state spin Hamiltonian parameters (*i.e.*, *g*-values and zero-field splitting parameters). Such studies have only been performed for a limited number of Mn^{IV}=O complexes.[12,13] Because of this paucity of data, the relationship, if any, between ground-state spin Hamiltonian parameters, geometric structure, and/ or chemical reactivity is unknown.

Notes and References

1. McEvoy, J. P.; Brudvig, G. W., *Chem. Rev.* **2006,** *106*, 4455-4483.
2. Wu, A. J.; Penner-Hahn, J. E.; Pecoraro, V. L., *Chem. Rev.* **2004,** *104*, 903-938.
3. Hage, R.; Lienke, A., *Angew. Chem., Int. Ed. Engl.* **2006,** *45*, 206-222.
4. Lansky, D. E.; Narducci Sarjeant, A. A.; Goldberg, D. P., *Angew. Chem., Int. Ed. Engl.* **2006,** *45*, 8214-8217.
5. Prokop, K. A.; de Visser, S. P.; Goldberg, D. P., *Angew. Chem., Int. Ed. Engl.* **2010,** *49*, 5091-5095.
6. Arunkumar, C.; Lee, Y.-M.; Lee, J. Y.; Fukuzumi, S.; Nam, W., *Chem. Eur. J.* **2009,** *15*, 11482-11489.
7. Groves, J. T.; Lee, J.; Marla, S. S., *J. Am. Chem. Soc.* **1997,** *119*, 6269-6273.
8. Taguchi, T.; Gupta, R.; Lassalle-Kaiser, B.; Boyce, D. W.; Yachandra, V. K.; Tolman, W. B.; Yano, J.; Hendrich, M. P.; Borovik, A. S., *J. Am. Chem. Soc.* **2012,** *134*, 1996-1999.
9. Collins, T. J.; Gordon-Wylie, S. W., *J. Am. Chem. Soc.* **1989,** *111*, 4511-4513.
10. Garcia-Bosch, I.; Company, A.; Cady, C. W.; Styring, S.; Browne, W. R.; Ribas, X.; Costas, M., *Angew. Chem., Int. Ed. Engl.* **2011,** *50*, 5648-5653.
11. Wu, X.; Seo, M. S.; Davis, K. M.; Lee, Y.-M.; Chen, J.; Cho, K.-B.; Pushkar, Y. N.; Nam, W., *J. Am. Chem. Soc.* **2011,** *133*, 20088-20091.
12. Sawant, S. C.; Wu, X.; Cho, J.; Cho, K.-B.; Kim, S. H.; Seo, M. S.; Lee, Y.-M.; Kubo, M.; Ogura, T.; Shaik, S.; Nam, W., *Angew. Chem., Int. Ed. Engl.* **2010,** *49*, 8190-8194.
13. Parsell, T. H.; Behan, R. K.; Green, M. T.; Hendrich, M. P.; Borovik, A. S., *J. Am. Chem. Soc.* **2006,** *128*, 8728-8729.

14. Yin, G.; Danby, A. M.; Kitko, D.; Carter, J. D.; Scheper, W. M.; Busch, D. H., *J. Am. Chem. Soc.* **2007,** *129*, 1512-1513.
15. Parsell, T. H.; Yang, M.-Y.; Borovik, A. S., *J. Am. Chem. Soc.* **2009,** *131*, 2762-2763.
16. Wang, Y.; Shi, S.; Wang, H.; Zhu, D.; Yin, G., *Chem. Commun.* **2012,** *48*, 7832-7834.
17. Shi, S.; Wang, Y.; Xu, A.; Wang, H.; Dajian, Z.; Roy, S. B.; Jackson, T. A.; Busch, D. H.; Yin, G., *Angew. Chem., Int. Ed. Engl.* **2011,** *50*, 7321-7324.
18. Ayougou, K.; Bill, E.; Charnock, J. M.; Garner, C. D.; Mandon, D.; Trautwein, A. X.; Weiss, R.; Winkler, H., *Angew. Chem., Int. Ed. Engl.* **1995,** *34*, 343-346.
19. Kurahashi, T.; Kikuchi, A.; Tosha, T.; Shiro, Y.; Kitagawa, T.; Fujii, H., *Inorg. Chem.* **2008,** *47*, 1674-1686.
20. Kurahashi, T.; Kikuchi, A.; Shiro, Y.; Hada, M.; Fujii, H., *Inorg. Chem.* **2010,** *49*, 6664-6672.
21. Hansel, C. M.; Zeiner, C. A.; Santelli, C. M.; Webb, S. M., *Proc. Natl. Acad. Sci.* **2012,** *109*, 12621-12625.
22. Armarego, W. L. F.; Perrin, D. D., *Purification of Laboratory Chemicals*. Butterworth-Heinemann: Oxford, U.K., 1997.
23. Goldsmith, C. R.; Jonas, R. T.; Stack, T. D. P., *J. Am. Chem. Soc.* **2001,** *124*, 83-96.
24. Chang, J.; Plummer, S.; Berman, E. S. F.; Striplin, D.; Blauch, D., *Inorg. Chem.* **2004,** *43*, 1735-1742.
25. Lubben, M.; Meetsma, A.; Wilkinson, E. C.; Feringa, B.; Que, L., Jr., *Angew. Chem., Int. Ed. Engl.* **1995,** *34*, 1512-1514.
26. Geiger, R. A.; Leto, D. F.; Chattopadhyay, S.; Dorlet, P.; Anxolabéhère-Mallart, E.; Jackson, T. A., *Inorg. Chem.* **2011,** *50*, 10190-10203.
27. International Tables for Crystallography, Vol A, 4th ed., Kluwer: Boston (1996).
28. George, G. N. *EXAFSPAK; Stanford Synchrotron Radiation Laboratory; Stanford, CA, 1990.*, 1990.
29. Rehr, J. J.; Mustre de Leon, J.; Zabinsky, S. I.; Albers, R. C., *J. Am. Chem. Soc.* **1991,** *113*, 5135-5140.
30. Neese, F., *ORCA - an ab initio, Density Functional and Semiempirical Program Package, Version 2.8*, University of Bonn, 2011. *ORCA - an ab initio, Density Functional and Semiempirical Program Package, Version 2.8, University of Bonn, 2009.*
31. Becke, A. D., *J. Chem. Phys.* **1986,** *84*, 4524-4529.
32. Perdew, J. P., *Phys. Rev. B* **1986,** *33*, 8822-8824.
33. Schäfer, A.; Horn, H.; Ahlrichs, R., *J. Chem. Phys.* **1992,** *97*, 2571-2577.
34. Schäfer, A.; Huber, C.; Ahlrichs, R., *J. Chem. Phys.* **1994,** *100*, 5829-5835.
35. Neese, F., *J. Comput. Chem.* **2003,** *24*, 1740-1747.
36. Perez-Benito, J. F.; Brillas, E.; Arias, C., *Can. J. Chem.* **1990,** *68*, 79-81.
37. Chattopadhyay, S.; Geiger, R. A.; Yin, G.; Busch, D. H.; Jackson, T. A., *Inorg. Chem.* **2010,** *49*, 7530-7535.
38. Rajendiran, T. M.; Kampf, J. W.; Pecoraro, V. L., *Inorg. Chim. Acta* **2002,** *339*, 497-502.
39. Leto, D. F.; Ingram, R.; Day, V. W.; Jackson, T. A., *Chem. Commun.* **2013,** *49*, 5378-5380.
40. Yin, G.; Danby, A. M.; Kitko, D.; Carter, J. D.; Scheper, W. M.; Busch, D. H., *J. Am. Chem. Soc.* **2008,** *130*, 16245-16253.
41. Klinker, E. J.; Shaik, S.; Hirao, H.; Que, L., *Angew. Chem., Int. Ed. Engl.* **2009,** *48*, 1291-1295.
42. A potential complication for this rate comparison is the difference in solvents (Table 4.4). **2** reacts with DHA at essentially the same rate in 1:1 CF_3CH_2OH:CH_2Cl_2, though the KIE drops to 8.7. In other solvents **2** has limited stability or does not form.
43. Cho, K.-B.; Shaik, S.; Nam, W., *J. Phys. Chem. Lett.* **2012,** *3*, 2851-2856.
44. In the absence of any substrate, the thermal decay of 2 yields a similar product, as judged by electronic absorption spectroscopy.
45. Mayer, J. M., *Acc. Chem. Res.* **2010,** *44*, 36-46.

Chapter 5

Mn K-edge X-ray Absorption Studies of Oxo- and Hydroxo-manganese(IV) Complexes: Experimental and Theoretical Insights into XANES Properties

This work has been submitted as a full paper to *Inorganic Chemistry*.

5.1. Introduction.

Mn K-edge XAS has featured prominently in the study of Mn enzymes and synthetic Mn compounds.[1,2] For example, the oxygen-evolving complex (OEC) in photosystem II, which contains a Mn_4O_5Ca cluster that converts H_2O to protons and O_2, has been studied extensively by Mn XAS.[3-7] These studies have provided important insights into structural changes in the OEC during the oxidation cycle, and have highlighted the propensity for this cluster to undergo photodegradation upon X-ray irradiation.[5-8] Mn XAS has also been widely utilized in the characterization of the bacterial enzyme Mn catalase (MnCAT), which employs a dimanganese active site to disproportionate H_2O_2.[1,9] Notably, XAS studies confirmed the dimanganese(III,III) and dimanganese(II,II) forms of MnCAT are the active forms of the enzyme.[9] With regard to synthetic systems, Mn K-edge XAS has played a critical role in the characterization of high-valent oxo- and hydroxo-manganese species[10-16] that model intermediates commonly proposed in biological and synthetic oxidation reactions.[13,15,17-22] Although several Mn^V–oxo adducts have been structurally characterized by X-ray diffraction,[23-26] Mn K-edge XAS has been commonly employed to determine metal-ligand bond lengths for high-valent oxo- and hydroxo-manganese adducts that have thus far eluded structural characterization by X-ray diffraction.[10-22,27] A major advantage of the XAS technique is that crystalline samples are not required.

K-edge XAS spectra are divided into two regions: the extended X-ray absorption fine structure (EXAFS) region, which occurs beyond the K-edge; and the X-ray absorption near edge structure (XANES) region, which is within ~10 eV of the K-edge. Analysis of EXAFS and XANES data provide complementary information about the metal center. Accurate (~0.02 Å) metal–ligand and, in the case of multinuclear species, metal–metal, distances can be extracted from the EXAFS region,[28] while the XANES region is reflective of the oxidation state and

coordination environment of the metal. The energy of the absorption K-edge (metal 1s-to-4p transition) is sensitive to the effective nuclear charge of the absorbing metal atom due to 1s core-hole shielding effects.[5] Pre-edge features, which commonly occur ~10 eV before the edge, arise from electric-quadrupole-allowed metal 1s-to-3d transitions that have a low intrinsic XAS intensity. However, these electric-dipole (parity) forbidden metal 1s-to-3d transitions can gain intensity through metal 3d-4p mixing induced by low symmetry distortions and/or be mediated by metal-ligand covalency.[29-33] Thus, the pre-edge energy and intensity, and edge energy, are useful probes of metal oxidation state, site geometry, and metal-ligand covalency. However, the fact that the XANES properties are not isolated signatures of a single property of the metal center, but instead are impacted by a conglomerate of effects, complicates the analysis of XANES data.[31,34] Consequently, the pre-edge region is often used to infer changes in the metal oxidation state and/or site geometry by comparisons with well-characterized model compounds. XAS studies of Mn^{V}–oxo and –nitrido model complexes have revealed intense pre-edge features that are attributed to short axial Mn–oxo and Mn–nitrido distances.[35-37] However, the lack of an intense pre-edge feature does not confirm the absence of a Mn^{V}–oxo species. For example, the presence of a sixth ligand *trans* to the oxo in [Mn^{V}(O)(TDCPP)] (TDCPP = meso-tetrakis(2,6-dichlorophenyl)porphinato dianion) significantly diminished the Mn pre-edge intensity.[38] Thus, care must be taken when inferring specific structural motifs on the basis of XANES data alone.

A detailed and quantitative analysis of the pre-edge region involving a complement of experiment and theory can provide significant insight into the electronic structure of the metal.[29-31,33] Detailed experimental and computational analysis of Fe K-edge XANES spectra has proven to be a valuable tool for studying the electronic *and* geometric structure of Fe^{IV}–oxo complexes.[39-41] In addition, such an analysis provides insight into the physical basis for XANES

properties, rather than treating such data at a phenomenological level. Application of this combined experimental and theoretical approach to the analysis of high-valent Mn XANES spectra is limited to formally Mn^{V}–oxo and Mn^{V}–nitrido complexes,[37,42] as well as Mn^{IV} dithiolene complexes.[43] Such studies have been enabled by recently described time-dependent density functional theory (TD-DFT) methods that have been successfully used for the accurate prediction of XANES properties for a variety of monomeric Fe compounds[29,30] and monomeric and dimeric Mn compounds.[34,44] Notably, Roemelt and co-workers established and validated a TD-DFT method for a set of 16 monomeric Mn^{II} and Mn^{III} compounds, successfully reproducing the shape, intensity, and energy of the experimental pre-edge XANES spectra.[34]

In this chapter, Mn K-edge XAS and TD-DFT methods are used to explore the geometric and electronic structure of a pair of hydroxo- and oxomanganese(IV) complexes, $[Mn^{IV}(OH)_2(Me_2EBC)]^{2+}$ (**2**) and $[Mn^{IV}(O)(OH)(Me_2EBC)]^{+}$ (**3**), that are supported by the ethylene cross-bridged macrocyclic ligand Me_2EBC (Me_2EBC is 4,11-dimethyl-1,4,8,11-tetraazabicyclo[6.6.2]hexadecane) and differ only by a proton (Figure 5.1). $[Mn^{II}(Cl_2)(Me_2EBC)]$ (**1**), from which **2** and **3** are derived, is included in the analysis for comparison. While the crystal structures of **1** and **2** have been reported,[27,45] the EXAFS data presented here provide the first structural parameters for **3**, adding to the limited structural information available for monomeric Mn^{IV}–oxo complexes.[10-16] To gain insight into the nature of the XANES pre-edge transitions of these complexes, and to explore the XANES properties of manganese(IV) complexes in general, we performed TD-DFT calculations for **2** and **3**, as well as for a set of oxo- and hydroxo-manganese(IV) complexes with diverse geometries and supporting ligands. Excellent agreement is observed between the experimental and calculated XANES spectra, indicating that the TD-DFT method is robust in predicting XANES spectra for high-valent Mn complexes. The effects

of coordination geometry and ligand properties on pre-edge transitions of Mn^{IV}–oxo and Mn^{IV}–hydroxo species are discussed.

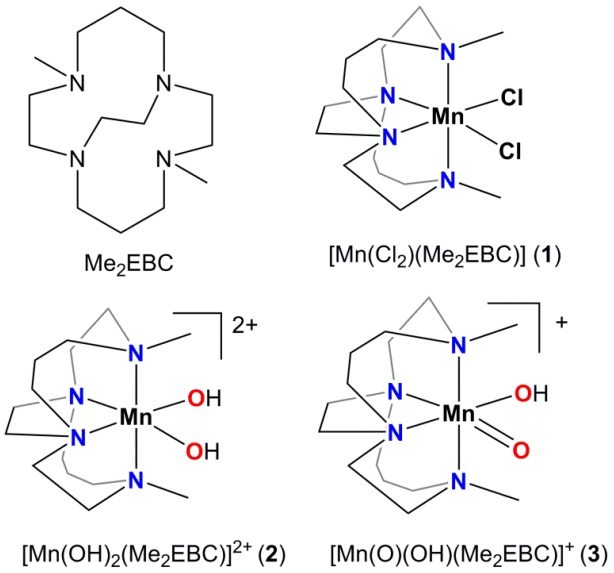

Figure 5.1. Structure of Me_2EBC ligand and complexes $[Mn^{II}(Cl_2)(Me_2EBC)]$ (**1**), $[Mn^{IV}(OH)_2(Me_2EBC)]^{2+}$ (**2**), and $[Mn^{IV}(O)(OH)(Me_2EBC)]^{+}$ (**3**).

5.2. Experimental and Computational Methods.

5.2.1. Materials. $[Mn^{IV}(OH)_2(Me_2EBC)](PF_6)_2$ was generated by oxidizing $[Mn^{II}(Cl_2)(Me_2EBC)]$ (**1**) with H_2O_2 (30% aqueous solution) in the presence of NH_4PF_6 in deionized H_2O, as described previously.[45] $[Mn^{IV}(O)(OH)(Me_2EBC)]^{+}$ (**3**) was prepared by adjusting the pH of an aqueous solution of **2** to 8.8 with 0.3 M NaOH.[18,45] **2** has a pK_a in water of 6.86(4), ensuring >98% formation of **3** at a pH of 8.8.[18,27]

5.2.2. Mn K-edge XAS Experiments. (A) Sample Preparation. A 2% (w/w) dispersion of **1** in boron nitride was prepared by grinding 4 mg of **1** with 196 mg boron nitride into a fine powder with a mortar and pestle. For the EXAFS sample of **2**, a 29 mM solution of **2** was prepared by dissolving 9.6 mg (0.015 mmol) of the PF_6^- salt of **2** in 0.5 mL deionized H_2O at 25 ^oC. Approximately 200 µL of this solution were transferred to an XAS sample holder. The

XANES sample of **2** was prepared from a 9.7 mM aqueous solution of **2**. For the EXAFS sample of **3**, an 8.4 mM solution of **3** was prepared by dissolving 26.8 mg (0.042 mmol) of the PF_6^- salt of **2** in 5 mL deionized H_2O at 25 ^oC. The pH was adjusted to 8.8 by the addition of 0.3 M NaOH (0.140 mL). The formation of **3** from **2** was monitored by electronic absorption spectroscopy. Once the formation of **3** was completed, five samples were prepared by transferring approximately 200 µL of **3** into separate XAS sample holders. The XANES sample of **3** (pH = 8.8) was prepared by adjusting the pH of a 9.7 mM aqueous solution of **2** with 0.3 M NaOH to a final pH of 8.8. All samples were immediately flash-frozen in liquid N_2 and stored under liquid nitrogen prior to XAS data collection.

(B) XAS Data Collection. EXAFS and XANES spectra were recorded on beamline X3B at the National Synchrotron Light Source (NSLS), Brookhaven National Lab (storage ring conditions, 2.8 GeV, 100 - 300 mA). Mn K-edge X-ray absorption spectra over the energy range 6.4 – 7.4 keV (Si(111) monochromater) were recorded on frozen solutions, or, in the case of **1**, a powder sample, maintained at 20 K with a helium Displex closed-cycle cryostat. For EXAFS data, XAS spectra were obtained as fluorescence excitation spectra using either a solid-state 13-element (**1**) or a 31-element (**2** and **3**) germanium detector (Canberra). Contamination of higher harmonics radiation was minimized by using a harmonic rejection mirror. The background fluorescence signal was reduced by use of a 6 µm chromium filter for **1** and **2** and a 3 µm filter for **3**. A manganese foil spectrum was recorded concomitantly for internal energy calibration, and the first inflection point of the K-edge energy was assigned to 6539.0 eV. Spectra were measured with 5 eV steps below the edge (6359 – 6529 eV), 0.3 eV steps in the edge region (6529 – 6564 eV), and steps equivalent to 0.05 $Å^{-1}$ increments above the edge. The X-ray flux at 6.6 to 7.1 keV was $2(1) \times 10^{10}$ photons $\times$ s^{-1} $\times$ mm^{-2}. Under these conditions, it was observed that

complex **3** was photoreduced after each scan, as the edge energy shifted ~0.9 eV to lower energy in the second scan and shifted ~0.3 eV to lower energy in subsequent scans on the same spot. Thus, the effects of photoreduction on the EXAFS data set were minimized by reducing the X-ray flux and collecting only one scan per sample spot on three different samples for complex **3**. The EXAFS spectra of complexes **1** (2% w/w in boron nitride), **2** (29 mM in H_2O), and **3** (8.4 mM in H_2O, pH 8.8) represent the average of 8, 12, and 11 scans, respectively. To investigate the photoreduction of **3**, five sequential scans, under conditions of high X-ray flux, were collected on the same sample spot for two different samples.

Additional Mn K-edge XANES data, which provided higher resolution over a wider energy window, were obtained for **2** and **3** using a solid-state 31-element germanium detector (Canberra) with a 3 μm chromium filter. Spectra were measured with 5 eV steps below the edge (6359 – 6518 eV), 0.3 eV steps in the edge region (6518 – 6569 eV), steps equivalent to 0.05 $Å^{-1}$ increments above the edge (6569 - 6676 eV), and steps equivalent to 0.1 $Å^{-1}$ increments at higher energy. The XANES spectrum of **2** represents the average of four consecutive scans from one sample. The XANES spectrum of **3** represents the average of six scans from six sample spots collected under conditions of low X-ray flux.

(C) EXAFS Data Analysis. EXAFS data reduction and averaging were performed using the program EXAFSPAK.[46] Pre-edge background intensity was removed by fitting a Gaussian function to the pre-edge background and subtracting this function from the whole spectrum. The spectrum was then fit with a three-segment spline with fourth-order polynomial components to remove low-frequency background. EXAFS refinement was carried out on $k^3\chi(k)$ data, using phase and amplitude functions obtained from *FEFF*, version 6,[47] and structural models of **1**, **2**, and **3** obtained from DFT geometry optimizations (*vide infra*). For each fit, the parameters *r*

(average distance between Mn and scattering atom) and σ^2 (Debye-Waller factor) were optimized, while *n*, the number of atoms in the shell, was kept fixed. *n* was varied by integer steps systematically. The goodness-of-fit (GOF) was evaluated by the parameter *F*, where $F = \Sigma (\chi_{calcd} - \chi_{expt})^2 / N$, and *N* is the number of data points. The threshold energy, E_0, in electronvolts ($k = 0$ point) was kept at a common, variable value for every shell of a given fit.

(D) XANES Data Analysis. Mn K-edge pre-edge data were fit using EDG_FIT in EXAFSPAK.[46] Second derivative spectra were used to help determine the number and position of peaks. Pre-edge features were fit using pseudo-Voigt line shapes (sums of Lorentzian and Gaussian functions), and the energy position, full width at half-maximum (FWHM), and peak height were varied.[31] A fixed 1:1 ratio of Lorentzian to Gaussian functions successfully reproduced the pre-edge features. The rising edge and background under the pre-edge features were also fit with pseudo-Voigt line shapes. Good fits reproduced the pre-edge features using a minimum number of peaks. The fits were performed over three energy ranges and reported peak area (height × FWHM) and peak energy are based on the average of all three fits.

5.2.3. Density Functional Theory Computations. (A) General Considerations. All DFT calculations were carried out using the ORCA program package, versions 2.8 and 2.9.[48] Full geometry optimizations were performed using the Becke-Perdew (BP86) functional[49,50] in conjunction with the TZVP (for Mn, N, O, and Cl) and SVP (for C and H) basis sets[51,52] and were treated at the spin-unrestricted level. Because these calculations employed a resolution of the identity approximation (RI),[53] the SV/J and TZV/J auxiliary basis sets were also used.[51,52] All optimizations were performed without symmetry constraints. Numerical frequency calculations were performed on all optimized structures to ensure that the optimized structures represent true minima. A dense integration grid (ORCA Grid5) and tight convergence criteria were enforced

for all geometry optimizations. Calculations were converged to the S = 5/2 state for **1** (high-spin Mn^{II}) and the S = 3/2 state for all Mn^{IV} complexes. Cartesian coordinates for all geometry optimized models can be found in Appendix A.5 (Tables A.5.8 – A.2.25).

The crystal-structure coordinates of **1**[54] and **2**[27] were utilized as starting points for full geometry optimizations. Previously published DFT geometry-optimized coordinates were used as initial structures of **3**,[18] $[Mn^{IV}(O)(N4py)]^{2+}$,[15] $[Mn^{IV}(O)(Bn\text{-}TPEN)]^{2+}$,[16] and the models were subjected to full geometry optimization. Models of $[Mn^{IV}(O)(salen)]$ and $[Mn^{IV}(OH)(salen)]^{+}$ were built by replacing the aqua ligand in the XRD structure of $[Mn^{III}(OH_2)(salen)]^{+}$ with an oxo and hydroxo ligand, respectively.[14] For $[Mn^{IV}(O)(T_{piv}PP)]$,[10] an initial model was constructed using the known structure of the ligand and DFT geometry-optimizations were performed. The initial model of $[Mn^{IV}(O)(H_3buea)]^{-}$ was built by replacing Fe^{III} with Mn^{IV} in the DFT-optimized coordinates of $[Fe^{III}(O)(H_3buea)]^{2-}$.[55] From the optimized coordinates of $[Mn^{IV}(O)(H_3buea)]^{-}$, the model of $[Mn^{V}(O)(H_3buea)]$ was optimized to the S = 1 spin state.

To reduce the computational cost of the TD-DFT computations for the salen- and porphyrin-containing complexes, the salen ligand in the optimized models of $[Mn^{IV}(O)(salen)]$ and $[Mn^{IV}(OH)(salen)]^{+}$ was truncated by replacing the mesityl groups with methyl groups. In addition, the porphyrinic ligand in the optimized model of $[Mn^{IV}(O)(T_{piv}PP)]$ was truncated by replacing the pivalamidophenyl groups with methyl groups. After truncation, full DFT geometry-optimizations were performed.

(B) XAS Calculations. The Mn K-edge XANES spectra were calculated using the TD-DFT method within the Tamm–Dancoff approximation.[56,57] The B3LYP functional[58-60] and def2-SVP (for C and H) and def2-TZVP(-f) (for Mn, N, O, and Cl) basis sets were utilized for these calculations.[61] Scalar relativistic effects were taken into account at the ZORA level[62,63] and a

dense integration grid (ORCA Grid4) and tight convergence criteria were enforced. As established previously, the calculated spectra were shifted 32.6 eV to higher energy to correct for systematic errors in the level of theory (*i.e.*, density functional, basis set, etc.).[34] The calculated spectra using def2-SVP (for C and H) and def2-TZVP(-f) (for Mn, N, O, and Cl) basis sets were ~0.2 eV lower in energy than the calculated spectra using the larger def2-TZVP(-f) basis set for all atoms (Figure A.5.1), within the error of the energy correction of 32.6 ± 0.2 eV.[34] Computed XANES data were plotted by applying a Gaussian fit with a 1 eV broadening. The calculated intensities include electric dipole, electric quadrupole, and magnetic dipole contributions, as described in Appendix A.5. The calculated area (A) was obtained from the calculated intensity (I) according to the correlation $A = 6.01I + 1.79$, as established for a set of monomeric Mn^{II} and Mn^{III} compounds.[34] MO plots were generated using the program gOpenMol.

To determine if truncation of the salen ligand had a significant effect on the calculated pre-edge spectrum of [Mn^{IV}(O)(salen)], TD-DFT calculations were performed using a DFT-optimized model of the full, untruncated [Mn^{IV}(O)(salen)] model. The calculated pre-edge intensity for the truncated model of [Mn^{IV}(O)(salen)] was within 5% of the calculated intensity for the complete complex of [Mn^{IV}(O)(salen)] (Figure A.5.2), indicating a marginal impact on the pre-edge intensity due to the truncation. Thus, unless noted otherwise, calculations for the salen- and porphyrin-containing complexes were performed using truncated versions of the ligand. When the TD-DFT calculations for [Mn^{IV}(O)(H_3buea)]$^-$ were carried out in a continuum dielectric using the conductor like screening model COSMO,[64] with dimethylformamide as the solvent, the energy of the individual transitions decreased by >0.1 eV. The pre-edge intensity decreased by ~10% relative to the gas-phase calculation (Figure A.5.1, bottom).

5.3. Results and Analysis.

5.3.1. Experimental XAS Data. (A) EXAFS Data and Fitting Results for 1, 2, and 3.

The Fourier transform (R' space) of the EXAFS spectrum of **1** exhibits a broad peak at $R' \approx 2.0$ Å that is best accounted for by two shells of scatterers 2.47 (two Cl scatterers) and 2.29 Å (four N scatterers), as shown in Figure 5.2A and Table 5.1. The distances of the Cl and N scatterers are in good agreement with the average Mn−Cl and Mn−N distances of 2.455 and 2.334 Å observed in the X-ray diffraction structure of **1** (Table 5.2).[54] Fits modeling the two smaller peaks at $R' \approx$ 2.6 and 2.9 Å using two Mn•••C shells at 3.03 and 3.21 Å (4 and 6 C atoms, respectively) improve the overall goodness-of-fit (Table 5.1 and A.5.1). In the X-ray diffraction structure of **1**, two C atoms are located at a Mn•••C distance of ~3.00 Å, ten C atoms at Mn•••C distances ranging from 3.10 to 3.26 Å (average Mn•••C distance 3.18 Å), and two C atoms are located at a Mn•••C distance of ~3.65 Å.[54] Thus, all structural parameters obtained from EXAFS fits of **1** are in excellent agreement with the corresponding XRD structure.

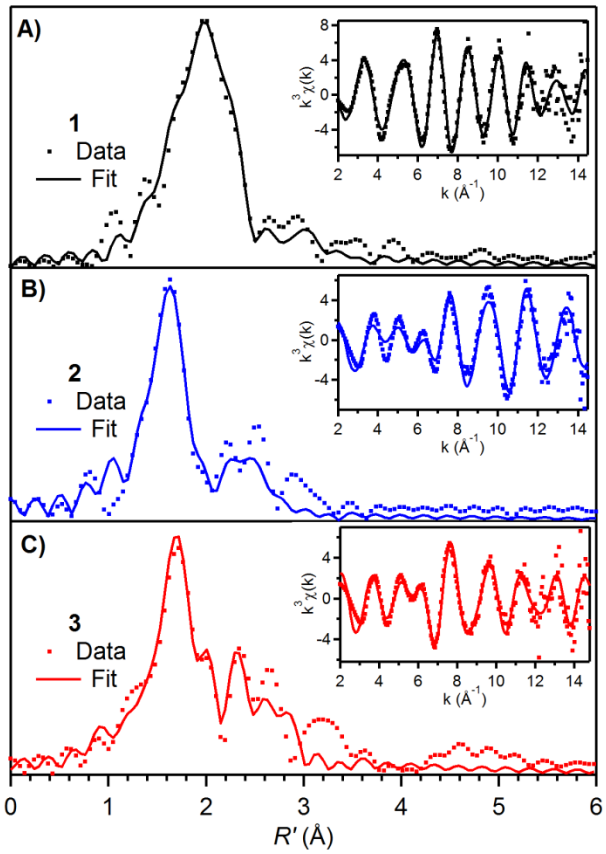

Figure 5.2. Fourier transforms of Mn K-edge EXAFS data [$k^3\chi(k)$] and raw EXAFS spectra (insets), experimental data (−) and fits (···) for (A) [$Mn^{II}(Cl_2)(Me_2EBC)$] (**1**), (B) $[Mn^{IV}(OH)_2(Me_2EBC)]^{2+}$ (**2**), and (C) $[Mn^{IV}(O)(OH)(Me_2EBC)]^{+}$ (**3**). Details regarding EXAFS fits are in Table 5.1.

Table 5.1. EXAFS Fitting Results for $[Mn^{II}(Cl_2)(Me_2EBC)]$ (**1**), $[Mn^{IV}(OH)_2(Me_2EBC)]^{2+}$ (**2**), and $[Mn^{IV}(O)(OH)(Me_2EBC)]^{+}$ (**3**).[a]

1		Mn−Cl			Mn−N			Mn···C			
	fit[b]	*n*	*r*(Å)	$\sigma^2 \times 10^3$ (Å^2)	*n*	*r*(Å)	$\sigma^2 \times 10^3$ (Å^2)	n	*r*(Å)	$\sigma^2 \times 10^3$ (Å^2)	F-factor
	1				6	2.36	1.73				0.497
	2	2	2.47	1.52	4	2.28	4.42				0.407
	4	2	2.47	1.70	4	2.30	4.48	4	3.22	3.20	0.383
	5	2	2.47	1.76	4	2.30	4.53	6	3.18	9.77	0.383
	9	***2***	***2.47***	***1.42***	***4***	***2.29***	***4.19***	***4***	***3.03***	***3.05***	***0.359***
								6	***3.21***	***2.78***	
2		Mn−O			Mn−N			Mn···C			
	fit[b]	*n*	*r*(Å)	$\sigma^2 \times 10^3$ (Å^2)	*n*	*r*(Å)	$\sigma^2 \times 10^3$ (Å^2)	n	*r*(Å)	$\sigma^2 \times 10^3$ (Å^2)	F-factor
	1				6	1.99	1.94				0.701
	2	2	1.79	1.04	4	2.08	3.30				0.502
	7	2	1.80	0.95	4	2.08	3.64	4	2.94	3.64	0.441
	8	***2***	***1.80***	***0.92***	***4***	***2.08***	***3.67***	***6***	***2.94***	***6.89***	***0.436***
3		Mn−O			Mn−N			Mn···C			
	fit[b]	*n*	*r*(Å)	$\sigma^2 \times 10^3$ (Å^2)	*n*	*r*(Å)	$\sigma^2 \times 10^3$ (Å^2)	n	*r*(Å)	$\sigma^2 \times 10^3$ (Å^2)	F-factor
	1	2	1.77	8.11	4	2.12	2.44				0.583
	2	1	1.71	1.49	4	2.11	2.56				0.572
		1	1.84	1.61							
	3	1	1.72	1.44	4	2.11	2.86	4	3.02	2.64	0.481
		1	1.84	1.21							
	4	1	1.72	1.45	4	2.11	2.83	5	3.02	4.03	0.487
		1	1.84	1.26							
	10	***1***	***1.71***	***1.53***	***4***	***2.11***	***2.68***	***4***	***2.88***	***4.04***	***0.468***
		1	***1.84***	***1.44***				***6***	***3.02***	***2.54***	

[a]Fourier transform ranges as follows: **1**: 2 – 14.5 Å^{-1} (resolution 0.126 Å); **2**: 2 – 14.8 Å^{-1} (resolution 0.123 Å); **3**: 2 – 14.8 Å^{-1} (resolution 0.123 Å). [b]The fit number is in reference to all fits considered, as presented in Appendix A.6 (Table A.5.1).

Table 5.2. Comparison of Mn-Ligand Bond Lengths from X-ray Diffraction (XRD), EXAFS fits and DFT Computations for $[Mn^{II}(Cl_2)(Me_2EBC)]$ (**1**), $[Mn^{IV}(OH)_2(Me_2EBC)]^{2+}$ (**2**), and $[Mn^{IV}(O)(OH)(Me_2EBC)]^{+}$ (**3**).

1[a]	XRD (Å)	EXAFS (Å)	DFT (Å)
Mn-Cl(1)	2.456(2)	2.47	2.509
Mn-Cl(2)	2.455(2)	2.47	2.509
Mn-N(3)	2.347(4)	2.29	2.436
Mn-N(4)	2.333(4)	2.29	2.436
Mn-N(5)	2.325(4)	2.29	2.367
Mn-N(6)	2.332(4)	2.29	2.367
2[b]			
Mn-OH(1)	1.811(2)	1.80	1.814
Mn-OH(2)	1.811(2)	1.80	1.814
Mn-N(3)	2.110(3)	2.08	2.205
Mn-N(4)	2.110(3)	2.08	2.205
Mn-N(5)	2.090(2)	2.08	2.139
Mn-N(6)	2.090(2)	2.08	2.139
3[c]			
Mn-O(1)		1.71	1.682
Mn-OH(2)		1.84	1.838
Mn-N(3)		2.11	2.156
Mn-N(4)		2.11	2.150
Mn-N(5)		2.11	2.184
Mn-N(6)		2.11	2.261

[a]XRD data from reference [54]. [b]XRD data from reference 27; DFT structure from reference 18. [c]DFT structure from reference 18.

The Fourier-transformed EXAFS spectrum of **2** exhibits a sharp peak centered at $R' \approx 1.6$ Å with less prominent peaks at $R' \approx 2.2$, 2.5, and 2.9 Å (Figure 5.2B). The prominent FT peak at ~1.6 Å arises from the first-coordination sphere and is best fit with two shells of N/O scatterers at distances of 1.80 Å, corresponding to the pair of hydroxo ligands, and 2.08 Å, corresponding to the four nitrogen atoms of the tetradentate Me_2EBC ligand (Table 5.1). These Mn−ligand distances compare quite favorably to the corresponding distances observed in the X-ray structure of **2**, which had Mn–OH and average Mn−N distances of 1.811 and 2.10 Å, respectively (Table 5.2).[27] The shorter Mn−N distances of **2** compared to **1** are expected given the increase in Mn oxidation state (from 2+ to 4+) and the concomitant reduction in ionic radius. The less-prominent FT peaks in the EXAFS spectrum of **2** at $R' \approx 2.2$ and 2.5 Å are best fit with a single shell of six

C atoms at 2.94 Å. In the X-ray diffraction structure of **2**, twelve C atoms of the ligand are located at Mn•••C distances ranging between 2.86 – 3.04 Å (average Mn•••C distance 2.97 Å) and two C atoms of the ligand are located at a Mn•••C distance of 3.47 Å.

With the limited stability of **3** in basic media, structural analysis by X-ray diffraction has not been possible.[45] Thus, the EXAFS data described here provide the first Mn−ligand bond lengths for **3**. The Fourier-transformed EXAFS spectrum of **3** exhibits a sharp peak centered at $R' \approx 1.7$ Å with a shoulder at ~2.0 Å and weaker features at 2.3, 2.6, and 3.2 Å (Figure 5.2C). The first coordination sphere of **3** is best fit with three shells of N/O atoms at distances of 1.71 (one O scatterer), 1.84 (one O scatterer), and 2.11 Å (four N scatterers). The shells at 1.71 and 1.84 Å are best fit with one oxygen atom each, corresponding to the oxo and hydroxo ligands, respectively. Fits with only a single shell of two O atoms resulted in a Mn–O distance of 1.77 Å with an unreasonably high Debye-Waller factor (8.11×10^{-3} Å^2; Fit 1 in Table 5.1). The EXAFS data for **3** also require two Mn•••C shells at 2.88 and 3.02 Å (4 and 6 C atoms, respectively).

Metric parameters from the EXAFS data of **3** are in good agreement with a structure derived from DFT computations (Table 5.2).[18] The DFT-optimized structure of **3** features a Mn=O distance of 1.682 Å, slightly shorter than the EXAFS-determined distance of 1.71 Å. The short Mn=O distance in **3**, as compared to the Mn−OH distances in **2**, is indicative of the expected Mn=O double-bond character and is consistent with Mn^{IV}=O bond lengths observed for other Mn(IV) centers with terminal oxo ligands (1.673 – 1.706 Å by DFT computations; 1.69 Å from EXAFS analysis).[10,15,16,20] The computed 1.838 Å Mn–OH bond length in **3** is in excellent agreement with the EXAFS-determined distance (1.84 Å). The DFT-computed model of **3** shows a longer Mn−N distance *trans* to the oxo ligand (2.261 Å), an expected outcome of the strong

donating ability of the oxo ligand. However, the EXAFS data for **3** are best fit with only a single shell of N scatterers, and thus, this computational prediction is not directly verifiable.

(B) X-ray Photoreduction of 3. Although **2** showed no evidence of photoreduction in twelve sequential scans on one spot of one sample, **3** was readily photoreduced under identical experimental conditions (at 20 K and with the same X-ray flux). Thus, the data described above were collected under conditions of reduced X-ray flux and by irradiating separate spots on the sample. Under conditions of high flux, photoreduction of **3** was evident by a 0.9 eV red-shift in the edge energy on the second scan (Figure 5.3). No shift was observed in the position of the pre-edge peak, but the intensity of this feature decreased in subsequent scans (Figure 5.3). In sequential scans, the edge energy red-shifted in approximately 0.3 eV increments and the pre-edge peak intensity continued to decrease. Photoreduction of high-valent Mn complexes has been observed previously.[1,6,7,15,28,65] Elegant XAS studies of the Mn_4Ca-containing OEC have shown that system to be very sensitive to X-ray photoreduction.[28] Indeed, upon X-ray irradiation, the XANES properties of the OEC convert from those characteristic of the oxo-bridged cluster to signals most consistent with aqueous Mn^{II}; *i.e.*, the cluster is almost completely destroyed upon prolonged X-ray irradiation. It is, to us, unexpected that the monocationic complex **3** should be *more* susceptible to X-ray photoreduction than the dicationic complex **2**. In addition, the dramatic change in photostability between **2** and **3**, which differ only by a H^+, was not anticipated. The observed experimental behavior underscores the need to use caution when performing X-ray studies of higher oxidation state manganese centers, as it is challenging to predict when photoreduction will readily occur.

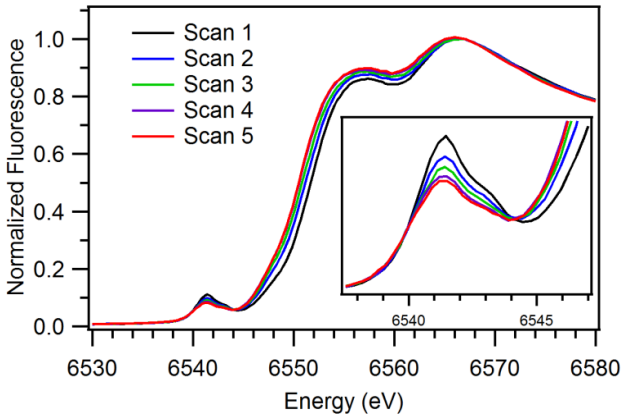

Figure 5.3. The Mn K-edge XANES spectra of **3** as it is photoreduced. Each trace represents the average of two scans collected from different sample spots.

(C) Experimental XANES Data. The Mn K-edge XANES of **1**, **2**, and **3** are shown in Figure 5.4 and summarized in Table 5.3. The XANES spectrum of the manganese(II) complex **1** displays a small pre-edge feature with low intensity at 6540.4 eV, and the intense rising edge feature at 6547.1 eV. The pre-edge and edge energies are consistent with other six-coordinate Mn^{II} complexes.[34] The energy of the edge and pre-edge features of **2** are respectively blue-shifted by almost 5 eV (6552.0 eV) and 0.6 eV (6541.0 eV) relative to **1**, as expected for the higher Mn oxidation state in **2**. In addition to the blue-shift in pre-edge energy, a notable increase in the pre-edge height is observed, and fits of the pre-edge region reveal a shoulder at 6543.2 eV (Figure A.5.3). The edge energy of **3** (6551.8 eV) is nearly equivalent to that of **2**, although the pre-edge peak of **3** (6541.2 eV) is double the intensity of that of **2** and has a resolved shoulder at 6543.3 eV (Table 5.3). As the intensity of the pre-edge features of both **2** and **3** are too great to arise from electric-quadrupole transitions,[66] their intensity likely derives through Mn 4p-3d mixing allowed by low symmetry distortions. Electric-dipole transitions carry an intensity two orders of magnitude greater than that of electric-quadrupole transitions.[66] Therefore, only a small

amount of 3d-4p mixing is required to cause a sizable increase in pre-edge peak intensity.[31] Because the Mn oxidation state and coordination number remain unchanged between **3** and **2**, the dramatic increase in pre-edge intensity for the former complex is attributed to the short Mn^{IV}=O distance of 1.71 Å (Table 5.2), which introduces a large deviation from centrosymmetry.

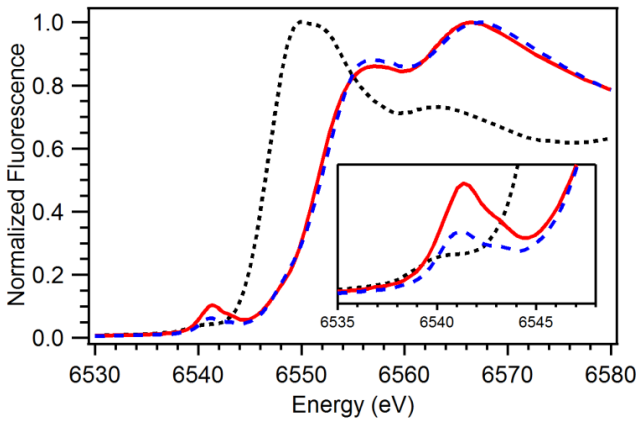

Figure 5.4. Mn K-edge XANES of $[Mn^{II}(Cl_2)(Me_2EBC)]$ (**1**; black, dotted line), $[Mn^{IV}(OH)_2(Me_2EBC)]^{2+}$ (**2**; blue, dashed line), and $[Mn^{IV}(O)(OH)(Me_2EBC)]^{+}$ (**3**; red, solid line) obtained at 20 K.

Table 5.3. Mn K-edge XANES Properties of $[Mn^{II}(Cl_2)(Me_2EBC)]$ (**1**), $[Mn^{IV}(OH)_2(Me_2EBC)]^{2+}$ (**2**), $[Mn^{IV}(O)(OH)(Me_2EBC)]^{+}$ (**3**) and other Mn^{IV}=O and Mn^{IV}–OH complexes (see Scheme 5.1).

	edge energy (eV)	pre-edge energy (eV)	pre-edge peak height[a]	area[b]	ref.
1	6547.1	6540.4	0.041	3.9	[c]
2	6552.0	6541.0	0.066	5.0	[c]
		6543.2	0.052	2.0	
3	6551.8	6541.2	0.103	10.5	[c]
		6543.3	0.072	3.7	
$[Mn^{IV}(O)(N4py)]^{2+}$	6550.8	6541.9	0.077	12.7	15
$[Mn^{IV}(O)(Bn\text{-}TPEN)]^{2+}$	NR[d]	6541.6	NR[d]	NR[d]	16
$[Mn^{IV}(O)(T_{piv}PP)]$	6551.2	~6541[e]	NR[d]	NR[d]	10
$[Mn^{IV}(O)(salen)]$	6549.9	6538.9	0.046	NR[d]	14
$[Mn^{IV}(OH)(salen)]^{+}$	6549.9	6539.0	0.044	NR[d]	14

[a]To permit comparison to the peak heights reported for other Mn^{IV}–OH and Mn^{IV}=O complexes, we have normalized each XANES spectrum with respect to the most intense fluorescence peak (see Figure 5.4). [b]Experimental areas have been multiplied by 100. [c]This work. [d]NR = not reported. [e]The pre-edge feature for this complex was reported as being "some 10 eV lower in energy than the edge"; see reference 10.

(D) Comparison of Experimental Pre-edge and Edge Energies. Only a few monomeric oxo- and hydroxo-manganese(IV) complexes have been studied by XAS, and all these complexes feature either a pseudo-octahedral or square pyramidal coordination geometry.[10,14-16] The structures of these complexes are shown in Scheme 5.1 and discussed in more detail in section 1.6.1 of Chapter 1. Although none of these complexes have been characterized crystallographically, their structures are inferred on the basis of spectroscopic data and, in some cases, DFT-derived models.

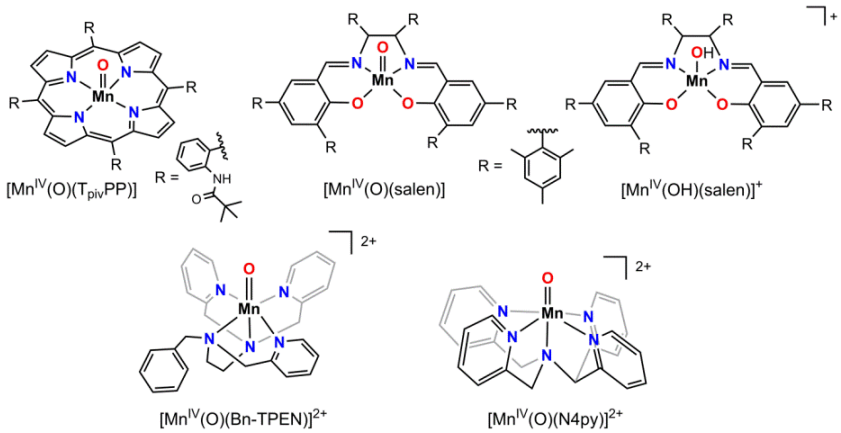

Scheme 5.1. Molecular structures of oxo- and hydroxo-manganese(IV) complexes. These structures are inferred on the basis of spectroscopic data and, in some cases, from models developed using DFT methods.

For this series of oxomanganese(IV) complexes, the observed pre-edge and edge energies span a range of 3 eV (6538.9 – 6541.9 eV) and approximately 2 eV (6549.9 – 6552.0 eV), respectively (see Table 5.3). The pre-edge energy decreases with the overall charge on the oxomanganese(IV) complex, with the highest energies observed for the dicationic complexes $[Mn^{IV}(O)(N4py)]^{2+}$ and $[Mn^{IV}(O)(Bn\text{-}TPEN)]^{2+}$ (6541.9 and 6541.6 eV, respectively).[15,16] The monocationic complex **3** shows only a marginally lower pre-edge peak energy (6541.2 eV), and

the neutral [Mn^{IV}(O)(salen)] complex has the lowest pre-edge energy by far (6538.9 eV). It should be noted, however, that the [Mn^{IV}(O)(salen)] XAS spectrum was calibrated to Cu foil, whereas the other oxomanganese(IV) complexes were calibrated either to the K-edge energy of the first inflection point of a manganese foil spectrum[10,14,15] or to the pre-edge peak maximum of a $KMnO_4$ powder spectrum.[16] Thus, the low pre-edge energy of [Mn^{IV}(O)(salen)] is potentially an artifact of calibration.

(E) Comparison of Experimental Pre-edge Intensities. Because the pre-edge peak height of **3** is nearly double that of **2** (0.103 and 0.066 for the height of the pre-edge peak maxima; see Table 5.3), it is unexpected that the pre-edge peak height of [Mn^{IV}(O)(salen)] is nearly equivalent to that of [Mn^{IV}(OH)(salen)]$^+$ (0.046 and 0.044, respectively). The similarities in peak height for these complexes is even more unusual given that EXAFS data for the [Mn^{IV}(O)(salen)] complex were fit to give a Mn=O distance of 1.58 Å (the corresponding Mn–OH distance in [Mn^{IV}(OH)(salen)]$^+$ is 1.83 Å).[14] The 1.58 Å distance is quite short for a Mn^{IV}=O species.[10,15,16] While a very pronounced pre-edge feature would be expected for such a short Mn^{IV}=O distance, mitigating factors such as the influence of the metal coordination environment or Mn-salen covalency could potentially modulate the pre-edge intensity. These complexities underscore the need for a combined experimental and theoretical analysis of Mn^{IV}=O complexes to investigate the physical basis for XANES properties.

5.3.2. TD-DFT-Computed XANES Spectra. (A) Calculated XANES Properties for 1, 2, and 3: General Considerations. To explore the performance of TD-DFT calculations for the XANES properties of Mn^{IV} centers, and to gain insight into the origin of pre-edge transitions for these complexes, we first compare the calculated Mn pre-edge features of **2** and **3** with those observed experimentally (calculations for complex **1** were also performed for comparison).

These complexes serve as excellent points for validation, as they are structurally characterized (**1** and **2** by XRD and EXAFS, and **3** by EXAFS alone), and the Mn-ligand distances obtained from DFT-optimized models are in excellent agreement with those determined experimentally (Table 5.2). TD-DFT calculations were performed using DFT-optimized models of **1**, **2**, and **3**. (Separate TD-DFT calculations using a model derived directly from XRD coordinates for **2** showed only minor differences when using XRD- versus DFT-derived models; see Figure A.5.4.) The calculated pre-edge spectra are compared to the corresponding experimental pre-edge spectra in Figure 5.5 (right and left, respectively). The XANES properties are summarized in Table 5.4. Using a previously described protocol, the calculated spectra were shifted 32.6 eV to higher energy to correct for systematic errors in the level of theory (*i.e.*, density functional, basis set, etc.).[34] For all three complexes, the TD-DFT-calculated XANES spectra consist of two features (Figure 5.5, right). The bands at lower energy (~6539 – 6544 eV) correspond to pre-edge Mn 1s-to-3d transitions. The bands above 6544 eV arise from metal-to-ligand charge-transfer (MLCT) transitions. In the experimental spectra, the MLCT transitions are often concealed within the rising edge, and, therefore, experimental energies are difficult to determine. Furthermore, the calculated energy for these transitions are highly dependent on the percentage of Hartree-Fock (HF) exchange incorporated into the density functional.[34] On the basis of these considerations, the MLCT transitions will not be addressed further.

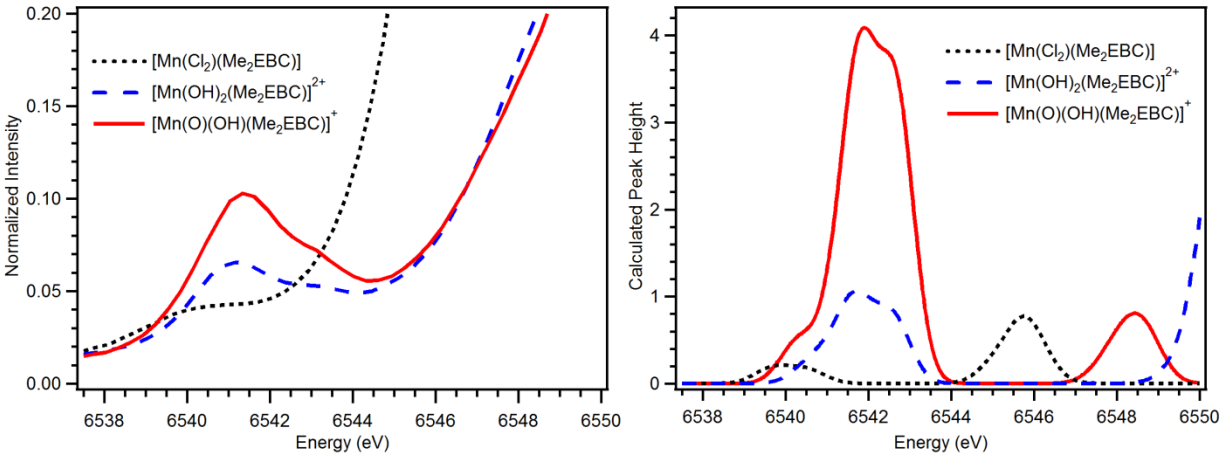

Figure 5.5. Experimental (left) and calculated (right) pre-edge regions of **1** (black, dotted line), **2** (blue, dashed line), and **3** (red, solid line). For the calculated spectra, a 32.6 eV energy shift and 1 eV Gaussian broadening were applied.

Table 5.4. Experimental and Calculated Pre-edge Energies (eV), Heights, Areas, Cacluated Mn 4p Character in Acceptor MOs, and Mn=O and Mn−OH Distances.

	Experimental[a]			Calculated				
Complex	Pre-edge Energy	Height	Area[b]	Pre-edge Energy[c]	Intensity[d]	Area[d]	Mn 4p (%) [f]	Distance Mn–O(H)
$[Mn^{II}(Cl_2)(Me_2EBC)]$	6540.4	0.041	3.9	6540.2	0.12	2.5	0.7	
$[Mn^{IV}(OH)_2(Me_2EBC)]^{2+}$	6541.0 6543.2	0.066 0.052	6.9	6541.7 6542.5	0.66	5.8	1.5	1.814[e]
$[Mn^{IV}(O)(OH)(Me_2EBC)]^{+}$	6541.2 6543.3	0.103 0.072	14.2	6541.9 6542.6	2.63	17.6	6.9	1.680 1.834[e]
$[Mn^{IV}(O)(N4py)]^{2+}$ [g]	6541.9	0.077	12.7	6542.4	2.21	15.1	5.4	1.673
$[Mn^{IV}(O)(Bn\text{-}TPEN)]^{2+}$ [h]	6541.6	NR	NR	6542.3	2.24	15.2	4.0	1.678
$[Mn^{IV}(O)(T_{piv}PP)]$ [i]	~6541	NR	NR	6542.0	4.33	27.8	19.9	1.662
$[Mn^{IV}(O)(salen)]$ [j]	6538.9	0.046	NR	6541.9	4.13	26.6	11.7	1.670
$[Mn^{IV}(OH)(salen)]^{+}$ [j]	6539.0	0.044	NR	6541.4	1.69	11.9	6.8	1.810[e]
$[Mn^{IV}(O)(salen)(C_3H_5N)]$				6542.3	3.05	20.1	3.3	1.675
$[Mn^{IV}(OH)(salen)(C_3H_5N)]^{+}$				6541.5 6542.3	0.87	7.0	1.8	1.818[e]
$[Mn^{IV}(O)(H_3buea)]^{-}$				6541.3 6542.3	2.62	17.5	13.5	1.715
$[Mn^{V}(O)(H_3buea)]$				6541.3 6542.8	3.18	20.9	13.1	1.696

[a]To permit comparison to the calculated peak heights, each XANES spectrum is normalized with respect to the most intense fluorescence peak. [b]Total pre-edge area multiplied by 100. [c]The calculated energy includes a 32.6 eV shift. [d]The calculated intensity and area determined as described in the experimental section and Appendix A.5. [e]Mn–OH distance. [f]Represents the sum of Mn 4p (%) for all of the acceptor MOs contributing to the transitions within the pre-edge envelope. [g]Experimental data from reference 15. [h]Experimental data from reference 16. [i]Experimental data from reference 10. [j]Experimental data from reference 14.

As the oxidation state of the Mn ion increased from +2 in **1** to +4 in **2** and **3**, the calculated pre-edge energies for **2** and **3** (6541.7 and 6541.9 eV, respectively) blue-shift relative to that of **1** (6540.2 eV). However, the TD-DFT calculations for **2** and **3** over-estimated the energy of the dominant pre-edge transition by 0.7 eV compared to experiment (Figure 5.5 and Table 5.4). In contrast, the experimental pre-edge areas of **2** and **3** (6.9 and 14.2, respectively) are in excellent absolute agreement with the calculated areas (5.8 and 17.6, respectively; Table 5.4). Although, the calculated intensity ratio for the pre-edge of **3** to **2** is overestimated

(calculated and experimental ratios are 4:1 and 2:1, respectively). A broader pre-edge peak is calculated for **3**, consistent with the experimental observation (Figure 5.5). Overall, the TD-DFT-calculated spectra are in excellent agreement with the experimental data. Given that the TD-DFT computations successfully reproduce the XANES properties of **1**, **2**, and **3**, it is warranted to use these calculations to more rigorously assign the pre-edge features of these complexes.

(B) Spectral Assignments for the XANES Region of 1. The electronic transitions contributing to the pre-edge feature in **1** can be well-understood by examining the Mn 3d orbital splitting pattern shown in Figure 5.6 (left). Because **1** is high-spin (S = 5/2), 1s-to-3d XAS transitions will originate in the 1s β-spin orbital and terminate in one of the five 3d β-spin orbitals, in each case giving a $(1s)^1(3d)^6$ excited configuration. Thus, five excited states can potentially contribute to the pre-edge region. As shown in Figure 5.6 (left), the β-spin 3d manifold of **1** is split in a pseudo-octahedral fashion, with the t_{2g}-type orbitals (98β, 99β, and 100β) approximately 1 eV below the e_g-type orbitals (103β and 105β). The 1 eV splitting of the t_{2g}- and e_g-derived orbitals is comparable to the 10Dq values of $[Mn^{II}(L)_6]^{n+}$ complexes with weak- to moderate-field ligands (L = Cl^-, H_2O, or ethylenediamine; 0.93, 1.05, 1.25 eV, respectively).[67] In the TD-DFT calculations, the pre-edge feature at ~6540.2 eV reflects the 3d orbital splitting pattern (Figure 5.5, right). Specifically, there are a set of three transitions at lower energy, contributing to the shoulder at 6539.7 eV (Figure A.5.5), that correspond to excitations into the unoccupied t_{2g}-derived orbitals (98β, 99β, and 100β). A set of two transitions at higher energy (6540.5 eV) arise from excitations into the unoccupied e_g-derived orbitals (103β and 105β). Together, the five acceptor molecular orbitals (MOs) contain <1% total Mn 4p character (Table 5.4). Thus, the pre-edge transitions gain minimal dipole-allowed intensity from Mn 3d–4p orbital mixing. The TD-DFT calculations provide excellent support for the

assignment that the pre-edge intensity in **1** arises predominantly from the electric-quadrupole mechanism.

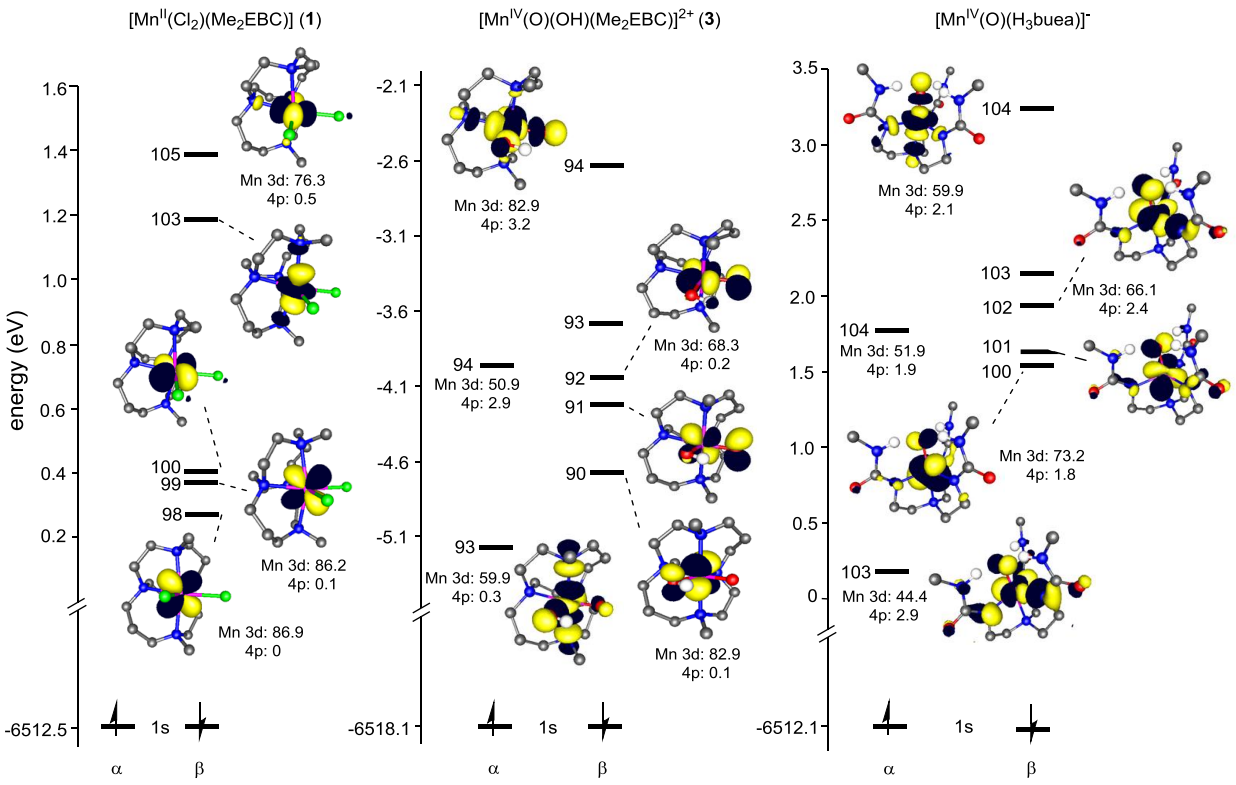

Figure 5.6. MO diagram of $[Mn^{II}(Cl_2)(Me_2EBC)]$ (**1**), $[Mn^{IV}(O)(OH)(Me_2EBC)]^+$ (**3**), and $[Mn^{IV}(O)(H_3buea)]^-$. The energies are for the spin unrestricted Kohn-Sham orbitals. The percent of Mn 3d and 4p character and representative surface contour plots for individual Kohn-Sham d orbitals are given.

(C) Spectral Assignments for the XANES Regions of 2 and 3. The 3d-orbital splitting patterns of **2** and **3** were discussed previously within the context of MCD investigations of these complexes.[18] Those results will be briefly summarized here to provide a framework for understanding the XANES data. Both **2** and **3** are high-spin (S = 3/2). Thus, the e_g-derived α-spin orbitals (93α and 94α for both **2** and **3**), and all β-spin Mn 3d-based orbitals, are unoccupied (see Figure 5.6, center, for the Mn 3d orbital splitting for **3**). The e_g-derived MOs are split

considerably in both complexes. For **2**, the $3d_{xy}$ MO, which is σ-antibonding with both hydroxide ligands, is highest in energy (in this complex, the *y*-axis bisects the HO–Mn–OH angle).[18] For **3**, a strong σ-antibonding interaction with the oxo ligand along the *z*-axis (the Mn=O vector) pushes the $3d_{z^2}$ MO above the $3d_{x^2-y^2}$ MO (Figure 5.6, center). Complex **3** also displays a larger splitting of the t_{2g}-derived MOs compared to **2**, which reflects the strong π-donating properties of the oxo ligand. For both complexes, the α-spin (majority spin) Mn 3d orbitals are stabilized by ~1.3–1.9 eV relative to their β-spin counterparts because of spin polarization due to electron exchange.

For the dihydroxo complex **2**, excitations of Mn 1s-α and 1s-β electrons into the respective α- and β-$3d_{xy}$ orbitals (94α and 94β) contribute ~80% of the intensity of the pre-edge feature. These transitions are split by 1 eV (6541.6 and 6542.6 eV, respectively) due to the exchange stabilization of the α-spin manifold. The pre-edge feature of **2** gains additional intensity (<20%) from excitations into the α- and β-$3d_{z^2}$ orbitals at 6541.1 and 6541.8 eV, respectively (93α and 93β). Excitations terminating in the d_{xy} MOs are more intense because of the higher percentage of Mn 4p character in the $3d_{xy}$ MOs (1.2%) than the $3d_{z^2}$ MOs (0.3%). This increased mixing renders the calculated oscillator strengths for the transitions into the $3d_{xy}$ orbitals an order of magnitude greater than those involving the $3d_{z^2}$ orbitals (Table A.5.2). The low-energy shoulder in the pre-edge feature of **2** (Figure 5.5, right) arises from three weak transitions corresponding to excitations into the unoccupied β-$3d_{xz}$, $3d_{yz}$, and $3d_{xy}$ orbitals that contain minimal 4p character (<0.1%).

For the oxohydroxo complex **3**, the pre-edge feature derives ~90% of its intensity from two transitions into the unoccupied α-and β-$3d_{z^2}$ orbitals (6541.8 and 6542.7 eV, respectively). The acceptor orbitals (94α and β) contain a relatively large admixture of Mn 4p character

(6.1%), giving significant dipole-allowed intensity. This accounts for the calculated pre-edge intensity of **3** being nearly four times that of **2** (Table 5.4).

In summary, the different XANES properties of **2** and **3** can be directly understood on the basis of 4p-mixing into the respective Mn–OH ($3d_{xy}$) and Mn=O ($3d_{z^2}$) orbitals. Only minor (<20%) pre-edge intensity derives from excitations into Mn π-type MOs. To determine how these specific results are affected by perturbations in ligand type, as well as the geometry of the Mn center, we extended our computational investigations to a series of Mn^{IV}=O and Mn^{IV}–OH complexes (Scheme 5.1).

(D) TD-DFT XANES Calculations for Other Mn^{IV}=O and Mn^{IV}–OH Complexes: General Considerations. DFT calculations were used to obtain structural models of $[Mn^{IV}(O)(N4py)]^{2+}$ and $[Mn^{IV}(O)(Bn\text{-}TPEN)]^{2+}$ (six-coordinate);[15,16] $[Mn^{IV}(O)(salen)]$, $[Mn^{IV}(OH)(salen)]^{+}$, and $[Mn^{IV}(O)(T_{piv}PP)]$ (five-coordinate, square pyramidal);[10,14] and $[Mn^{IV}(O)(H_3buea)]^{-}$ (five-coordinate, trigonal bipyramidal).[20] Although no crystal structures are available for comparison, EXAFS distances have been reported for the majority of these complexes.[10,14-16] With few exceptions, the DFT-computed metric parameters are in excellent agreement with the experimental distances (Table 5.5 and A.5.3). The most egregious deviation between experiment and theory is the Mn^{IV}=O distance of $[Mn^{IV}(O)(salen)]$; the DFT-computed distance of 1.670 Å is significantly longer than the 1.58 Å obtained from EXAFS analysis.[14] The 1.58 Å EXAFS distance for $[Mn^{IV}(O)(salen)]$ is more consistent with a tetragonal oxomanganese(V) unit (1.55 – 1.56 Å from X-ray crystallographic and EXAFS studies),[23-26,35] and it is hard to reconcile this exceptionally short bond length with both the computational result and the range of EXAFS distances for other oxomanganese(IV) species (1.69 - 1.71 Å; see Tables 5.5 and 5.2). We note that previous studies have shown that the DFT level of theory used

here is quite accurate for the short M=O distances of high-valent metal-oxo species.[40,68,69] Therefore, in our discussion of the XANES properties of [Mn^{IV}(O)(salen)], we assume that the DFT distance is reliable.

Table 5.5. Manganese-Ligand Bond Lengths (Å) for DFT-Optimized Models of Mn^{IV}=O and Mn^{IV}–OH Complexes Parameters.

Complex	Mn–O(H)[a]	Mn–N_{eq}[a,b]	Mn–N_{ax}[a,c]	Mn–O[a,d]	Ref
[Mn^{IV}(O)(N4py)]$^{2+}$	1.673 (1.69)	2.02 (2.00)	2.14 (2.24)		15
[Mn^{IV}(O)(Bn-TPEN)]$^{2+}$	1.678 (1.69)	2.07 (2.04)	2.19 (2.40)		16
[Mn^{IV}(O)(T_{piv}PP)]	1.662 (1.69)	2.01 (2.00)			10
[Mn^{IV}(O)(salen)]	1.670 (1.58)	1.99 (1.99)		1.90 (1.81)	14
[Mn^{IV}(O)(salen)(CH_3CH_2CN)]	1.675	1.96	2.31	1.93	
[Mn^{IV}(OH)(salen)]$^{+}$	1.810 (1.83)[e]	1.98 (1.98)		1.85 (1.83)	14
[Mn^{IV}(OH)(salen)(CH_3CH_2CN)]$^{+}$	1.818[e]	1.99	2.13	1.87	
[Mn^{IV}(O)(H_3buea)]$^{-}$	1.715	1.98	2.17		
[Mn^{V}(O)(H_3buea)]	1.696	1.89	2.13		

[a]Distances determined from analysis of EXAFS data are provided in parenthesis. [b]Average Mn–N_{eq} (equatorial) distance. [c]Mn–N_{ax} (axial) distance. [d]Average Mn–O (phenolate) distance. [e]Mn^{IV}–OH distance.

TD-DFT-computed XANES properties for all five complexes are shown in Figure 5.7 and summarized in Table 5.4. Some general trends can be immediately noted. All calculated pre-edge energies are in good agreement with the experimental values; most deviations are less than 1 eV. Larger deviations are observed for the [Mn^{IV}(O)(salen)] and [Mn^{IV}(OH)(salen)]$^{+}$ complexes, but this could be related to the different energy calibration protocol used for these complexes (*vide supra*). With regard to pre-edge intensity, the most intense features are predicted for [Mn^{IV}(O)(salen)] and [Mn^{IV}(O)(T_{piv}PP)]. This is expected, given that the lack of a ligand *trans* to the oxo in these square pyramidal complexes introduces a large deviation from centrosymmetry along this axis. The complexes [Mn^{IV}(O)(N4py)]$^{2+}$, [Mn^{IV}(O)(Bn-TPEN)]$^{2+}$, and [Mn^{IV}(O)(H_3buea)]$^{-}$ all have similar peak heights (Table 5.4), although the last complex shows a much broader pre-edge signal, and, therefore, a greater pre-edge area (Figure 5.7). Finally, the Mn^{IV}–OH complex [Mn^{IV}(OH)(salen)]$^{+}$ displays the smallest pre-edge peak area.

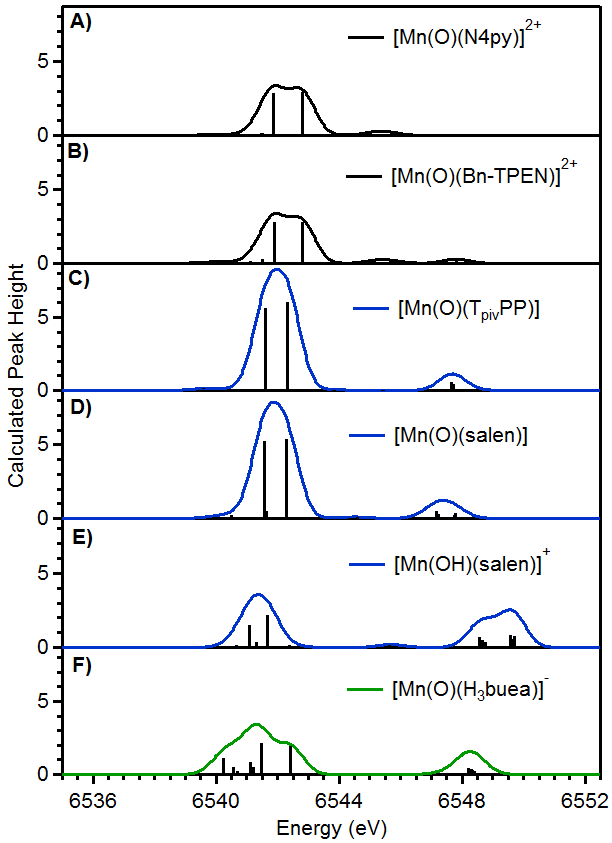

Figure 5.7. TD-DFT calculated XANES spectra for A) $[Mn^{IV}(O)(N4py)]^{2+}$, B) $[Mn^{IV}(O)(Bn\text{-}TPEN)]^{2+}$, C) $[Mn^{IV}(O)(T_{piv}PP)]$, D) $[Mn^{IV}(O)(salen)]$, E) $[Mn^{IV}(OH)(salen)]^{+}$, and F) $[Mn^{IV}(O)(H_3buea)]^{-}$. Sticks mark individual electronic transitions. Note that the same y-scale is used for all plots.

(E) Spectral Assignments for the XANES Spectra of $[Mn^{IV}(O)(T_{piv}PP)]$ and $[Mn^{IV}(O)(salen)]$. The calculated pre-edge intensities for the square pyramidal $[Mn^{IV}(O)(T_{piv}PP)]$ and $[Mn^{IV}(O)(salen)]$ complexes arise predominantly (>90%) from excitations into the α- and β-d_{z^2} orbitals (Mn^{IV}=O σ* MO). These acceptor MOs contain 11 - 20% Mn 4p character (Table 5.4). The lack of pseudo-inversion symmetry along the Mn=O axis greatly increases $3d_{z^2}$-$4p_z$ mixing, and, thus, pre-edge intensity. Consequently, $[Mn^{IV}(O)(T_{piv}PP)]$ and $[Mn^{IV}(O)(salen)]$ show a nearly two-fold increase in pre-edge height compared to six-

coordinate oxomanganese(IV) complexes (Figure 5.7), which arises from an increase in 3d-4p mixing by a factor of 2 - 3 (Table 5.4).

(F) Spectral Assignments for the XANES Spectra of $[Mn^{IV}(O)(N4py)]^{2+}$ and $[Mn^{IV}(O)(Bn\text{-}TPEN)]^{2+}$. The calculated pre-edge energies of $[Mn^{IV}(O)(N4py)]^{2+}$ and $[Mn^{IV}(O)(Bn\text{-}TPEN)]^{2+}$ are at higher energy, and with lower intensity, than that of **3**, fully consistent with the experimental data (Table 5.4).[15,16] For both $[Mn^{IV}(O)(N4py)]^{2+}$ and $[Mn^{IV}(O)(Bn\text{-}TPEN)]^{2+}$, the Mn $3d_{z^2}$ MO is highest in energy due to a strong σ-antibonding interaction with the oxo ligand. Similar to the other oxomanganese(IV) complexes, excitations into the unoccupied α- and β-$3d_{z^2}$ orbitals (Mn^{IV}=O σ* MOs) give rise to two dominant transitions split by 0.9 eV that contribute >90% of the intensity to the pre-edge feature (Table A.5.4). The acceptor d_{z^2} orbitals for $[Mn^{IV}(O)(N4py)]^{2+}$ contain a smaller admixture of Mn 4p character than **3** (5.4 and 6.9%, respectively), consistent with the lower experimental pre-edge peak height of $[Mn^{IV}(O)(N4py)]^{2+}$ than that of **3** (0.077 and 0.103, respectively; Table 5.4). The pre-edge intensity for $[Mn^{IV}(O)(Bn\text{-}TPEN)]^{2+}$ was not reported and thus cannot be compared here.[16]

(G) Spectral Assignments for the XANES Spectra of $[Mn^{IV}(O)(H_3buea)]^-$. Although XAS data have not been reported for $[Mn^{IV}(O)(H_3buea)]^-$, its inclusion in our computational investigations is important, as this complex represents a rare example of a Mn^{IV}=O unit in a trigonal bipyramidal geometry. This geometry gives rise to a Mn 3d orbital splitting pattern distinct from that of **3** and other Mn^{IV}=O units in an octahedral or square pyramidal geometry. The DFT-derived 3d MO splitting pattern for $[Mn^{IV}(O)(H_3buea)]^-$ shows a deviation from that expected for a complex with idealized C_{3v} symmetry (Figure 5.6, right). In this idealized geometry, the $3d_{z^2}$ orbital (Mn^{IV}=O σ* MO; 104β) would lie above two sets of *e*-type orbitals:

$3d_{x^2-y^2}$, $3d_{xy}$ (Mn^{IV}–N_{eq} σ*; 103β and 102β); and $3d_{xz}$, $3d_{yz}$ (Mn^{IV}=O π*; 101β and 100β). For an S = 3/2 system such as $[Mn^{IV}(O)(H_3buea)]^-$, this splitting would give a Jahn-Teller active ^4E ground state, which arises from the $(e)^2(e)^1$ electron configuration. Jahn-Teller distortions are noted in the asymmetric Mn^{IV}–N_{eq} bond lengths and N_{eq}–Mn^{IV}–N_{eq} angles in the DFT model of $[Mn^{IV}(O)(H_3buea)]^-$ (Table A.5.6). Inequivalent Mn^{IV}–N_{eq} bond lengths and N_{eq}–Mn^{IV}–N_{eq} angles were also evident in a previously described DFT structure of $[Mn^{IV}(O)(H_3buea)]^-$.[20] These distortions break the degeneracy of two sets of *e* orbitals, as shown in Figure 5.6 (right). In addition, mixing of the parent *e* orbitals leads to a small amount of oxo π-character in the $3d_{x^2-y^2}$ and $3d_{xy}$ MOs (103β and 102β).

This bonding pattern, which is distinct from that of **3** (Figure 5.6, center) leads to a XANES spectrum broader than those of octahedral or square pyramidal Mn^{IV}=O compounds (Figure 5.7). The XANES spectra of those complexes are completely dominated by excitations terminating in the α- and β-d_{z^2} orbitals (Mn^{IV}=O σ^*). These excitations are split by 0.9 eV, which defines the width of the pre-edge feature. For $[Mn^{IV}(O)(H_3buea)]^-$, the TD-DFT calculations predict a broad (~3 eV) pre-edge feature with intense peaks at 6541.3 and 6542.3 eV, and a shoulder at 6540.2 eV (Figure 5.7F and Table 5.4). The two peaks at highest energy correspond to excitations to the α- and β-$3d_{z^2}$ orbitals (104α and 104β; Mn^{IV}=O σ*) that contain 4% total Mn 4p character. The shoulder at 6540.2 eV arises from a transition terminating in the α-$3d_{x^2-y^2}$ MO (103α) that contains 2.9% Mn 4p character. Although there is less Mn 4p character in the α- and β-d_{z^2} orbitals in $[Mn^{IV}(O)(H_3buea)]^-$ than in six-coordinate oxomanganese(IV) complexes, the trigonal symmetry allows for $4p_{x,y}$ mixing into the $3d_{xy}$ and $3d_{x^2-y^2}$ orbitals. Thus, the broader pre-edge feature of $[Mn^{IV}(O)(H_3buea)]^-$ is due to the presence of excitations terminating in the

$3d_{xy}$ and $3d_{x^2-y^2}$ orbitals, which gain electric dipole character and cause a distribution of pre-edge intensity over a larger number of transitions that span a wider range of energy. Importantly, the related Fe^{III} complex, $[Fe^{III}(O)(H_3buea)]^{2-}$, shows a broad pre-edge feature (~3 eV) in the experimental XANES spectrum that is likely of similar origin.[55]

5.4. Discussion.

Mn K-edge XAS has been used for decades to aid in the characterization of biological and synthetic manganese complexes. In particular, this technique has played a critical role in defining manganese-ligand distances for oxomanganese(IV) complexes.[10,12-16] In this study, Mn K-edge XAS was used to determine metric parameters, and to explore the XANES properties of a manganese(II) and two manganese(IV) complexes supported by the tetradentate Me_2EBC ligand. Specifically, the first structural data for $[Mn^{IV}(O)(OH)(Me_2EBC)]^+$ (**3**) were obtained from EXAFS fits. This analysis revealed a Mn=O distance of 1.71 Å and a Mn–OH distance of 1.84 Å, in excellent agreement with the previously reported DFT structure.[18] Thus, these data permit the unambiguous identification of this species as a rare example of an oxohydroxomanganese(IV) complex, corroborating previous assignments.[18,22,27] This work also allowed for a direct structural and XANES comparison between Mn^{IV}=O and Mn^{IV}–OH adducts (**2** and **3**, respectively) that differ by only a proton. TD-DFT calculations reveal that the different XANES properties of **2** and **3** can be directly understood on the basis of 4p-mixing into the Mn $3d_{xy}$ and $3d_{z^2}$ orbitals, respectively, that reflect the dominant hydroxo- and oxo-manganese σ-interactions. In contrast, the weak pre-edge peak of the manganese(II) complex **1** is due solely to electric-quadrupole allowed 1s-to-3d transitions; *i.e.*, Mn 3d-4p mixing is so minor as to not introduce significant dipole-character in these transitions.

5.4.1. Correlation between XANES Properties and Geometric Structure for Mn^{IV}=O and Mn^{IV}–OH Complexes. Oxomanganese(IV) complexes exhibit moderately intense pre-edge features that have been qualitatively linked to short Mn=O distances that range from 1.67 - 1.71 Å.[12-14] This trend is illustrated in Figure 5.8 (top), where the TD-DFT-calculated pre-edge areas are compared with the DFT-calculated Mn–O distance of Mn^{IV}=O and Mn^{IV}–OH complexes. In general, the calculated pre-edge areas decrease as the Mn–O distance increases. The spectral assignments afforded by the TD-DFT computations provide insights into the basis for this correlation. The pre-edge features of oxomanganese(IV) complexes are dominated by excitations to the Mn=O σ* MOs (the Mn $3d_z^2$ MOs), as these orbitals contain an appreciable admixture of Mn 4p character. However, the extent of 3d-4p mixing is modulated by both the Mn=O (or Mn^{IV}–OH) distance *and* the Mn coordination geometry. Thus, a better correlation is observed between the calculated pre-edge area and the sum of Mn 4p character (%) in all acceptor MOs (Figure 5.8, bottom), as the latter parameter is reflective of the entire Mn^{IV} ligand field and not just the Mn–O distance. Two points of comparison well-illustrate this point. First, for both oxo- and hydroxomanganese(IV) adducts, the calculated pre-edge area of square pyramidal complexes (blue squares, Figure 5.8, top) is greater than that of six-coordinate complexes with similar Mn–O distances by roughly a factor of two (black circles, Figure 5.8, top). This is because the greatest Mn $3d_z^2$-$4p_z$ mixing is observed for the square pyramidal complexes that lack a ligand *trans* to the oxo. Second, the calculated pre-edge area of a square pyramidal Mn^{IV}–OH adduct (11.9) is only slightly lower than that of pseudo-octahedral Mn^{IV}=O adducts (15.1 - 17.6). On the basis of these comparisons, the assignment of Mn^{IV}–OH versus Mn^{IV}=O motifs using XANES data alone is not advisable.

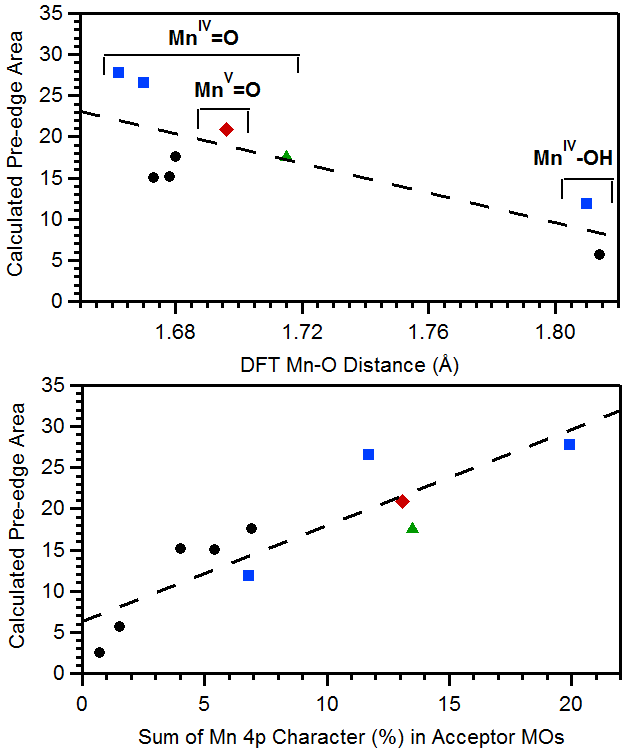

Figure 5.8. Calculated pre-edge area as a function of Mn–O distance in the DFT-optimized structures (top) and of the total Mn 4p character in the acceptor MOs for the electronic transitions within the pre-edge peak (bottom, see Table 5.4). Black circles mark data for **1**, **2**, **3**, $[Mn^{IV}(O)(N4py)]^{2+}$, and $[Mn^{IV}(O)(Bn\text{-}TPEN)]^{2+}$; blue squares mark data for $[Mn^{IV}(O)(salen)]$, $[Mn^{IV}(OH)(salen)]^{+}$, and $[Mn^{IV}(O)(T_{piv}PP)]$; the green triangle marks data for $[Mn^{IV}(O)(H_3buea)]^{-}$; and the red diamond marks data for $[Mn^{V}(O)(H_3buea)]$.

Importantly, the Mn^{IV} geometry also influences the breadth of the pre-edge feature. For the six-coordinate oxomanganese(IV) complexes, the total breadth of the calculated pre-edge features are around 1 eV and reflect the exchange stabilization of the majority-spin orbitals relative to their minority-spin counterparts. In contrast, the trigonal bipyramidal oxomanganese(IV) complex $[Mn^{IV}(O)(H_3buea)]^{-}$ shows a pre-edge peak with an area similar to that of the six-coordinate oxomanganese(IV) complexes, but with a breadth of around 3 eV. This is because $[Mn^{IV}(O)(H_3buea)]^{-}$ displays total 3d-4p mixing on par with that of the square pyramidal complexes; however, the 4p character is more evenly distributed throughout the 3d

manifold. Although experimental XANES data for a trigonal bipyramidal oxomanganese(IV) complex have not yet been reported, our computations predict such a species could be expected to show a pre-edge area similar to that of square pyramidal Mn^{IV}=O complexes, but with a smaller pre-edge height. These considerations highlight the importance of reporting pre-edge area, and not height of pre-edge maxima, when comparing pre-edge features of different complexes.

5.4.2. Pre-edge Energies and Intensities: Experiment *versus* Theory. In general, the experimental XANES properties for the nine Mn^{IV} complexes investigated in this study are well reproduced using a TD-DFT method initially calibrated using a large test set of Mn^{II} and Mn^{III} complexes.[34] To better judge the success of this correlation in the present case, experimental and calculated pre-edge peak energies and areas are compared in Figures 5.9 and 5.10, respectively. A linear correlation, albeit with some scatter, is observed between the experimental and calculated pre-edge energies of **1**, **2**, **3**, $[Mn^{IV}(O)(N4py)]^{2+}$, and $[Mn^{IV}(O)(Bn\text{-}TPEN)]^{2+}$. The calculated pre-edge energies for **2**, **3**, $[Mn^{IV}(O)(N4py)]^{2+}$, and $[Mn^{IV}(O)(Bn\text{-}TPEN)]^{2+}$ are systematically over-estimated by approximately 0.5 eV relative to experiment (Figure 5.9 and Table 5.4). The $[Mn^{IV}(O)(salen)]$ and $[Mn^{IV}(OH)(salen)]^{+}$ complexes are large outliers to this trend, as the experimental energies are nearly 2 eV lower than the theoretical values. The most likely explanation for this deviation is the use of a different method for energy calibration of the XAS data. The $[Mn^{IV}(O)(salen)]$ and $[Mn^{IV}(OH)(salen)]^{+}$ samples were calibrated to Cu foil,[14] whereas the other oxomanganese(IV) samples were calibrated either to manganese foil[10,14,15] or to $KMnO_4$ powder.[16] An alternate explanation would be that the $[Mn^{IV}(O)(salen)]$ and $[Mn^{IV}(OH)(salen)]^{+}$ samples underwent photoreduction during X-ray irradiation.

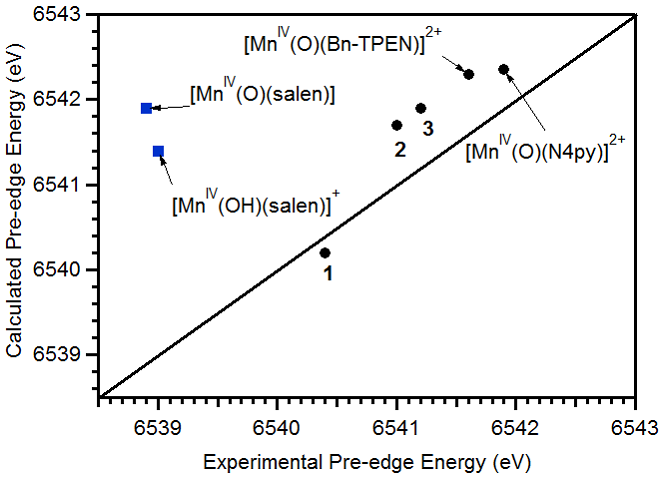

Figure 5.9. Correlation between the calculated pre-edge energy (with the +32.6 eV energy correction) and the experimental pre-edge energy for $[Mn^{II}(Cl_2)(Me_2EBC)]$ (**1**), $[Mn^{IV}(OH)_2(Me_2EBC)]^{2+}$ (**2**), $[Mn^{IV}(O)(OH)(Me_2EBC)]^{+}$ (**3**), $[Mn^{IV}(O)(N4py)]^{2+}$, $[Mn^{IV}(O)(Bn\text{-}TPEN)]^{2+}$, $[Mn^{IV}(O)(salen)]$ and $[Mn^{IV}(OH)(salen)]^{+}$.

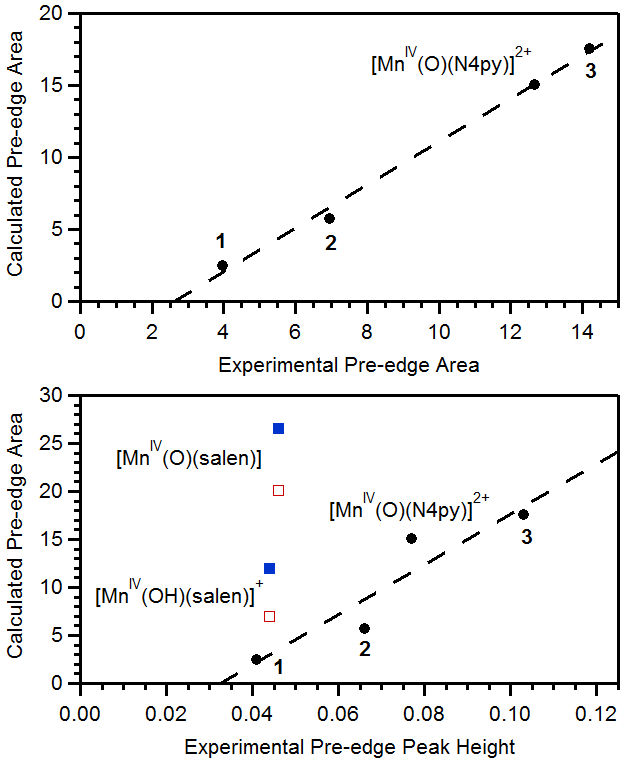

Figure 5.10. Correlation between the calculated pre-edge intensity and experimental area of the pre-edge peaks (top) for complexes $[Mn^{II}(Cl_2)(Me_2EBC)]$ (**1**), $[Mn^{IV}(OH)_2(Me_2EBC)]^{2+}$ (**2**), $[Mn^{IV}(O)(OH)(Me_2EBC)]^{+}$ (**3**), and $[Mn^{IV}(O)(N4py)]^{2+}$ and pre-edge peak height (bottom). Also included in bottom panel are model complexes $[Mn^{IV}(O)(salen)]$ (blue solid square), $[Mn^{IV}(OH)(salen)]^{+}$ (blue solid square), $[Mn^{IV}(O)(salen)(CH_3CH_2CN)]$ (red open square), and $[Mn^{IV}(OH)(salen)(CH_3CH_2CN)]^{+}$ (red open square).

An excellent correlation, with minimal scatter, is also obtained between the calculated pre-edge areas and experimental areas of **1**, **2**, **3**, and $[Mn^{IV}(O)(N4py)]^{2+}$ (Figure 5.10, top). These are the only compounds examined in this study for which the areas of pre-edge peaks were determined. For other complexes, only pre-edge peak heights were reported.[14] Because of the variable widths of the pre-edge features, the pre-edge area is a far better parameter with which to assess the agreement with experiment. Nonetheless, a linear correlation, albeit with more scatter, is also observed between the calculated areas and experimental pre-edge peak heights for **1**, **2**, **3**, and $[Mn^{IV}(O)(N4py)]^{2+}$ (Figure 5.10, bottom). Although the experimental pre-edge peak height

for $[Mn^{IV}(OH)(salen)]^+$ is low compared to the theoretically predicted value, it is near the border of the scatter of the observed correlation. However, the low experimental height for $[Mn^{IV}(O)(salen)]$ is clearly an outlier.

On the basis of the cumulative experimental and theoretical findings discussed in this work, it is hard to reconcile the small experimental pre-edge intensity of $[Mn^{IV}(O)(salen)]$ with the EXAFS-determined bond length of 1.58 Å, just as it is hard to reconcile this short distance with the DFT-derived model of $[Mn^{IV}(O)(salen)]$ (Table 5.5). The distance in the DFT-optimized structure (1.670 Å) is consistent with that of other Mn^{IV}=O complexes. In an attempt at reconciliation, we developed additional models of $[Mn^{IV}(O)(salen)]$ and $[Mn^{IV}(OH)(salen)]^+$ that included a coordinated solvent ligand (propionitrile, CH_3CH_2CN) *trans* to the oxo. As shown in Figure 5.10 (red open squares; bottom), and summarized in Table 5.4, the inclusion of the *trans* solvent ligand lowers the predicted pre-edge areas for both complexes. For $[Mn^{IV}(OH)(salen)(CH_3CH_2CN)]^+$, the predicted pre-edge area is now quite consistent with the correlation observed for the other complexes. However, for $[Mn^{IV}(O)(salen)(CH_3CH_2CN)]$, the relationship between the calculated pre-edge area and the experimental pre-edge peak height is still an outlier. In addition, the inclusion of the *trans* solvent ligand leads to a slight elongation in the Mn^{IV}=O bond length (Table 5.4), rather than a contraction.

5.4.3. Comparison to Oxomanganese(V) Systems. It is useful to frame the results of the present study within the context of high-valent oxomanganese species in general. In particular, the Mn K-edge XANES properties of S = 0 oxomanganese(V) adducts have been the subject of several experimental and/or theoretical studies.[35-38] That work has revealed a strong correlation between pre-edge intensity and coordination geometry.[37] For example, square pyramidal oxomanganese(V) species show incredibly intense pre-edges features, much more intense than

those of oxomanganese(IV) adducts.[36] The absence of such signals during time-resolved XAS studies of the S_3 to S_4 transition of the OEC suggests that a square pyramidal oxomanganese(V) adduct is not involved in water oxidation.[70] However, as described by Yano and co-workers, reduced Mn 3d-4p mixing in six-coordinate oxomanganese(V) adducts gives rise to much weaker edges when compared to that of their square pyramidal analogues.[37] Our present work on oxo- and hydroxomanganese(IV) complexes underscores the conclusions of Yano *et al.* that "caution must be exercised in using the pre-edge spectrum as an isolated signature of oxidation state".[37]

To date, XANES studies on oxomanganese(V) complexes have been limited to low-spin (S = 0) oxomanganese(V) adducts with tetragonal symmetry (*i.e.*, pseudo-octahedral or square pyramidal geometry).[35-38] Recently, Borovik and co-workers have described the first example of a high-spin (S = 1) oxomanganese(V) species, $[Mn^{V}(O)(H_3buea)]$.[71] Given that this complex could have considerably different XANES properties than its low-spin (S = 0) counterparts, we applied the TD-DFT protocol to predict the pre-edge properties of this species.

The DFT-optimized structure of $[Mn^{V}(O)(H_3buea)]$ displays C_{3v} symmetry, with equivalent $Mn^{V}–N_{eq}$ distances and $N_{eq}–Mn^{V}–N_{eq}$ angles of 1.885 Å and 118.35º (Figure 5.11, right). The $Mn^{V}–N_{eq}$ bond lengths are reduced considerably compared to the $[Mn^{IV}(O)(H_3buea)]^{-}$ complex. The Mn 3d orbital splitting diagram of $[Mn^{V}(O)(H_3buea)]$ (Figure A.5.7) shows a trigonal ligand-field splitting of the Mn 3d orbitals, confirming the qualitative orbital splitting pattern predicted by Borovik and co-workers.[71] This splitting pattern gives rise to a $^3A_2$ ground state, from the $(e)^2$ configuration, and thus this complex is not subject to a Jahn-Teller distortion. Importantly, the Mn–oxo distance in $[Mn^{V}(O)(H_3buea)]$ is reduced by less than 0.02 Å compared to that of $[Mn^{IV}(O)(H_3buea)]^{-}$ (1.696 and 1.715 Å, respectively). The small perturbation in the

Mn-oxo distance reflects the fact that the Mn=O π* MOs ($3d_{xz}$, and $3d_{yz}$) are singly-occupied in both the $[Mn^{V}(O)(H_3buea)]$ and $[Mn^{IV}(O)(H_3buea)]^-$ complexes.

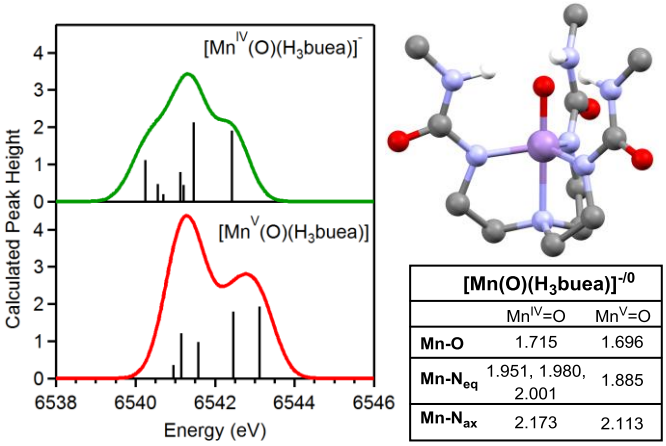

[Mn(O)(H$_3$buea)]$^{-/0}$		
	Mn^{IV}=O	Mn^{V}=O
Mn-O	1.715	1.696
Mn-N$_{eq}$	1.951, 1.980, 2.001	1.885
Mn-N$_{ax}$	2.173	2.113

Figure 5.11. Comparison of TD-DFT calculated XANES spectra for $[Mn^{IV}(O)(H_3buea)]^-$ (green trace, top) and $[Mn^{V}(O)(H_3buea)]$ (red trace, bottom). Sticks mark individual electronic transitions. The optimized structure of $[Mn^{V}(O)(H_3buea)]$, along with the key metric parameters for $[Mn^{IV}(O)(H_3buea)]^-$ and $[Mn^{V}(O)(H_3buea)]$ (Table A.5.6), are presented on the right.

The calculated XANES spectrum of $[Mn^{V}(O)(H_3buea)]$ reveals two pre-edge peaks at 6541.3 and 6542.8 eV (Figure 5.11, left). The pre-edge maxima for both $[Mn^{IV}(O)(H_3buea)]^-$ and $[Mn^{V}(O)(H_3buea)]$ are calculated to be at 6451.3 eV, despite the higher oxidation state of Mn in $[Mn^{V}(O)(H_3buea)]$. However, the intensity of this band derives from a different set of pre-edge transitions in $[Mn^{V}(O)(H_3buea)]$ than for $[Mn^{IV}(O)(H_3buea)]^-$. For $[Mn^{IV}(O)(H_3buea)]^-$, the intensity of the band at 6541.3 eV derives predominantly from a transition terminating in the α-$3d_{z^2}$ (Mn^{IV}=O σ*) MO. In contrast, for $[Mn^{V}(O)(H_3buea)]$, the intense band at 6541.3 eV (~60% overall pre-edge intensity) is comprised of three pairs of transitions (split by only 0.6 eV) that cumulatively contribute to the intensity of this feature. The intensity of this band predominantly arises from two pairs of transitions terminating in the degenerate α-$3d_{xy}$ and α-$3d_{x^2-y^2}$ MOs and

degenerate β-3d_{xy} and β-3$d_{x^2-y^2}$ (Mn^V–N_{eq} σ*) MOs. These sets of α- and β-spin orbitals are split by only 0.4 eV, reflecting the smaller spin polarization in the *S* = 1 complex, and contain a total of 7.7% Mn 4p character. This enhanced Mn 3d-4$p_{x,y}$ mixing is due to the shorter Mn^V–N_{eq} distances in the oxomanganese(V) complex (Figure 5.11, right). The higher-energy band at 6542.8 eV for [Mn^V(O)(H_3buea)] arises from two excitations terminating in the α- and β-3d_{z^2} orbitals that are split by ~0.6 eV and contain 3.4% Mn 4p character. Compared to [Mn^{IV}(O)(H_3buea)]$^-$, the transition into the β-3d_{z^2} orbital is blue-shifted by 0.7 eV for [Mn^V(O)(H_3buea)], consistent with the higher Mn oxidation state.

The calculated XANES properties of [Mn^V(O)(H_3buea)] are in excellent agreement with the correlations observed for the oxo- and hydroxomanganese(IV) complexes (Figures 5.9 and 5.10). The overall calculated pre-edge area of [Mn^V(O)(H_3buea)] is only ~20% greater than that of [Mn^{IV}(O)(H_3buea)]$^-$ (17.5 and 20.9, respectively) and falls within the range of calculated areas for the Mn^{IV}=O species (15.1 – 27.8). Low-spin oxomanganese(V) complexes with much shorter Mn–O bond lengths (~1.54 Å) show much more intense pre-edge transitions.[23,24,35] Thus, if a trigonal bipyramidal Mn^V=O adduct were to be formed during OEC turnover, it would present a very modest pre-edge feature that could easily be mistaken for that of an Mn^{IV}=O species.

5.5. Summary.

We have applied a combined experimental and computational analysis to understand the XANES properties of oxo- and hydroxomanganese(IV) complexes and an *S* = 1 oxomanganese(V) species. Using detailed assignments of pre-edge features developed using TD-DFT computations, the intense pre-edge features of Mn^{IV}=O adducts are primarily attributed to excitations to the Mn=O σ* MOs that contain significant 3d-4p mixing. Nonetheless, the

intensities and breadths of the pre-edge signals are strongly influenced not only by the Mn=O distance but also the local coordination geometry of the Mn center. For example, significant Mn 3d-4$p_{x,y}$ mixing in trigonal bipyramidal Mn-oxo adducts increases the breadth of the pre-edge signal. In particular, our computations provide strong evidence that Mn^{IV}–OH, Mn^{IV}=O, and even Mn^{V}=O species can show pre-edge peaks of comparable area and height, dependent on the specifics of the ligand field. Thus, great caution should be taken in making structural assignments regarding such complexes on the basis of XANES data alone.

Notes and References.

1. Wu, A. J.; Penner-Hahn, J. E.; Pecoraro, V. L., *Chem. Rev.* **2004,** *104*, 903-938.
2. Yachandra, V. K., *Adv. Photosynth. Respir.* **2005,** *22*, 235-260.
3. Penner-Hahn, J., Structural characterization of the Mn site in the photosynthetic oxygen-evolving complex. In *Metal Sites in Proteins and Models Redox Centres*, Hill, H. A. O.; Sadler, P. J.; Thomson, A. J., Eds. Springer Berlin Heidelberg: 1998; Vol. 90, pp 1-36.
4. Yachandra, V. K.; Sauer, K.; Klein, M. P., *Chem. Rev.* **1996,** *96*, 2927-2950.
5. Yano, J.; Yachandra, V., *Photosynth. Res.* **2009,** *102*, 241-254.
6. McEvoy, J. P.; Brudvig, G. W., *Chem. Rev.* **2006,** *106*, 4455-4483.
7. Pecoraro, V. L.; Hsieh, W.-Y., *Inorg. Chem.* **2008,** *47*, 1765-1778.
8. Robblee, J. H.; Messinger, J.; Cinco, R. M.; McFarlane, K. L.; Fernandez, C.; Pizarro, S. A.; Sauer, K.; Yachandra, V. K., *J. Am. Chem. Soc.* **2002,** *124*, 7459-7471.
9. Waldo, G. S.; Penner-Hahn, J. E., *Biochemistry* **1995,** *34*, 1507-1512.
10. Ayougou, K.; Bill, E.; Charnock, J. M.; Garner, C. D.; Mandon, D.; Trautwein, A. X.; Weiss, R.; Winkler, H., *Angew. Chem., Int. Ed. Engl.* **1995,** *34*, 343-346.
11. Bortolini, O., *Nouv. J. Chim.* **1986,** *10*, 39 - 49.
12. Chen, J.; Lee, Y.-M.; Davis, K. M.; Wu, X.; Seo, M. S.; Cho, K.-B.; Yoon, H.; Park, Y. J.; Fukuzumi, S.; Pushkar, Y. N.; Nam, W., *J. Am. Chem. Soc.* **2013,** *135*, 6388-6391.
13. Kurahashi, T.; Kikuchi, A.; Shiro, Y.; Hada, M.; Fujii, H., *Inorg. Chem.* **2010,** *49*, 6664-6672.
14. Kurahashi, T.; Kikuchi, A.; Tosha, T.; Shiro, Y.; Kitagawa, T.; Fujii, H., *Inorg. Chem.* **2008,** *47*, 1674-1686.
15. Leto, D. F.; Ingram, R.; Day, V. W.; Jackson, T. A., *Chem. Commun.* **2013,** *49*, 5378-5380.
16. Wu, X.; Seo, M. S.; Davis, K. M.; Lee, Y.-M.; Chen, J.; Cho, K.-B.; Pushkar, Y. N.; Nam, W., *J. Am. Chem. Soc.* **2011,** *133*, 20088-20091.
17. Arunkumar, C.; Lee, Y.-M.; Lee, J. Y.; Fukuzumi, S.; Nam, W., *Chemistry--A European Journal* **2009,** *15*, 11482-11489.
18. Chattopadhyay, S.; Geiger, R. A.; Yin, G.; Busch, D. H.; Jackson, T. A., *Inorg. Chem.* **2010,** *49*, 7530-7535.

19. Garcia-Bosch, I.; Company, A.; Cady, C. W.; Styring, S.; Browne, W. R.; Ribas, X.; Costas, M., *Angew. Chem., Int. Ed. Engl.* **2011,** *50*, 5648-5653.
20. Parsell, T. H.; Behan, R. K.; Green, M. T.; Hendrich, M. P.; Borovik, A. S., *J. Am. Chem. Soc.* **2006,** *128*, 8728-8729.
21. Sawant, S. C.; Wu, X.; Cho, J.; Cho, K.-B.; Kim, S. H.; Seo, M. S.; Lee, Y.-M.; Kubo, M.; Ogura, T.; Shaik, S.; Nam, W., *Angew. Chem., Int. Ed. Engl.* **2010,** *49*, 8190-8194.
22. Yin, G.; Danby, A. M.; Kitko, D.; Carter, J. D.; Scheper, W. M.; Busch, D. H., *J. Am. Chem. Soc.* **2007,** *129*, 1512-1513.
23. Collins, T. J.; Gordon-Wylie, S. W., *J. Am. Chem. Soc.* **1989,** *111*, 4511-4513.
24. Collins, T. J.; Powell, R. D.; Slebodnick, C.; Uffelman, E. S., *J. Am. Chem. Soc.* **1990,** *112*, 899-901.
25. MacDonnell, F. M.; Fackler, N. L. P.; Stern, C.; O'Halloran, T. V., *J. Am. Chem. Soc.* **1994,** *116*, 7431-7432.
26. Miller, C. G.; Gordon-Wylie, S. W.; Horwitz, C. P.; Strazisar, S. A.; Peraino, D. K.; Clark, G. R.; Weintraub, S. T.; Collins, T. J., *J. Am. Chem. Soc.* **1998,** *120*, 11540-11541.
27. Yin, G.; McCormick, J. M.; Buchalova, M.; Danby, A. M.; Rodgers, K.; Day, V. W.; Smith, K.; Perkins, C. M.; Kitko, D.; Carter, J. D.; Scheper, W. M.; Busch, D. H., *Inorg. Chem.* **2006,** *45*, 8052-8061.
28. Yano, J.; Kern, J.; Irrgang, K.-D.; Latimer, M. J.; Bergmann, U.; Glatzel, P.; Pushkar, Y.; Biesiadka, J.; Loll, B.; Sauer, K.; Messinger, J.; Zouni, A.; Yachandra, V. K., *Proc. Natl. Acad. Sci.* **2005,** *102*, 12047-12052.
29. Chandrasekaran, P.; Stieber, S. C. E.; Collins, T. J.; Que, J. L.; Neese, F.; DeBeer, S., *Dalton Trans.* **2011,** *40*, 11070-11079.
30. DeBeer George, S.; Petrenko, T.; Neese, F., *J. Phys. Chem. A* **2008,** *112*, 12936-12943.
31. Westre, T. E.; Kennepohl, P.; DeWitt, J. G.; Hedman, B.; Hodgson, K. O.; Solomon, E. I., *J. Am. Chem. Soc.* **1997,** *119*, 6297-6314.
32. Randall, C. R.; Shu, L.; Chiou, Y.-M.; Hagen, K. S.; Ito, M.; Kitajima, N.; Lachicotte, R. J.; Zang, Y.; Que, L., *Inorg. Chem.* **1995,** *34*, 1036-1039.
33. DeBeer George, S.; Brant, P.; Solomon, E. I., *J. Am. Chem. Soc.* **2005,** *127*, 667-674.
34. Roemelt, M.; Beckwith, M. A.; Duboc, C.; Collomb, M.-N.; Neese, F.; DeBeer, S., *Inorg. Chem.* **2011,** *51*, 680-687.
35. Lansky, D. E.; Mandimutsira, B.; Ramdhanie, B.; Clausén, M.; Penner-Hahn, J.; Zvyagin, S. A.; Telser, J.; Zhan, R.; Ou, Z.; Kadish, K. M.; Zakharov, L.; Rheingold, A. L.; Goldberg, D. P., *Inorg. Chem.* **2005,** *44*, 4485-4498.
36. Weng, T.-C.; Hsieh, W.-Y.; Uffelman, E. S.; Gordon-Wylie, S. W.; Collins, T. J.; Pecoraro, V. L.; Penner-Hahn, J. E., *J. Am. Chem. Soc.* **2004,** *126*, 8070-8071.
37. Yano, J.; Robblee, J.; Pushkar, Y.; Marcus, M. A.; Bendix, J.; Workman, J. M.; Collins, T. J.; Solomon, E. I.; DeBeer George, S.; Yachandra, V. K., *J. Am. Chem. Soc.* **2007,** *129*, 12989-13000.
38. Song, W. J.; Seo, M. S.; DeBeer George, S.; Ohta, T.; Song, R.; Kang, M. J.; Tosha, T.; Kitagawa, T.; Solomon, E. I.; Nam, W., *J. Am. Chem. Soc.* **2007,** *129*, 1268-1277.
39. England, J.; Martinho, M.; Farquhar, E. R.; Frisch, J. R.; Bominaar, E. L.; Münck, E.; Que, L., *Angew. Chem., Int. Ed. Engl.* **2009,** *48*, 3622-3626.
40. Jackson, T. A.; Rohde, J.-U.; Seo, M. S.; Sastri, C. V.; DeHont, R.; Ohta, T.; Stubna, A.; Kitagawa, T.; Münck, E.; Nam, W.; Que, L., Jr., *J. Am. Chem. Soc.* **2008,** *130*, 12394-12407.

41. Rohde, J.-U.; Torelli, S.; Shan, X.; Lim, M. H.; Klinker, E. J.; Kaizer, J.; Chen, K.; Nam, W.; Que, L., Jr., *J. Am. Chem. Soc.* **2004,** *126*, 16750-16761.
42. Lassalle-Kaiser, B.; Hureau, C.; Pantazis, D. A.; Pushkar, Y.; Guillot, R.; Yachandra, V. K.; Yano, J.; Neese, F.; Anxolabehere-Mallart, E., *Energy Environ. Sci.* **2010,** *3*, 924-938.
43. Banerjee, P.; Sproules, S.; Weyhermüller, T.; DeBeer George, S.; Wieghardt, K., *Inorg. Chem.* **2009,** *48*, 5829-5847.
44. Krewald, V.; Lassalle-Kaiser, B.; Boron, T. T.; Pollock, C. J.; Kern, J.; Beckwith, M. A.; Yachandra, V. K.; Pecoraro, V. L.; Yano, J.; Neese, F.; DeBeer, S., *Inorg. Chem.* **2013,** *52*, 12904-12914.
45. Yin, G.; Danby, A. M.; Kitko, D.; Carter, J. D.; Scheper, W. M.; Busch, D. H., *J. Am. Chem. Soc.* **2008,** *130*, 16245-16253.
46. George, G. N. *EXAFSPAK*, Stanford Synchrotron Radiation Laboratory; Stanford, CA, 1990.
47. Rehr, J. J.; Mustre de Leon, J.; Zabinsky, S. I.; Albers, R. C., *J. Am. Chem. Soc.* **1991,** *113*, 5135-5140.
48. Neese, F., *ORCA - an ab initio, Density Functional and Semiempirical Program Package, Version 2.8*, University of Bonn, 2011. *ORCA - an ab initio, Density Functional and Semiempirical Program Package, Version 2.8, University of Bonn, 2009.*
49. Becke, A. D., *Phys. Rev. A: At., Mol., Opt. Phys.* **1988,** *38*, 3098.
50. Perdew, J. P., *Phys. Rev. B* **1986,** *33*, 8822-8824.
51. Schäfer, A.; Horn, H.; Ahlrichs, R., *J. Chem. Phys.* **1992,** *97*, 2571-2577.
52. Schäfer, A.; Huber, C.; Ahlrichs, R., *J. Chem. Phys.* **1994,** *100*, 5829-5835.
53. Neese, F., *J. Comput. Chem.* **2003,** *24*, 1740-1747.
54. Hubin, T. J.; McCormick, J. M.; Collinson, S. R.; Buchalova, M.; Perkins, C. M.; Alcock, N. W.; Kahol, P. K.; Raghunathan, A.; Busch, D. H., *J. Am. Chem. Soc.* **2000,** *122*, 2512-2522.
55. Dey, A.; Hocking, R. K.; Larsen, P.; Borovik, A. S.; Hodgson, K. O.; Hedman, B.; Solomon, E. I., *J. Am. Chem. Soc.* **2006,** *128*, 9825-9833.
56. Hirata, S.; Head-Gordon, M., *Chem. Phys. Lett.* **1999,** *302*, 375-382.
57. Hirata, S.; Head-Gordon, M., *Chem. Phys. Lett.* **1999,** *314*, 291-299.
58. Becke, A. D., *J. Chem. Phys.* **1993,** *98*, 1372-1377.
59. Becke, A. D., *J. Chem. Phys.* **1993,** *98*, 5648-5652.
60. Lee, C.; Yang, W.; Parr, R. G., *Phys. Rev. B* **1988,** *37*, 785-789.
61. Weigend, F.; Ahlrichs, R., *Phys. Chem. Chem. Phys.* **2005,** *7*, 3297-3305.
62. Lenthe, E. v.; Baerends, E. J.; Snijders, J. G., *J. Chem. Phys.* **1993,** *99*, 4597-4610.
63. van Wüllen, C., *J. Chem. Phys.* **1998,** *109*, 392-399.
64. Klamt, A.; Schuurmann, G., *J. Chem. Soc., Perkin Trans. 2* **1993**, 799-805.
65. Dubois, L.; Jacquamet, L.; Pecaut, J.; Latour, J.-M., *Chem. Commun.* **2006**, 4521-4523.
66. Shadle, S. E.; Penner-Hahn, J. E.; Schugar, H. J.; Hedman, B.; Hodgson, K. O.; Solomon, E. I., *J. Am. Chem. Soc.* **1993,** *115*, 767-776.
67. Gray, H. B., *Electrons and Chemical Bonding*. W. A. Benjamin: New York,, 1964; p xv, 223.
68. Green, M. T., *J. Am. Chem. Soc.* **2006,** *128*, 1902-1906.
69. Neese, F., *J. Biol. Inorg. Chem.* **2006,** *11*, 702-711.
70. Haumann, M.; Liebisch, P.; Müller, C.; Barra, M.; Grabolle, M.; Dau, H., *Science* **2005,** *310*, 1019-1021.
71. Taguchi, T.; Gupta, R.; Lassalle-Kaiser, B.; Boyce, D. W.; Yachandra, V. K.; Tolman, W. B.; Yano, J.; Hendrich, M. P.; Borovik, A. S., *J. Am. Chem. Soc.* **2012,** *134*, 1996-1999.

Chapter 6.

Electron Paramagnetic Resonance Studies of Oxo- and Hydroxo-manganese(IV) Complexes: Insight into Ground-state Electronic Properties.

6.1. Introduction.

Electron paramagnetic resonance **(**EPR) spectroscopy is one of the primary tools for elucidating the geometric and electronic structures of active-site manganese centers in enzymes and proteins.[1-6] This technique is also commonly employed in the characterization of high-valent manganese adducts proposed as key intermediates in oxidation reactions catalyzed by synthetic manganese compounds.[7-12] In many cases, EPR spectroscopy is used primarily to determine the oxidation state and/ or nuclearity of the predominant manganese species. Although useful as a characterization tool, this approach does not maximize the information content of most EPR data sets.

The EPR spectra of spin systems with $S > 1/2$ contain information on i) the Zeeman interaction of the unpaired electrons and the magnetic field, ii) the zero-field splitting (ZFS) that reflect spin-spin interactions in the ground electronic state and spin-orbit couplings with low-lying excited states, and iii) hyperfine couplings between electron and nuclear spins. In such systems the ground-state electronic properties are described by the spin Hamiltonian in Eq. 1.

$$H = \beta B g \hat{S} + D\left[\hat{S}_z^2 - \frac{1}{3}S(S+1)\right] + E\left(\hat{S}_x^2 - \hat{S}_y^2\right) + \hat{S}A\hat{I} \qquad (1)$$

The first term represents the Zeeman splitting, where β is the Bohr magneton, B is the applied magnetic field, g is the Landé g-factor (2.0023 for a free electron), and $\hat{S}$ is the spin angular momentum operator. The middle two terms describe the ZFS interaction, where D and E are the axial and rhombic ZFS parameters, respectively, and $\hat{S}_x$, $\hat{S}_y$, and $\hat{S}_z$ are the spin angular momentum operators using the coordinate system of the **D** tensor. The final term describes the hyperfine interaction, where A is the hyperfine matrix and $\hat{I}$ is the nuclear spin operator. The spin Hamiltonian operates on a basis set of $|S, m_s\rangle$ functions that diagonalize the **D** tensor. The

ZFS interaction removes the degeneracy of the $2S + 1$ magnetic sublevels $m_S = S, S - 1, \ldots, -S$ in the absence of a magnetic field and, for non-integer spin systems, produces sets of non-degenerate Kramer's doublets ($m_s = \pm 1/2, \pm 3/2$, etc.; see Figure 6.1). For systems where $S = 3/2$, such as manganese(IV) centers, the energy separation of the $m_s = \pm 1/2$ and $m_s = \pm 3/2$ Kramers doublets, is $2D$ at zero field for a purely axial system (*i.e.*, $|D| > 0$; $E = 0$; see Figure 6.1, left). With rhombic ZFS (*i.e.*, $|D| > 0$; $|E| > 0$), the doublets are subject to additional energetic separation, as shown in Figure 6.1 (right).[13] The ratio of E and D is defined by a rhombicity term (E/D), which ranges from zero at the axial limit to 1/3 at the rhombic limit. Thus, for an $S = 3/2$ system, the field position and intensity of the allowed EPR transitions ($\Delta m_s = \pm 1$) are sensitive to the axial ZFS parameter (D) and the rhombicity (E/D). Hyperfine interactions with a single $I = 5/2$ spin of the Mn nucleus will split the EPR transitions between the Kramers doublets into sets of six lines.

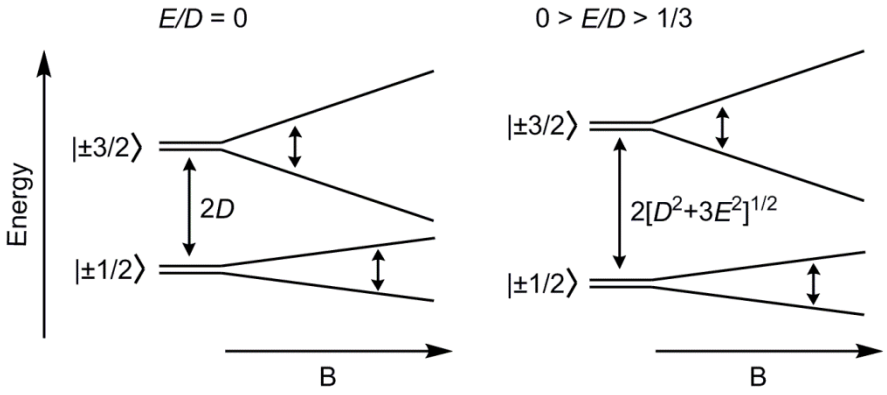

Figure 6.1. Energies of the magnetic sublevels (m_s) of an $S = 3/2$ spin system at zero-field and as a function of the applied magnetic field (B) in the presence of axial (left) and rhombic (right) zero-field splitting with $|D| > 0$.

ZFSs for Mn^{II}, Mn^{III}, and Mn^{IV} ions are excellent reporters of minor structural perturbations.[14-16] In some cases, the zero-field splitting parameters of manganese ions have been

correlated with the geometric and electronic properties of the metal center.[14] For high-spin (S = 2) Mn^{III} centers of tetragonal symmetry, the sign of D is, in general, correlated to the axial Mn-ligand bond distortions that determine the orbital ground state.[16] Elongation of the axial bonds, which is commonly observed for complexes with square pyramidal and pseudo-octahedral coordination environments, results in $D < 0$, whereas a compression of the axial metal-ligand bonds results in $D > 0$.[16] An exception to this correlation was observed for an octahedral *trans*-di(iodide)-manganese(III) supported by a neutral N_4 ligand. For that complex, strong mixing of the electronic ground state with low-lying charge-transfer excited states involving iodide, a ligand with an unusually large spin-orbit coupling constant, caused the correlation to break down.[17] For Mn^{II} centers with N/O-based ligands, the magnitude of D is correlated with coordination number.[14] Five-coordinate Mn^{II} complexes generally exhibit D-values that are greater than that of six-coordinate complexes, in some cases by up to an order of magnitude.[14] A correlation between the ZFS of Mn^{II} complexes and the corresponding Mn^{II}/Mn^{III} reduction potential has also been postulated.[18]

In contrast to these general, albeit rather limited, correlations for Mn^{II} and Mn^{III} systems, there are essentially no correlations describing the structural influences on ZFS parameters for Mn^{IV} systems. Indeed, although EPR spectroscopy is routinely employed for the identification of high-spin (S = 3/2) monomeric Mn^{IV} centers, precise ground-state spin Hamiltonian parameters have rarely been reported for Mn^{IV} ions.[8,19-22] This is largely due to the fact that the axial ZFSs of monomeric Mn^{IV} centers are often of the same magnitude as the microwave frequencies used in conventional X-band EPR spectrometers (~9.4 GHz or 0.3 cm^{-1}). This results in overlapping transitions that complicate spectral simulations. Consequently, analysis of X-band EPR data collected for Mn^{IV} centers is often limited to indicate whether $|D| \approx 0.3$ cm^{-1} or $|D| >> 0.3$ cm^{-1},

based on the relative intensities of the resonances at g_{eff} = 4 and g_{eff} = 2.[8,21,23-32] When $|D| >> 0.3$ cm^{-1}, the rhombicity can be estimated from the *g*-value of the low-field transition, where this transition is observed at g_{eff} = 4.1 and 5.5 at the axial (*E/D* = 0) and rhombic (*E/D* = 1/3) limits, respectively.[20,22,33] A more rigorous analysis of the spin Hamiltonian parameters requires extensive computer simulation of X-band EPR spectra and/ or the use of larger microwave frequencies.[8,13,19-22] At much larger microwave frequencies (95 – 700 GHz) and magnetic fields, where $|D| << h\nu$, *D* and *E* can be accurately determined directly from the positions of the EPR resonances of Mn^{IV} centers.[22,34]

To develop a fundamental understanding of the physical factors that contribute to ZFS in Mn^{IV} centers, and to rationalize any observed experimental correlations, a combined experimental and computational approach is required. In addition, suitable manganese(IV) complexes with experimentally well-defined structures *and* ZFS parameters are required to evaluate computational predictions. Theoretical methods based on density functional theory (DFT) and multireference ab initio methods have shown success in calculating ZFS parameters for a broad range of well-defined Mn^{II} and Mn^{III} compounds.[15,35-37] Due to the relatively small *D* values in Mn^{II} compounds (0 – 1.3 cm^{-1}), the accurate calculation of ZFSs with DFT methods has been particularly challenging.[36,37] In one of the more significant findings from DFT calibration studies, it was reported that the use of geometry-optimized models of Mn^{II} complexes significantly decreased the accuracy of the predicted ZFS parameters.[14,37] This result calls into question the use of such methods for compounds that are not structurally characterized, which represents a major limitation of this approach. For Mn^{III} compounds, DFT calculations do not fair as poorly, although benchmark studies have shown that this method tends to underestimate the of magnitude *D*.[15] Zero-field splitting parameters have been more accurately predicted for

Mn^{III} compounds using ab initio methods based on a complete active space self-consistent field (CASSCF) treatment.[15,38] An advantage of this method is that it can be used to predict ZFS for high symmetry systems with degenerate ground and/ or excited-states. Such systems cannot be properly treated by a single-determinant method such as DFT.[38] Unlike for DFT methods, however, significant user input is necessary to select the correct active-space for the CASSCF calculations. In addition, CASSCF methods are more computationally expensive than DFT and often require the use of truncated models. For some systems, CASSCF and DFT methods work equally well, though it is very difficult to predict when this will be the case.

As a first step in developing spectro-structural correlations on the basis of ZFS parameters for Mn^{IV} centers, we have applied X- and Q-band EPR spectroscopy, along with computer simulations, to investigate the ground-state spin Hamiltonian parameters of $[Mn^{IV}(OH)_2(Me_2EBC)]^{2+}$ and $[Mn^{IV}(O)(OH)(Me_2EBC)]^{+}$, a pair of complexes that feature Mn^{IV}=O and Mn^{IV}–OH moieties with identical coordination environments (Figure 6.2). $[Mn^{IV}(OH)_2(Me_2EBC)]^{2+}$ and $[Mn^{IV}(O)(OH)(Me_2EBC)]^{+}$ are an ideal pair of complexes to investigate the effects of structure on ZFS parameters because they are structurally characterized and feature nearly identical ligand environments. The ZFS parameters presented here add to the limited information available for oxo- and hydroxomanganese(IV) complexes,[8,19,39] and can be used to evaluate theoretical models for computing ZFS (*i.e.*, DFT and multi-reference ab initio methods). The geometric and electronic structures of $[Mn^{IV}(OH)_2(Me_2EBC)]^{2+}$ and $[Mn^{IV}(O)(OH)(Me_2EBC)]^{+}$ have previously been explored by X-ray absorption spectroscopy (Chapter 5) and by electronic absorption and magnetic circular dichroism (MCD) spectroscopy.[40]

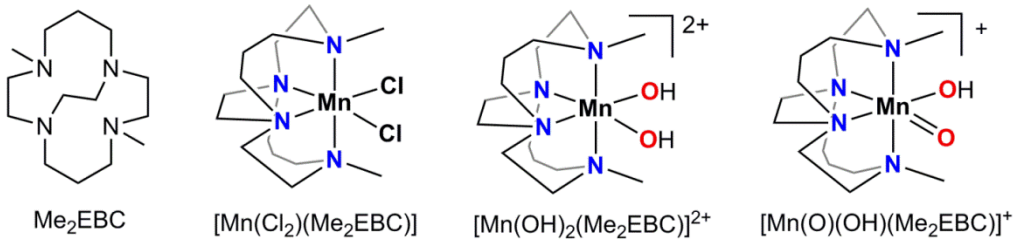

Figure 6.2. Structure of Me_2EBC ligand and complexes $[Mn^{II}(Cl_2)(Me_2EBC)]$, $[Mn^{IV}(OH)_2(Me_2EBC)]^{2+}$, and $[Mn^{IV}(O)(OH)(Me_2EBC)]^{+}$.

6.2. Experimental Methods.

6.2.1. EPR Sample Preparation. $[Mn^{IV}(OH)_2(Me_2EBC)](PF_6)_2$ and $[Mn^{IV}(O)(OH)(Me_2EBC)]^{+}$ were prepared as described in Chapter 5.2. The X-band EPR sample of $[Mn^{II}(Cl_2)(Me_2EBC)]$ was prepared by dissolving 2.8 mg of the manganese(II) complex in 3.0 mL of (4:1) acetone:water (2.45 mM) and transferring ~250 μL of this solution to a 4 mm quartz EPR tube. The X-band EPR sample of $[Mn^{IV}(OH)_2(Me_2EBC)]^{2+}$ was prepared by dissolving 30.3 mg of $[Mn^{IV}(OH)_2(Me_2EBC)](PF_6)_2$ in 25 mL of (4:1) acetone:water mixture at 298 K and transferring ~250 μL of this solution to a 4 mm quartz EPR tube. The pH of the remaining solution was adjusted to 8.7 by the addition of 0.3 M NaOH (360 μL). To ensure complete formation of $[Mn^{IV}(O)(OH)(Me_2EBC)]^{+}$ in an acetone:water (4:1) solvent mixture, the reaction was monitored by electronic absorption spectroscopy as the pH was adjusted to 8.7 (Figure A.6.1). Once the formation of $[Mn^{IV}(O)(OH)(Me_2EBC)]^{+}$ was completed, approximately 250 μL of this solution were transferred to a 4 mm quartz EPR tube. Q-band samples of $[Mn^{IV}(O)(OH)(Me_2EBC)]^{+}$ and $[Mn^{IV}(OH)_2(Me_2EBC)]^{2+}$ were prepared by the same method, except 30 μL of 1.0 mM solutions were transferred to 1.6 mm quarts EPR tubes. All samples were immediately flash-frozen in liquid N_2 and stored under liquid nitrogen prior to EPR data collection.

6.2.2. EPR Spectroscopy. X-band (9.4 GHz) spectra were collected on a Bruker EMXPlus spectrometer equipped with an Oxford ESR900 continuous-flow liquid helium cryostat and an Oxford ITC503 temperature system to monitor and regulate the temperature. A dual mode cavity (Bruker ER4116DM) was used. Spectra were recorded under non-saturating conditions using 100 kHz field modulation. Other parameters (temperature, number of scans, microwave frequency, modulation amplitude, microwave power, and time constant) are given in the captions of the appropriate figures. Linear baseline corrections were subtracted from the 5 K X-band EPR spectra of $[Mn^{IV}(OH)_2(Me_2EBC)]^{2+}$ and $[Mn^{IV}(O)(OH)(Me_2EBC)]^{+}$ to correct for baseline drift at higher fields.

Q-band (35 GHz) spectra were collected by our collaborator Prof. Joshua Telser (Roosevelt University) in Prof. Brian Hoffman's lab at Northwestern University. Spectra were recorded under non-saturating conditions using 100 kHz field modulation. Other parameters (temperature, microwave frequency, modulation amplitude, and time constant) are given in the captions of the appropriate figures.

6.2.3. EPR Data Simulations. The EPR simulations were performed using the *EasySpin* program written by Prof. S. Stoll (University of Washington).[41] The X-band EPR spectra of $[Mn^{IV}(OH)_2(Me_2EBC)]^{2+}$ and $[Mn^{IV}(O)(OH)(Me_2EBC)]^{+}$ were well reproduced using an $S = 3/2$ spin system with an isotropic g-value ($g = 2$). A Gaussian line shape (full-width half-maximum = 4 mT) was applied to broaden the resonances in the simulated spectra. The hyperfine coupling constant (A in MHz) from ^{55}Mn ($I = 5/2$) hyperfine interactions were included in simulations. (The hyperfine coupling constant obtained from experimental spectra is defined as a with units of magnetic field (mT or G), and can be converted to A (Hz) by the relation: $hA = g\beta a$.)[42] The axial (D) and rhombic (E) zero-field splitting parameters, and Gaussian distributions of the scalar

parameters D and E (D-strain), were systematically varied. All simulation parameters are included in the caption of the appropriate figures. Attempts to simulate Q-band EPR spectra were unsuccessful since an unknown amount of Mn^{II} was present in both samples.

6.3. Results and Analysis.

6.3.1. X-band EPR Spectroscopy. X-band, perpendicular-mode EPR spectra of $[Mn^{IV}(OH)_2(Me_2EBC)]^{2+}$ and $[Mn^{IV}(O)(OH)(Me_2EBC)]^{+}$, collected on frozen acetone:water (4:1) solutions at 5 K, are shown in Figure 6.3. Both compounds display dominant resonances at $g_{eff} \approx 3 - 6$ and weaker resonances at higher fields. This spectral pattern, featuring a strong signal at low-field and relatively weaker signals at high-fields, is characteristic of high-spin (S = 3/2) monomeric Mn^{IV} centers for which the magnitude of D is larger than the energy of the incident microwave photon ($D >> 0.32$ cm^{-1} for X-band).[8,10,19-21,43]

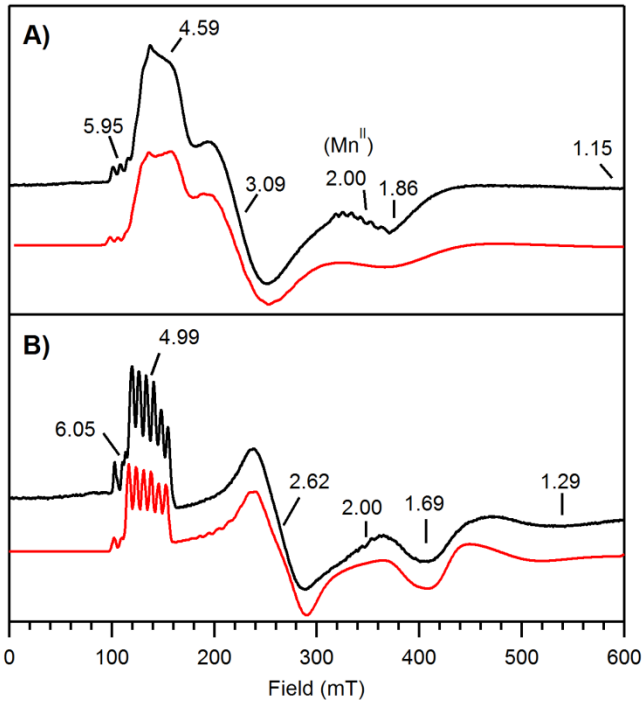

Figure 6.3. (A) Experimental (black) and simulated (red) X-band, perpendicular-mode EPR spectra of a frozen 1.9 mM acetone:water (4:1) solution of $[Mn^{IV}(OH)_2(Me_2EBC)]^{2+}$. The experimental spectrum represents the average of 5 scans. Spin-Hamiltonian parameters used for simulation: D = 0.5 cm^{-1}, E/D = 0.147, g = 2.00, A = 210 MHz ≈ 7.5 mT, linewidth = 4 mT, and D-strain = [4000, 1400 MHz]. **(B):** Experimental (black) and simulated (red) X-band, perpendicular-mode EPR spectra of a frozen 1.9 mM acetone:water (4:1) solution of $[Mn^{IV}(O)(OH)(Me_2EBC)]^{+}$. The experimental spectrum represents the average of 10 scans. Spin-Hamiltonian parameters used for simulation: D = 1.0 cm^{-1}, E/D = 0.223, g = 2.00, A = [220, 204, 210 MHz] ≈ [7.8, 7.3, 7.5 mT], linewidth = 4 mT, and D-strain = [4000, 500 MHz]. The g-values of each transition are shown. Experimental recording conditions: 9.6378 and 9.6375 GHz microwave frequencies for $[Mn^{IV}(OH)_2(Me_2EBC)]^{2+}$ (**A**) and $[Mn^{IV}(O)(OH)(Me_2EBC)]^{+}$ (**B**), respectively, T = 5 K, 2.000 mW microwave power, 0.6 mT modulation amplitude, 100 kHz modulation frequency, and 163.84 ms time constant.

(A) $[Mn^{IV}(OH)_2(Me_2EBC)]^{2+}$. The experimental EPR spectrum of $[Mn^{IV}(OH)_2(Me_2EBC)]^{2+}$ displays a positive resonance at g_{eff} = 4.59 with a shoulder on the low-field side (g_{eff} = 5.95), a prominent derivative-shaped signal at g_{eff} = 3.09, and weaker negative resonances at g_{eff} = 1.86, and 1.15. These signals are characteristic of X-band EPR spectra collected for $3d^3$ ions with rhombic electronic distortions ($0 < E/D < 1/3$).[8,10,19-22,43] Three

partially-resolved hyperfine lines are detected for the weak signal at g_{eff} = 5.95 with a = 7.5 mT, consistent with hyperfine constants observed for other Mn^{IV} centers (a > 6.6 mT; *cf.* Table 6.1).[8] Relative to the signal intensity at g_{eff} = 4.59, the intensity of the hyperfine lines at g_{eff} = 5.95 is much lower, indicating that the latter signals arise from transitions within the excited Kramers doublet. For an S = 3/2 system, the ground Kramers depends on the sign of D, with the m_s = ±1/2 and ±3/2 doublets being lowest in energy for D > 0 and D < 0, respectively. To determine the sign of D, EPR spectra were collected from 5 – 25 K (Figure A.6.3). The intensity of both resonances at g_{eff} = 5.95 and 4.59 show inverse temperature dependence (Figure 6.4), which indicates D is positive.[8,19-21] Thus, with D > 0, the resonances at g_{eff} = 4.59 and 5.95 arise from the ground (m_s = ±1/2) and excited (m_s = ±3/2) doublets, respectively. To determine the magnitude of D, the temperature dependences of the signal intensities at g_{eff} = 4.59 and 5.95 were fit to calculated temperature-dependent curves for different D-values (Figure A.6.4, top). Due to the large baseline drift in the variable-temperature EPR spectra at high-field (Figure A.6.3), reasonable fits were not obtained. Thus, additional variable-temperature spectra are needed to determine the magnitude of D for $[Mn^{IV}(OH)_2(Me_2EBC)]^{2+}$.

The EPR spectrum of $[Mn^{IV}(OH)_2(Me_2EBC)]^{2+}$ also displays a low-intensity, six-line, derivative-shaped signal centered at g_{eff} = 2.00. Analysis of the splitting of this signal reveals a hyperfine coupling constant of a = 8.8 mT. This a value is larger than expected for a Mn^{IV} center, but is consistent with a values commonly observed for Mn^{II} ions.[19] Notably, the X-band EPR spectrum of $[Mn^{II}(Cl_2)(Me_2EBC)]$ (Figure A.6.2) features an intense resonance at g_{eff} = 2.00 with well-resolved hyperfine coupling (a = 8.9 mT). Thus, the low-intensity signal at g_{eff} = 2.00 observed in the EPR spectrum of $[Mn^{IV}(OH)_2(Me_2EBC)]^{2+}$ likely derives from a small amount of $[Mn^{II}(Cl_2)(Me_2EBC)]$ present in the sample.

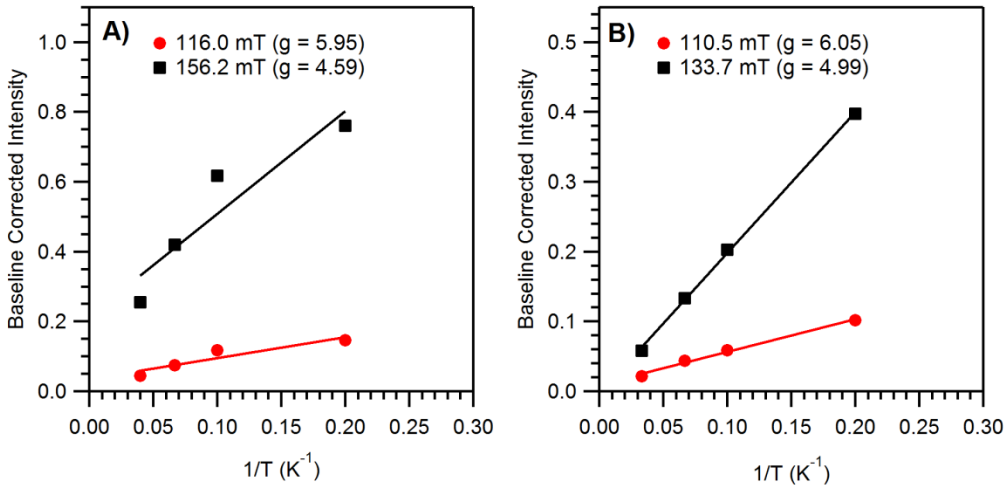

Figure 6.4. (A) Signal intensity of resonances at g_{eff} = 5.95 (m_s = ±3/2) and 4.59 (m_s = ±1/2) for $[Mn^{IV}(OH)_2(Me_2EBC)]^{2+}$ collected at T = 5, 10, 15, and 25 K. **(B)** Signal intensity of resonances at g_{eff} = 6.05 (m_s = ±3/2) and 4.99 (m_s = ±1/2) for $[Mn^{IV}(O)(OH)(Me_2EBC)]^{+}$ collected at T = 5, 10, 15, and 30 K. Baseline corrected by subtracting intensity at 95 mT for **(A)** and 100 mT for **(B)**.

Table 6.1. Zero-field Splitting Parameters and Hyperfine Constants for Mn^{IV} Complexes.

Complex[a]	D (cm^{-1})	E/D	a (mT)	ref.
$[Mn^{IV}(OH)_2(Me_2EBC)]^{2+}$	≥0.5	0.15(2)	7.5	[b]
$[Mn^{IV}(OH)(H_3buea)]$ [c]	+0.88(5)	0.31(1)	7.5	19
	+0.67(5)	0.17(1)		
$[Mn^{IV}(O)(OH)(Me_2EBC)]^{+}$	+1.0(5)	0.22(1)	7.7	[b]
$[Mn^{IV}(O)(H_3buea)]^{-}$	+3.0	0.26	6.6	8
$[Mn^{IV}(O)(OH_2)(BQCN)]^{2+}$	+2	0	ND[c]	39
$[Mn^{IV}(O)(N4py)]^{2+}$	ND[d]	ND[d]	7.6	10
$[Mn^{IV}(^tBu_3\text{-terpy})_2]^{4+}$	+1.33(6)	0.27	6.7	20
$[Mn^{IV}(OMe)_3(TACN)]^{+}$	+0.250(5)	0	ND[d]	22
$[Mn^{IV}(L^{Me})_2]$	+1.6(4)	0.17(1)	7.2	21

[a] H_3buea = tris[(*N*′-*tert*-butylureaylato)-*N*-ethylene]aminato; BQCN = *N*,*N*′-dimethyl- *N*,*N*′-bis(8-quinolyl)cyclohexanedimaine; H_2L^{Me} = methylamino-*N*,*N*-bis(2-methylene-4,6-dimethylphenol) $^tBu_3$-terpy = 4,4′,4″-tri-*tert*-butyl-2,2′:6′,2″-terpyridine; Me_3-TACN = 1,4,7-trimethyl-1,4,7-triazacyclononane; [b] This work. [c] Two distinct S = 3/2 species observed. [d] Not determined.

The experimental X-band EPR spectrum of $[Mn^{IV}(OH)_2(Me_2EBC)]^{2+}$ was simulated using isotropic g = 2.00 and A = 210 MHz values and D = +0.5 cm^{-1} and E/D = 0.147 (Figure

6.3A). Large *D*-strain parameters (4000, 1400 MHz), which account for distributions in the zero-field splitting parameters *D* and *E*, were required to reproduce the broad features of the experimental spectrum. The spectrum could also be reproduced using larger *D*-values (up to 3 cm^{-1}) with E/D = 0.15(2), as long as the *D*-strain parameters are increased accordingly. In contrast, when the simulations are performed with $D < 0.5$ cm^{-1}, the signal intensity of the resonances at low-field (<100 mT) and high-field (>500 mT) increase considerably relative to the resonances at g_{eff} = 5.95 and 4.95. Thus, from the X-band data alone, we can conclude that D = 3.0 to 0.5 cm^{-1} and E/D = 0.15(2) for $[Mn^{IV}(OH)_2(Me_2EBC)]^{2+}$.

(B) $[Mn^{IV}(O)(OH)(Me_2EBC)]^{+}$. The experimental spectrum of $[Mn^{IV}(O)(OH)(Me_2EBC)]^{+}$ is qualitatively similar to that of $[Mn^{IV}(OH)_2(Me_2EBC)]^{2+}$ (Figure 6.3A and B), with a few notable exceptions. First, the g_{eff} values of $[Mn^{IV}(O)(OH)(Me_2EBC)]^{+}$ are shifted relative to those of $[Mn^{IV}(OH)_2(Me_2EBC)]^{2+}$, implying a larger rhombic distortion. In particular, the g_{eff} values of $[Mn^{IV}(O)(OH)(Me_2EBC)]^{+}$ are characteristic of X-band EPR spectra of $3d^3$ ions in systems with $E/D \geq 0.15$.[8,19-21] Second, the low-field, positive signals at g_{eff} = 6.05, 4.99 in the EPR spectrum of $[Mn^{IV}(O)(OH)(Me_2EBC)]^{+}$ displays well-resolved hyperfine splittings (a = 7.7 and 7.3 mT). The intensity of both resonances at g_{eff} = 6.05 and 4.99 reveal inverse temperature dependence from 5 – 30 K, indicating $D > 0$ (Figure 6.4 and A.6.3).[8,19-21] Fits of signal intensity at g_{eff} = 4.99 and 6.05 temperature dependence to calculated temperature-dependent curves for different *D*-values revealed D = +1.0 (±0.5) cm^{-1} (Figure A.6.4, bottom). The experimental spectrum of $[Mn^{IV}(O)(OH)(Me_2EBC)]^{+}$ was well-simulated using an isotropic g = 2.00 value and anisotropic *A*-values (220, 204, 210 MHz), with D = +1.0 cm^{-1} and E/D = 0.223 (Figure 6.3B).

6.3.2. Q-band EPR Spectroscopy. EPR data collected at two or more microwave frequencies often allow for the accurate and precise determination of ZFS parameters from spectral simulations of the data at each frequency.[13,22,34] Hence, to more accurately determine the magnitude of *D*, Q-band (35 GHz or 1.17 cm^{-1}), perpendicular-mode EPR spectra were collected for samples of $[Mn^{IV}(OH)_2(Me_2EBC)]^{2+}$ and $[Mn^{IV}(O)(OH)(Me_2EBC)]^{+}$ at 2 K. The Q-band EPR spectra, obtained under rapid-passage conditions, display absorption-type EPR signals over the range of 0 – 1500 mT (Figure 6.5). For $[Mn^{IV}(OH)_2(Me_2EBC)]^{2+}$, the Q-band EPR spectrum displays an intense resonance centered at ~1250 mT (g_{eff} = 2) with well-resolved hyperfine coupling (a = 9.6 mT). This signal is consistent with a significant contribution from a Mn^{II} contaminant.[19,44] A similar resonance at ~1250 mT is observed in the Q-band EPR spectrum of $[Mn^{IV}(O)(OH)(Me_2EBC)]^{+}$, however, the signal intensity of this feature is greatly diminished relative to that observed in the $[Mn^{IV}(OH)_2(Me_2EBC)]^{2+}$ sample. Presumably this contaminant is $[Mn^{II}(Cl_2)(Me_2EBC)]$, though this assignment cannot be confirmed in the absence of an authentic Q-band EPR spectrum of $[Mn^{II}(Cl_2)(Me_2EBC)]$. Analyses of the Q-band EPR data for $[Mn^{IV}(OH)_2(Me_2EBC)]^{2+}$ and $[Mn^{IV}(O)(OH)(Me_2EBC)]^{+}$ are complicated by these additional resonances from the Mn^{II} contaminant. Without knowing the relative amounts of Mn^{II} and Mn^{IV} present in the samples, and in the absence of variable-temperature data, it is difficult to assign the individual transitions or determine the zero-field splitting parameters from spectral simulations of the data.

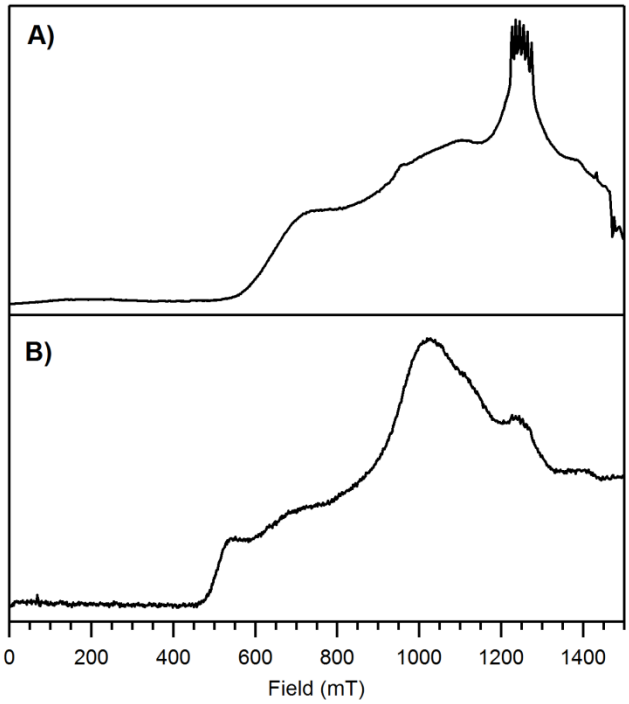

Figure 6.5. Q-band, perpendicular-mode, absorption-type EPR spectra of frozen 1.0 mM acetone:water (4:1) solutions of **(A)** $[Mn^{IV}(OH)_2(Me_2EBC)]^{2+}$ and **(B)** $[Mn^{IV}(O)(OH)(Me_2EBC)]^{+}$ collected under rapid passage conditions. Each spectrum represents the average of 4 scans. Recording conditions: **(A)** T = 2 K, 35.007 GHz microwave frequency, 0.1 mT modulation amplitude, and 16 ms time constant. **(B)**: T = 2 K, 35.052 GHz microwave frequency, 0.1 mT modulation amplitude, and 16 ms time constant.

6.4. Discussion.

In this study, EPR spectroscopy and computer simulations were used to determine the zero-field splitting parameters of $[Mn^{IV}(OH)_2(Me_2EBC)]^{2+}$ and $[Mn^{IV}(O)(OH)(Me_2EBC)]^{+}$. The signal intensity of the low-field transitions for both $[Mn^{IV}(OH)_2(Me_2EBC)]^{2+}$ and $[Mn^{IV}(O)(OH)(Me_2EBC)]^{+}$ revealed inverse temperature dependence, indicating $D > 0$. Simulation of the X-band EPR spectrum of $[Mn^{IV}(O)(OH)(Me_2EBC)]^{+}$, in addition to fits of the variable-temperature EPR data, revealed D = +1.0 (±0.5) cm^{-1} and E/D = 0.22(1). These ZFS parameters are in good agreement with those of the other two Mn^{IV}=O complexes for which both

D and *E* have been determined, $[Mn^{IV}(O)(H_3buea)]^-$ and $[Mn^{IV}(O)(OH_2)(BQCN)]^{2+}$ (Table 6.1).[8,39] Although additional variable-temperature X-band EPR data are needed to accurately determine the magnitude of *D* for $[Mn^{IV}(OH)_2(Me_2EBC)]^{2+}$, a lower-limit of $D \geq 0.5$ cm^{-1} can be set based on the spectral simulations and the relative intensities of the resonance at $g_{eff} \approx 5$ and 2. Higher-quality Q-band EPR data should also aid in the determination of the ZFS parameters. Simultaneous fits to both Q- and X-band EPR spectra with the same spin Hamiltonian parameters should yield a unique result for *D* and *E*. Unfortunately, the currently available Q-band EPR spectra for $[Mn^{IV}(OH)_2(Me_2EBC)]^{2+}$ and $[Mn^{IV}(O)(OH)(Me_2EBC)]^+$ contain an unknown amount of Mn^{II} contaminant that precludes detailed computer simulations of these spectra.

The ground-state properties of $[Mn^{IV}(O)(OH)(Me_2EBC)]^+$ are significantly perturbed by the loss of a proton from $[Mn^{IV}(OH)_2(Me_2EBC)]^{2+}$, as evidenced by the difference in field positions and relative intensities of the resonances observed in the X-band EPR spectra (Figure 6.3). In addition, the resonance at $g_{eff} \approx 4.99$ in the EPR spectrum of $[Mn^{IV}(O)(OH)(Me_2EBC)]^+$ displays resolved hyperfine coupling that is not observed for $[Mn^{IV}(OH)_2(Me_2EBC)]^{2+}$. The EPR spectrum of $[Mn^{IV}(O)(OH)(Me_2EBC)]^+$ is more rhombic than that of $[Mn^{IV}(OH)_2(Me_2EBC)]^{2+}$ (E/D = 0.22(1) and 0.15(2), respectively), which is presumably due to the short Mn^{IV}=O bond of $[Mn^{IV}(O)(OH)(Me_2EBC)]^+$. The $[Mn^{IV}(O)(OH)(Me_2EBC)]^+$ complex also appears to display an axial ZFS larger than that of $[Mn^{IV}(OH)_2(Me_2EBC)]^{2+}$, which is in line with previous, albeit quite limited, comparisons of Mn^{IV}=O and Mn^{IV}-OH adducts (Table 6.1).

The axial ZFS parameter and rhombicity for $[Mn^{IV}(OH)_2(Me_2EBC)]^{2+}$ and $[Mn^{IV}(O)(OH)(Me_2EBC)]^+$ were previously determined by variable-temperature, variable-field magnetic circular dichroism (VTVH MCD) experiments.[40] This method has been used to

accurately determine the ZFS parameters of monomeric Mn^{IV}, Co^{II} (S = 3/2) and V^{III} (S = 1) centers, although with larger uncertainties (~2-3 cm^{-1}) than obtained from high-frequency EPR experiments.[33,45,46] The ZFS parameters obtained from the EPR studies described here provide an opportunity for comparison. The VTVH MCD data of both $[Mn^{IV}(OH)_2(Me_2EBC)]^{2+}$ and $[Mn^{IV}(O)(OH)(Me_2EBC)]^{+}$ were well-fit with D = -1.0 and E/D = 0.05.[40] While the magnitude of D from the VTVH MCD method is consistent with EPR-determined values ($D \geq 0.5$ cm^{-1}), the sign of D and the rhombicity determined by this method are in poor agreement with the EPR data. Notably, while VTVH MCD simulations often provide good estimates for magnitudes of D, such analysis tend to be marginally sensitive to the sign of D. In contrast, the sign of D is unequivocally determined from the variable-temperature EPR data.

While systematic calibration studies have been performed for Mn^{II} and Mn^{III} systems, DFT and multireference ab initio methods have not yet been tested for calculating the ZFS parameters of Mn^{IV} complexes. This is largely due to the fact that precise ZFS splitting parameters have only been determined for a limited number of Mn^{IV} complexes (Table 6.1).[8,19-22] In addition, few monomeric Mn^{IV} complexes, and no oxomanganese(IV) complexes, have been structurally characterized by X-ray diffraction.[9,12,21,26] Since $[Mn^{IV}(OH)_2(Me_2EBC)]^{2+}$ and $[Mn^{IV}(O)(OH)(Me_2EBC)]^{+}$ have been structurally characterized by X-ray diffraction and X-ray absorption spectroscopy, respectively, and the ZFS parameters have been determined from EPR spectroscopy, these complexes are well-suited to test DFT and multireference ab initio methods for predicting ZFS parameters of Mn^{IV} centers. Future studies should re-investigate the variable-temperature X-band EPR behavior of $[Mn^{IV}(OH)_2(Me_2EBC)]^{2+}$, as well as the Q-band EPR spectra of both $[Mn^{IV}(OH)_2(Me_2EBC)]^{2+}$ and $[Mn^{IV}(O)(OH)(Me_2EBC)]^{+}$ in order to provide more precise ZFS parameters. Once these parameters have been obtained, one can begin to

evaluate the applicability of various computational methods for computing ZFS parameters for Mn^{IV} centers.

Notes and References.

1. McEvoy, J. P.; Brudvig, G. W., *Chem. Rev.* **2006,** *106*, 4455-4483.
2. Messinger, J.; Badger, M.; Wydrzynski, T., *Proceedings of the National Academy of Sciences* **1995,** *92*, 3209-3213.
3. Pecoraro, V. L.; Baldwin, M., J.; Caudle, M. T.; Hsieh, W.-Y.; Law, N., A., *Pure Appl. Chem.* **1998,** *70*, 925-929.
4. Gunderson, W. A.; Zatsman, A. I.; Emerson, J. P.; Farquhar, E. R.; Que, L.; Lipscomb, J. D.; Hendrich, M. P., *J. Am. Chem. Soc.* **2008,** *130*, 14465-14467.
5. Cotruvo, J. A.; Stich, T. A.; Britt, R. D.; Stubbe, J., *J. Am. Chem. Soc.* **2013**.
6. Leto, D. F.; Jackson, T. A., *J. Biol. Inorg. Chem.* **2014,** *19*, 1-15.
7. Kurahashi, T.; Kikuchi, A.; Tosha, T.; Shiro, Y.; Kitagawa, T.; Fujii, H., *Inorg. Chem.* **2008,** *47*, 1674-1686.
8. Parsell, T. H.; Behan, R. K.; Green, M. T.; Hendrich, M. P.; Borovik, A. S., *J. Am. Chem. Soc.* **2006,** *128*, 8728-8729.
9. Yin, G.; Danby, A. M.; Kitko, D.; Carter, J. D.; Scheper, W. M.; Busch, D. H., *J. Am. Chem. Soc.* **2008,** *130*, 16245-16253.
10. Leto, D. F.; Ingram, R.; Day, V. W.; Jackson, T. A., *Chem. Commun.* **2013,** *49*, 5378-5380.
11. Wu, X.; Seo, M. S.; Davis, K. M.; Lee, Y.-M.; Chen, J.; Cho, K.-B.; Pushkar, Y. N.; Nam, W., *J. Am. Chem. Soc.* **2011,** *133*, 20088-20091.
12. Garcia-Bosch, I.; Company, A.; Cady, C. W.; Styring, S.; Browne, W. R.; Ribas, X.; Costas, M., *Angew. Chem., Int. Ed. Engl.* **2011,** *50*, 5648-5653.
13. Telser, J.; Krzystek, J.; Ozarowski, A., *J. Biol. Inorg. Chem.* **2014,** *19*, 297-318.
14. Duboc, C.; Collomb, M.-N.; Neese, F., *Appl. Magn. Reson.* **2010,** *37*, 229-245.
15. Duboc, C.; Ganyushin, D.; Sivalingam, K.; Collomb, M.-N. l.; Neese, F., *J. Phys. Chem. A* **2010,** *114*, 10750-10758.
16. Krzystek, J.; Yeagle, G. J.; Park, J.-H.; Britt, R. D.; Meisel, M. W.; Brunel, L.-C.; Telser, J., *Inorg. Chem.* **2003,** *42*, 4610-4618.
17. Mossin, S.; Weihe, H.; Barra, A. L., *J. Am. Chem. Soc.* **2002,** *124*, 8764.
18. Gätjens, J.; Sjödin, M.; Pecoraro, V. L.; Un, S., *J. Am. Chem. Soc.* **2007,** *129*, 13825-13827.
19. Gupta, R.; Taguchi, T.; Borovik, A. S.; Hendrich, M. P., *Inorg. Chem.* **2013,** *52*, 12568-12575.
20. Romain, S.; Baffert, C.; Duboc, C.; Leprêtre, J.-C.; Deronzier, A.; Collomb, M.-N., *Inorg. Chem.* **2009,** *48*, 3125-3131.
21. Weyhermüller, T.; Paine, T. K.; Bothe, E.; Bill, E.; Chaudhuri, P., *Inorg. Chim. Acta* **2002,** *337*, 344-356.
22. Duboc, C.; Collomb, M.-N., *Chem. Commun.* **2009**, 2715-2717.
23. Camenzind, M. J.; Hollander, F. J.; Hill, C. L., *Inorg. Chem.* **1983,** *22*, 3776-3784.
24. Davies, J. J.; Smith, S. R. P.; Wertz, J. E., *Physical Review* **1969,** *178*, 608.
25. Dutta, S.; Basu, P.; Chakravorty, A., *Inorg. Chem.* **1991,** *30*, 4031-4037.

26. Hartman, J. R.; Foxman, B. M.; Cooper, S. R., *Inorg. Chem.* **1984,** *23*, 1381-1387.
27. Min, K. S.; Weyermuller, T.; Wieghardt, K., *Dalton Trans.* **2004**, 178-186.
28. Mukhopadhyay, R.; Bhattacharjee, S.; K. Pal, C.; Karmakar, S.; Bhattacharyya, R., *J. Chem. Soc., Dalton Trans.* **1997**, 2267-2272.
29. Pradeep, C. P.; Zacharias, P. S.; Das, S. K., *Polyhedron* **2005,** *24*, 1410-1416.
30. Rajendiran, T. M.; Kampf, J. W.; Pecoraro, V. L., *Inorg. Chim. Acta* **2002,** *339*, 497-502.
31. Charnock, J. M.; Garner, C. D.; Trautwein, A. X.; Bill, E.; Winkler, H.; Ayougou, K.; Mandon, D.; Weiss, R., *Angew. Chem., Int. Ed. Engl.* **1995,** *34*, 343-346.
32. Kessissoglou, D. P.; Li, X.; Butler, W. M.; Pecoraro, V. L., *Inorg. Chem.* **1987,** *26*, 2487-2492.
33. Bane, K.; Geiger, R. A.; Chabolla, S. A.; Jackson, T. A., *Inorg. Chim. Acta* **2012,** *380*, 135-140.
34. Krzystek, J.; Ozarowski, A.; Telser, J., *Coord. Chem. Rev.* **2006,** *250*, 2308-2324.
35. Duboc, C.; Phoeung, T.; Zein, S.; Pécaut, J.; Collomb, M.-N.; Neese, F., *Inorg. Chem.* **2007,** *46*, 4905-4916.
36. Rich, J.; Castillo, C. E.; Romero, I.; Rodríguez, M.; Duboc, C.; Collomb, M.-N., *Eur. J. Inorg. Chem.* **2010,** *2010*, 3658-3665.
37. Zein, S.; Duboc, C.; Lubitz, W.; Neese, F., *Inorg. Chem.* **2007,** *47*, 134-142.
38. Neese, F., *J. Am. Chem. Soc.* **2006,** *128*, 10213-10222.
39. Sawant, S. C.; Wu, X.; Cho, J.; Cho, K.-B.; Kim, S. H.; Seo, M. S.; Lee, Y.-M.; Kubo, M.; Ogura, T.; Shaik, S.; Nam, W., *Angew. Chem., Int. Ed. Engl.* **2010,** *49*, 8190-8194.
40. Chattopadhyay, S.; Geiger, R. A.; Yin, G.; Busch, D. H.; Jackson, T. A., *Inorg. Chem.* **2010,** *49*, 7530-7535.
41. Stoll, S.; Schweiger, A., *J. Magn. Reson.* **2006,** *178*, 42-55.
42. Que, L., *Physical Methods in Bioinorganic Chemistry: Spectroscopy and Magnetism*. University Science Books: 2000.
43. Lassalle-Kaiser, B.; Hureau, C.; Pantazis, D. A.; Pushkar, Y.; Guillot, R.; Yachandra, V. K.; Yano, J.; Neese, F.; Anxolabehere-Mallart, E., *Energy Environ. Sci.* **2010,** *3*, 924-938.
44. Smoukov, S. K.; Telser, J.; Bernat, B. A.; Rife, C. L.; Armstrong, R. N.; Hoffman, B. M., *J. Am. Chem. Soc.* **2002,** *124*, 2318-2326.
45. Krzystek, J.; Fiedler, A. T.; Sokol, J. J.; Ozarowski, A.; Zvyagin, S. A.; Brunold, T. C.; Long, J. R.; Brunel, L.-C.; Telser, J., *Inorg. Chem.* **2004,** *43*, 5645-5658.
46. Krzystek, J.; Zvyagin, S. A.; Ozarowski, A.; Fiedler, A. T.; Brunold, T. C.; Telser, J., *J. Am. Chem. Soc.* **2004,** *126*, 2148-2155.

Chapter 7

Summary

This work has been reproduced in part from: R. A. Geiger, D. F. Leto, S. Chattopadhyay, P. Dorlet, E. Anxolabéhère-Mallart, and T. A. Jackson, *Inorg. Chem.*, 2011, **50**, 10190-10203, with permission from the American Chemical Society; D. F. Leto, S. Chattopadhyay, V. W. Day and T. A. Jackson, *Dalton Trans.*, 2013, **42**, 13014 - 13025, with permission from The Royal Society of Chemistry; D. F. Leto, R. Ingram, V. W. Day and T. A. Jackson, *Chem. Commun.*, 2013, **49**, 5378-5380 with permission from The Royal Society of Chemistry; D. F. Leto and T. A. Jackson, *Inorg. Chem.*, 2014, *submitted.*

This dissertation has focused on the synthesis, characterization, and reactivity of small molecule model complexes featuring peroxo-, hydroxo-, and oxo-manganese motifs. A novel mononuclear Mn^{II} complex, $[Mn^{II}(N4py)(OTf)](OTf)$, supported by a pentadentate aminopyridyl ligand, was synthesized, and its conversion to a peroxo- and oxo-manganese species using various oxidants was investigated. For example, when an acetonitrile solution of $[Mn^{II}(N4py)(OTf)]^{+}$ is treated with superoxide at -40 ^{o}C, a peroxomanganese(III) intermediate, $[Mn^{III}(O_2)(N4py)]^{+}$ is formed. The geometric and electronic structure of $[Mn^{III}(O_2)(N4py)]^{+}$ was investigated using a combined spectroscopic and computational approach. Electronic absorption, magnetic circular dichroism (MCD) and variable-temperature, variable-field MCD data, coupled with DFT and TD-DFT investigations of hypothetical structural models, provide strong evidence that $[Mn^{III}(O_2)(N4py)]^{+}$ consists of a side-on peroxomanganese(III) unit with the supporting N4py ligand bound in an unusual tetradentate fashion. Hexacoordination is thus strongly preferred for peroxomanganese(III) adducts, and dissociation of a pyridine arm is thermodynamically favored.

The reactivity of $[Mn^{II}(N4py)(OTf)]^{+}$ with superoxide and hydrogen peroxide was further explored, revealing a reaction landscape that is unique among synthetic mononuclear Mn^{II} complexes. The peroxomanganese(III) species, $[Mn^{III}(O_2)(N4py)]^{+}$, generated from addition of superoxide to a solution of $[Mn^{II}(N4py)(OTf)]^{+}$, was subsequently shown to react with additional $[Mn^{II}(N4py)(OTf)]^{+}$ to form a heterovalent bis(μ-oxo)dimanganese(III,IV) complex, $[Mn^{III}Mn^{IV}(\mu\text{-}O)_2(N4py)_2]^{3+}$. This conversion of two Mn^{II} species to an oxo-bridged $Mn^{III}Mn^{IV}$ compound using O_2^{-} as oxidant mimics the formation of the $Mn^{III}Mn^{IV}$ form of Mn ribonucleotide reductase. The oxo-bridged dimer was independently prepared by treating $[Mn^{II}(N4py)(OTf)]^{+}$ with excess hydrogen peroxide and was characterized structurally by X-ray

crystallography, which revealed the N4py was ligand bound in a tetradentatate fashion. The tetradentate binding of the N4py ligand in the X-ray diffraction (XRD) structure of $[Mn^{III}Mn^{IV}(\mu\text{-}O)_2(N4py)_2]^{3+}$ supports our conclusion that the N4py ligand is bound in a tetradentate fashion in the peroxomanganese(III) complex $[Mn^{III}(O_2)(N4py)]^{+}$ from spectroscopic and computational studies**.**

A mononuclear oxomanganese(IV) complex, $[Mn^{IV}(O)(N4py)]^{2+}$, was generated at room temperature by the addition of an oxygen-atom transfer agent, iodosylbenzene, to a solution of $[Mn^{II}(N4py)(OTf)]^{+}$. This oxomanganese(IV) complex was characterized by various spectroscopic methods, such as electronic absorption, electron paramagnetic resonance (EPR), MCD, and Mn K-edge X-ray absorption spectroscopies. Detailed kinetic investigations on the reactivity of $[Mn^{IV}(O)(N4py)]^{2+}$ with hydrocarbons, including determination of activation parameters and kinetic isotope effect, revealed the reaction proceeds by an initial hydrogen-atom abstraction. $[Mn^{IV}(O)(N4py)]^{2+}$ is moderately stable at room temperature, yet is one of the more reactive non-porphyrinic oxomanganese(IV) complexes for C-H bond activation. The basis for the high reactivity of this complex is currently unknown, although it is notable that $[Mn^{IV}(O)(N4py)]^{2+}$ displays a relatively high one-electron reduction potential of 800 mV (versus SCE).

Few mononuclear hyroxo- and oxo-manganese(IV) complexes have been characterized by Mn K-edge X-ray absorption spectroscopy (XAS), a technique featuring prominently in the study of Mn enzymes and synthetic Mn compounds. To this end, Mn K-edge XAS was used to gain insights into the geometric and electronic structures of $[Mn^{II}(Cl)_2(Me_2EBC)]$, $[Mn^{IV}(OH)_2(Me_2EBC)]^{2+}$ and $[Mn^{IV}(O)(OH)(Me_2EBC)]^{+}$, a series of complexes supported by the same tetradentate, macrocyclic ligand. Analysis of extended X-ray absorption fine structure

(EXAFS) data for $[Mn^{IV}(O)(OH)(Me_2EBC)]^+$ revealed Mn–O scatterers at 1.71 and 1.84 Å and Mn–N scatterers at 2.11 Å. The EXAFS analysis provided the first unambiguous support for the formulation of this species as an oxohydroxomanganese(IV) adduct. EXAFS-determined structural parameters for $[Mn^{II}(Cl)_2(Me_2EBC)]$ and $[Mn^{IV}(OH)_2(Me_2EBC)]^{2+}$ are consistent with previously-reported crystal structures. The Mn pre-edge energies and intensities of these complexes were examined within the context of data for other oxo- and hydroxomanganese(IV) adducts, and time-dependent density functional theory (TD-DFT) computations were used to predict pre-edge properties for all compounds considered. This combined experimental and computational analysis revealed a correlation between the Mn–O(H) distances and pre-edge peak areas of Mn^{IV}=O and Mn^{IV}–OH complexes, but this trend was strongly modulated by the Mn^{IV} coordination geometry. Mn 3d-4p mixing, which primarily accounts for the pre-edge intensities, is not solely a function of the Mn–O(H) bond length; the coordination geometry also has a large effect on the distribution of pre-edge intensity. For tetragonal Mn^{IV}=O centers, more than 90% of the pre-edge intensity comes from excitations to the Mn=O σ* MO. Trigonal bipyramidal oxomanganese(IV) centers likewise feature excitations to the Mn=O σ* MO, but also show intense transitions to $3d_{x^2-y^2}$ and $3d_{xy}$ MOs because of enhanced 3d-$4p_{x,y}$ mixing. This gives rise to a broader pre-edge feature for trigonal Mn^{IV}=O adducts. These results underscore the importance of reporting experimental pre-edge areas rather than peak heights. Finally, the TD-DFT method was applied to understand the pre-edge properties of a recently reported S = 1 Mn^{V}=O adduct.

The zero-field splitting (ZFS) parameters of $[Mn^{IV}(OH)_2(Me_2EBC)]^{2+}$ and $[Mn^{IV}(O)(OH)(Me_2EBC)]^+$ were investigated by X- and Q-band EPR spectroscopy and computer simulations. The ZFS parameters obtained for these two structurally characterized Mn^{IV}

complexes add to the limited information available for oxo- and hydroxomanganese(IV) complexes. In addition, the ZFS parameters of $[Mn^{IV}(OH)_2(Me_2EBC)]^{2+}$ and $[Mn^{IV}(O)(OH)(Me_2EBC)]^{+}$ can be used to evaluate theoretical models for computing ZFS (*i.e.*, DFT and multi-reference ab initio methods) with the goal of developing spectro-structural correlations on the basis of ZFS parameters for Mn^{IV} centers.

Appendix A.1.

A.1.1. X-Ray Diffraction Experiments for $[Mn^{III}Mn^{IV}(\mu\text{-}O)_2(\kappa^4\text{-}N4py)_2]^{3+}$ (3). (A) $[Mn(O)(C_{23}H_{21}N_5)]_2 \bullet 2.8\ CF_3SO_3 \bullet 0.2\ PF_6 \bullet 2\ CH_3CN$ (3a). Green single crystals of the CH_3CN solvated mixed salt, $[Mn(O)(C_{23}H_{21}N_5)]_2 \bullet 2.8\ CF_3SO_3 \bullet 0.2\ PF_6$ (**3a**), obtained from slow diffusion of diethyl ether into an acetonitrile solution of **3** at -20 ^oC, are, at 100(2) K, triclinic, space group $P\ \bar{1} - C_i^1$ (No. 2) with a = 11.0548(5) Å, b = 11.7210(4) Å, c = 12.1500(4) Å, α = 96.673(2)°, β = 105.695(3)°, γ = 91.203(3)°, V = 1503.1(1) $Å^3$ and Z = 1 formula units {d_{calcd} = 1.552 g/cm^3; μ_a(CuKα) = 5.235 mm^{-1}}. A full set of unique diffracted intensities (5685 frames with counting times of 5 to 12 seconds and an ω- or ϕ-scan width of 0.50°) was measured[1] for a single-domain specimen using monochromated CuKα radiation (λ= 1.54178 Å) on a Bruker Proteum Single Crystal Diffraction System equipped with Helios multilayer optics, an APEX II CCD detector and a Bruker MicroSTAR microfocus rotating anode X-ray source operating at 45 kV and 60 mA. Lattice constants were determined with the Bruker SAINT software package using peak centers for 5256 reflections.[2] A total of 13860 integrated reflection intensities having 2θ(CuKα) < 139.58° were produced using the Bruker program SAINT;[1] 5187 of these were unique and gave R_{int} = 0.046. The data were corrected empirically for variable absorption effects using equivalent reflections; the relative transmission factors ranged from 0.629 to 1.000. The Bruker software package SHELXTL was used to solve the structure using "direct methods" techniques. All stages of weighted full-matrix least-squares refinement were conducted using F_o^2 data with the SHELXTL Version 2010.3-0 software package.[3]

All entities appear to be disordered. The Mn^{III}/Mn^{IV} mixed-valence $\{[Mn(O)(C_{23}H_{21}N_5)]_2\}^{3+}$ cationic dimer utilizes a crystallographic inversion center at (0, ½, ½) in the unit cell. The first triflate anion has two (61% / 39%) different orientations in the asymmetric unit. The second triflate is disordered about a crystallographic inversion center at (0, 1, 0) in the

unit cell and shares this volume with a $[PF_6]^-$ anion 20% of the time. The final structural model incorporated anisotropic thermal parameters for all nonhydrogen atoms of the metal dimer, CH_3CN solvent molecule, both partial-occupancy orientations for the first $[O_3SCF_3]^-$ anion, the S and three F atoms of the second $[O_3SCF_3]^-$ anion and the P atom of the $[PF_6]^-$ anion. Isotropic thermal parameters were utilized for the oxygen and carbon atoms of the second $[O_3SCF_3]^-$ anion, the F atoms of the $[PF_6]^-$ anion and all hydrogen atoms of the metal dimer and CH_3CN solvent molecule of crystallization.

Surprisingly, even with all of this disorder, a difference Fourier clearly revealed all of the hydrogen atoms bonded to carbon atoms in the dimer. This permitted identification of the non-coordinated nitrogen atom N(5) since it had no significant residual electron density near it but carbon atom C(20) did. The hydrogen atoms were initially included in the structural model as individual isotropic atoms whose parameters were allowed to vary in least-squares refinement cycles. They were later placed at fixed idealized positions (sp^2- or sp^3-hybridized geometry and C-H bond lengths of 0.95 – 1.00 Å) with variable isotropic thermal parameters. The acetonitrile methyl group was incorporated in the structural model as a rigid group (using idealized sp^3-hybridized geometry and C–H bond lengths of 0.98 Å) with idealized "staggered" geometry. The methyl hydrogen atoms were assigned fixed isotropic thermal parameters with values 1.50 times the equivalent isotropic thermal parameter of the methyl carbon atom. The bond lengths and angles for the second triflate and the minor-occupancy (39%) orientation for the first triflate were restrained to have values similar to those for the major-occupancy (61%) orientation of the first triflate anion. Octahedral geometry was imposed on the $[PF_6]^-$ anion by restraining the nonbonded F---F distances to be appropriate multiples of a free-variable P-F bond length that refined to a final value of 1.36(1) Å. The anisotropic thermal parameters of the second triflate

sulfur atom, S(2), and the $[PF_6]^-$ phosphorus atom, P, were also restrained to have identical values.

A total of 529 parameters were refined using 68 restraints, 5187 data and weights of w = 1/ $[\sigma^2(F^2) + (0.1982\ P)^2 + (1.2325\ P)]$, where P = $(F_O^2 + 2F_C^2)/ 3$. Final agreement factors at convergence for **3a** are: R_1(unweighted, based on F) = 0.089 for 4319 independent absorption-corrected "observed" reflections having 2θ(CuKα) < 139.58° and I > 2σ(I); R_1(unweighted, based on F) = 0.099 and wR_2(weighted, based on F^2) = 0.262 for all 5187 independent absorption-corrected reflections having 2θ(CuKα)< 139.58°. The largest shift/s.u. was 0.001 in the final refinement cycle. The final difference map had maxima and minima of 0.92 and -0.68 $e^-/Å^3$, respectively.

(B) $[Mn(O)(C_{23}H_{21}N_5)]_2 \bullet 3\ PF_6 \bullet 0.5\ H_2O$ (3b). Green single crystals of the hydrated salt, $[Mn(O)(C_{23}H_{21}N_5)]_2 \bullet 3\ PF_6 \bullet 0.5\ H_2O$ (**3b**), obtained from slow diffusion of diethyl ether into butyronitrile solution of **3** at -20 °C, are, at 100(2) K, monoclinic, space group P21/c – C_{2h}^5 (No. 2) with a = 25.7399(6) Å, b = 12.5771(3) Å, c = 17.9093(4) Å, β = 105.427(1)°, V = 5588.9(2) $Å^3$ and Z = 4 formula units {d_{calcd} = 1.568 g/cm^3; μ_a(CuKα) = 5.472 mm^{-1}}. A full set of unique diffracted intensities (5575 frames with counting times of 5 to 12 seconds and an ω- or ϕ-scan width of 0.50°) was measured for a single-domain specimen using monochromated CuKα radiation (λ= 1.54178 Å) on a Bruker Proteum Single Crystal Diffraction System equipped with Helios multilayer optics, an APEX II CCD detector and a Bruker MicroSTAR microfocus rotating anode X-ray source operating at 45 kV and 60 mA. Lattice constants were determined with the Bruker SAINT software package using peak centers for 9940 reflections. A total of 47713 integrated reflection intensities having 2θ(CuKα) < 138.44° were produced using the

Bruker program SAINT; 9913 of these were unique and gave R_{int} = 0.044. The data were corrected empirically for variable absorption effects using equivalent reflections; the relative transmission factors ranged from 0.745 to 1.000.

Since the second PF_6^- anion (containing phosphorus atom P2) in this structure is bonded to itself across a crystallographic inversion center it must be disordered. A common occupancy factor for the seven nonhydrogen atoms of this anion refined to 0.51. The occupancy factors were therefore fixed at 0.50 in subsequent refinement cycles. The P1 phosphorus atom of the first PF_6^- anion occupies another crystallographic inversion center. There are therefore a total of three (two half occupancy and two full occupancy) PF_6^- anions per Mn dimer and this is critical to the proper identification of the dinuclear cation with Mn^{III} and Mn^{IV} metals bridged unsymmetrically by two O^{2-} ligands. The asymmetric unit also contains two partial-occupancy water molecules of crystallization in the vicinity of the half-occupancy PF_6^- anion. These water solvent molecules of crystallization are disordered equally between two closely spaced (1.87 Å) sites in the unit cell and presumably represent a half-occupancy water that occupies the same space as the disordered half-occupancy PF_6^- anion; each water oxygen site is occupied a fourth of the time. Whereas the various metric parameters for the anions could have been restrained to have more uniform values, this was not done because it was felt that this might bias the structural results since one must correctly identify the number and nature of the anions in this structure to properly identify the cationic dimer. Nitrogen atoms in the non-coordinated pyridine rings were identified based on the values of equivalent isotropic thermal parameters with all ring atoms modeled as carbon; these also corresponded to the ring orientations observed for compound **3a** where ring hydrogens were observed in a difference Fourier.

The final structural model incorporated anisotropic thermal parameters for all nonhydrogen atoms and isotropic thermal parameters for all hydrogen atoms of the metal dimer. Hydrogen atoms were included in the structural model for the dimer at fixed idealized positions (sp^2- or sp^3-hybridized geometry and C-H bond lengths of 0.95 - 1.00 Å) with isotropic thermal parameters fixed at values 1.2 times the equivalent isotropic thermal parameter of the carbon atom to which they are covalently bonded. The pyridine ring containing carbon atoms C(2B)-C(6B) appears to be disordered between two closely-separated sites. The anisotropic thermal parameters for five carbon atoms [C(3B), C(4B), C(5B), C(6B) and C(22B)] were mildly restrained to have more isotropic values. Hydrogen atoms were not located or included for the disordered partial-occupancy water molecules of crystallization.

A total of 745 parameters were refined using 30 restraints, 9913 data and weights of $w = 1/ [\sigma^2(F^2) + (0.1375\ P)^2 + (39.086\ P)]$, where $P = (F_O^2 + 2F_C^2)/ 3$. Final agreement factors at convergence for **3b** are: R_1(unweighted, based on F) = 0.126 for 7847 independent absorption-corrected "observed" reflections having $2\theta(CuK\alpha) < 138.44°$ and $I > 2\sigma(I)$; R_1(unweighted, based on F) = 0.146 and wR_2(weighted, based on F^2) = 0.330 for all 9913 independent absorption-corrected reflections having $2\theta(CuK\alpha) < 138.44°$. The largest shift/s.u. was 0.000 in the final refinement cycle. The final difference map had maxima and minima of 1.91 and -1.13 $e^-/Å^3$, respectively.

Table A.1. XRD structural parameters for $[Mn^{III}Mn^{IV}(\mu\text{-}O)_2(N4py)_2](OTf)_{2.8}(PF_6)_{0.2}$ (**3a**) and $[Mn^{III}Mn^{IV}(\mu\text{-}O)_2(N4py)_2](PF_6)_3$ (**3b**)

	$[Mn^{III}Mn^{IV}(\mu\text{-}O)_2(N4py)_2]\bullet (OTf)_{2.8}(PF_6)_{0.2}$ **(3a)**	$[Mn^{III}Mn^{IV}(\mu\text{-}O)_2(N4py)_2](PF_6)_3$ **(3b)**
Empirical formula	$C_{52.80}H_{48}F_{9.60}Mn_2N_{12}O_{10.40}P_{0.20}S_{2.80}$	$C_{46}H_{42}F_{18}Mn_2N_{10}O_{2.50}P_3$
Formula weight	1405.27	1319.69
Temperature	100(2) K	100(2) K
Wavelength	1.54178 Å	1.54178 Å
Crystal system	Triclinic	Monoclinic
Space group	$P\bar{1} - C_i^1$ (No. 2)	$P2_1/c - C_{2h}^5$ (No.14)
Unit cell dimensions	a = 11.0548(5) Å	a = 25.7399(6) Å
	b = 11.7210(4) Å	b = 12.5771(3) Å
	c = 12.1500(4) Å.	c = 17.9093(4) Å
	α = 96.673(2)°	α = 90°
	β = 105.695(3)°	β = 105.4270(10)°
	γ = 91.203(3)°	γ = 90°
Volume	1503.1(1) $Å^3$	5588.9(2) $Å^3$
Z	1	4
Density (calculated)	1.552 Mg/m^3	1.568 Mg/m^3
Absorption coefficient	5.235 mm^{-1}	5.472 mm^{-1}
F(000)	716	2660
Crystal size	0.13 x 0.06 x 0.01 mm^3	0.08 x 0.07 x 0.02 mm^3
Theta range for data collection	3.80 to 69.79°.	3.56 to 69.22°.
Index ranges	-13<=h<=11	-30<=h<=30
	-14<=k<=10	-12<=k<=14
	-14<=l<=14	-20<=l<=21
Reflections collected	13860	47713
Independent reflections	5187 [R(int) = 0.046]	9913 [R(int) = 0.044]
Completeness to theta = 66.00°	94.6 %	97.9 %
Absorption correction	Multi-scan	Multi-scan
Max. and min. transmission	1.000 and 0.629	1.000 and 0.745
Refinement method	Full-matrix least-squares on F^2	Full-matrix least-squares on F^2
Data / restraints / parameters	5187 / 68 / 529	9913 / 30 / 745
Goodness-of-fit on F^2	1.015	1.092
Final R indices [I>2sigma(I)]	R_1 = 0.089, wR_2 = 0.250	R_1 = 0.126, wR_2 = 0.319
R indices (all data)	R_1 = 0.099, wR_2 = 0.262	R_1 = 0.146, wR_2 = 0.330
Largest diff. peak and hole	0.92 and -0.68 $e/Å^3$	1.91 and -1.13 $e/Å^3$

$R_1 = \Sigma \, ||F_O| - |F_C|| \, / \, \Sigma \, |F_O|$

$wR_2 = \{ \, \Sigma \, [w(F_O^2 - F_C^2)^2] \, / \, \Sigma \, [w(F_O^2)^2] \, \}^{1/2}$

A.1.2. X-Ray Diffraction Experiments for [Mn^{II}(N4py)(OTf)](OTf). Yellow crystals of $[Mn(C_{23}H_{21}N_5)(O_3SCF_3)]_2[O_3SCF_3][ClO_4]$ are, at 100(2) K, monoclinic, space group $P2_1 - C_2^2$ (No. 4).[4] with **a** = 10.178(3) Å, **b** = 19.832(5) Å, **c** = 14.229(4) Å, **β** = 107.156(4)°, V = 2744(1) $Å^3$ and Z = 2 formula units {d_{calcd} = 1.684 g/cm^3; μ_a(MoKα) = 0.728 mm^{-1}} (Table A.1.2). A full hemisphere of diffracted intensities (1850 10-second frames with an ω scan width of 0.30°) was measured for a single-domain specimen using graphite-monochromated MoKα radiation (λ= 0.71073 Å) on a Bruker SMART APEX CCD Single Crystal Diffraction System.[1] X-rays were provided by a fine-focus sealed X-ray tube operated at 50 kV and 30 mA. Lattice constants were determined with the Bruker SAINT software package using peak centers for 7778 reflections. A total of 25171 integrated reflection intensities having 2θ((MoKα) < 58.36° were produced using the Bruker program SAINT;[2] 13119 of these were unique and gave R_{int} = 0.058 with a coverage which was 92.7% complete. The data were corrected empirically for variable absorption effects using equivalent reflections; the relative transmission factors ranged from 0.926 to 1.000. The Bruker software package SHELXTL was used to solve the structure using "direct methods" techniques. All stages of weighted full-matrix least-squares refinement were conducted using F_o^2 data with the SHELXTL Version 6.10 software package.[3]

The final structural model incorporated anisotropic thermal parameters for all nonhydrogen atoms and isotropic thermal parameters for all hydrogen atoms. All hydrogen atoms were included in the structural model as idealized atoms (assuming sp^2- or sp^3-hybridization of the carbon atoms and C-H bond lengths of 0.95 - 1.00 Å). The isotropic thermal parameters of all hydrogen atoms were fixed at values 1.2 times the equivalent isotropic thermal parameter of the carbon atom to which they are covalently bonded. A total of 784 parameters were refined using 1 restraint, 13119 data and weights of $w = 1/ [\sigma^2(F^2) + (0.0580\ P)^2]$ where P =

$[F_O^2 + 2F_C^2] / 3$. Final agreement factors at convergence are: R_1(unweighted, based on F) = 0.060 for 10673 independent absorption-corrected "observed" reflections having 2θ (MoKα) < 58.36° and I > 2σ(I); R_1(unweighted, based on F) = 0.074 and wR_2(weighted, based on F^2) = 0.125 for all 13119 independent absorption-corrected reflections having 2θ(MoKα) < 58.36°. The largest shift/s.u. was 0.000 in the final refinement cycle. The final difference map had maxima and minima of 0.88 and -0.44 $e^-/Å^3$, respectively. The absolute structure was determined experimentally using anomalous dispersion of the X-rays; the Flack absolute structure parameter refined to a final value of 0.00(2).

The asymmetric unit contains two $[Mn(C_{23}H_{21}N_5)(O_3SCF_3)]^+$ cations, one $(O_3SCF_3)^-$ anion and one $(ClO_4)^-$ anion (Figure A.1.1). The $(ClO_4)^-$ anion was introduced in one of the final steps in the ligand synthesis when the N4py perchlorate salt is isolated.[5-6]

Table A.1.2. Crystal data and structure refinement for $Mn(C_{23}H_{21}N_5)(O_3SCF_3)]_2[O_3SCF_3][ClO_4]$.

Empirical formula	$C_{49}H_{42}ClF_9Mn_2N_{10}O_{13}S_3$	
Formula weight	1391.44	
Temperature	100(2) K	
Wavelength	0.71073 Å	
Crystal system	Monoclinic	
Space group	$P2_1 - C_2^2$ (No. 4)	
Unit cell dimensions	**a** = 10.178(3) Å	α = 90000°
	b = 19.832(5) Å	β = 107.156(4)°
	c = 14.229(4) Å	γ = 90.000°
Volume	2744.4(12) $Å^3$	
Z	2	
Density (calculated)	1.684 Mg/m^3	
Absorption coefficient	0.728 mm^{-1}	
F(000)	1412	
Crystal size	0.26 x 0.26 x 0.13 mm^3	
Theta range for data collection	2.42° to 29.18°	
Index ranges	$-13 \leq h \leq 13$, $-27 \leq k \leq 27$, $-19 \leq l \leq 18$	
Reflections collected	25171	
Independent reflections	13119 [R_{int} = 0.058]	
Completeness to theta = 29.18°	92.7 %	
Absorption correction	Multi-scans	
Max. and min. transmission	1.000 and 0.926	
Refinement method	Full-matrix least-squares on F^2	
Data / restraints / parameters	13119 / 1 / 784	
Goodness-of-fit on F^2	0.988	
Final R indices [I>2sigma(I)]	R_1 = 0.060, wR_2 = 0.119	
R indices (all data)	R_1 = 0.074, wR_2 = 0.125	
Absolute structure parameter	0.000(15)	
Largest diff. peak and hole	0.88 and -0.44 $e^-/Å^3$	

$R_1 = \Sigma \, ||F_O| - |F_C|| \, / \, \Sigma \, |F_O|$

$wR_2 = \{ \, \Sigma \, [w(F_O^2 - F_C^2)^2] \, / \, \Sigma \, [w(F_O^2)^2] \, \}^{1/2}$

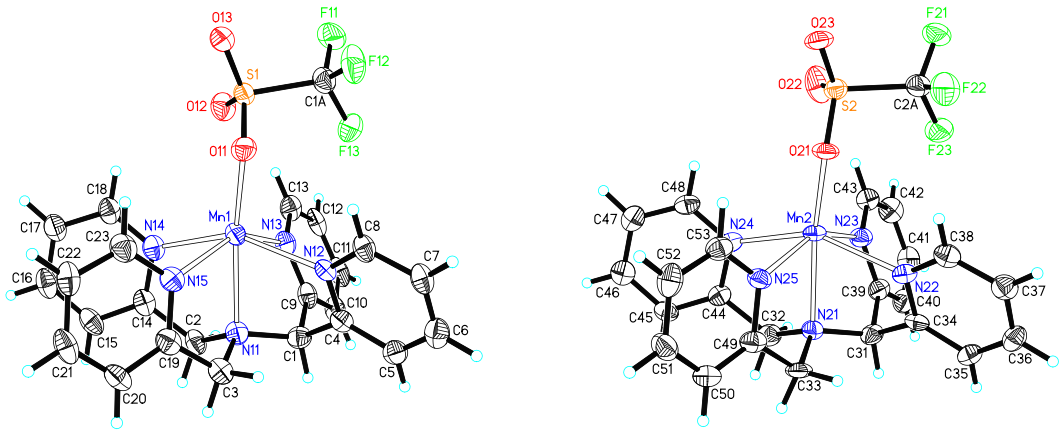

Figure A.1.1. Molecular structures of the two $[Mn^{II}(N4py)(OTf)]^{+}$ cations found in the asymmetric unit of $[Mn(C_{23}H_{21}N_5)(O_3SCF_3)]_2[O_3SCF_3][ClO_4]$, showing 50% probability ellipsoids.

Table A.1.3. Selected bond lengths (Å) and angles (°) for $[Mn(C_{23}H_{21}N_5)(O_3SCF_3)]_2[O_3SCF_3][ClO_4]$.

Mn(1)-O(11)	2.125(3)	O(11)-Mn(1)-N(14)	116.80(13)	N(14)-Mn(1)-N(11)	76.53(14)
Mn(1)-N(14)	2.255(4)	O(11)-Mn(1)-N(13)	117.19(13)	N(13)-Mn(1)-N(15)	148.25(14)
Mn(1)-N(13)	2.271(4)	O(11)-Mn(1)-N(15)	94.42(12)	N(13)-Mn(1)-N(12)	81.18(13)
Mn(1)-N(15)	2.271(4)	O(11)-Mn(1)-N(12)	92.09(12)	N(13)-Mn(1)-N(11)	74.17(13)
Mn(1)-N(12)	2.278(4)	O(11)-Mn(1)-N(11)	161.24(13)	N(15)-Mn(1)-N(12)	95.63(13)
Mn(1)-N(11)	2.289(4)	N(14)-Mn(1)-N(13)	88.81(13)	N(15)-Mn(1)-N(11)	74.57(13)
		N(14)-Mn(1)-N(15)	76.68(13)	N(12)-Mn(1)-N(11)	74.32(13)
		N(14)-Mn(1)-N(12)	150.76(14)	S(1)-O(11)-Mn(1)	119.9(2)
Mn(2)-O(21)	2.107(3)	O(21)-Mn(2)-N(24)	115.8(1)	N(24)-Mn(2)-N(21)	76.1(1)
Mn(2)-N(24)	2.247(4)	O(21)-Mn(2)-N(23)	116.0(1)	N(23)-Mn(2)-N(25)	150.5(1)
Mn(2)-N(23)	2.265(4)	O(21)-Mn(2)-N(25)	93.1(1)	N(23)-Mn(2)-N(22)	79.9(1)
Mn(2)-N(25)	2.231(4)	O(21)-Mn(2)-N(22)	94.4(1)	N(23)-Mn(2)-N(21)	74.7(1)
Mn(2)-N(22)	2.288(4)	O(21)-Mn(2)-N(21)	162.8(1)	N(25)-Mn(2)-N(22)	93.5(1)
Mn(2)-N(21)	2.308(3)	N(24)-Mn(2)-N(23)	89.8(1)	N(25)-Mn(2)-N(21)	75.9(1)
		N(24)-Mn(2)-N(25)	81.5(1)	N(22)-Mn(2)-N(21)	73.6(1)
		N(24)-Mn(2)-N(22)	149.6(1)	S(2)-O(21)-Mn(2)	132.1(2)

References.

1. *Data Collection: SMART Software Reference Manual*. Bruker-AXS. 5465 E. Cheryl Parkway, Madison, WI 53711-5373 USA, 1998.
2. Data Reduction: SAINT Software Reference Manual (1998). Bruker-AXS, 6300 Enterprise Dr., Madison, WI 53719-1173, USA.
3. G. M. Sheldrick (2000). SHELXTL Version 6.10 Reference Manual. Bruker-AXS, 5465 E. Cheryl Parkway, Madison, WI 53711-5373 USA.
4. International Tables for Crystallography, Vol A, 4th ed., Kluwer: Boston (1996).
5. Chang, J.; Plummer, S.; Berman, E. S. F.; Striplin, D.; Blauch, D., *Inorg. Chem.* **2004,** *43*, 1735-1742.
6. Lubben, M.; Meetsma, A.; Wilkinson, E. C.; Feringa, B.; Que, L., Jr., *Angew. Chem., Int. Ed. Engl.* **1995,** *34*, 1512-1514.

Appendix A.2.

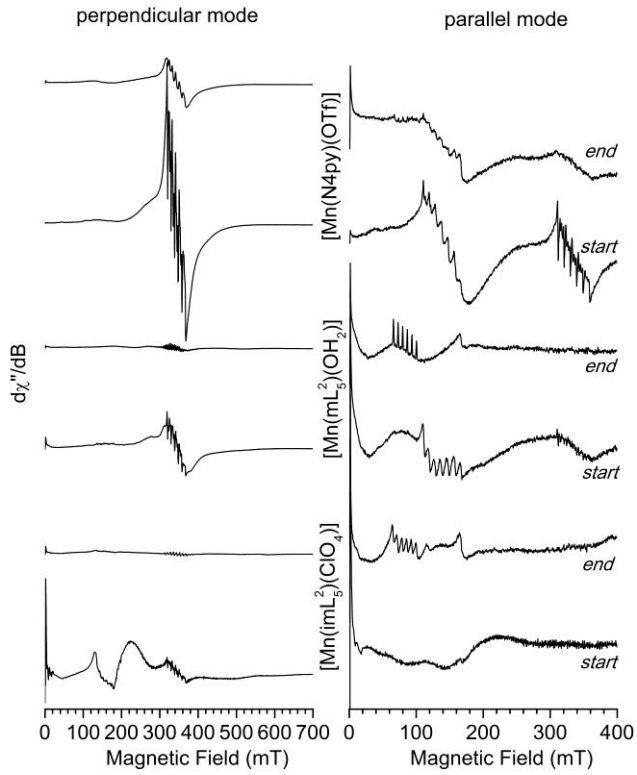

Figure A.2.1. Electron paramagnetic resonance spectra for the solutions of complexes before and after the in situ electrochemical generation of superoxide, recorded with perpendicular-mode (left panels) and parallel-mode (right panels) detection. Experimental conditions: microwave frequencies 9.63 GHz (⊥) and 9.41 GHz (//); microwave power 1 mW; field modulation amplitude 0.7 mT; T = 4 K.

Table A.2.1. Gaussian Parameters used to Fit Electronic Absorption and Magnetic Circular Dichroism Data Collected for $[Mn^{III}(O_2)(mL_5^2)]^+$, $[Mn^{III}(O_2)(imL_5^2)]^+$, and $[Mn^{III}(O_2)(N4py)]^+$

	$[Mn^{III}(O_2)(imL_5^2)]^+$			$[Mn^{III}(O_2)(mL_5^2)]^+$			$[Mn^{III}(O_2)(N4py)]^+$		
band	energy (cm^{-1})	fwhm (cm^{-1})	$f_{exp} \times 10^3$	energy (cm^{-1})	fwhm (cm^{-1})	$f_{exp} \times 10^3$	energy (cm^{-1})	fwhm (cm^{-1})	$f_{exp} \times 10^3$
1	Abs: 17 200	3663	3.58	Abs: 17 120	4496	1.84	Abs: 16 300	4579	3.64
	MCD: 16 720	3330		MCD: 15 325	4163		MCD: 15 064	3663	
2	Abs: 22 800	3830	0.883	Abs: 23 000	4163	1.38	Abs: 23 000	4579	2.85
	MCD: 23 800	3830		MCD: 21 500	4496		MCD: 23 670	3330	
3	Abs: 27 000	4163	3.53	Abs: 26 900	4163	2.68	Abs: 27 510	4329	5.28
	MCD: 26 400	4163		MCD: 25 900	4995		MCD: 27 710	3913	
4	Abs: 32 200	4163	13.8	Abs: 31 000	4163	14.39	Abs: 31 044	4163	16.38
	MCD: 32 800	4163		MCD: 30 900	4995		MCD: 30 960	3913	

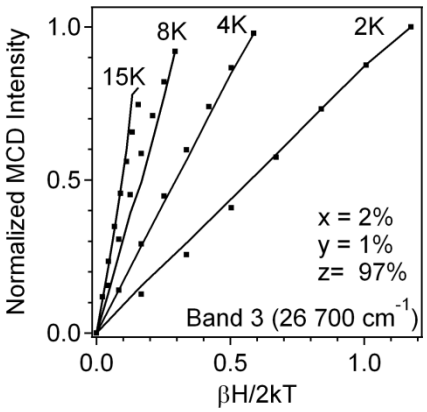

Figure A.2.2. VTVH MCD data collected for $[Mn^{III}(O_2)(mL_5^2)]^+$ (dots) and fits (solid lines) at 26 700 cm^{-1} using D = -2.9 cm^{-1}, E/D = 0.075, g_{iso} = 2.0, and polarizations listed in the inset.

Table A.2.2. Transition Polarizations and ZFS Parameters Determined from fits of VTVH MCD Data Collected for $[Mn^{III}(O_2)(mL_5^2)]^+$, $[Mn^{III}(O_2)(imL_5^2)]^+$, and $[Mn^{III}(O_2)(N4py)]^+$ at the Energies Indicated.

					Polarization (%)		
	band	energy (cm^{-1})	D (cm^{-1})	E/D	x	y	z
$[Mn^{III}(O_2)(mL_5^2)]^+$	1	15 300	-2.9	0.075	15	81	4
		16 700			5	89	6
	2	26 600			2	1	97
	3	30 800			<1	<1	100
$[Mn^{III}(O_2)(imL_5^2)]^+$	1	16 700	-2.0	0.30	33	40	27
	2	25 600			100	<1	<1
	3	32 800			11	2	87
$[Mn^{III}(O_2)(N4py)]^+$	1	15 100	-1.5	0.25	20	29	51
	2	23 700			8	7	85
	3	27 700			<1	2	98
	4	30 000			7	5	89

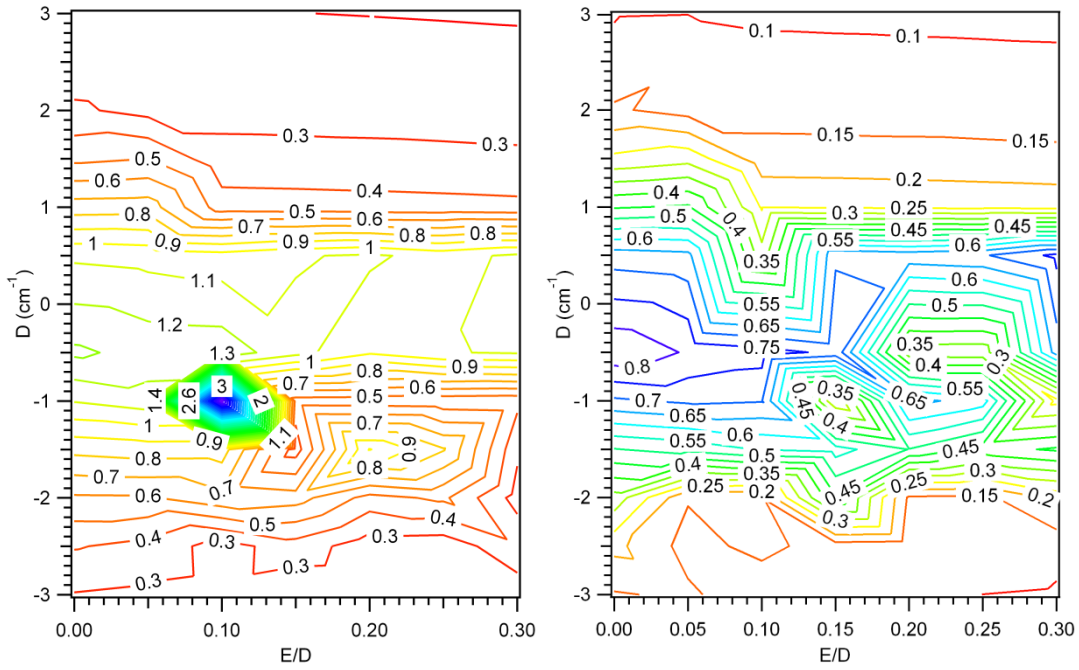

Figure A.2.3. Contour plot of χ^2 values as a function of ZFS parameters *D* and *E/D* for fits of VTVH MCD data collected for $[Mn^{III}(O_2)(mL_5^2)]^+$ at 26 667 (left) and 30 800 (right) cm^{-1}.

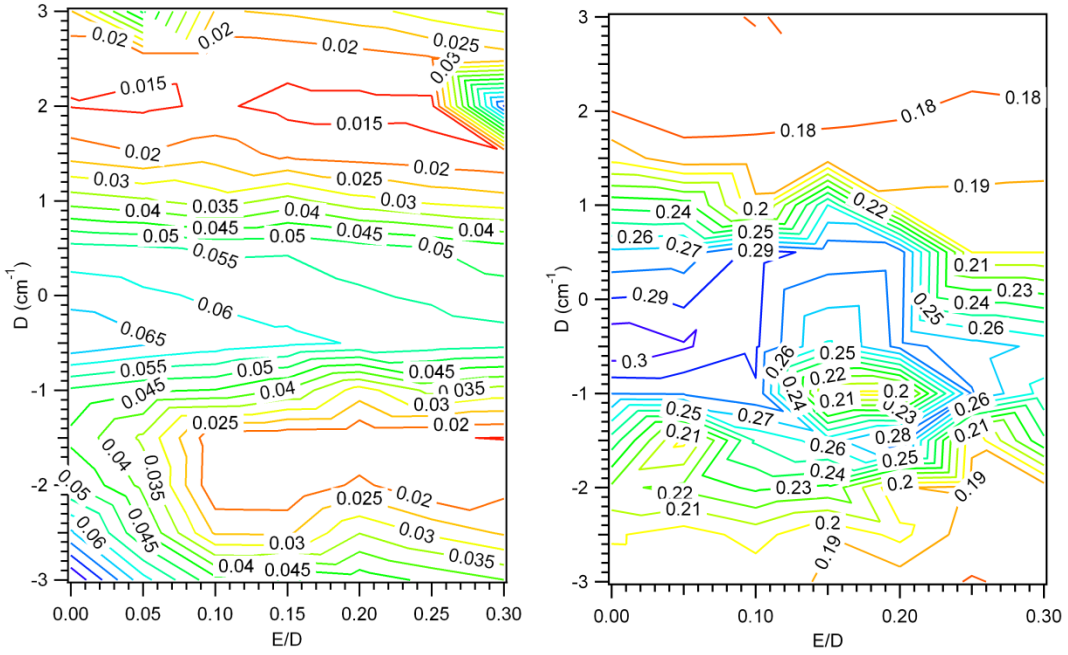

Figure A.2.4. Contour plot of χ^2 values as a function of ZFS parameters *D* and *E/D* for fits of VTVH MCD data collected for $[Mn^{III}(O_2)(imL_5^2)]^+$ at 16 700 (left) and 25 600 (right) cm^{-1}.

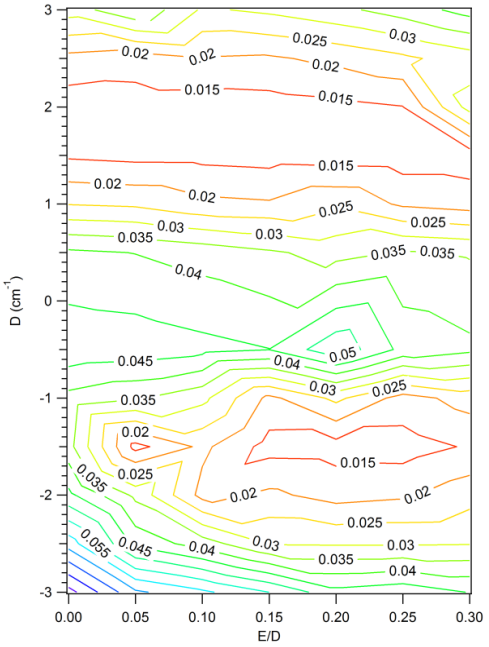

Figure A.2.5. Contour plot of χ^2 values as a function of ZFS parameters *D* and *E/D* for fits of VTVH MCD data collected for $[Mn^{III}(O_2)(N4py)]^+$ at 14 700 cm^{-1}.

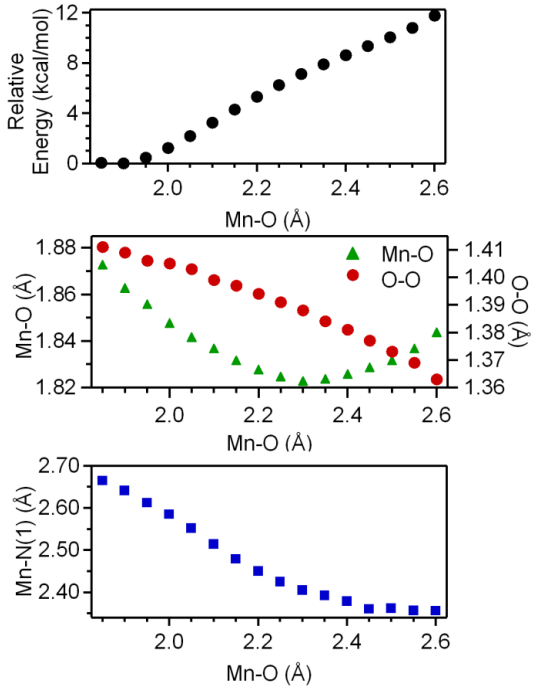

Figure A.2.6. Relative energy (top), Mn-O and O-O bond lengths (center), and Mn-N(1) bond lengths (bottom) as a function of the Mn-O distance for $[Mn^{III}(O_2)(mL_5^2)]^+$ determined by a relaxed surface scan using DFT computations.

Table A.2.3. MO Energies (eV) and Compositions (%) for $[Mn^{III}(O_2)(mL_5^2)\text{-}N(3)]^+$ from Spin Unrestricted B3LYP DFT Computations.

Spin-up MOs	*xz* (105α)	*yz* (109α)	z^2 (110α)	x^2-y^2 (113α)	O_2 p_{op}* (114α)	*xy* (115α)
Energy	-10.855	-10.221	-9.836	-9.014	-8.319	-4.842
Mn 3d	57.3	33.0	24.9	39.2	5.3	30.7
z^2	5.9	1.1	13.3	12	0.2	0.3
xz	39.5	1.1	8.6	1.9	0.5	0.1
yz	0.4	25.8	0.5	0.3	4.4	1.7
x^2-y^2	9.9	2.2	1.1	14.5	0	9.8
xy	1.6	2.8	1.4	10.5	0.2	18.8
O_2 2p	16.5	17.3	5.1	11.3	92.1	48.3
mL_5^2 (N 2p)	7.3	24.5	38.9	32.8	0.1	5.9

Spin-down MOs	*xz* (115β)	*yz* (117β)	z^2 (119β)	x^2-y^2 (120β)	*xy* (121β)
Energy	-3.5525	-3.3707	-3.0977	-2.8354	-2.5497
Mn 3d	43.1	71.1	70.6	76.8	67.6
z^2	4.3	6.7	41.6	9.9	0.2
xz	26	1.3	20.3	9.4	0.8
yz	0	57.7	2.2	5	7.3
x^2-y^2	4.8	4.7	5.9	33	18.7
xy	8	0.7	0.6	19.5	40.6
O_2 2p	1.7	5.1	2.4	4.0	19.2
mL_5^2 (N 2p)	13.6	5.6	5.2	5.3	3.9

Table A.2.4. Relative Energies (kcal/mol) and Metric Parameters for $[Mn^{III}(O_2)(imL_5^2)\text{-}N(3)]^+$ Models from a DFT Relaxed Surface Scan of the Mn-N(1) Distance.

Mn-N(1)[a]	Relative Energy	Mn-O	O-O	Mn-N(2)	Mn-N(3)	Mn-N(4)	Mn-N(5)
2.70	0	1.858 1.860	1.430	2.360	5.408	2.087	2.088
2.60	0.33	1.860 1.864	1.428	2.370	5.415	2.095	2.093
2.50	1.16	1.861 1.868	1.427	2.385	5.429	2.108	2.094
2.40	2.61	1.864 1.870	1.425	2.401	5.442	2.124	2.096
2.30	4.78	1.866 1.869	1.425	2.432	5.459	2.161	2.089
2.20	7.11	1.849 1.862	1.429	2.442	5.428	2.299	2.063
2.10	9.26	1.843 1.858	1.433	2.446	5.386	2.360	2.066
2.00	12.82	1.840 1.860	1.436	2.459	5.355	2.404	2.067

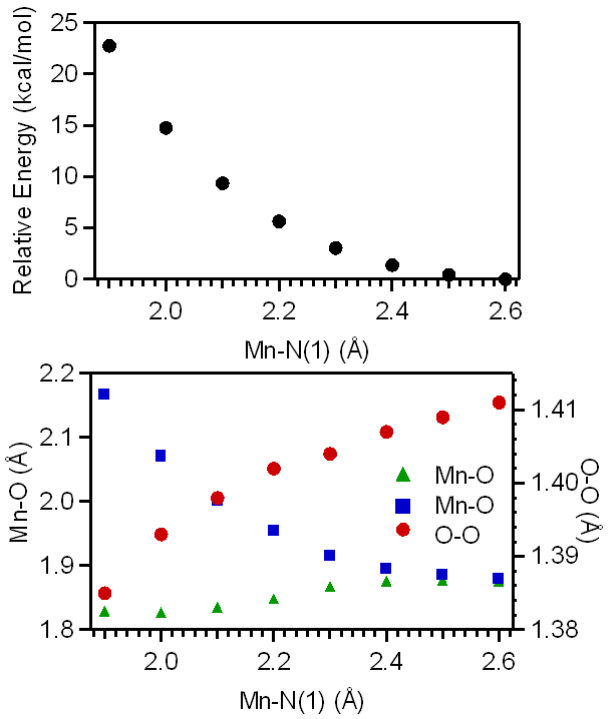

Figure A.2.7. Total energy and Mn-O and O-O bond lengths as a function of the Mn-N(1) distance of $[Mn^{III}(O_2)(mL_5^{2})]^{+}$ determined by a relaxed surface scan using DFT computations.

Table A.2.5. Cartesian coordinates (Å) for DFT energy minimized $[Mn^{III}(O_2)(mL_5{}^2)\text{-}N(1)]^+$ model.

Atom	x	y	z
Mn	-0.040375	-0.009896	-0.015145
O	1.838127	-0.035004	-0.018102
O	1.318816	1.277773	-0.011925
N	0.113550	-2.365762	0.043816
N	-0.071852	-0.551423	2.199579
N	-2.505980	-0.978628	0.016108
N	-1.510896	1.598319	0.058151
N	-0.032341	-0.700254	-2.187726
C	-2.784574	1.410643	0.495131
C	0.385704	-1.791954	2.486335
C	0.968683	-2.667165	-1.131570
C	0.565244	-2.225529	3.811734
C	-3.691658	2.477969	0.598031
C	-0.139820	-0.038384	4.560249
C	0.817232	-2.656361	1.315160
C	0.528691	-1.918960	-2.376356
C	-0.316196	0.305136	3.213860
C	-2.345650	-2.317403	0.608932
C	-0.332294	0.052516	-3.265885
C	0.459329	-1.642619	-4.781729
C	-3.153059	-0.003516	0.900868
C	-3.278129	3.771591	0.246918
C	0.771690	-2.429827	-3.663084
C	0.300785	-1.336135	4.863604
C	-1.195731	-3.067170	-0.065550
C	-1.114013	2.849486	-0.283558
C	-1.963079	3.959441	-0.204838
C	-0.099119	-0.371088	-4.580881
C	-3.190647	-1.022357	-1.287880
H	1.023829	-3.761049	-1.336858
H	1.996502	-2.321720	-0.895606
H	0.924228	-3.245923	4.013240
H	-4.716647	2.287511	0.949364
H	-0.346592	0.697880	5.349904
H	1.893101	-2.433369	1.154062
H	0.745602	-3.735511	1.585774
H	-0.662393	1.309416	2.922803
H	-3.275846	-2.931366	0.521407
H	-2.144912	-2.198292	1.690894
H	-0.776038	1.038649	-3.057979
H	0.651589	-2.018130	-5.797945
H	-2.788206	-0.178971	1.935225
H	-4.264737	-0.110531	0.929568
H	-3.975704	4.619631	0.319172
H	1.213533	-3.430134	-3.782877
H	0.443349	-1.651905	5.908065
H	-1.119980	-4.098160	0.350569
H	-1.421431	-3.181196	-1.144271
H	-0.071981	2.940474	-0.625385
H	-1.591111	4.951615	-0.497041
H	-0.354812	0.284024	-5.425685
H	-3.199754	-0.012637	-1.740584

H	-4.245361	-1.375475	-1.188650
H	-2.657027	-1.693353	-1.985019

Table A.2.6. Cartesian coordinates (Å) for DFT energy minimized $[Mn^{III}(O_2)(mL_5^2)\text{-}N(4)]^+$ model.

Atom	x	y	z
Mn	0.083111	-0.272717	0.325625
O	1.870545	-0.622704	0.636999
O	1.625567	0.749040	0.304688
N	0.083375	-0.935365	-1.947538
N	-0.879343	-2.245026	0.532424
N	-0.362437	-0.487010	2.556998
N	-1.482469	0.877692	-0.457337
C	-0.324536	-1.793758	2.914704
C	-0.565736	0.197379	-2.644784
C	-0.248496	-2.194059	4.258183
C	-1.629437	0.884157	-1.811519
C	-0.490935	-3.009380	-0.690313
C	-2.365306	1.563837	0.309454
C	-3.602539	2.287804	-1.623901
C	-0.280682	-2.799210	1.774818
C	-0.171323	-1.211230	5.256619
C	-2.694426	1.574108	-2.417727
C	-0.723959	-2.185847	-1.961104
C	-0.281877	0.455315	3.520195
C	-0.180615	0.141436	4.881741
C	-3.432676	2.286938	-0.229434
C	-2.356488	-2.180899	0.677899
C	1.492883	-1.137833	-2.366232
C	1.748447	-1.615954	-3.793760
N	0.722372	-1.607043	-4.668866
C	3.047986	-2.031531	-4.155618
C	3.284618	-2.442099	-5.473900
C	2.218308	-2.433531	-6.388239
C	0.961706	-2.009872	-5.933673
H	-0.968117	-0.098842	-3.635735
H	0.225551	0.950912	-2.846326
H	-0.235823	-3.263676	4.516129
H	-1.051916	-3.968949	-0.750119
H	0.583736	-3.262074	-0.595470
H	-2.196783	1.518555	1.395803
H	-4.436358	2.836180	-2.087671
H	0.784686	-3.031136	1.563080
H	-0.774568	-3.751928	2.073220
H	-0.099576	-1.499757	6.316086
H	-2.796804	1.552199	-3.513268
H	-0.501009	-2.801159	-2.857951
H	-1.792740	-1.902812	-2.039874
H	-0.285185	1.501991	3.176744
H	-0.111083	0.944786	5.628934
H	-4.117634	2.832833	0.434701
H	-2.619275	-1.561957	1.555392
H	-2.781371	-3.200619	0.815270

H	-2.813836	-1.723959	-0.217524
H	1.966124	-1.838065	-1.649098
H	2.020109	-0.176813	-2.188049
H	3.860558	-2.029134	-3.412205
H	4.288275	-2.770263	-5.784338
H	2.355132	-2.752054	-7.431751
H	0.095280	-1.990292	-6.617006

Table A.2.7. Cartesian coordinates (Å) for DFT energy minimized $[Mn^{III}(O_2)(mL_5^2)\text{-}N(3)]^+$ model.

Atom	x	y	z
Mn	0.057307	-0.006508	-0.031598
O	1.917927	-0.112338	-0.041800
O	1.460732	1.233520	-0.063578
N	-2.125883	-0.937872	-0.614383
N	-1.348433	1.571041	0.668170
N	-0.098867	-0.048982	-2.269989
C	-1.977693	-1.561339	-1.944630
C	-1.092942	-0.746150	-2.867731
C	-2.772997	1.122890	0.595367
C	0.793691	0.618559	-3.035298
C	-0.319086	-0.077149	-5.059588
C	-1.243631	-0.771426	-4.264223
C	-3.022246	0.241962	-0.626948
C	0.723549	0.625120	-4.434239
C	-1.138735	2.776384	-0.181537
C	-0.908290	1.838882	2.090321
C	-1.689911	2.900593	2.847199
N	-2.886862	2.509907	3.343817
C	-1.176021	4.198378	3.039091
C	-1.934535	5.126037	3.771767
C	-3.605770	3.408779	4.038338
C	-3.177064	4.725714	4.282396
H	-2.965298	-1.763580	-2.421844
H	-1.489551	-2.549775	-1.797032
H	-0.190202	4.473981	2.634557
H	-3.461233	1.994637	0.579648
H	-3.007810	0.585591	1.534607
H	1.574905	1.159750	-2.479158
H	-0.413416	-0.084004	-6.156465
H	0.164730	2.106806	2.033505
H	-1.000424	0.880719	2.640613
H	-1.555964	6.144566	3.945856
H	-2.072256	-1.334210	-4.719817
H	-4.098051	-0.052021	-0.666571
H	-2.811247	0.805039	-1.558202
H	-4.574721	3.054831	4.429703
H	-3.804953	5.415169	4.865859
H	1.473565	1.177741	-5.018207
H	-0.072889	3.067428	-0.152989
H	-1.763545	3.625314	0.171416
H	-1.408620	2.546409	-1.229128
C	-2.482693	-1.935701	0.410440

C	-1.255007	-2.651307	0.938371
N	-0.100180	-1.936389	0.940936
C	-1.314968	-3.953782	1.458242
C	-0.159418	-4.525645	2.011589
C	1.027818	-3.777188	2.023194
C	1.017446	-2.490770	1.473115
H	-3.237487	-2.669582	0.044874
H	-2.957449	-1.409630	1.264793
H	-2.263452	-4.510756	1.428346
H	-0.185772	-5.544788	2.424726
H	1.958745	-4.181869	2.444536

Table A.2.8. Cartesian coordinates (Å) for DFT energy minimized $[Mn^{III}(O_2)(imL_5{}^2)\text{-}N(1)]^+$ model.

Atom	x	y	z
Mn	-0.110378	-0.081700	0.105360
O	1.753282	0.067550	0.157722
O	1.115486	1.334951	0.114143
N	-2.716472	-1.113751	0.004929
N	-1.812374	1.783354	-0.035718
N	-0.764685	0.424401	2.183144
N	-1.234065	2.041368	3.639884
N	-0.814901	-4.220134	-0.509941
N	-0.120040	-2.175688	0.003750
N	-0.599125	0.231450	-2.057980
N	-0.965306	1.687626	-3.700331
C	-0.816941	0.939115	4.375152
C	-1.425611	2.594020	1.142114
C	-3.500024	-0.034801	-0.608824
C	-2.455717	-2.264640	-0.866126
C	-3.218276	1.314962	0.064851
C	-3.241246	-1.546775	1.305601
C	-0.534391	-0.052708	3.456996
C	-1.177782	1.688360	2.316699
C	0.919529	-3.056951	0.237043
C	-1.155051	-2.896127	-0.451842
C	0.502858	-4.332225	-0.081381
C	-1.556315	3.357065	4.192875
C	-1.644950	-5.324351	-0.994047
C	-1.500747	2.446334	-1.318230
C	-1.062582	1.447037	-2.355114
C	-0.394860	0.559810	-4.277980
C	-0.175444	-0.330964	-3.246745
C	-1.290835	2.930833	-4.398969
H	-0.762870	0.968591	5.467685
H	-2.181897	3.378001	1.386858
H	-0.475675	3.114503	0.896568
H	-4.602604	-0.223540	-0.551267
H	-3.240063	0.014603	-1.683508
H	-2.362489	-1.896920	-1.909909
H	-3.283233	-3.018130	-0.862496
H	-3.915079	2.081585	-0.351837
H	-3.456249	1.227937	1.143532

H	-2.540474	-2.270158	1.765683
H	-4.246194	-2.028408	1.212740
H	-3.320496	-0.689245	1.998146
H	-0.177077	-1.071789	3.634398
H	1.886207	-2.710360	0.614280
H	1.008954	-5.300587	-0.035845
H	-2.412791	3.800367	3.651200
H	-0.685415	4.039993	4.123515
H	-1.838324	3.240807	5.254406
H	-1.660021	-5.355935	-2.101957
H	-2.679122	-5.219928	-0.617037
H	-1.229584	-6.274020	-0.613561
H	-0.657663	3.148065	-1.144135
H	-2.359409	3.058908	-1.686804
H	-0.197512	0.505698	-5.352886
H	0.271898	-1.329085	-3.282689
H	-1.395359	2.720211	-5.478245
H	-0.492189	3.686784	-4.255000
H	-2.250128	3.337812	-4.028422

Table A.2.9. Cartesian coordinates (Å) for DFT energy minimized $[Mn^{III}(O_2)(imL_5^2)\text{-}N(4)]^+$ model.

Atom	x	y	z
Mn	-0.278416	-0.011384	0.037694
O	1.232619	0.973609	-0.421266
O	0.497456	0.502219	-1.558344
N	-2.198105	-0.873758	-0.730833
N	-1.722912	1.962563	0.088237
N	-0.700316	0.213513	2.048725
N	-1.556116	1.323750	3.767876
N	-0.147116	-3.829876	-1.729838
N	0.148320	-2.200044	-0.241727
N	-3.010286	4.576683	-0.197107
N	-1.509557	5.332676	-1.679834
C	-1.045064	0.130583	4.266370
C	-1.627575	2.471510	1.477105
C	-2.975388	0.281029	-1.269012
C	-1.753980	-1.818159	-1.792840
C	-3.068776	1.427520	-0.256858
C	-2.969455	-1.610227	0.303244
C	-0.522651	-0.550766	3.188675
C	-1.325682	1.343683	2.422304
C	1.144984	-3.138554	-0.065122
C	-0.609953	-2.634785	-1.254152
C	0.977261	-4.157467	-0.981561
C	-1.208910	2.939668	-0.898998
C	-1.924330	4.269489	-0.905652
C	-2.400456	6.370696	-1.442709
C	-3.313365	5.884178	-0.525854
C	-2.154000	2.392866	4.571715
C	-0.660828	-4.587448	-2.871617
C	-0.378148	5.355029	-2.604018
H	-1.108416	-0.119315	5.329443

H	-2.531959	3.046330	1.773193
H	-0.785061	3.195889	1.510953
H	-4.000831	-0.038374	-1.566575
H	-2.458636	0.628071	-2.185239
H	-1.410671	-1.217394	-2.662628
H	-2.594614	-2.461730	-2.143258
H	-3.729419	2.229706	-0.649163
H	-3.541196	1.068414	0.678370
H	-2.355353	-2.435448	0.706464
H	-3.907495	-2.026580	-0.128013
H	-3.228128	-0.937066	1.138940
H	-0.041606	-1.532261	3.155824
H	1.919009	-3.023899	0.700865
H	1.539917	-5.076451	-1.170168
H	-1.246643	2.457654	-1.898958
H	-0.121759	3.059510	-0.698442
H	-2.292987	7.339134	-1.939820
H	-4.170743	6.403004	-0.082466
H	-2.954160	2.893668	3.997396
H	-1.389339	3.141033	4.859739
H	-2.592166	1.953210	5.484795
H	-0.353904	-5.643705	-2.770583
H	-0.260478	-4.186285	-3.824166
H	-1.765937	-4.544019	-2.891426
H	-0.582768	4.739419	-3.503315
H	0.535282	4.971864	-2.109707
H	-0.193079	6.395453	-2.923063

Table A.2.10. Cartesian coordinates (Å) for DFT energy minimized $[Mn^{III}(O_2)(imL_5^2)\text{-}N(3)]^+$ model.

Atom	x	y	z
Mn	-0.187728	0.090569	-0.144612
O	1.632997	0.126733	-0.520689
O	0.849293	0.784550	-1.520419
N	-0.409494	-2.105235	-0.976457
N	-2.473511	-0.956195	0.902413
N	0.022514	-0.207969	1.911351
N	-0.486129	-0.655699	4.023849
N	-1.837384	1.299420	-0.564339
N	-3.917559	2.048877	-0.749298
N	-0.911732	-4.256490	-3.278485
N	1.227916	-3.771801	-3.749051
C	0.884334	-0.425786	3.973272
C	-2.409453	-0.573674	2.318873
C	-1.762938	-2.685228	-0.744874
C	-2.304816	-2.402398	0.655277
C	0.633720	-2.906089	-0.285720
C	1.187306	-0.152887	2.656784
C	-0.973846	-0.508484	2.756483
C	-3.583996	-0.325396	0.179010
C	-3.128978	1.008666	-0.347432
C	-3.080699	3.039774	-1.251367

C	-1.793895	2.563484	-1.128565
C	-0.105810	-2.024817	-2.451301
C	0.053949	-3.342947	-3.152970
C	-0.352994	-5.301770	-3.978042
C	0.967405	-5.020114	-4.287559
C	-1.254092	-0.932062	5.240038
C	-5.381043	2.096519	-0.741246
C	2.481728	-3.033198	-3.898730
H	1.507362	-0.486836	4.869995
H	-3.005929	-1.251723	2.977495
H	-2.859394	0.438584	2.424541
H	-1.762260	-3.779720	-0.938937
H	-2.441105	-2.257163	-1.510812
H	-3.259032	-2.964527	0.799430
H	-1.597325	-2.783286	1.418954
H	1.617981	-2.429977	-0.454675
H	0.652165	-3.955068	-0.655241
H	0.447498	-2.915117	0.805043
H	2.149551	0.075922	2.188645
H	-4.507526	-0.226540	0.798708
H	-3.866596	-0.976765	-0.675698
H	-3.478038	3.983630	-1.634849
H	-0.842240	3.029858	-1.400870
H	0.801132	-1.401851	-2.557002
H	-0.937130	-1.454834	-2.913522
H	-0.928577	-6.201324	-4.225759
H	1.735334	-5.577724	-4.832355
H	-2.052423	-1.667135	5.028024
H	-1.705482	-0.003570	5.642949
H	-0.576551	-1.360008	6.000209
H	-5.704345	3.151373	-0.783535
H	-5.773364	1.646837	0.189716
H	-5.799707	1.556394	-1.613847
H	3.280866	-3.741081	-4.181598
H	2.767736	-2.550580	-2.945689
H	2.396969	-2.255878	-4.684805

Table A.2.11. Cartesian coordinates (Å) for DFT energy minimized $[Mn^{III}(O_2)(N4py)\text{-}N(1)]^+$ model.

Atom	x	y	z
Mn	12.912087	4.188144	4.591290
O	13.333852	5.950958	4.131357
O	12.333182	5.873460	5.131090
N	14.498016	3.601042	6.111296
N	14.553060	3.553205	3.143717
N	11.390059	3.342753	5.999974
N	11.401313	3.358449	3.079507
N	13.053828	1.682087	4.582842
C	14.760781	2.292588	6.330677
C	10.942327	2.090152	5.756113
C	14.810561	2.248362	2.899213
C	10.987503	2.089396	3.302891
C	10.874864	4.052102	2.052246

C	10.841886	4.055830	7.004192
C	15.886868	1.881241	7.065200
C	9.349984	2.241209	7.563126
C	15.934868	1.837536	2.161654
C	13.731063	1.284697	5.833957
C	13.774885	1.245412	3.375650
C	15.395474	4.487703	2.648245
C	15.326162	4.536710	6.621491
C	16.458145	4.209730	7.380517
C	11.591533	1.424329	4.545852
C	16.805273	2.807998	1.645410
C	9.474025	2.190713	1.423568
C	16.746090	2.853647	7.599597
C	9.904093	3.506895	1.198015
C	16.525949	4.161628	1.887700
C	9.816106	3.541276	7.810560
C	9.922919	1.499025	6.516560
C	10.024306	1.466251	2.494990
H	11.251035	5.079300	1.923944
H	11.246191	5.069342	7.148268
H	16.084282	0.809418	7.219841
H	8.548526	1.806014	8.178782
H	16.119195	0.765751	1.991947
H	14.206231	0.282549	5.734853
H	12.962946	1.183052	6.628821
H	14.249239	0.248019	3.520661
H	13.038033	1.118324	2.554729
H	15.141837	5.532015	2.885638
H	15.058207	5.581734	6.397157
H	17.102038	5.005195	7.781386
H	11.338630	0.338134	4.538668
H	17.691556	2.509876	1.065257
H	8.717634	1.728459	0.771455
H	17.633484	2.553515	8.177067
H	9.497312	4.107892	0.372178
H	17.176278	4.959857	1.503213
H	9.393872	4.156111	8.618154
H	9.585626	0.475978	6.294551
H	9.711270	0.431566	2.698878

Table A.2.12. Cartesian coordinates (Å) for DFT energy minimized $[Mn^{III}(O_2)(N4py)\text{-}N(2)]^+$ model.

Atom	x	y	z
Mn	0.333596	0.348908	-1.157580
O	1.468233	1.133067	-2.419364
O	1.830277	1.423987	-1.072280
N	-3.352714	-0.759656	2.536270
N	1.336232	-1.436351	-0.336454
N	-1.211100	1.840657	-0.638903
N	-1.111122	-0.507608	-2.377718
N	-1.196423	-0.706434	0.390712
C	-2.029862	-0.864761	2.804179
C	-2.407572	1.292479	-0.319485

C	0.593723	-2.397854	0.261728
C	-2.327433	-0.684453	-1.791046
C	-0.944946	-0.815865	-3.684137
C	-1.082603	3.181615	-0.692511
C	-1.543441	-1.494721	3.966781
C	-3.403646	3.476223	-0.090574
C	1.181104	-3.562441	0.781373
C	-1.080359	-0.228186	1.798855
C	-0.906827	-2.153081	0.292373
C	2.674835	-1.592883	-0.437736
C	-4.221261	-1.276742	3.423890
C	-3.831344	-1.908580	4.617388
C	-2.417156	-0.238398	-0.334990
C	2.569696	-3.734579	0.665741
C	-3.250198	-1.507074	-3.870161
C	-2.461088	-2.019154	4.891621
C	-1.993232	-1.316127	-4.465861
C	3.331723	-2.731608	0.045464
C	-2.161353	4.037841	-0.427382
C	-3.531895	2.077536	-0.032431
C	-3.418620	-1.187863	-2.512566
H	0.060907	-0.644946	-4.096028
H	-0.081055	3.556872	-0.953891
H	-0.459799	-1.563987	4.150408
H	-4.266295	4.121248	0.134350
H	0.554934	-4.324109	1.270057
H	-1.232201	0.869261	1.797734
H	-0.032186	-0.404622	2.114453
H	-1.378898	-2.733019	1.115463
H	-1.343445	-2.542983	-0.650083
H	3.213817	-0.759990	-0.915754
H	-5.290693	-1.173759	3.170529
H	-4.588367	-2.301902	5.311190
H	-3.354180	-0.605108	0.130881
H	3.052162	-4.639887	1.064092
H	-4.092932	-1.903743	-4.455657
H	-2.108046	-2.506802	5.813015
H	-1.818391	-1.551866	-5.524962
H	4.422675	-2.821206	-0.058635
H	-2.021993	5.127438	-0.480182
H	-4.482093	1.600839	0.248373
H	-4.387405	-1.328866	-2.011782

Table A.2.13. Cartesian coordinates (Å) for DFT energy minimized $[Mn^{III}(O_2)(N4py)\text{-}N(3)]^+$ model.

Atom	x	y	z
Mn	17.802407	6.331929	10.282467
O	17.007306	6.677106	11.935712
O	16.457637	7.467243	10.890416
N	18.231396	7.623218	8.597762
N	18.865141	4.975927	8.536481
N	16.389024	4.695247	9.739521
N	19.477998	5.389840	11.191615

N	22.012322	5.096297	7.725004
C	17.635624	8.841940	8.543293
C	17.792542	9.706156	7.454392
C	18.591958	9.294656	6.375595
C	19.210612	8.037738	6.433725
C	19.015872	7.225349	7.563341
C	19.718127	5.880990	7.698785
C	17.742072	4.443105	7.732373
C	19.586589	3.903934	9.251692
C	16.587939	3.986383	8.603295
C	15.733849	2.936325	8.228944
C	14.633728	2.631790	9.046146
C	14.425974	3.380792	10.214917
C	15.332229	4.402129	10.528580
C	20.147180	4.382043	10.574372
C	21.254147	3.763538	11.178119
C	21.671799	4.188804	12.447212
C	20.969456	5.225731	13.082128
C	19.879001	5.799463	12.420451
C	21.162549	6.034802	8.196909
C	21.581809	7.087725	9.033655
C	22.936159	7.161141	9.397242
C	23.820183	6.185594	8.914724
C	23.305421	5.173704	8.084638
H	17.018978	9.103722	9.417221
H	17.287986	10.682498	7.456662
H	18.730943	9.943882	5.497897
H	19.845901	7.680673	5.609442
H	19.831608	5.437096	6.684825
H	18.067884	3.624340	7.049639
H	17.375566	5.268203	7.083539
H	20.385202	3.441997	8.631462
H	18.844180	3.108724	9.477928
H	15.927222	2.370164	7.305767
H	13.948265	1.814883	8.774235
H	13.577104	3.177428	10.883256
H	15.237980	5.018263	11.436132
H	21.778786	2.953879	10.650270
H	22.536850	3.715949	12.935623
H	21.256503	5.589731	14.078256
H	19.280958	6.607728	12.869180
H	20.868011	7.843043	9.392734
H	23.294930	7.976100	10.044374
H	24.890869	6.208616	9.166053
H	23.966969	4.390672	7.675871

Appendix A.3.

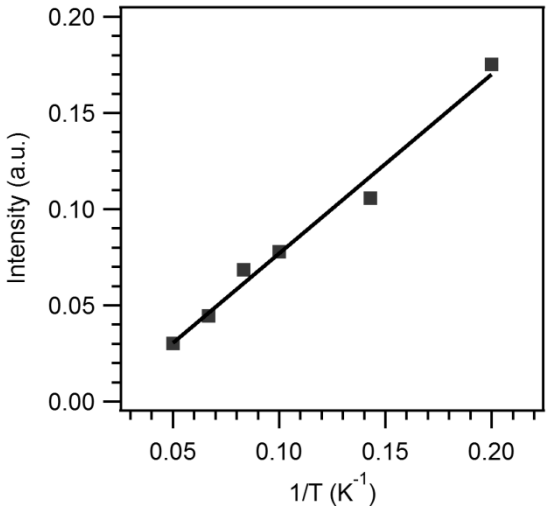

Figure A.3.1. Temperature dependence of the parallel-mode EPR intensity (75 mT) of a 5 mM butyronitrile solution of $[Mn^{III}(O_2)(N4py)]^+$ (**2**) with low-field baseline correction (T = 5 – 20 K).

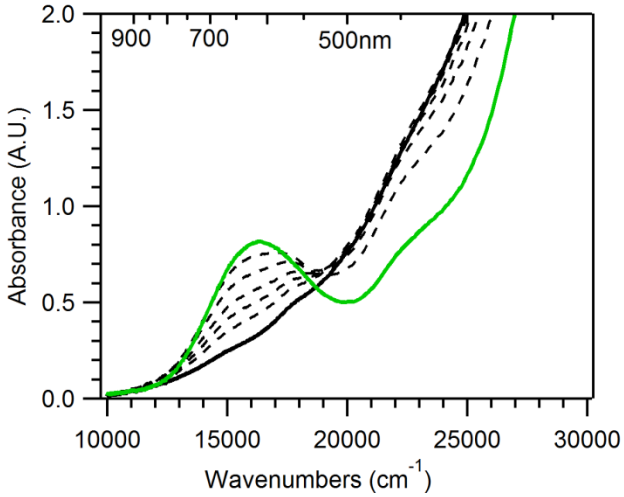

Figure A.3.2. Electronic absorption spectra of $[Mn^{III}(O_2)(N4py)]^+$ (**2**) (green), formed from the addition of 2 equivalents of KO_2 to 5 mM $[Mn^{II}(N4py)(OTf)]^+$ (**1**) in MeCN at -20 ^oC, and its decay over 3 hours (black).

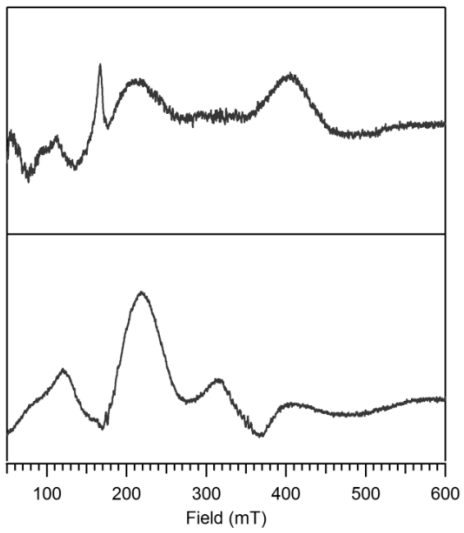

Figure A.3.3. *Top*: Parallel-mode X-band EPR spectrum of the decay products of a 5 mM solution of **2** in butyronitrile. $[Mn^{III}(O_2)(N4py)]^+$ (**2**) was formed by reaction with 2 equivalents KO_2. Recording conditions: T = 5 K, 9.3944 GHz microwave frequency, 2.0 mW microwave power, 0.4 mT modulation amplitude, 100 kHz modulation frequency, 81.92 ms time constant, and 15 000 point resolution. *Bottom*: Perpendicular-mode X-band EPR spectrum of the same solution. Recording conditions: T = 5 K, 9.6369 GHz microwave frequency, 0.0317 mW microwave power, 0.4 mT modulation amplitude, 100 kHz modulation frequency, 81.92 ms time constant, and 15 000 point resolution.

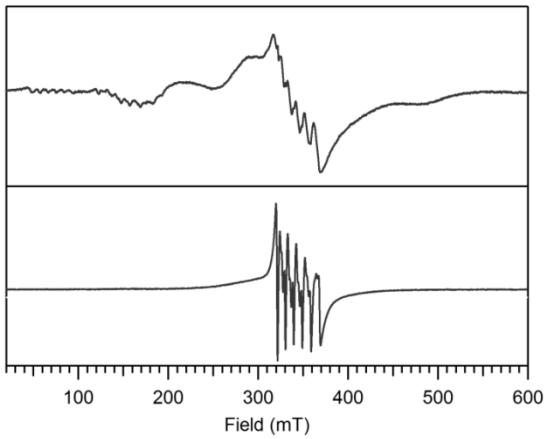

Figure A.3.4. *Top*: Perpendicular-mode X-band EPR spectrum of a 5 mM butyronitrile solution of $[Mn^{II}(N4py)(OTf)]^+$ (**1**). Recording conditions: T = 5 K, 9.6371 GHz microwave frequency, 0.002 mW microwave power, 0.4 mT modulation amplitude, 100 kHz modulation frequency, 81.92 ms time constant, and 15 000 point resolution. *Bottom*: Perpendicular-mode X-band EPR spectrum of 2 mM $[Mn(OTf)_2]$ in butyronitrile. Recording conditions: T = 5 K, 9.6369 GHz microwave frequency, 0.00796 mW microwave power, 0.4 mT modulation amplitude, 100 kHz modulation frequency, 81.92 ms time constant, and 7500 point resolution.

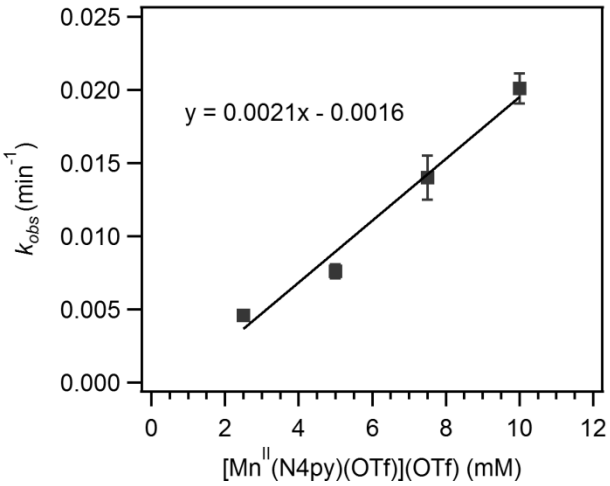

Figure A.3.5. Observed rate constant (k_{obs}) versus the initial concentration of $[Mn^{II}(N4py)(OTf)]^{+}$ (**1**), at -40 ^{o}C in MeCN. The k_{obs} values were determined by optically monitoring the rate of formation of $[Mn^{III}Mn^{IV}(\mu\text{-}O)_2(N4py)_2]^{3+}$ (**3**) at 17 700 cm^{-1}. Error bars represent ±1 standard deviation.

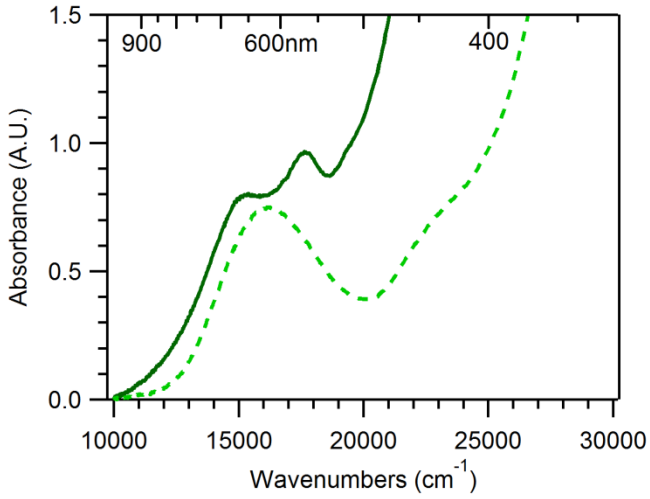

Figure A.3.6. Electronic absorption spectra of a 5 mM acetonitrile solution of $[Mn^{III}(O_2)(N4py)]^{+}$ (**2**) before (green dashed line) and after the addition of one equiv. $[Mn^{II}(N4py)(OTf)](OTf)$ (solid line) at -40 ^{o}C.

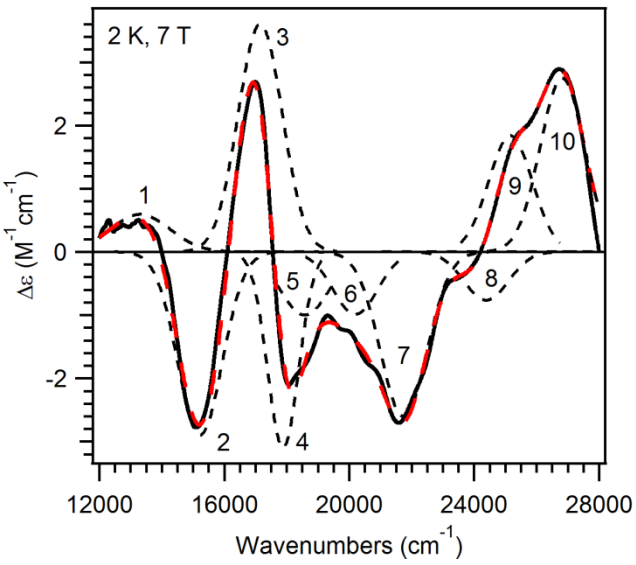

Figure A.3.7. 2 K, 7 T MCD spectrum of a 2.5 mM frozen solution of $[Mn^{III}Mn^{IV}(\mu\text{-}O)_2(N4py)_2]^{3+}$ (**3**) in PrCN (solid black line) Gaussian bands, and their sum, are shown as dashed black and red lines, respectively.

Table A.3.1. Energy and Widths (fwhm[a]) of Gaussian bands used in the Deconvoluted MCD Spectrum of $[Mn^{III}Mn^{IV}(\mu\text{-}O)_2(N4py)_2]^{3+}$ (**3**).

band	energy (cm^{-1})	fwhm (cm^{-1})
1	13 300	2250
2	15 260	1675
3	17 160	1675
4	17 890	1165
5	18 580	1675
6	20 210	1650
7	21 710	1770
8	24 400	1650
9	25 170	1650
10	26 830	1700

[a] fwhm = full width at half maximum.

Table A.3.2. EXAFS fitting results for $[Mn^{III}Mn^{IV}(\mu\text{-}O)_2(N4py)_2]^{3+}$ (**3**).[a]

	Mn−O			**Mn−N**			**Mn···C**			**Mn···Mn**			**GOF**
Fit	*n*	*r*	σ^2	*n*	*r*	σ^2	*n*	*r*	σ^2	*n*	*r*	σ^2	*F*
1				6	2.58	3.8							86.7
2	2	1.75	6.2	6	2.58	3.8							76.9
3	2	1.75	6.1	4	2.58	1.8							73.0
4	2	1.78	5.0	4	2.03	15.2				1	2.62	2.5	67.0
5	2	1.78	4.8	3	2.02	10.9				1	2.62	2.5	67.2
6	2	1.80	5.1	2	2.03	3.9				1	2.63	2.3	65.3
				2	2.21	8.9							
7	2	1.80	5.0	2	2.03	3.4				1	2.62	2.2	66.4
				1	2.20	2.5							
8	2	1.80	5.0	3	2.04	7.8				1	2.63	2.4	66.0
				1	2.25	4.0							
9	2	1.79	4.7	2	2.02	4.1	4	2.91	5.7	1	2.63	2.5	58.3
				1	2.19	4.7							
10	2	1.80	4.6	2	2.02	3.0	4	2.85	1.6	1	2.64	1.9	56.1
				1	2.20	2.3	4	2.99	1.8				
11	***2***	***1.79***	***4.2***	***2***	***2.00***	***3.6***	***4***	***2.81***	***4.4***	***1***	***2.63***	***1.8***	***56.6***
				1	***2.17***	***3.7***	***5***	***2.96***	***4.2***				
12	2	1.80	4.3	2	2.02	3.2	5	2.84	4.0	1	2.63	1.7	56.6
				1	2.19	2.9	5	2.98	3.7				
13	2	1.79	4.2	2	2.01	3.3	5	2.82	5.5	1	2.63	1.7	56.9
				1	2.17	3.2	6	2.97	5.1				
14	2	1.79	4.1	2	2.00	4.0	4	2.78	10.6	1	2.62	2.2	57.3
				1	2.16	5.0	8	2.93	8.8				
15	2	1.78	3.9	2	1.98	4.5	4	2.82	3.5	1	2.63	1.9	56.5
				2	2.13	10.2	5	2.97	3.7				
16	2	1.79	4.0	1	1.98	1.8	4	2.82	3.6	1	2.63	1.9	56.2
				2	2.08	9.9	5	2.97	3.7				

[a] Fourier transform range: k = 2 – 14.3 $Å^{-1}$ (resolution 0.128 Å). r is in Å, σ^2 (Debye-Waller factor) in × 10^3 $Å^2$, F is the weighted goodness-of-fit parameter × 10^2.

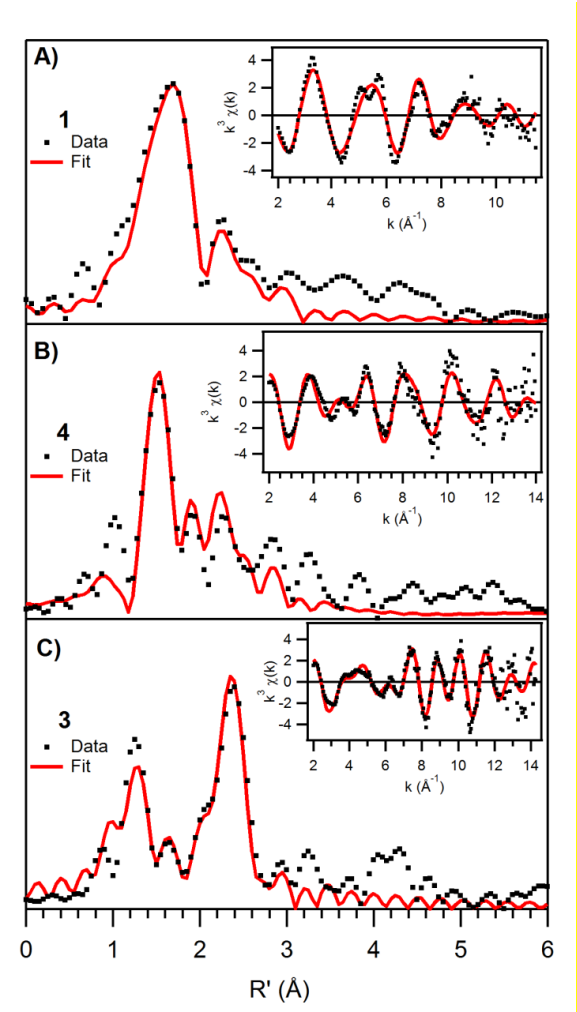

Figure A.3.8. Fourier transforms of Mn K-edge data $k^3\chi(k)$ and EXAFS spectra (inset) for A: $[Mn^{II}(N4py)(OTf)]^+$ (**1**); **B**: $[Mn^{IV}(O)(N4py)]^{2+}$ (**4**); and **C**: $[Mn^{III}Mn^{IV}(\mu\text{-}O)_2(N4py)_2]^{3+}$ (**3**), experimental data (dots) and fits (solid). Details regarding fits are given in Table A.3.3.

Table A.3.3. EXAFS fitting results for $[Mn^{II}(N4py)(OTf)]^{+}$ (**1**), $[Mn^{III}Mn^{IV}(\mu\text{-}O)_2(N4py)_2]^{3+}$ (**3**), and $[Mn^{IV}(O)(N4py)]^{2+}$ (**4**).

	Mn – O			**Mn – N**			**Mn • • • C**			**Mn • • • Mn**			**GOF**
	n	*r*	σ^2	*n*	*r*	σ^2	*n*	*r*	σ^2	*n*	*r*	σ^2	*F*
1	1	2.09	2.4	5	2.26	5.6	3 3	3.00 3.15	7.1 3.8				39.3
3	2	1.79	4.2	2 1	2.00 2.17	3.6 3.7	4 5	2.81 2.96	4.4 4.2	1	2.63	1.8	56.6
4	1	1.69	4.4	4 1	2.00 2.24	6.0 4.4	3 5	2.82 2.97	3.7 3.9				56.1

Fourier transform range for $[Mn^{II}(N4py)(OTf)]^{+}$: 2 – 11.5 $Å^{-1}$ (resolution 0.167 Å); $[Mn^{III}Mn^{IV}(\mu\text{-}O)_2(N4py)_2]^{3+}$: k = 2 – 14.3 $Å^{-1}$ (resolution 0.128 Å); $[Mn^{IV}(O)(N4py)]^{2+}$: k = 2 – 14.0 $Å^{-1}$ (resolution 0.131 Å). r is in Å, σ^2 (Debye-Waller factor) in 10^3 $Å^2$, F is a weighted goodness-of-fit parameter x 10^3.

Appendix A.4.

Table A.4.1. EXAFS Fitting Results for $[Mn^{II}(N4py)(OTf)](OTf)$ (**1**$(OTf)_2$) and $[Mn^{IV}(O)(N4py)]^{2+}$ (**2**).[a]

		Mn-O			Mn-N			Mn-C				
complex	fit	*n*	*r*(Å)	σ^2	*n*	*r*(Å)	σ^2	*n*	*r*(Å)	σ^2	E_0	*F*
1$(OTf)_2$	1				6	2.24	9.65				-4.57	113.9
	2	1	2.07	0.96	5	2.25	4.56				-6.24	107.2
	3	1	2.08	1.52	5	2.26	4.99	5	3.11	11.99	-4.93	79.1
	4	1	2.08	1.59	5	2.26	5.03	4	3.11	9.94	-4.97	81.3
	5	1	2.08	1.41	5	2.26	4.92	3	3.11	7.88	-5.14	84.5
	6	***1***	***2.09***	***2.38***	***5***	***2.26***	***5.55***	***3***	***3.00***	***7.06***	***-4.51***	***79.6***
								3	***3.15***	***3.75***		
2	1				6	2.00	11.06				-7.74	445.3
	2	1	1.68	3.91	5	1.98	8.18				-7.36	268.7
	3	1	1.69	4.53	4	2.01	6.18				-1.71	253.1
					1	2.25	3.40					
	4	1	1.68	4.32	4	2.02	6.51	1	2.96	0.75	-0.464	224.6
					1	2.26	2.86					
	5	1	1.68	4.31	4	2.02	6.47	3	2.95	4.79	-0.278	200.2
					1	2.26	2.74					
	6	1	1.68	3.72	5	2.00	8.70	3	2.91	6.14	-4.04	230.2
	7	1	1.68	3.52	5	1.99	8.72	3	2.87	3.59	-4.10	208.1
								1	3.00	-2.40		
	8	1	1.68	3.47	5	1.99	8.84	3	2.83	2.98	-3.94	205.2
								3	2.97	1.00		
	9	1	1.68	3.47	5	1.99	8.82	4	2.82	5.21	-4.08	209.6
								4	2.97	2.68		
	10	1	1.68	3.52	5	1.99	8.67	4	2.75	13.7	-5.00	216.6
								5	2.93	6.54		
	11	1	1.68	3.45	5	1.99	8.85	3	2.80	3.82	-3.97	210.7
								5	2.96	3.91		
	12	***1***	***1.69***	***4.39***	***4***	***2.00***	***6.02***	***3***	***2.82***	***3.74***	***-1.87***	***193.8***
					1	***2.24***	***5.48***	***5***	***2.97***	***3.89***		

[a] Fourier-transform range as follows: **1**$(OTf)_2$: 2 – 11.5 $Å^{-1}$ (resolution 0.167 Å); **2**: 2 – 14 $Å^{-1}$ (resolution 0.131 Å). σ^2 is in units of 10^3 $Å^2$.

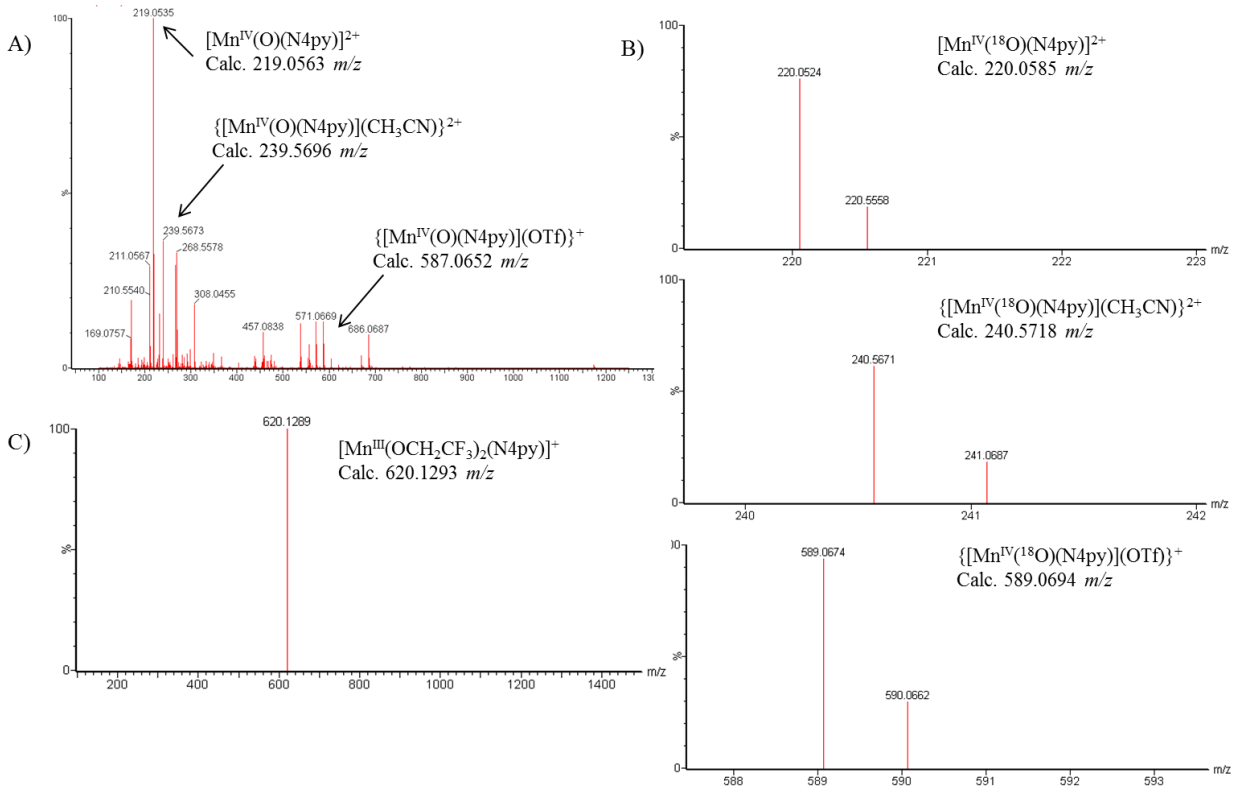

Figure A.4.1. ESI-MS spectra of A) complex $[Mn^{IV}(O)(N4py)]^{2+}$ (**2**), B) its exchange with $H_2{}^{18}O$, and C) complex **3**.

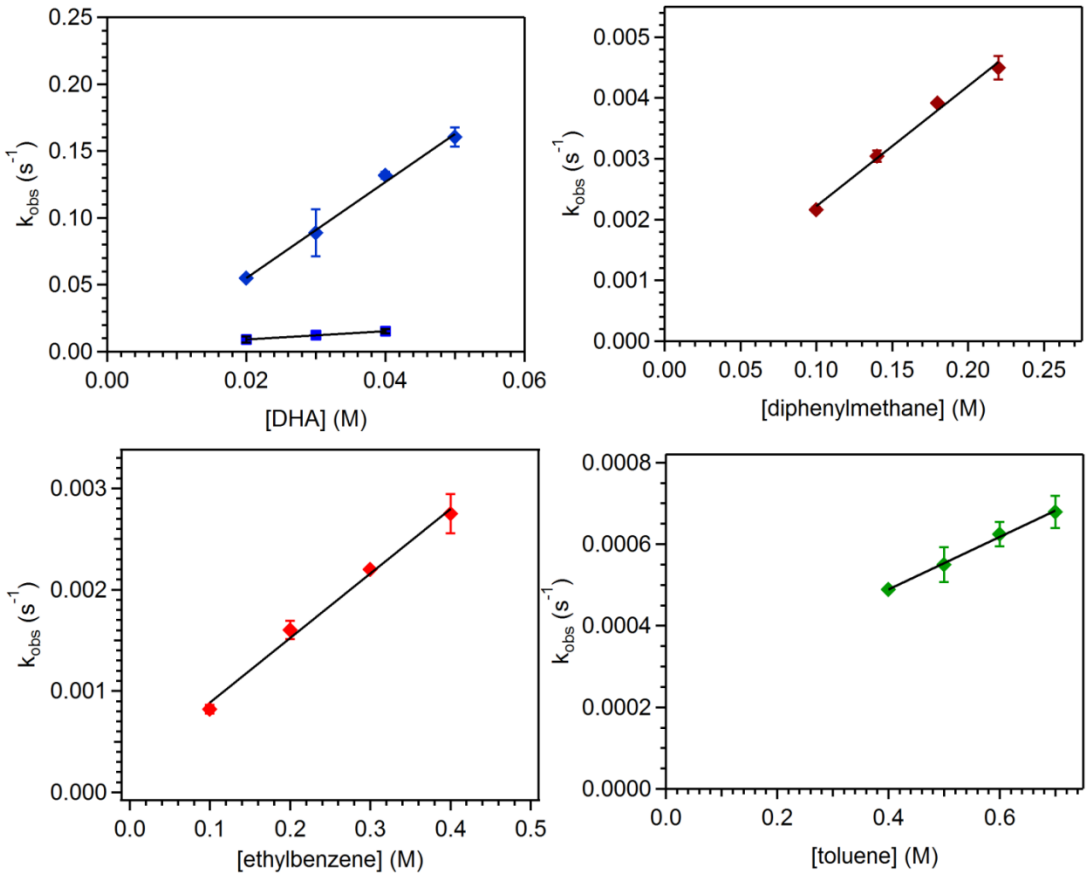

Figure A.4.2. Plots of pseudo-first order rate constants, k_{obs} (s^{-1}), against substrate concentration for a 1.9 mM solution of **2** in CF_3CH_2OH:CH_2Cl_2 (19:1) for (a) DHA and d_4-DHA and for a 2 mM solution of $[Mn^{IV}(O)(N4py)]^{2+}$ (**2**) in CF_3CH_2OH:CH_3CN (19:1) for (b) diphenylmethane, (c) ethylbenzene, and (d) toluene. The second-order rate constant, k_2 (M^{-1} s^{-1}), was calculated from the linear correlation of the observed rate and substrate concentration.

Table A.4.2. Corrected Second-order Rate Constants (k_2')[a] for Reaction of $[Mn^{IV}(O)(N4py)]^{2+}$ (**2**) with DHA, d_4-DHA, ethylbenzene, diphenylmethane, and toluene.

Substrate	k_2 ($M^{-1}s^{-1}$)	k_2' ($M^{-1}s^{-1}$)
DHA	3.6	0.90
d_4-DHA	0.32	0.079
diphenylmethane	0.020	0.0099
ethylbenzene	0.0057	0.0019
toluene	0.00064	0.00021

[a] (k_2') is the second-order rate constant corrected for the number of reactive C–H bonds.

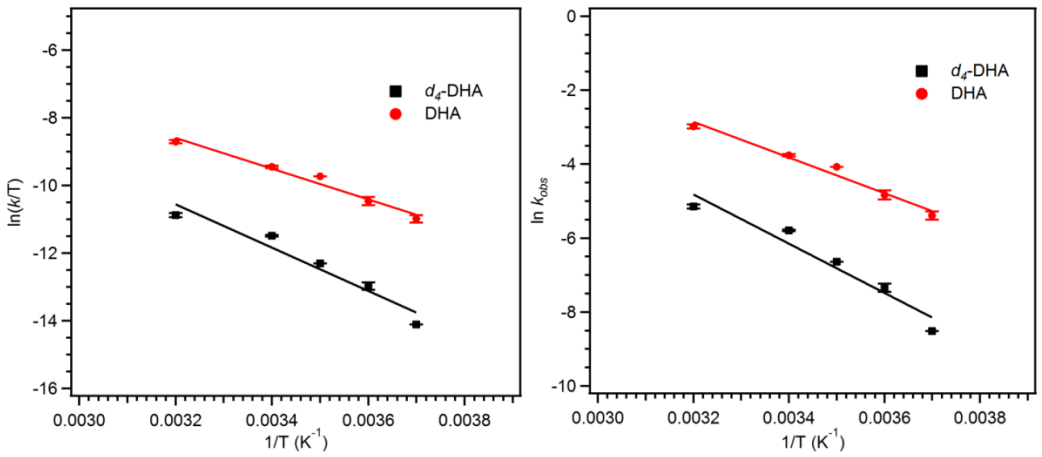

Figure A.4.3. Eyring plots (left) and Arrhenius plots (right) for the hydrogen atom abstraction of DHA (0.01 M, red dots) and *d*$_4$-DHA (0.01 M, black squares) by complex $[Mn^{IV}(O)(N4py)]^{2+}$ (**2**) (1 mM) in CF_3CH_2OH:CH_2Cl_2 (1:1).

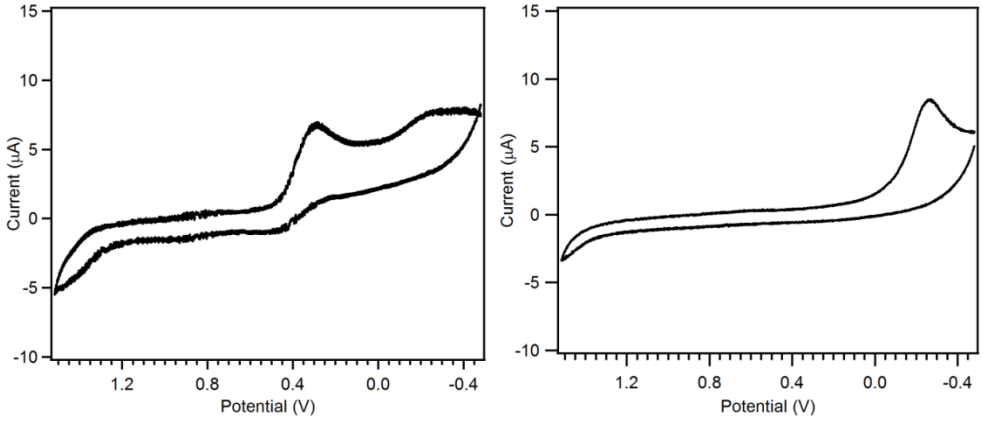

Figure A.4.4. Cyclic voltammograms of a 2 mM solution of $[Mn^{IV}(O)(N4py)]^{2+}$ (**2**) (left) and a 5 mM solution of PhIO (right) recorded in CF_3CH_2OH:CH_2Cl_2 (1:1) with 0.1 M NBu_4PF_6 as the supporting electrolyte. Voltammograms were recorded at 25 ^oC at 50 mV s^{-1} using a platinum working electrode, a platinum wire auxiliary electrode, and a glass-encased non-aqueous silver/silver chloride reference electrode. The reference Ag/Ag^+ electrode was monitored with the external Cp_2Fe/Cp_2Fe^+ couple. The cyclic voltammogram of PhIO was collected under the same conditions as for complex **2**, without the addition of $[Mn^{II}(N4py)(OTf)](OTf)$ (**1**$(OTf)_2$).

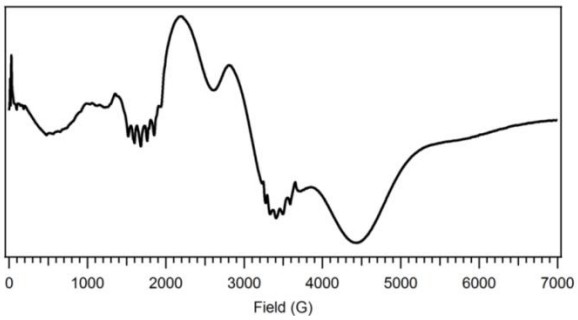

Figure A.4.5. X-band, perpendicular-mode EPR spectrum of a frozen 2 mM CF_3CH_2OH solution of **1**$(OTf)_2$. Recording conditions: T = 5 K, 9.634 GHz microwave frequency, 0.5024 mW microwave power, 6 G modulation amplitude, 100 kHz modulation frequency, 81.92 ms time constant, and 11 667 point resolution.

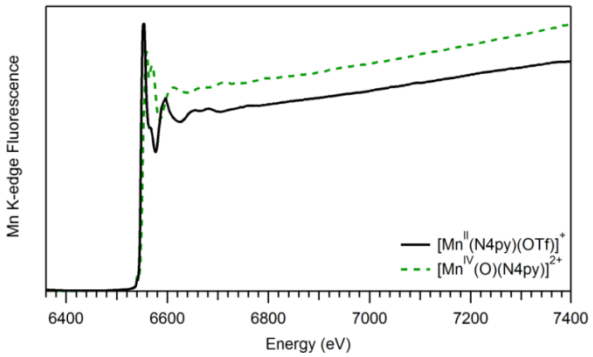

Figure A.4.6. Mn K-edge X-ray absorption spectra of $[Mn^{II}(N4py)(OTf)]^+$ (solid trace) and $[Mn^{IV}(O)(N4py)]^{2+}$ (dashed trace).

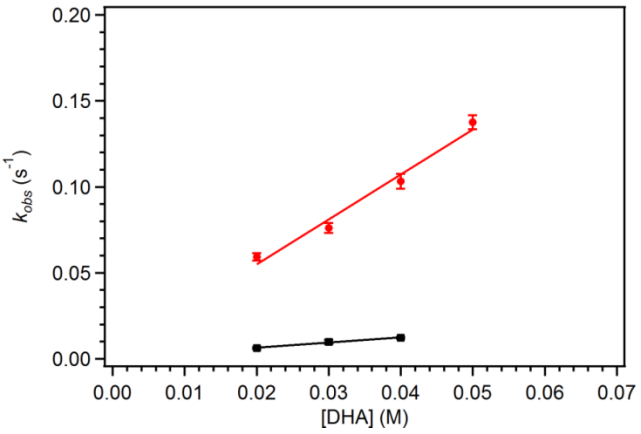

Figure A.4.7. Pseudo-first order rate constants, k_{obs} (s^{-1}) versus substrate concentration for a 1.9 mM solution of $[Mn^{IV}(O)(N4py)]^{2+}$ (**2**) in CF_3CH_2OH:CH_2Cl_2 (1:1) for DHA (red dots) and d_4-DHA (black squares). The second-order rate constant, k_2 (M^{-1} s^{-1}), was calculated from the linear correlation of the observed rate and substrate concentration.

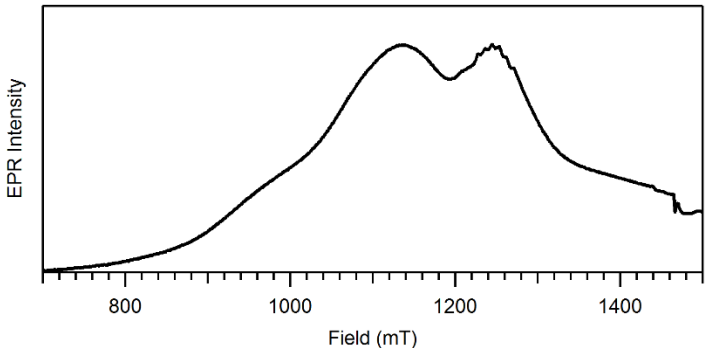

Figure A.4.8. Q-band, perpendicular-mode, absorption-type EPR spectra of frozen 2 mM solutions of CF_3CH_2OH solution of $[Mn^{IV}(O)(N4py)]^{2+}$ (**2**) collected under rapid passage conditions. Spectrum represents the average of 4 scans. Recording conditions: T = 2 K, 35.176 GHz microwave frequency, 0.1 mT modulation amplitude, and 16 ms time constant.

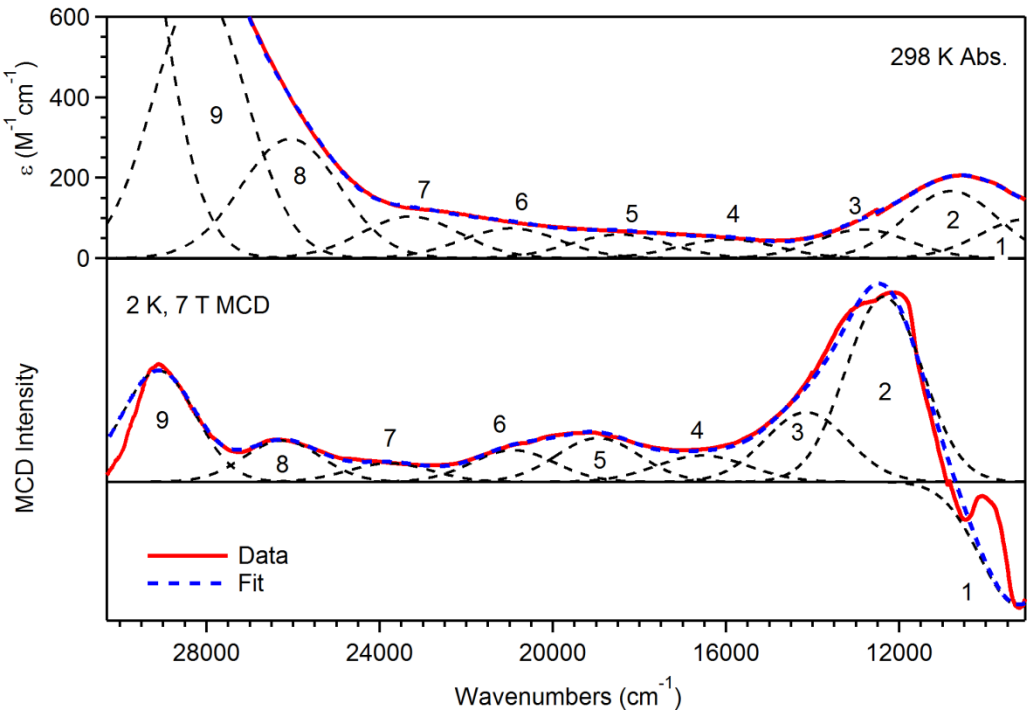

Figure A.4.9. Top: 298 K electronic absorption spectrum of 2.0 mM CF_3CH_2OH solution of $[Mn^{IV}(O)(N4py)]^{2+}$ (**2**). **Bottom:** 2 K, 7 T magnetic circular dichroism spectrum of a 7.5 mM frozen CF_3CH_2OH:C_2H_5OH (1:1) solution of **2** (solid red line). Gaussian bands, and their sum, are shown as dashed black and blue lines, respectively. Bands are labelled from low energy to high energy.

Table A.4.3. Energy and Widths (fwhm[a]) of Gaussian bands used in the Deconvoluted MCD and Electronic Absorption Spectrum of $[Mn^{IV}(O)(N4py)]^{2+}$ (**2**).

$[Mn^{IV}(O)(N4py)]^{+}$		
band	Energy (cm^{-1})	fwhm[a] (cm^{-1})
1	Abs: 9 075 MCD: 9250	2500 2080
2	Abs: 10 800 MCD: 12 350	2500 2080
3	Abs: 12 845 MCD: 14 150	2500 2250
4	Abs: 15 960 MCD: 16 550	2660 2500
5	Abs: 18 460 MCD: 18 955	2660 2250
6	Abs: 20 980 MCD: 20 915	2660 2250
7	Abs: 23 280 MCD: 23 771	2660 2250
8	Abs: 26 060 MCD: 26 240	2660 2080
9	Abs: 28 140 MCD: 29 100	2500 2000

[a] fwhm = full width at half maximum.

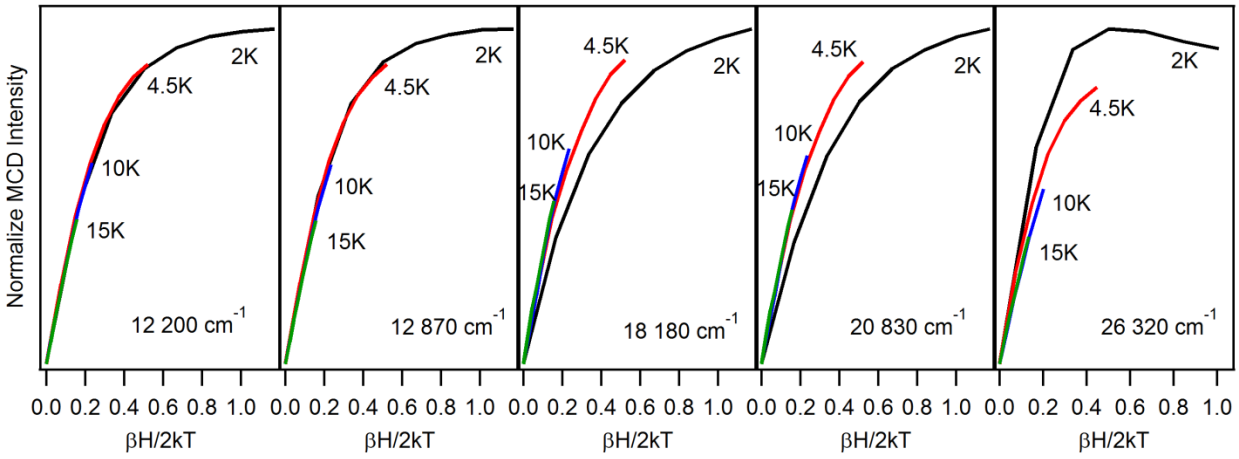

Figure A.4.10. VTVH MCD data for $[Mn^{IV}(O)(N4py)]^{2+}$ (**2**) collected at the indicated energies at 2, 4.5, 10, and 15 K.

Table A.4.5. Cartesian coordinates (Å) for DFT-optimized structure of $[Mn^{IV}(O)(N4py)]^{2+}$ (**2**).

Atom	x	y	z
Mn	0.000000	0.000000	0.000000
O	0.000000	-0.000000	-1.673290
N	2.000097	0.014236	0.251314
N	0.000000	-2.000888	0.251818
N	-0.090775	2.003667	0.324508
N	-2.004826	0.078980	0.323362
N	0.015103	-0.015765	2.138293
C	2.437871	0.102655	1.539094
C	-0.574706	2.290307	1.565952
C	-0.085096	-2.439032	1.539642
C	-2.294583	0.560283	1.565248
C	-2.990615	-0.289393	-0.519952
C	0.272512	2.991871	-0.518755
C	3.804281	0.014658	1.838801
C	-0.301640	4.649229	1.147097
C	0.015404	-3.804453	1.839939
C	1.383001	0.387134	2.593256
C	-0.379142	-1.386204	2.593125
C	0.165528	-2.881761	-0.764585
C	2.882128	-0.142532	-0.765479
C	4.258607	-0.221833	-0.531232
C	-1.051835	1.044413	2.313049
C	0.188481	-4.725198	0.792955
C	-4.651608	0.273273	1.145842
C	4.726257	-0.148949	0.791363
C	-4.337268	-0.203222	-0.136233
C	0.257752	-4.257333	-0.529764
C	0.177792	4.337636	-0.134630
C	-0.690040	3.608967	2.014981
C	-3.613970	0.667284	2.014232
H	-2.669446	-0.640739	-1.511425
H	0.626274	2.671780	-1.509658
H	4.144353	0.080240	2.883039
H	-0.381249	5.697254	1.473147
H	-0.047580	-4.144639	2.884298
H	1.642302	-0.102081	3.554741
H	1.379460	1.479466	2.792062
H	0.110421	-1.641836	3.555411
H	-1.471814	-1.390081	2.789995
H	0.221539	-2.434459	-1.768285
H	2.435035	-0.202154	-1.769058
H	4.948910	-0.345629	-1.377864
H	-1.278813	1.269703	3.376158
H	0.268642	-5.800942	1.010718
H	-5.700223	0.346143	1.471721
H	5.802807	-0.218849	1.008701
H	-5.124154	-0.502924	-0.843235
H	0.388752	-4.946765	-1.376023
H	0.473203	5.127043	-0.840859
H	-1.078797	3.826178	3.020792
H	-3.833666	1.053766	3.020358

Appendix A.5.

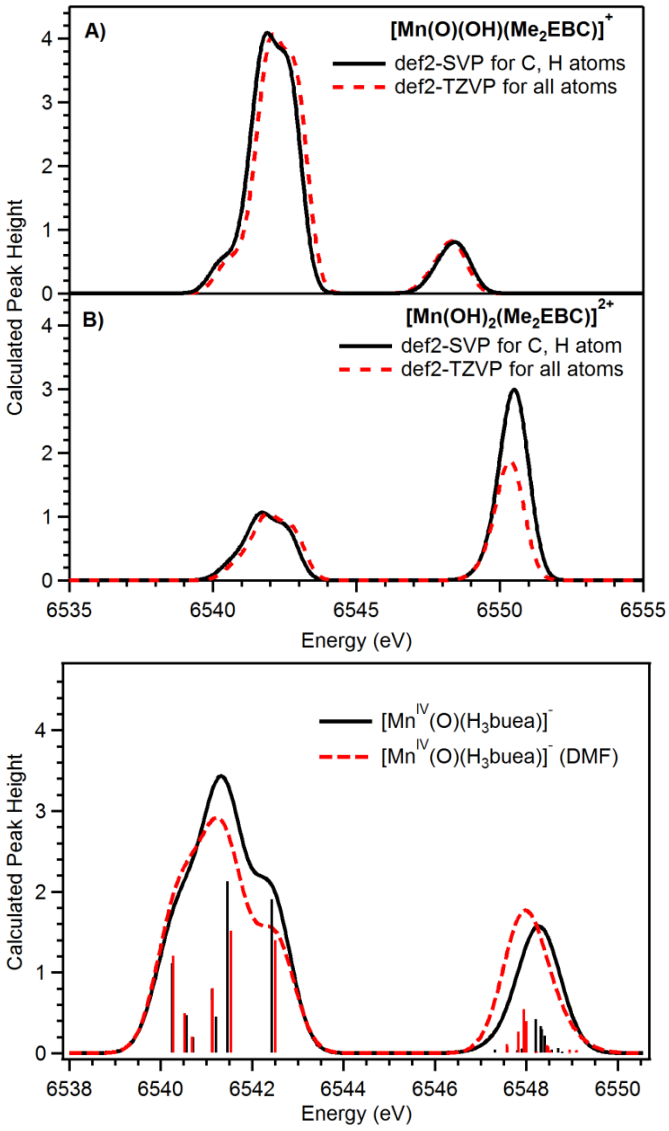

Figure A.5.1. Top: Comparison of the calculated XANES spectra using either the def2-TZVP(-f) basis set for all atoms (dashed red trace) or the combination of def2-SVP (for C and H) and def2-TZVP(-f) (for Mn, N, and O) basis sets (solid black trace). The comparison is for A) $[Mn^{IV}(O)(OH)(Me_2EBC)]^+$ (**3**) and B) $[Mn^{IV}(OH)_2(Me_2EBC)]^{2+}$ (**2**). **Bottom:** Comparison of the calculated XANES spectra for $[Mn^{IV}(O)(H_3buea)]^-$ in the gas phase (solid black trace) and using COSMO with DMF as solvent (red dashed trace). Sticks mark individual electronic transitions. A +32.6 eV energy shift and 1 eV Gaussian broadening were applied to all calculated spectra.

The calculated intensity is obtained from the sum of the squares of electric-dipole, magnetic-dipole, and electric-quadrupole transition moments from all contributing excited states:[1]

$$I = c \sum_F (f_{0F}^{ed})^2 + (f_{0F}^{md})^2 + (f_{0F}^{eq})^2$$

with $c = \frac{1}{4.33 \cdot 10^{-9}} \frac{1}{\sqrt{\pi}} \frac{2\sqrt{\log 2}}{FWHM}$

where *FWHM* was chosen to be 1 eV.

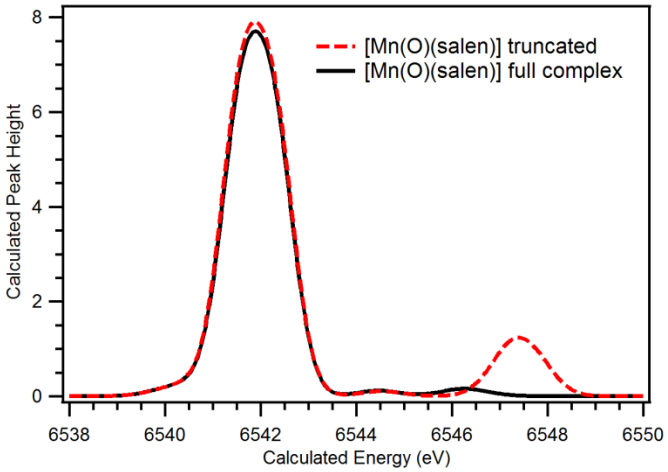

Figure A.5.2. Comparison of the calculated XANES spectra for [Mn^{IV}(O)(salen)] using a DFT-optimized model of the full structure of [Mn^{IV}(O)(salen)] (solid black trace) versus that using the truncated salen ligand (red dashed trace). The XANES features above 6544 eV are due to metal-to-ligand charge-transfer transitions. In the experimental spectrum, these transitions are concealed by the rising edge and thus not observable. A previous study noted that the TD-DFT-computed energies of these transitions are highly dependent on the chosen density functional.

Table A.5.1. Complete EXAFS Fitting Results for $[Mn^{II}(Cl_2)(Me_2EBC)]$ (**1**), $[Mn^{IV}(OH)_2(Me_2EBC)]^{2+}$ (**2**), and $[Mn^{IV}(O)(OH)(Me_2EBC)]^{+}$ (**3**).[a]

1		Mn−Cl			Mn−N			Mn···C			
	fit	*n*	*r*(Å)	$\sigma^2 \times 10^3$ (Å^2)	*n*	*r*(Å)	$\sigma^2 \times 10^3$ (Å^2)	n	*r*(Å)	$\sigma^2 \times 10^3$ (Å^2)	F-factor
	1				6	2.36	1.73				0.497
	2	2	2.47	1.52	4	2.28	4.42				0.407
	3	2	2.47	3.19	4	2.29	4.72	2	2.40	0.26	0.409
	4	2	2.47	1.70	4	2.30	4.48	4	3.22	3.20	0.383
	5	2	2.47	1.76	4	2.30	4.53	6	3.18	9.77	0.383
	6	2	2.47	1.39	4	2.29	4.09	4	3.21	1.22	0.359
								2	3.04	0.27	
	7	2	2.47	1.41	4	2.29	4.12	4	3.21	1.16	0.361
								2	3.04	0.00	
	8	2	2.47	1.43	4	2.29	4.14	4	3.22	0.79	0.378
								4	3.06	3.83	
	9	***2***	***2.47***	***1.42***	***4***	***2.29***	***4.19***	***4***	***3.03***	***3.05***	***0.359***
								6	***3.21***	***2.78***	
	10	2	2.47	1.43	4	2.29	4.26	8	3.20	4.69	0.362
								4	3.32	2.75	
	11	2	2.47	1.43	4	2.29	4.10	6	3.23	2.85	0.362
								8	3.05	9.03	
	12	2	2.47	1.41	4	2.29	4.18	6	3.22	2.64	0.360
								6	3.04	5.88	
2		Mn−O			Mn−N			Mn···C			
	fit	*n*	*r*(Å)	$\sigma^2 \times 10^3$ (Å^2)	*n*	*r*(Å)	$\sigma^2 \times 10^3$ (Å^2)	n	*r*(Å)	$\sigma^2 \times 10^3$ (Å^2)	F-factor
	1				6	1.99	1.94				0.701
	2	2	1.79	1.04	4	2.08	3.30				0.502
	3				2	2.04	-3.00				0.695
	4	2	1.79	0.99	4	2.08	3.45				0.500
	5	2	1.80	2.24	2	2.06	-1.70				0.489
					2	2.17	-0.30				
	6	2	1.79	0.97	4	2.09	3.55	6	2.94	6.74	0.440
	7	2	1.80	0.95	4	2.08	3.64	4	2.94	3.64	0.441
	8	***2***	***1.80***	***0.92***	***4***	***2.08***	***3.67***	***6***	***2.94***	***6.89***	***0.436***
	9	2	1.81	0.84	4	2.07	3.47	4	2.97	4.15	0.429
								3	2.19	5.65	
	10	2	1.80	0.92	4	2.08	3.64	8	2.95	9.53	0.437
3		Mn−O			Mn−N			Mn···C			
	fit	*n*	*r*(Å)	$\sigma^2 \times 10^3$ (Å^2)	*n*	*r*(Å)	$\sigma^2 \times 10^3$ (Å^2)	n	*r*(Å)	$\sigma^2 \times 10^3$ (Å^2)	F-factor
	1	2	1.77	8.11	4	2.12	2.44				0.583
	2	1	1.71	1.49	4	2.11	2.56				0.572
		1	1.84	1.61							
	3	1	1.72	1.44	4	2.11	2.86	4	3.02	2.64	0.481
		1	1.84	1.21							
	4	1	1.72	1.45	4	2.11	2.83	5	3.02	4.03	0.487
		1	1.84	1.26							
	5	1	1.71	0.93	4	2.11	2.98	4	2.89	2.65	0.460
		1	1.84	0.50				4	3.03	0.09	
	6	1	1.71	1.57	4	2.11	2.72	5	2.89	4.20	0.465
		1	1.84	1.47				4	3.03	0.39	
	7	1	1.72	1.82	4	2.11	2.55	5	2.89	5.55	0.469
		1	1.85	2.01				5	3.03	1.93	
	8	1	1.71	1.35	4	2.11	2.89	4	2.90	2.45	0.457
		1	1.84	1.00				3	3.03	-1.00	
	9	1	1.71	1.30	4	2.11	2.80	4	2.88	3.31	0.464
		1	1.84	1.12				5	3.02	3.02	
	10	***1***	***1.71***	***1.53***	***4***	***2.11***	***2.68***	***4***	***2.88***	***4.04***	***0.468***
		1	***1.84***	***1.44***				***6***	***3.02***	***2.54***	
	11	1	1.73	2.45	4	2.12	2.45	5	3.02	3.60	0.463
		1	1.85	2.87				1	2.35	3.14	

[a]Fourier transform ranges are as follows: **1**: 2 – 14.5 Å^{-1} (resolution 0.126 Å); **2**: 2 – 14.8 Å^{-1} (resolution 0.123 Å); **3**: 2 – 14.8 Å^{-1} (resolution 0.123 Å).

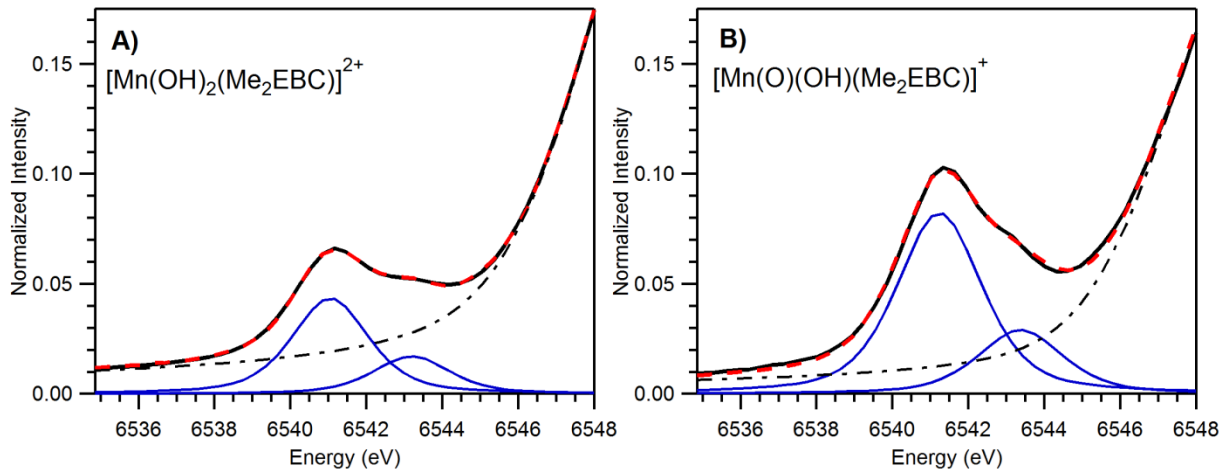

Figure A.5.3. Mn K-edge pre-edge data (solid black trace) and respective fits (red dashed trace) for A) $[Mn^{IV}(OH)_2(Me_2EBC)]^{2+}$ (**2**) and B) $[Mn^{IV}(O)(OH)(Me_2EBC)]^{+}$ (**3**). Broken black traces represent fits to the background; the solid blue traces represent fits to the pre-edge peaks.

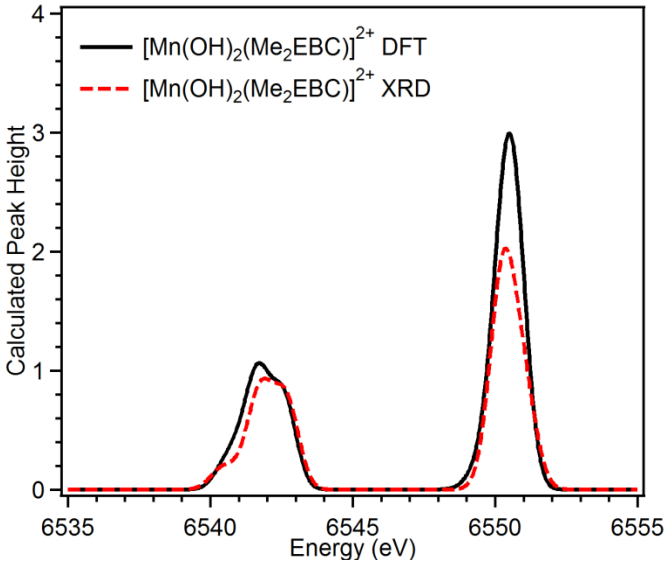

Figure A.5.4. Comparison of the calculated XANES spectra for $[Mn^{IV}(OH)_2(Me_2EBC)]^{2+}$ (**2**) using a DFT-optimized model (solid black trace) and using a model directly taken from the XRD coordinates (red dashed trace).

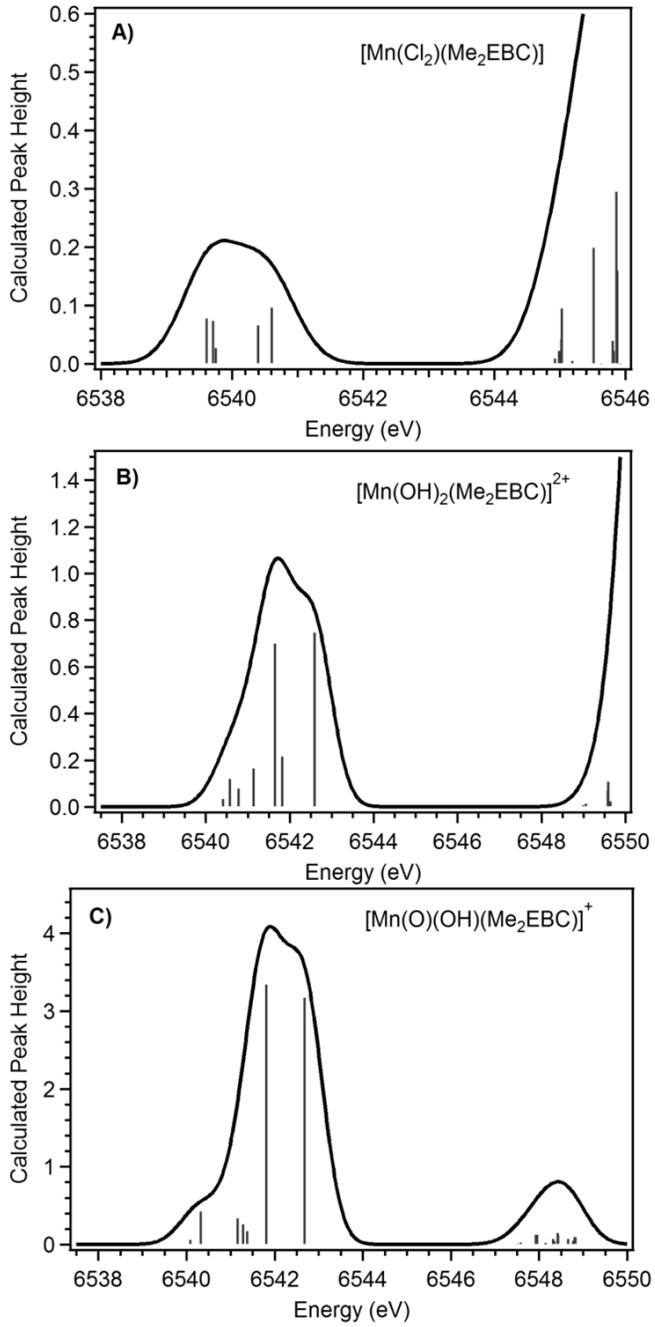

Figure A.5.5. TD-DFT calculated XANES spectra for A) $[Mn^{II}(Cl_2)(Me_2EBC)]$ (**1**), B) $[Mn^{IV}(OH)_2(Me_2EBC)]^{2+}$ (**2**), and C) $[Mn^{IV}(O)(OH)(Me_2EBC)]^{+}$ (**3**). Sticks mark individual electronic transitions.

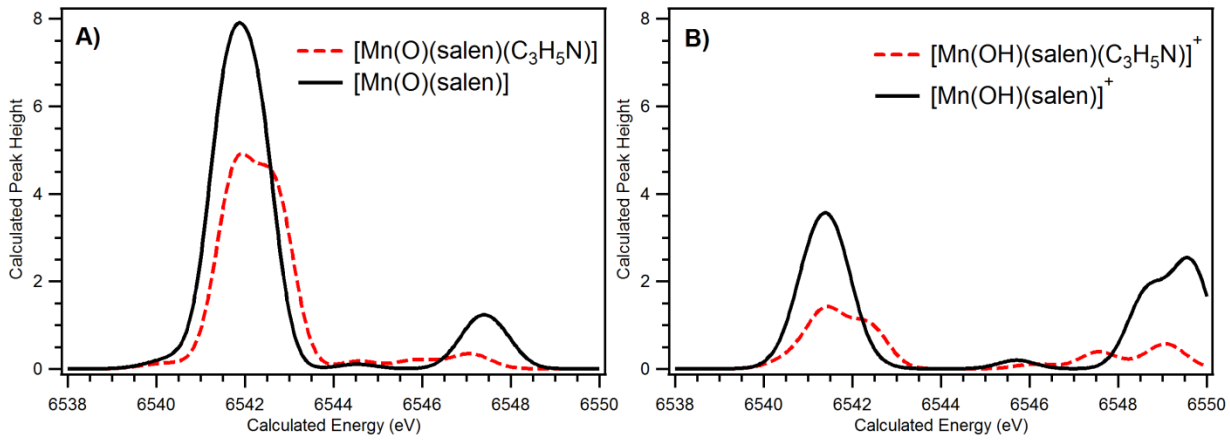

Figure A.5.6. Comparison of the calculated XANES spectra for A) [Mn^{IV}(O)(salen)] (solid black trace) and [Mn^{IV}(O)(salen)(C_3H_5N)] (red dashed trace) and B) [Mn^{IV}(OH)(salen)]$^+$ (solid black trace) and [Mn^{IV}(OH)(salen)(C_3H_5N)]$^+$ (red dashed trace).

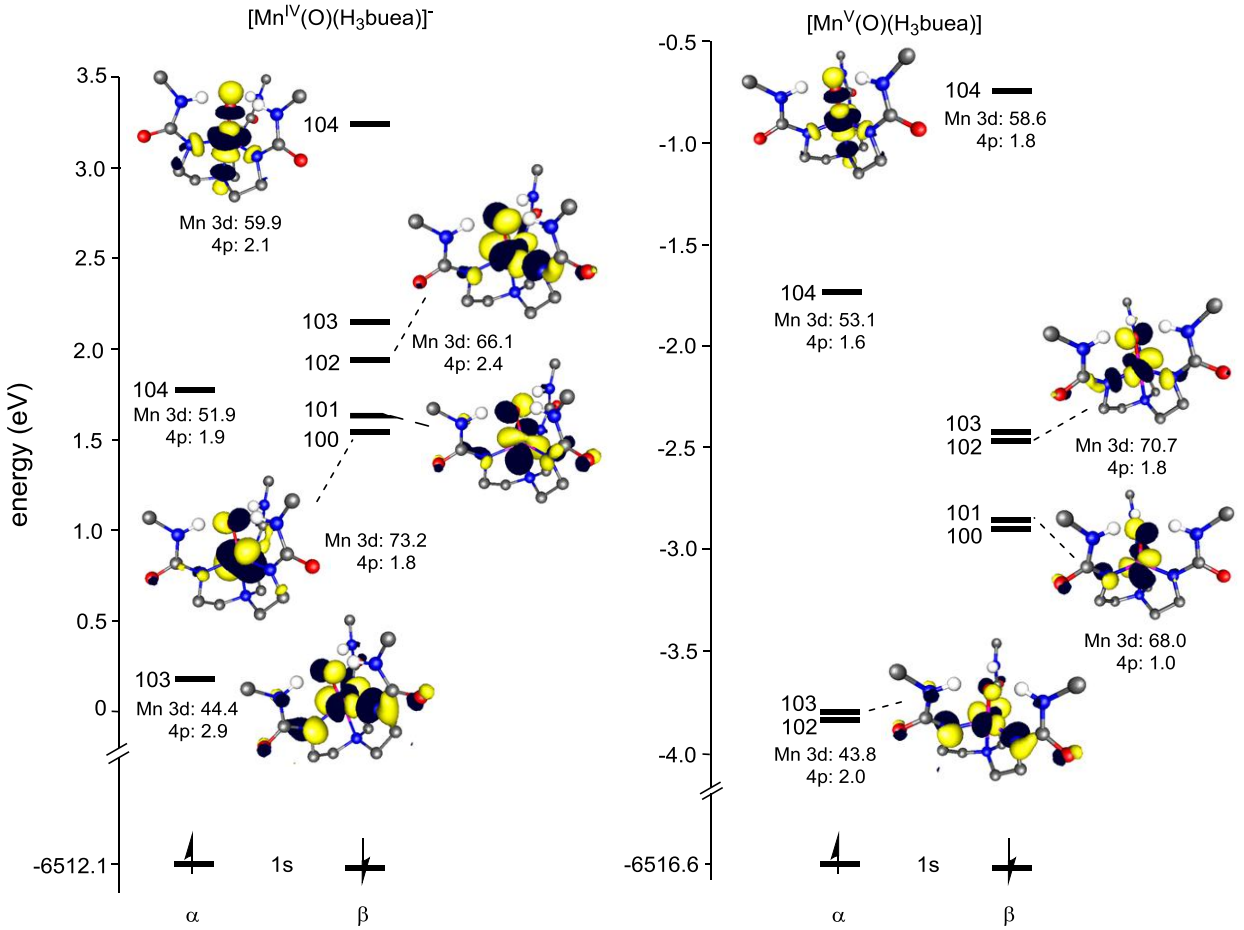

Figure A.5.7. MO diagrams for $[Mn^{IV}(O)(H_3buea)]^-$ and $[Mn^{V}(O)(H_3buea)]$ showing the core 1s MOs and the unoccupied Mn 3d-based α- and β-orbitals. The energies are for the spin unrestricted Kohn-Sham orbitals. The percent of Mn 3d and 4p character and representative surface contour plots for individual Kohn-Sham d orbitals are given.

Table A.5.2. TD-DFT Calculated Energies (eV), Oscillator Strengths, and Percent Contributions from Dominant One-Electron Excitations for the Major XANES Transitions of $[Mn^{II}(Cl_2)(Me_2EBC)]$ (**1**), $[Mn^{IV}(OH)_2(Me_2EBC)]^{2+}$ (**2**), and $[Mn^{IV}(O)(OH)(Me_2EBC)]^{+}$ (**3**).

complex	state	energy	$f_{osc} \times 10^3$	transition[a]	%	acceptor MO composition			
1						Mn 3d	Mn 4p		
	1	6539.8	0.0001	$1s\beta \rightarrow 98\beta$ (yz)	91	86.9	>0.1		
	2	6539.9	0.0006	$1s\beta \rightarrow 99\beta$ (xz)	92	86.2	0.1		
	3	6540.6	0.0001	$1s\beta \rightarrow 100\beta$ (xy)	92	86.8	>0.1		
	4	6540.6	0.0005	$1s\beta \rightarrow 103\beta$ (z^2)	94	80.7	0.1		
	5	6540.8	0.0016	$1s\beta \rightarrow 105\beta$ (x^2-y^2)	89	76.3	0.5		
2						Mn 3d	Mn 4p	OH 2p	OH 2p
	5	6541.6	0.0245	$1s\alpha \rightarrow 94\alpha$ (xy)	99	52.4	0.5	11.3	11.2
	6	6541.8	0.0059	$1s\beta \rightarrow 93\beta$ (z^2)	98	69.0	0.2	1.6	1.7
	7	6542.6	0.0259	$1s\beta \rightarrow 94\beta$ (xy)	99	65.6	0.7	6.9	7.0
3						Mn 3d	Mn 4p	OH 2p	O 2p
	1	6540.3	0.0012	$1s\beta \rightarrow 90\beta$ (xy)	96	82.9	0.1	8.1	0.5
	2	6540.5	0.0144	$1s\alpha \rightarrow 93\alpha$ (x^2-y^2)	99	59.9	0.3	8.2	2.3
	3	6541.4	0.0109	$1s\beta \rightarrow 92\beta$ (yz)	58	68.3	0.2	0.1	20.2
				$1s\beta \rightarrow 93\beta$ (x^2-y^2)	38	70.1	0.3	5.2	1.1
	4	6541.5	0.0081	$1s\beta \rightarrow 91\beta$ (xz)	91	64.6	0.4	1.0	26.8
	5	6541.6	0.0037	$1s\beta \rightarrow 93\beta$ (x^2-y^2)	57	70.1	0.3	5.2	1.1
				$1s\beta \rightarrow 92\beta$ (yz)	38	68.3	0.2	0.1	20.2
	6	6541.8	0.1238	$1s\alpha \rightarrow 94\alpha$ (z^2)	98	50.9	2.9	6.0	22.7
	7	6542.7	0.1172	$1s\beta \rightarrow 94\beta$ (z^2)	96	58.5	3.2	4.0	14.8

[a] The α and β designations correspond to spin-up (majority spin) and spin-down (minority spin) MOs, respectively.

Table A.5.3. Comparison of DFT-Optimized Manganese-Ligand Bond Lengths (Å) for Truncated and Full Models of Mn^{IV} Salen and Porphyrin Complexes.

complex	Mn–O(H)[a]	Mn–N_{eq}[a,b]	Mn–O[a,d]	Ref.
$[Mn^{IV}(O)(T_{piv}PP)]$ [e]	1.666 (1.69)	2.03 (2.00)		2
$[Mn^{IV}(O)(T_{piv}PP)]$ [f]	1.662	2.01		
$[Mn^{IV}(O)(salen)]$ [e]	1.676 (1.58)	1.98 (1.99)	1.90 (1.81)	3
$[Mn^{IV}(O)(salen)]$ [f]	1.670	1.99	1.90	
$[Mn^{IV}(OH)(salen)]^{+}$ [e]	1.814 (1.83)[g]	1.97 (1.98)	1.86 (1.83)	3
$[Mn^{IV}(OH)(salen)]^{+}$ [f]	1.810[g]	1.98	1.85	

[a]Distances determined from analysis of EXAFS data are provided in parenthesis. [b]Average Mn–N_{eq} (equatorial) distance. [c]Mn–N_{ax} (axial) distance. [d]Average Mn–O (phenolate) distance. [e]Full, untruncated model. [f]Truncated model. [g]Mn^{IV}–OH distance.

Table A.5.4. TD-DFT Calculated Energies (eV), Oscillator Strengths, and Percent Contributions from Dominant One-Electron Excitations for the Major XANES Transitions of $[Mn^{IV}(O)(N4py)]^{2+}$ and $[Mn^{IV}(O)(Bn\text{-}TPEN)]^{2+}$.

complex	state	energy	$f_{osc} \times 10^3$	transition[a]	%	acceptor MO composition		
$[Mn(O)(N4py)]^{2+}$						Mn 3d	Mn 4p	O 2p
	6	6541.9	0.1059	$1s\alpha \rightarrow 120\alpha\ (z^2)$	94	50.4	2.4	20.9
	7	6542.8	0.1071	$1s\beta \rightarrow 123\beta\ (z^2)$	95	57	2.9	15.5
$[Mn(O)(Bn\text{-}TPEN)]^{2+}$						Mn 3d	Mn 4p	O 2p
	6	6541.9	0.1038	$1s\alpha \rightarrow 135\alpha\ (z^2)^b$	39	26.2	0.7	10.5
				$1s\alpha \rightarrow 132\alpha\ (z^2)^b$	39	19.3	1.4	7.5
				$1s\alpha \rightarrow 134\alpha\ (z^2)^b$	17	8.9	0.4	4.4
	7	6542.8	0.1038	$1s\beta \rightarrow 137\beta\ (z^2)$	89	54.9	2.3	14.3

[a] The α and β designations correspond to spin-up (majority spin) and spin-down (minority spin) MOs, respectively. [b] For $[Mn^{IV}(O)(Bn\text{-}TPEN)]^{2+}$ $3d_{z^2}$ character is distributed over three MOs.

Table A.5.5. TD-DFT Calculated Energies (eV), Oscillator Strengths, and Percent Contributions from Dominant One-Electron Excitations for the Major XANES Transitions of $[Mn^{IV}(O)(T_{piv}PP)]$, $[Mn^{IV}(O)(salen)]$, and $[Mn^{IV}(OH)(salen)]^{+}$.

complex	state	energy	$f_{osc} \times 10^3$	transition[a]	%	composition of acceptor MO		
$[Mn(O)(T_{piv}PP)]$						Mn 3d	Mn 4p	O 2p
	4	6541.8	0.2096	$1s\alpha \rightarrow 117\alpha\ (z^2)$	95	42.0	8.7	28.1
	7	6541.8	0.2243	$1s\beta \rightarrow 117\beta\ (z^2)$	88	48.0	11.2	15.9
[Mn(O)(salen)]						Mn 3d	Mn 4p	O 2p
	4	6541.8	0.1948	$1s\alpha \rightarrow 114\alpha\ (z^2)$	64	34.6	6.1	22.3
				$1s\alpha \rightarrow 115\alpha\ (x^2\text{-}y^2)$	18	47.2	0.9	3.3
	7	6541.8	0.2004	$1s\beta \rightarrow 114\beta\ (z^2)$	62	39.5	7.2	13.8
$[Mn(OH)(salen)]^{+}$						Mn 3d	Mn 4p	O 2p
	3	6541.3	0.0551	$1s\alpha \rightarrow 112\alpha\ (z^2)$	90	40.1	3.0	19.1
	6	6541.9	0.0808	$1s\beta \rightarrow 113\beta\ (z^2)$	45	38.7	3.2	5.4
				$1s\beta \rightarrow 112\beta\ (xz)$	43	43.2	2.0	5.4

[a] The α and β designations correspond to spin-up (majority spin) and spin-down (minority spin) MOs, respectively.

Table A.5.6. Comparison of Mn-Ligand Bond Lengths (Å) and Angles (°) from DFT Computations for $[Mn^{IV}(O)(H_3buea)]^{-}$ and $[Mn^{V}(O)(H_3buea)]$.

	$[Mn^{IV}(O)(H_3buea)]^{-}$	$[Mn^{V}(O)(H_3buea)]$
Mn–O	1.715	1.696
$Mn–N_{eq}$	1.951, 1.980, 2.001	1.885
$Mn–N_{ax}$	2.173	2.133
	Bond Angles	Bond Angles
$N_{eq}–Mn–N_{eq}$	130.91, 109.75, 112.98	118.35
$N_{eq}–Mn–O$	96.42, 97.46, 101.82	97.44

Table A.5.7. TD-DFT Calculated Energies (eV), Percent Contributions from Dominant One-Electron Excitations for Major XANES Transitions of $[Mn^{IV}(O)(H_3buea)]^-$ and $[Mn^{V}(O)(H_3buea)]$.

complex	state	energy	$f_{osc} \times 10^3$	transition[a]	acceptor MO composition		
$[Mn^{IV}(O)(H_3buea)]^-$					Mn 3d	Mn 4p	O 2p
	1	6540.2	0.0414	$1s\alpha \rightarrow 103\alpha$ ($xy/x^2\text{-}y^2$)	44.4	2.9	6.7
	2	6540.6	0.0174	$1s\beta \rightarrow 100\beta$ (xz/yz)	73.2	1.8	7.3
	3	6540.7	0.0073	$1s\beta \rightarrow 101\beta$ (xz/yz)	71.3	0.8	7.4
	4	6541.1	0.0295	$1s\beta \rightarrow 102\beta$ ($xy/x^2\text{-}y^2$)	66.1	2.4	9.8
	5	6541.2	0.0168	$1s\beta \rightarrow 103\beta$ ($xy/x^2\text{-}y^2$)	70.6	1.6	6.7
	6	6541.5	0.0790	$1s\alpha \rightarrow 104\alpha$ (z^2)	51.9	1.9	18.0
	7	6542.4	0.0709	$1s\beta \rightarrow 104\beta$ (z^2)	59.9	2.1	11.2
$[Mn^{V}(O)(H_3buea)]$					Mn 3d	Mn 4p	O 2p
	1	6541.0	0.0117	101β (xz/yz)	68.0	1.0	10.3
	2	6541.0	0.0117	100β (xz/yz)	68.0	1.0	10.3
	3	6541.1	0.0438	$1s\alpha \rightarrow 102\alpha$ ($xy/x^2\text{-}y^2$)	43.8	2.0	3.5
	4	6541.1	0.0438	$1s\alpha \rightarrow 103\alpha$ ($xy/x^2\text{-}y^2$)	43.9	2.0	23.5
	5	6541.6	0.0349	$1s\beta \rightarrow 102\beta$ ($xy/x^2\text{-}y^2$)	70.7	1.8	10.9
	6	6541.6	0.0348	$1s\beta \rightarrow 103\beta$ ($xy/x^2\text{-}y^2$)	60.7	1.9	10.9
	7	6542.5	0.0666	$1s\alpha \rightarrow 104\alpha$ (z^2)	53.1	1.6	15.2
	8	6543.1	0.0718	$1s\beta \rightarrow 104\beta$ (z^2)	58.6	1.8	12.2

[a] The α and β designations correspond to spin-up (majority spin) and spin-down (minority spin) MOs, respectively.

References

1. Roemelt, M.; Beckwith, M. A.; Duboc, C.; Collomb, M.-N.; Neese, F.; DeBeer, S., Inorg. Chem. **2011,** 51, 680-687.
2. Ayougou, K.; Bill, E.; Charnock, J. M.; Garner, C. D.; Mandon, D.; Trautwein, A. X.; Weiss, R.; Winkler, H., Angew. Chem., Int. Ed. Engl. **1995,** 34, 343-346.
3. Kurahashi, T.; Kikuchi, A.; Tosha, T.; Shiro, Y.; Kitagawa, T.; Fujii, H., Inorg. Chem. **2008,** 47, 1674-1686.

Table A.5.8. Cartesian Coordinates for DFT-optimized Model of $[Mn^{II}(Cl)_2(Me_2EBC)]$ (**1**).

Atom	x	y	z
Mn	0.000030	0.275198	-0.000029
Cl	-1.810229	2.024714	0.096672
Cl	1.809467	2.025521	-0.096751
N	0.218711	-0.132014	2.389715
N	-0.218576	-0.131993	-2.389753
N	-1.473081	-1.561563	-0.162965
N	1.473001	-1.561661	0.162965
C	-0.960850	-0.839829	2.998256
C	-2.254866	-0.775862	2.181026
C	-2.355324	-1.793255	1.036478
C	-2.302318	-1.152390	-1.331026
C	-1.493454	-0.891555	-2.609876
C	0.961103	-0.839614	-2.998290
C	2.254996	-0.775886	-2.180831
C	2.355108	-1.793562	-1.036518
C	1.493687	-0.891414	2.609795
C	2.302384	-1.152343	1.330860
C	0.624369	-2.754030	0.439833
C	-0.624516	-2.754029	-0.439632
C	0.312938	1.231840	2.968748
C	-0.312969	1.231874	-2.968735
H	-1.138141	-0.423005	4.015682
H	-0.690127	-1.904135	3.152721
H	-2.431008	0.253048	1.804788
H	-3.093223	-1.004133	2.874113
H	-3.409001	-1.837862	0.687480
H	-2.129078	-2.803518	1.438615
H	-2.832581	-0.229681	-1.023044
H	-3.073684	-1.925069	-1.564500
H	-2.151409	-0.345626	-3.318713
H	-1.253489	-1.850914	-3.108392
H	1.138563	-0.422511	-4.015570
H	0.690427	-1.903885	-3.153088
H	2.431138	0.252930	-1.804315
H	3.093448	-1.004049	-2.873837
H	3.408777	-1.838750	-0.687559
H	2.128365	-2.803634	-1.438849
H	1.253912	-1.850727	3.108493
H	2.151688	-0.345296	3.318441
H	2.832574	-0.229643	1.022710
H	3.073820	-1.924965	1.564292
H	0.319358	-2.741911	1.501329
H	1.195629	-3.698369	0.291004
H	-0.319484	-2.742069	-1.501128
H	-1.195859	-3.698301	-0.290695
H	-0.621840	1.784797	2.755652
H	0.468641	1.187768	4.072334
H	1.147329	1.779946	2.493377
H	0.621723	1.784947	-2.755565
H	-1.147461	1.779846	-2.493389
H	-0.468619	1.187822	-4.072329

Table A.5.9. Cartesian Coordinates for DFT-optimized Model of $[Mn^{IV}(OH)_2(Me_2EBC)]^{2+}$ (**2**) (gas-phase optimization).

Atom	x	y	z
Mn	0.000000	0.000000	0.000000
O	-1.236960	-0.499146	1.228804
O	-1.151822	0.633303	-1.249563
H	-2.173798	-0.230437	1.107614
H	-2.114812	0.471291	-1.144884
N	0.174058	2.022079	0.861350
N	-0.038534	-2.029690	-0.860173
N	1.525094	-0.871850	1.220768
N	1.634038	0.694429	-1.193313
C	0.828481	2.081437	2.238213
C	0.784911	0.798363	3.060580
C	1.798202	-0.237992	2.581315
C	1.005870	-2.266295	1.446899
C	0.626743	-2.960573	0.143246
C	0.628884	-2.163285	-2.225548
C	0.743497	-0.884201	-3.047297
C	1.857991	0.032655	-2.549541
C	0.956658	2.871647	-0.129485
C	1.278198	2.138019	-1.427049
C	2.853776	0.517594	-0.324534
C	2.771829	-0.833535	0.373423
C	-1.219812	2.570050	0.997541
C	-1.482422	-2.418289	-1.021025
H	0.343084	2.911141	2.793065
H	1.886491	2.380823	2.098021
H	-0.237042	0.378995	3.131175
H	1.080487	1.070500	4.096471
H	1.876453	-1.063454	3.318086
H	2.800948	0.233631	2.533971
H	0.127281	-2.164002	2.110760
H	1.772424	-2.871519	1.979731
H	-0.052298	-3.805433	0.374867
H	1.516153	-3.407015	-0.340367
H	0.063330	-2.933966	-2.789533
H	1.644134	-2.579107	-2.067338
H	-0.223701	-0.353119	-3.135179
H	1.024648	-1.188728	-4.078177
H	2.040923	0.843449	-3.284042
H	2.800658	-0.548225	-2.485290
H	1.881948	3.216173	0.369898
H	0.380594	3.786996	-0.372014
H	0.405314	2.134090	-2.106131
H	2.116809	2.653094	-1.945931
H	2.881991	1.330015	0.425811
H	3.780106	0.608255	-0.930770
H	2.721903	-1.644737	-0.377111
H	3.671541	-1.026749	0.995529
H	-1.781476	1.974832	1.740586
H	-1.163580	3.619030	1.357173
H	-1.730858	2.548511	0.019636
H	-1.960955	-1.764652	-1.773109
H	-2.004708	-2.338717	-0.052100

H	-1.537766	-3.467318	-1.380649

Table A.5.10. Cartesian Coordinates for DFT-optimized Model of $[Mn^{IV}(OH)_2(Me_2EBC)]^{2+}$ (**2**) (COSMO optimization).

Atom	x	y	z
Mn	0.000005	-0.006665	-0.000003
O	-1.356774	1.202885	0.076175
O	1.356810	1.202854	-0.076143
H	-1.096819	2.146002	0.167854
H	1.096893	2.145977	-0.167874
N	0.181290	-0.068722	2.183930
N	-0.181215	-0.068703	-2.183972
N	-1.428750	-1.581122	-0.134202
N	1.428666	-1.581193	0.134215
C	-0.988082	-0.721380	2.906034
C	-2.308789	-0.755997	2.149027
C	-2.324747	-1.830609	1.067918
C	-2.292146	-1.147049	-1.283086
C	-1.470185	-0.801045	-2.515223
C	0.988331	-0.721054	-2.906105
C	2.308908	-0.756028	-2.148883
C	2.324519	-1.830838	-1.067967
C	1.470440	-0.800771	2.515156
C	2.292213	-1.147090	1.282961
C	0.620420	-2.815899	0.438060
C	-0.620556	-2.815908	-0.437882
C	0.274116	1.350638	2.658538
C	-0.274399	1.350658	-2.658508
H	-1.107933	-0.188673	3.870387
H	-0.694961	-1.758949	3.154011
H	-2.590076	0.238011	1.754008
H	-3.089832	-1.040368	2.883783
H	-3.353154	-1.974009	0.682222
H	-2.017493	-2.794655	1.517298
H	-2.865765	-0.273067	-0.927362
H	-3.010630	-1.955739	-1.533882
H	-2.084893	-0.179102	-3.193102
H	-1.207061	-1.713531	-3.078855
H	1.108390	-0.187955	-3.870212
H	0.695254	-1.758520	-3.154562
H	2.590313	0.237858	-1.753643
H	3.090000	-1.040397	-2.883590
H	3.352884	-1.974683	-0.682318
H	2.016897	-2.794698	-1.517493
H	1.207590	-1.713071	3.079225
H	2.085185	-0.178432	3.192626
H	2.865916	-0.273237	0.927063
H	3.010615	-1.955844	1.533789
H	0.336063	-2.809914	1.505591
H	1.233127	-3.724884	0.273947
H	-0.336166	-2.810055	-1.505404
H	-1.233313	-3.724844	-0.273690
H	-0.670902	1.877104	2.437263
H	0.435944	1.348176	3.755712
H	1.118343	1.857958	2.163395

H	0.670445	1.877384	-2.437103
H	-1.118822	1.857711	-2.163425
H	-0.436111	1.348212	-3.755698

Table A.5.11. Cartesian Coordinates for DFT-optimized Model of $[Mn^{IV}(O)(OH)(Me_2EBC)]^+$ (**3**) (gas-phase optimization).

Atom	x	y	z
Mn	0.000000	0.000000	0.000000
O	1.410801	1.171894	0.024643
O	-1.247812	1.125077	-0.008596
N	-0.044801	-0.080476	-2.156925
N	1.509198	-1.683468	0.190554
N	-0.044801	-0.080476	2.143551
N	-1.313906	-1.729622	-0.256165
H	1.036813	2.086918	0.065933
C	1.128878	-0.816647	-2.774444
C	2.446860	-0.670018	-2.011804
C	2.631911	-1.630103	-0.825203
C	2.022163	-1.396391	1.568993
C	0.876824	-1.194059	2.559219
C	-1.437894	-0.275923	2.718306
C	-2.524976	-0.864781	1.804169
C	-2.144917	-2.071596	0.949599
C	-1.359484	-0.720101	-2.561629
C	-2.181785	-1.257517	-1.374049
C	-0.503416	-2.917792	-0.660011
C	0.784857	-2.996763	0.155862
C	-0.010867	1.334299	-2.647915
C	0.482526	1.207759	2.697056
H	1.243751	-0.439894	-3.816336
H	0.866533	-1.890751	-2.865410
H	2.578605	0.377697	-1.674919
H	3.274880	-0.891575	-2.721919
H	3.564292	-1.346579	-0.293410
H	2.793837	-2.662192	-1.208643
H	2.627594	-0.470915	1.497563
H	2.683909	-2.220334	1.933273
H	1.293864	-0.982525	3.571082
H	0.275433	-2.118726	2.662533
H	-1.794784	0.723055	3.034004
H	-1.327220	-0.884027	3.645330
H	-2.918820	-0.059569	1.151745
H	-3.359118	-1.175645	2.472669
H	-3.064258	-2.594970	0.595024
H	-1.579128	-2.813576	1.552253
H	-1.148384	-1.518531	-3.304256
H	-1.980173	0.033516	-3.087268
H	-2.806838	-0.443230	-0.962202
H	-2.848115	-2.084314	-1.721208
H	-0.267464	-2.833447	-1.736339
H	-1.097581	-3.854902	-0.541326
H	0.545414	-3.304576	1.192243
H	1.439071	-3.800390	-0.251744
H	0.976182	1.776855	-2.410295
H	-0.169635	1.352673	-3.751196

H	-0.801243	1.907674	-2.124689
H	-0.112758	2.042479	2.276132
H	1.542663	1.336148	2.409579
H	0.389027	1.198333	3.808116

Table A.5.12. Cartesian Coordinates for DFT-optimized Model of $[Mn^{IV}(O)(OH)(Me_2EBC)]^+$ (**3**) (COSMO optimization).

Atom	x	y	z
Mn	-0.021607	0.051813	0.004032
O	-1.257699	1.211793	0.084293
O	1.384640	1.252391	-0.118006
H	0.971285	2.140532	-0.047043
N	0.115774	0.004084	2.144311
N	-0.254555	-0.078445	-2.135300
N	-1.342701	-1.656873	-0.100851
N	1.491185	-1.594579	0.094039
C	-1.221804	-0.165513	2.842450
C	-2.378556	-0.778899	2.041544
C	-2.053908	-1.993385	1.180922
C	-2.314749	-1.212638	-1.141481
C	-1.598774	-0.728273	-2.410684
C	0.857135	-0.835997	-2.836260
C	2.236571	-0.654430	-2.209747
C	2.538174	-1.550287	-0.998846
C	1.051751	-1.120770	2.497035
C	2.117492	-1.319555	1.428819
C	0.779208	-2.920170	0.125810
C	-0.573730	-2.854664	-0.565841
C	0.707987	1.284368	2.639643
C	-0.263070	1.317544	-2.668861
H	-1.541870	0.841768	3.165047
H	-1.030952	-0.751714	3.766770
H	-2.839026	0.004160	1.409968
H	-3.144670	-1.086935	2.782850
H	-2.985638	-2.539836	0.917485
H	-1.421434	-2.709354	1.740639
H	-2.895950	-0.385939	-0.697751
H	-3.010040	-2.043396	-1.396512
H	-2.254998	0.000105	-2.921942
H	-1.440395	-1.558842	-3.125069
H	0.867610	-0.496535	-3.893811
H	0.592319	-1.908851	-2.862146
H	2.391910	0.408363	-1.945613
H	2.991743	-0.909970	-2.981933
H	3.488941	-1.210446	-0.544213
H	2.709013	-2.590958	-1.343895
H	0.452708	-2.038909	2.633439
H	1.532641	-0.916508	3.477406
H	2.725698	-0.402406	1.318981
H	2.796247	-2.148948	1.729319
H	0.640765	-3.225733	1.178270
H	1.404713	-3.708052	-0.340789
H	-0.448421	-2.793701	-1.659044
H	-1.154950	-3.781800	-0.372426
H	0.098092	2.127255	2.267991

H	0.709797	1.281593	3.750601
H	1.739812	1.392123	2.266663
H	0.735110	1.767904	-2.526789
H	-1.007123	1.905061	-2.103078
H	-0.510730	1.301411	-3.751489

Table A.5.13. Cartesian Coordinates for DFT-optimized Model of $[Mn^{IV}(O)(N4py)]^{2+}$.

Atom	x	y	z
Mn	0.000000	0.000000	0.000000
O	0.000000	-0.000000	-1.673290
N	2.000097	0.014236	0.251314
N	0.000000	-2.000888	0.251818
N	-0.090775	2.003667	0.324508
N	-2.004826	0.078980	0.323362
C	2.437871	0.102655	1.539094
C	-0.574706	2.290307	1.565952
C	-0.085096	-2.439032	1.539642
N	0.015103	-0.015765	2.138293
C	-2.294583	0.560283	1.565248
C	-2.990615	-0.289393	-0.519952
C	0.272512	2.991871	-0.518755
C	3.804281	0.014658	1.838801
C	-0.301640	4.649229	1.147097
C	0.015404	-3.804453	1.839939
C	1.383001	0.387134	2.593256
C	-0.379142	-1.386204	2.593125
C	0.165528	-2.881761	-0.764585
C	2.882128	-0.142532	-0.765479
C	4.258607	-0.221833	-0.531232
C	-1.051835	1.044413	2.313049
C	0.188481	-4.725198	0.792955
C	-4.651608	0.273273	1.145842
C	4.726257	-0.148949	0.791363
C	-4.337268	-0.203222	-0.136233
C	0.257752	-4.257333	-0.529764
C	0.177792	4.337636	-0.134630
C	-0.690040	3.608967	2.014981
C	-3.613970	0.667284	2.014232
H	-2.669446	-0.640739	-1.511425
H	0.626274	2.671780	-1.509658
H	4.144353	0.080240	2.883039
H	-0.381249	5.697254	1.473147
H	-0.047580	-4.144639	2.884298
H	1.642302	-0.102081	3.554741
H	1.379460	1.479466	2.792062
H	0.110421	-1.641836	3.555411
H	-1.471814	-1.390081	2.789995
H	0.221539	-2.434459	-1.768285
H	2.435035	-0.202154	-1.769058
H	4.948910	-0.345629	-1.377864
H	-1.278813	1.269703	3.376158
H	0.268642	-5.800942	1.010718
H	-5.700223	0.346143	1.471721
H	5.802807	-0.218849	1.008701
H	-5.124154	-0.502924	-0.843235
H	0.388752	-4.946765	-1.376023

H	0.473203	5.127043	-0.840859
H	-1.078797	3.826178	3.020792
H	-3.833666	1.053766	3.020358

Table A.5.14. Cartesian Coordinates for DFT-optimized Model of $[Mn^{IV}(O)(BnTPEN)]^{2+}$.

Atom	x	y	z
Mn	7.542905	10.202935	3.415702
N	8.376700	11.985383	2.963924
N	6.518627	10.920655	5.029430
N	5.871170	11.219574	2.436675
N	6.405208	8.467879	3.090756
N	8.578101	9.336107	1.804707
O	8.710470	9.545157	4.425673
C	9.479385	12.496443	3.560035
C	0.038880	13.708700	3.137683
C	9.438310	14.397630	2.071393
C	8.291390	13.859280	1.458767
C	7.776688	12.642085	1.922954
C	6.555773	11.951466	1.334915
C	5.251394	12.186620	3.394656
C	5.444279	11.730229	4.818741
C	4.650043	12.176722	5.884088
C	4.990627	11.802899	7.194301
C	6.121459	10.995751	7.401598
C	6.861222	10.568832	6.294768
C	4.887952	10.162101	2.027734
C	5.553980	8.798210	1.886624
C	7.414020	7.423581	2.729043
C	8.404525	7.985866	1.749584
C	9.137752	7.183720	0.863849
C	10.096761	7.778242	0.031018
C	10.281296	9.167239	0.102390
C	9.505312	9.908204	0.999568
C	5.576243	8.007781	4.294723
C	4.821693	6.709370	4.114196
C	3.490604	6.707996	3.635107
C	2.784237	5.504189	3.482254
C	3.397057	4.283898	3.814786
C	4.711650	4.271926	4.312945
C	5.418032	5.475455	4.463871
H	9.900520	11.891206	4.376422
H	10.933902	14.100482	3.641970
H	9.854671	15.353581	1.719072
H	7.796979	14.384816	0.628236
H	5.886670	12.684727	0.832519
H	6.868863	11.214409	0.565927
H	4.181598	12.363824	3.155388
H	5.760026	13.167751	3.283541
H	3.780695	12.821703	5.687909
H	4.381267	12.144293	8.044739
H	6.431444	10.691158	8.411458
H	7.756398	9.932240	6.369042
H	4.366432	10.437072	1.085536
H	4.114047	10.121882	2.817947
H	4.787590	8.006781	1.743628

H	6.208180	8.776643	0.994934
H	6.917346	6.511902	2.337333
H	7.952783	7.153716	3.661196
H	8.959573	6.098730	0.838184
H	10.689945	7.166013	-0.664518
H	11.021353	9.681554	-0.526917
H	9.635500	10.994209	1.082836
H	4.875619	8.831423	4.526082
H	6.300220	7.935177	5.128473
H	2.981225	7.660399	3.411605
H	1.745823	5.519409	3.118856
H	2.841653	3.340587	3.703292
H	5.183665	3.320533	4.600592
H	6.435528	5.454351	4.886600

Table A.5.15. Cartesian Coordinates for DFT-optimized Model of [Mn^{IV}(O)(T_{piv}PP)] (full model).

Atom	x	y	z
Mn	0.116078	-0.349115	0.152565
O	1.330171	-0.652723	1.251607
N	-0.835125	-2.123415	0.383005
N	-1.245456	0.496490	1.389619
N	0.688548	1.510056	-0.429679
N	1.073299	-1.109716	-1.464280
N	0.798082	3.318208	3.974784
O	1.870499	2.350961	5.706984
N	-5.177496	-2.661207	0.975912
O	-4.998695	-0.427537	0.490760
N	2.727974	-4.781203	0.489450
O	4.360323	-6.195134	1.295794
N	1.050742	2.229764	-4.784335
O	0.769017	3.332396	-6.789943
C	-2.043143	-3.857875	1.342681
C	-1.083572	-4.428653	0.546191
C	-0.342421	-3.343398	-0.057430
C	-1.874680	-2.423067	1.250976
C	-2.323287	2.032095	2.761673
C	-2.992777	0.841843	2.880481
C	-2.297082	-0.119153	2.054162
C	-1.240918	1.813630	1.826384
C	-2.617673	-1.489206	1.999130
C	1.904368	3.242831	-1.391011
C	1.274880	3.754868	-0.284554
C	0.505411	2.677642	0.298297
C	1.550950	1.842505	-1.466030
C	-0.373661	2.831204	1.385873
C	2.147954	-2.631053	-2.855250
C	2.474319	-1.375306	-3.300116
C	1.838754	-0.432467	-2.404241
C	1.270595	-2.458899	-1.717774
C	0.675990	-3.523547	-1.012866
C	2.064123	0.957026	-2.435335
C	-0.461417	4.171994	2.054306
C	1.121153	-4.922534	-1.327284
C	2.975910	1.511149	-3.494675
C	-3.711584	-2.010092	2.880754
C	-1.153595	5.234435	1.435843
C	-1.243913	6.498599	2.038943
C	-0.654009	6.705966	3.296983
C	0.018092	5.657365	3.939600
C	0.146329	4.392920	3.323228
C	2.163648	-5.528943	-0.562212
C	2.581286	-6.842764	-0.882909
C	1.973126	-7.536094	-1.939006
C	0.944597	-6.948914	-2.693672
C	0.527778	-5.645644	-2.379870
C	-3.523544	-1.997554	4.282419
C	-4.457245	-2.568734	5.158921
C	-5.615437	-3.171775	4.642251
C	-5.836225	-3.174989	3.258581

C	-4.902437	-2.597557	2.372219
C	2.453837	2.147309	-4.660236
C	3.340818	2.659146	-5.635068
C	4.726062	2.540410	-5.452268
C	5.251895	1.916152	-4.309746
C	4.372689	1.406301	-3.341757
C	1.870358	3.260695	4.874369
C	3.110640	4.198980	4.743665
C	4.338870	3.249768	4.785921
C	3.193039	5.023625	3.442782
C	3.158915	5.123030	5.984649
C	-5.252495	-1.573200	0.118897
C	-5.667859	-1.877946	-1.349363
C	-6.933366	-1.037755	-1.642662
C	-4.502216	-1.398155	-2.247334
C	-5.954002	-3.366798	-1.631757
C	3.772662	-5.112159	1.345721
C	4.174007	-3.987173	2.343310
C	5.004861	-4.628033	3.472302
C	5.050032	-2.966962	1.569841
C	2.941861	-3.271298	2.944861
C	0.285150	2.794570	-5.790169
C	-1.258980	2.723769	-5.594074
C	-1.707185	1.999210	-4.308860
C	-1.770433	4.184618	-5.570002
C	-1.834043	1.991205	-6.829755
H	-2.790328	-4.360995	1.965037
H	-0.892735	-5.491336	0.362135
H	-2.567273	2.994888	3.224015
H	-3.897515	0.629255	3.457630
H	2.569037	3.756220	-2.094104
H	1.308325	4.779346	0.100168
H	2.450651	-3.599498	-3.267173
H	3.109051	-1.098540	-4.148410
H	-1.626831	5.054541	0.458218
H	-1.786034	7.312748	1.534970
H	-0.737118	7.683976	3.795409
H	0.437783	5.803352	4.945402
H	3.384659	-7.294696	-0.289635
H	2.314389	-8.556872	-2.171506
H	0.469898	-7.497926	-3.520855
H	-0.275055	-5.164450	-2.960142
H	-2.598430	-1.553616	4.680541
H	-4.271798	-2.553545	6.243460
H	-6.355652	-3.629533	5.315958
H	-6.757112	-3.616087	2.845758
H	2.920006	3.141935	-6.524790
H	5.401968	2.945008	-6.221491
H	6.339537	1.826096	-4.169159
H	4.765718	0.916522	-2.437482
H	0.258015	2.444501	4.015995
H	5.271373	3.850405	4.765935
H	4.347976	2.569965	3.909748
H	4.328867	2.628978	5.700787
H	4.199403	5.485989	3.372442
H	2.452907	5.843441	3.395503

H	3.057023	4.384986	2.546696
H	4.106536	5.700415	5.989384
H	3.109571	4.528448	6.918216
H	2.324521	5.854222	5.995040
H	-5.568192	-3.540615	0.635334
H	-7.220686	-1.137846	-2.709722
H	-6.748597	0.031892	-1.425424
H	-7.793111	-1.369988	-1.024524
H	-4.773028	-1.511919	-3.317439
H	-3.580211	-1.985773	-2.060526
H	-4.276098	-0.332565	-2.050552
H	-6.235512	-3.499475	-2.696389
H	-6.806148	-3.754537	-1.032671
H	-5.065400	-4.006873	-1.451520
H	2.310730	-3.856528	0.634338
H	5.349480	-3.842580	4.175252
H	5.888448	-5.158669	3.070239
H	4.405782	-5.365721	4.043011
H	5.403243	-2.174644	2.261995
H	4.483833	-2.469643	0.756374
H	5.939948	-3.459236	1.127467
H	3.272605	-2.573542	3.741056
H	2.235850	-3.993383	3.404069
H	2.385387	-2.645262	2.213743
H	0.535948	1.816334	-4.003343
H	-2.814520	1.992821	-4.249536
H	-1.343979	2.503721	-3.388832
H	-1.380756	0.938231	-4.286642
H	-2.879125	4.200931	-5.526110
H	-1.445439	4.725618	-6.479588
H	-1.384681	4.733081	-4.685838
H	-2.943160	1.997506	-6.796096
H	-1.498136	0.934172	-6.865292
H	-1.506260	2.487493	-7.763398

Table A.5.16. Cartesian Coordinates for DFT-optimized Model of [Mn^{IV}(O)(T_{piv}PP)] (truncated model).

Atom	x	y	z
Mn	0.145530	-0.351122	0.179221
O	1.353703	-0.563239	1.301266
N	-0.766194	-2.124209	0.419430
N	-1.221414	0.485024	1.390289
N	0.653932	1.491609	-0.435565
N	1.107593	-1.116934	-1.409016
C	-2.128243	-3.835190	1.175131
C	-1.059893	-4.416585	0.537406
C	-0.226621	-3.343866	0.041454
C	-1.922146	-2.403771	1.134829
C	-2.177286	1.953406	2.902223
C	-2.943992	0.813936	2.899718
C	-2.322032	-0.117030	1.983690
C	-1.119220	1.755126	1.936873
C	-2.714673	-1.462178	1.823382
C	1.629886	3.268313	-1.551133
C	1.166280	3.746788	-0.350045
C	0.531459	2.640358	0.330820
C	1.343625	1.850822	-1.584842
C	-0.223878	2.760411	1.515937
C	2.278206	-2.622020	-2.720309
C	2.440848	-1.379397	-3.281849
C	1.741677	-0.434633	-2.438097
C	1.421271	-2.457941	-1.567222
C	0.875601	-3.522785	-0.820278
C	1.806704	0.966715	-2.581563
C	-0.191239	4.073043	2.271717
C	1.385799	-4.927191	-1.070669
C	2.508753	1.546340	-3.793482
C	-3.973392	-1.939465	2.520086
H	-2.967201	-4.347815	1.657332
H	-0.884301	-5.486594	0.383361
H	-2.350700	2.865310	3.483465
H	-3.840154	0.620573	3.498622
H	2.149762	3.834903	-2.330821
H	1.217012	4.778249	0.014674
H	2.675825	-3.572409	-3.091970
H	3.017523	-1.131883	-4.179234
H	-0.940228	4.796861	1.882792
H	0.802384	4.553157	2.200039
H	-0.400679	3.923592	3.347040
H	2.459702	-4.923509	-1.334197
H	0.840110	-5.427847	-1.899902
H	1.276011	-5.560513	-0.170834
H	2.427628	0.877738	-4.669925
H	3.590697	1.715073	-3.602506
H	2.070414	2.518017	-4.088371
H	-4.436345	-2.789124	1.985376
H	-4.734709	-1.139179	2.572585
H	-3.768642	-2.272108	3.560759

Table A.5.17. Cartesian Coordinates for DFT-optimized Model of [Mn^{IV}(O)(salen)] (full model).

Atom	x	y	z
Mn	14.484208	8.493075	7.017385
O	15.451095	6.972952	7.619827
O	13.019589	8.039364	8.137288
O	15.290659	9.726910	7.814254
N	15.522612	8.520258	5.327732
N	13.342407	9.783352	6.031610
C	16.615639	6.503573	7.233622
C	17.349041	5.615765	8.095041
C	18.539794	5.046313	7.622444
C	19.079952	5.303120	6.331029
C	18.388202	6.199115	5.515580
C	17.182028	6.822397	5.945352
C	11.909167	8.695290	8.400269
C	11.038377	8.224771	9.442273
C	9.880679	8.957352	9.739913
C	9.494859	10.137013	9.044046
C	10.311781	10.554720	7.992446
C	11.503893	9.856872	7.648828
C	16.562002	7.766634	5.063588
C	15.024099	9.431481	4.252865
C	12.237496	10.302536	6.498671
C	14.026766	10.443641	4.887022
C	16.912286	5.336827	9.500953
C	16.425665	4.051744	9.861922
C	16.143022	3.781773	11.214672
C	16.326568	4.747570	12.222564
C	16.777296	6.022884	11.835248
C	17.071243	6.341419	10.494573
C	16.193462	2.981036	8.816762
C	16.076908	4.413412	13.676462
C	17.555405	7.727929	10.136799
C	20.356874	4.652999	5.885762
C	20.318667	3.440453	5.148382
C	21.531235	2.844355	4.745044
C	22.780740	3.412744	5.051194
C	22.794303	4.616451	5.783698
C	21.609087	5.246385	6.207166
C	18.999535	2.786604	4.798567
C	24.073416	2.756738	4.619751
C	21.673680	6.539421	6.990347
C	16.118743	10.117772	3.432128
C	17.161518	10.866929	4.057183
C	18.099025	11.533940	3.242195
C	18.062631	11.476691	1.837280
C	17.046043	10.707685	1.245914
C	16.076978	10.026938	2.010500
C	17.373743	10.936488	5.556263
C	19.088556	12.209355	1.003421
C	15.023381	9.222800	1.274352
C	11.344537	6.973437	10.207700
C	12.305574	6.988717	11.253779
C	12.516320	5.814976	12.000744

C	11.813927	4.623279	11.737112
C	10.879716	4.628721	10.686035
C	10.631355	5.781300	9.914795
C	13.090974	8.241911	11.563671
C	12.083911	3.369675	12.538179
C	9.623222	5.727534	8.786436
C	8.257123	10.892650	9.429876
C	7.018318	10.608971	8.797337
C	5.870430	11.332369	9.181242
C	5.912751	12.327950	10.173780
C	7.153000	12.592440	10.787988
C	8.324156	11.895273	10.436835
C	6.919851	9.545614	7.725196
C	4.671458	13.090637	10.580044
C	9.634217	12.214831	11.122961
C	13.095937	11.085351	3.857179
C	13.277268	12.460389	3.521209
C	12.450874	13.046901	2.544428
C	11.439725	12.325599	1.882452
C	11.263687	10.979050	2.241245
C	12.060798	10.342683	3.216986
C	14.334845	13.321797	4.181188
C	10.579107	12.984519	0.829319
C	11.709222	8.909019	3.567438
H	19.095235	4.376637	8.299688
H	18.785820	6.451128	4.518511
H	17.033139	7.885424	4.068176
H	9.240672	8.598754	10.563064
H	10.037004	11.447928	7.407302
H	11.798274	11.152753	5.940728
H	14.440569	8.789133	3.565812
H	14.640739	11.238270	5.353489
H	15.769595	2.780232	11.487749
H	16.916674	6.801304	12.604175
H	21.494431	1.901897	4.173266
H	23.761468	5.083587	6.035496
H	18.896148	12.115608	3.735213
H	16.999237	10.632473	0.147075
H	13.259941	5.834654	12.814015
H	10.323863	3.704681	10.453539
H	4.910905	11.106744	8.686338
H	7.213490	13.369143	11.569061
H	12.606319	14.109195	2.293213
H	10.469746	10.393107	1.748875
H	15.645373	2.119338	9.245791
H	15.605108	3.371820	7.961637
H	17.145317	2.593964	8.395558
H	15.901134	5.324716	14.282290
H	15.200987	3.744595	13.799401
H	16.949140	3.887437	14.123132
H	17.754429	8.327830	11.046315
H	18.489155	7.693280	9.538041
H	16.805185	8.275804	9.526020
H	18.400941	2.564259	5.706288
H	18.367936	3.447782	4.169534
H	19.154689	1.837679	4.248941

H	23.889148	1.859570	3.996817
H	24.706418	3.454217	4.031793
H	24.677556	2.439020	5.496280
H	22.720919	6.868005	7.138176
H	21.125449	7.355832	6.476121
H	21.203309	6.436398	7.990324
H	18.089092	10.147158	5.874551
H	17.826540	11.907803	5.838563
H	16.474721	10.772444	6.182018
H	20.119285	11.875522	1.246383
H	18.926996	12.048259	-0.080222
H	19.054604	13.303111	1.192400
H	14.999374	8.160825	1.599410
H	14.003926	9.634342	1.425241
H	15.224219	9.224983	0.185700
H	13.748494	8.516910	10.712855
H	12.424354	9.110004	11.748045
H	13.731040	8.102931	12.456238
H	11.275161	2.621956	12.416023
H	13.032542	2.888732	12.214658
H	12.186338	3.590109	13.620627
H	10.055382	6.103528	7.836254
H	9.270949	4.691104	8.616548
H	8.730687	6.354718	8.994514
H	7.562823	9.783102	6.852228
H	7.261099	8.557326	8.097474
H	5.879023	9.434703	7.363257
H	4.814864	14.186512	10.472712
H	3.795067	12.802361	9.967062
H	4.413280	12.905342	11.644506
H	10.052900	11.325844	11.638854
H	10.407670	12.539401	10.396360
H	9.509150	13.018793	11.874265
H	14.232863	13.339418	5.286762
H	15.360470	12.963917	3.954941
H	14.260637	14.368046	3.827324
H	10.073675	13.888627	1.228710
H	11.188342	13.316173	-0.038077
H	9.797468	12.298009	0.449839
H	11.012199	8.872542	4.431659
H	11.201133	8.413885	2.716679
H	12.577184	8.287734	3.854967

Table A.5.18. Cartesian Coordinates for DFT-optimized Model of [Mn^{IV}(O)(salen)] (truncated model).

Atom	x	y	z
Mn	14.548727	8.541842	7.053869
O	15.373024	6.908885	7.552091
O	13.203321	8.262614	8.356669
O	15.623837	9.661679	7.668407
N	15.453493	8.477572	5.276939
N	13.423252	9.885711	6.129935
C	16.552991	6.466174	7.173610
C	17.199841	5.468063	7.980544
C	18.440801	4.975136	7.574119
C	19.101195	5.394469	6.383155
C	18.457048	6.343583	5.593729
C	17.196000	6.898469	5.962104
C	12.019254	8.814488	8.517526
C	11.216277	8.383103	9.629376
C	9.956104	8.954924	9.811588
C	9.411506	9.949665	8.948331
C	10.192632	10.358840	7.871167
C	11.489108	9.813885	7.630403
C	16.562899	7.819255	5.059477
C	14.838296	9.349889	4.243741
C	12.232474	10.288360	6.498163
C	14.166136	10.516602	5.014439
C	16.516248	5.009053	9.241221
C	20.447433	4.816580	6.011745
C	15.790575	9.810448	3.138269
C	11.775634	7.336715	10.556368
C	8.040174	10.526353	9.215521
C	13.348198	11.451532	4.123995
H	18.934188	4.222010	8.212846
H	18.927725	6.687338	4.657046
H	9.354675	8.619561	10.674356
H	9.811108	11.127622	7.177886
H	17.068188	7.945225	4.084375
H	14.012561	8.756974	3.782488
H	11.733951	11.072056	5.899183
H	14.984386	11.090376	5.508929
H	16.317500	5.865917	9.917479
H	17.125928	4.259669	9.782156
H	15.523787	4.565241	9.017726
H	20.406278	3.710085	5.921780
H	21.214949	5.045768	6.781823
H	20.811945	5.219416	5.046341
H	16.196779	8.956916	2.561734
H	15.252790	10.447192	2.410720
H	16.639948	10.391726	3.551940
H	11.069346	7.103504	11.376516
H	12.737893	7.671064	10.996257
H	12.006658	6.400082	10.007792
H	7.757860	11.277725	8.452005
H	7.258363	9.737017	9.216554
H	7.993298	11.022760	10.208445
H	12.920798	12.292723	4.703664

H	12.518398	10.921250	3.611454
H	13.995787	11.904603	3.349877

Table A.5.19. Cartesian Coordinates for DFT-optimized Model of $[Mn^{IV}(O)(salen)(CH_3CH_2CN)]$ (truncated model).

Atom	x	y	z
Mn	14.548203	8.460711	6.944383
O	15.398852	6.786357	7.362350
O	13.271112	8.288416	8.379050
O	15.673643	9.418638	7.733692
N	15.581683	8.619965	5.244183
N	13.567970	10.014304	6.187149
C	16.614835	6.441590	7.016838
C	17.264109	5.393975	7.763409
C	18.543184	4.983342	7.388625
C	19.253210	5.538814	6.284991
C	18.617046	6.540369	5.556676
C	17.315202	7.015753	5.895095
C	12.067984	8.794750	8.460026
C	11.206506	8.325093	9.518745
C	9.918261	8.846248	9.632172
C	9.394378	9.843025	8.757480
C	10.233207	10.308765	7.749019
C	11.558317	9.809651	7.569698
C	16.724094	8.018446	5.050294
C	15.026333	9.617032	4.303664
C	12.365988	10.391310	6.531450
C	14.389222	10.727678	5.188928
C	16.532062	4.795803	8.935787
C	20.640968	5.047801	5.941179
C	16.010278	10.147411	3.259483
C	11.748890	7.289085	10.467774
C	7.989012	10.367212	8.946568
C	13.664039	11.813217	4.394121
H	19.028870	4.189187	7.982547
H	19.129211	6.993710	4.690554
H	9.276119	8.470221	10.448126
H	9.874425	11.092493	7.059524
H	17.308662	8.273820	4.146961
H	14.180343	9.113924	3.777411
H	11.908952	11.248188	6.002032
H	15.220627	11.185053	5.773632
H	16.254888	5.580705	9.669527
H	17.143994	4.026615	9.446209
H	15.574486	4.333035	8.616907
H	20.653040	3.953929	5.745731
H	21.356645	5.230466	6.771693
H	21.040495	5.553979	5.040126
H	16.409317	9.333725	2.622789
H	15.501666	10.856699	2.579387
H	16.865283	10.671528	3.733885
H	10.997916	7.004440	11.230496
H	12.658005	7.663262	10.983022

H	12.073193	6.376725	9.925176
H	7.736454	11.137156	8.190748
H	7.232750	9.556670	8.864726
H	7.854164	10.826351	9.949636
H	13.240737	12.587464	5.063561
H	12.840817	11.399172	3.774707
H	14.372263	12.333056	3.721491
C	11.757271	3.852802	5.677262
C	11.354262	5.230906	5.116006
C	12.286136	6.297511	5.486183
N	13.041185	7.121590	5.811981
H	11.798993	3.870185	6.783206
H	11.012729	3.093997	5.367561
H	12.750622	3.541697	5.300355
H	10.347221	5.527924	5.480253
H	11.289556	5.204252	4.006917

Table A.5.20. Cartesian Coordinates for DFT-optimized Model of $[Mn^{IV}(OH)(salen)]^{+}$ (full model).

Atom	x	y	z
Mn	14.488204	8.528170	6.984959
O	15.484353	7.095886	7.614228
O	13.008401	8.028708	7.992584
O	15.298608	9.850561	7.926460
N	15.540882	8.551290	5.306649
N	13.389763	9.840709	6.025109
C	16.669712	6.609008	7.260723
C	17.358061	5.717925	8.141150
C	18.577375	5.171126	7.702833
C	19.166756	5.452788	6.440176
C	18.489248	6.340990	5.598910
C	17.257463	6.935306	5.988370
C	11.941092	8.724418	8.357636
C	11.093224	8.229763	9.397972
C	9.988987	9.013056	9.772810
C	9.649435	10.252926	9.162176
C	10.454170	10.692240	8.105167
C	11.590303	9.950319	7.684765
C	16.626616	7.850097	5.084402
C	15.002848	9.418188	4.201071
C	12.310964	10.391460	6.528327
C	14.030673	10.458168	4.821069
C	16.840650	5.367776	9.502757
C	16.332697	4.060925	9.746874
C	15.954589	3.712534	11.055989
C	16.067453	4.611564	12.134956
C	16.550762	5.903659	11.862679
C	16.935829	6.302503	10.567452
C	16.184259	3.052687	8.627450
C	15.711862	4.186588	13.540573
C	17.432382	7.715458	10.350956
C	20.467780	4.825427	6.040727
C	20.476599	3.717144	5.152524
C	21.712649	3.139625	4.799454
C	22.935898	3.626045	5.295873
C	22.898373	4.728858	6.172759
C	21.690122	5.337256	6.558413
C	19.189766	3.144641	4.597249
C	24.250960	2.984758	4.918102
C	21.705443	6.525020	7.496648
C	16.062238	10.038124	3.293220
C	17.122776	10.841477	3.812649
C	18.031847	11.431430	2.912765
C	17.946113	11.249842	1.519571
C	16.910069	10.432563	1.034327
C	15.969302	9.821493	1.886693
C	17.384468	11.044703	5.292841
C	18.931462	11.914269	0.588309
C	14.889371	8.960568	1.262303
C	11.339539	6.915470	10.071177
C	11.840290	6.880243	11.399469
C	11.969527	5.633677	12.042035

C	11.615218	4.426145	11.412415
C	11.130343	4.489731	10.091604
C	10.988141	5.709164	9.405266
C	12.234814	8.148746	12.124919
C	11.768142	3.098415	12.117298
C	10.445845	5.722816	7.993017
C	8.463768	11.039368	9.628444
C	7.149905	10.595584	9.317276
C	6.051839	11.353438	9.770077
C	6.213095	12.528111	10.527429
C	7.526688	12.943942	10.824527
C	8.655987	12.227336	10.389187
C	6.913337	9.345284	8.496967
C	5.023441	13.318296	11.020354
C	10.043195	12.713569	10.752735
C	13.047641	11.045379	3.810677
C	13.204536	12.407531	3.412595
C	12.328560	12.946505	2.452642
C	11.293839	12.191440	1.867733
C	11.145522	10.858821	2.288941
C	11.991367	10.267489	3.250684
C	14.287687	13.301308	3.982204
C	10.384742	12.798552	0.826381
C	11.664057	8.847370	3.674590
H	16.053251	9.468139	8.433084
H	19.106401	4.487221	8.385976
H	18.919344	6.602117	4.618778
H	9.350265	8.640042	10.589533
H	10.201154	11.624633	7.575955
H	17.116523	7.989561	4.101353
H	14.388311	8.734446	3.584975
H	11.889384	11.256872	5.981523
H	14.649604	11.282370	5.225200
H	15.564141	2.697866	11.239593
H	16.643327	6.627817	12.688982
H	15.613030	2.166681	8.965218
H	15.656835	3.485677	7.752996
H	17.166955	2.689610	8.259194
H	15.526819	5.057667	14.199161
H	14.810373	3.541880	13.556752
H	16.536546	3.598162	13.997902
H	17.877096	8.132938	11.275331
H	18.191945	7.781175	9.547036
H	16.586090	8.386512	10.077880
H	21.716384	2.275722	4.114646
H	23.844024	5.132690	6.570911
H	18.471418	2.888042	5.403333
H	18.668478	3.863590	3.930465
H	19.382873	2.226608	4.009722
H	24.123682	2.223583	4.124298
H	24.980265	3.738632	4.556334
H	24.716966	2.482986	5.792743
H	22.741779	6.828911	7.739345
H	21.187407	7.402734	7.056663
H	21.190002	6.303352	8.454884
H	18.844607	12.053643	3.322800

H	16.826102	10.262083	-0.051007
H	18.079975	10.265675	5.675256
H	17.876518	12.020958	5.470256
H	16.488492	10.992453	5.938447
H	19.977613	11.733569	0.909837
H	18.823680	11.550928	-0.451596
H	18.786393	13.015450	0.576521
H	14.876956	7.929002	1.674685
H	13.876883	9.389419	1.413056
H	15.048373	8.868586	0.171268
H	12.356215	5.609127	13.073940
H	10.840549	3.557788	9.578411
H	12.908213	8.780379	11.510063
H	11.353681	8.776080	12.376826
H	12.755643	7.917923	13.074019
H	10.929302	2.412480	11.883024
H	12.701896	2.585691	11.799757
H	11.814514	3.220695	13.217169
H	11.212749	6.069651	7.268713
H	10.123624	4.711310	7.679148
H	9.574550	6.402622	7.890871
H	5.034251	11.012766	9.517682
H	7.679420	13.857864	11.422266
H	7.499354	9.353156	7.554716
H	7.208383	8.425648	9.045338
H	5.843692	9.240408	8.232007
H	5.101717	14.387972	10.735641
H	4.071920	12.925049	10.613472
H	4.954004	13.286890	12.128475
H	10.650159	11.913593	11.224626
H	10.612581	13.055904	9.862928
H	9.992940	13.564119	11.459420
H	12.462419	13.997894	2.150417
H	10.334549	10.249284	1.857722
H	14.242670	13.369574	5.090074
H	15.303696	12.943437	3.715312
H	14.187426	14.331301	3.590827
H	9.942368	13.751223	1.183556
H	10.946101	13.035949	-0.101994
H	9.556616	12.116518	0.554069
H	10.984643	8.840692	4.553916
H	11.139833	8.309767	2.860837
H	12.543900	8.242652	3.963095

Table A.5.21. Cartesian Coordinates for DFT-optimized Model of $[Mn^{IV}(OH)(salen)]^{+}$ (truncated model).

Atom	x	y	z
Mn	14.498009	8.520111	7.035339
O	15.432628	7.029145	7.605782
O	13.061693	8.089512	8.116934
O	15.492645	9.802781	7.836044
N	15.447161	8.473924	5.291766
N	13.406651	9.882570	6.116902
C	16.609965	6.541526	7.226149
C	17.250224	5.577530	8.065323
C	18.480128	5.058236	7.643175
C	19.118218	5.424899	6.423980
C	18.468043	6.352543	5.607962
C	17.220107	6.925608	5.984986
C	11.932674	8.721396	8.408457
C	11.142404	8.244122	9.499984
C	9.937409	8.904230	9.768985
C	9.457652	10.013937	9.016104
C	10.240059	10.460637	7.947866
C	11.477156	9.836838	7.627681
C	16.567258	7.825331	5.078564
C	14.819127	9.327293	4.234498
C	12.236090	10.322357	6.512515
C	14.149732	10.504816	4.984315
C	16.590972	5.157054	9.351449
C	20.444190	4.813589	6.045563
C	15.764727	9.758271	3.114394
C	11.621743	7.068033	10.306605
C	8.149389	10.669615	9.379354
C	13.315413	11.416755	4.087014
H	16.343204	9.434946	8.169260
H	18.978194	4.320362	8.294108
H	18.921196	6.653412	4.649649
H	9.328726	8.542563	10.614456
H	9.903096	11.315918	7.340399
H	17.060210	7.954278	4.099096
H	13.997766	8.711479	3.799277
H	11.774570	11.147172	5.941977
H	14.961341	11.099045	5.464682
H	16.411655	6.027880	10.014696
H	17.209390	4.420923	9.897760
H	15.595989	4.706153	9.158009
H	20.372122	3.707565	5.986350
H	21.221053	5.042703	6.804699
H	20.804826	5.184406	5.067449
H	16.157001	8.892061	2.547825
H	15.218151	10.377743	2.379341
H	16.619043	10.350656	3.500852
H	10.922341	6.834120	11.130538
H	12.624542	7.264063	10.737888
H	11.728822	6.165979	9.669712
H	7.900700	11.502190	8.694448
H	7.314364	9.938986	9.348123
H	8.179883	11.074910	10.412469

H	12.904367	12.277518	4.648771
H	12.478914	10.873054	3.601775
H	13.952395	11.848560	3.292962

Table A.5.22. Cartesian Coordinates for DFT-optimized Model of $[Mn^{IV}(OH)(salen)(CH_3CH_2CN)]^+$ (truncated model).

Atom	x	y	z
Mn	14.465157	8.346563	6.886214
O	15.468879	6.875927	7.454309
O	13.200564	8.174109	8.257490
O	15.504651	9.551643	7.765814
N	15.583840	8.535104	5.238339
N	13.496910	9.889858	6.098365
C	16.698259	6.505887	7.122615
C	17.351817	5.527257	7.939328
C	18.643102	5.123307	7.582175
C	19.342015	5.624424	6.448079
C	18.687842	6.568938	5.655675
C	17.375471	7.027265	5.967837
C	12.024195	8.749423	8.427330
C	11.220016	8.318652	9.533361
C	9.971466	8.920437	9.718200
C	9.453994	9.946423	8.875923
C	10.253266	10.367221	7.814481
C	11.533788	9.789910	7.565973
C	16.753606	7.975169	5.082766
C	15.001446	9.474383	4.244555
C	12.323670	10.316229	6.491259
C	14.305916	10.591450	5.069271
C	16.634475	4.974726	9.141975
C	20.735636	5.138099	6.133992
C	15.984625	9.993198	3.196210
C	11.751114	7.253029	10.454727
C	8.097472	10.548341	9.152008
C	13.534160	11.598776	4.218120
H	16.387789	9.159746	7.954368
H	19.143272	4.374353	8.218972
H	19.190800	6.978718	4.764562
H	9.358286	8.582468	10.570777
H	9.899902	11.170218	7.147066
H	17.337455	8.234118	4.181612
H	14.191293	8.906012	3.730737
H	11.889177	11.185038	5.965513
H	15.104080	11.122323	5.636569
H	16.344733	5.784870	9.842054
H	17.263772	4.245956	9.686181
H	15.689695	4.473048	8.847429
H	20.755413	4.037135	5.994010
H	21.436413	5.366800	6.964088
H	21.136617	5.605026	5.214231
H	16.418042	9.170362	2.595507
H	15.460035	10.652323	2.479947
H	16.811415	10.571789	3.656451
H	11.022360	7.007948	11.250047

H	12.697361	7.580494	10.932835
H	11.995780	6.324515	9.899168
H	7.834356	11.325687	8.409314
H	7.300864	9.775320	9.132064
H	8.063135	11.015948	10.158352
H	13.102689	12.408339	4.837721
H	12.717156	11.119096	3.640527
H	14.218107	12.093154	3.503534
C	10.856228	4.413157	5.783693
C	11.693244	5.166898	4.728797
C	12.546733	6.206392	5.299944
N	13.224544	7.021224	5.779190
H	10.177542	5.099885	6.324376
H	10.241973	3.646485	5.274623
H	11.504592	3.904061	6.521972
H	12.354516	4.470063	4.169443
H	11.039992	5.652463	3.971848

Table A.5.23. Cartesian Coordinates for DFT-optimized Model of $[Mn^{IV}(O)(H_3buea)]^-$ (gas-phase optimization).

Atom	x	y	z
Mn	10.792054	2.829577	26.575264
O	9.686365	2.977762	27.877305
O	12.925591	5.975218	28.444377
O	12.130882	-0.804635	28.174913
O	7.314831	2.416593	24.144174
N	7.491059	2.477418	26.433622
N	12.125432	2.764327	24.860201
N	9.417139	2.719391	25.125743
N	11.633818	1.111455	26.959269
N	11.377111	4.523479	29.339557
N	10.507189	0.611603	28.963432
N	12.006560	4.301858	27.100689
C	12.149144	4.998332	28.304799
C	11.268805	5.280061	30.565915
C	11.320575	3.268236	23.719906
C	9.929703	2.650532	23.757577
C	6.061854	2.435469	26.627132
C	8.024974	2.527617	25.173543
C	12.509418	1.335343	24.714063
C	12.753582	0.745739	26.094604
C	11.459969	0.250235	28.048797
C	10.148260	-0.271233	30.046835
C	13.295671	3.631631	25.165390
C	12.845373	4.810554	26.015076
H	11.839832	3.066520	22.751318
H	11.239182	4.367039	23.843020
H	9.256328	3.190205	23.057272
H	9.950336	1.598123	23.378826
H	5.849352	2.243916	27.697769
H	5.603719	1.625641	26.020864
H	5.552841	3.384895	26.333073
H	8.160549	2.687547	27.211089
H	13.401105	1.235583	24.049698
H	11.661433	0.808791	24.236604
H	12.839861	-0.359000	26.032551
H	13.729034	1.101958	26.511514
H	9.979101	1.482838	28.758484
H	9.528166	0.287753	30.775504
H	11.054976	-0.649721	30.563927
H	9.569860	-1.164388	29.708956
H	13.796793	3.951897	24.220720
H	14.014967	3.025089	25.748379
H	13.721672	5.355430	26.425153
H	12.288879	5.551387	25.387290
H	10.601467	3.892953	29.035982
H	10.772694	4.654346	31.334974
H	10.685736	6.226771	30.453884
H	12.276779	5.562782	30.931159

Table A.5.24. Cartesian Coordinates for DFT-optimized Model of $[Mn^{IV}(O)(H_3buea)]^-$ (COSMO optimization).

Atom	x	y	z
Mn	10.784226	2.861769	26.538995
O	9.659774	3.051029	27.836866
O	12.968650	5.912787	28.504020
O	12.075103	-0.746711	28.196339
O	7.330242	2.413775	24.107903
N	7.529693	2.311660	26.393426
N	12.099922	2.775797	24.859766
N	9.413936	2.797375	25.089999
N	11.525406	1.095247	26.898473
N	11.364427	4.499650	29.352111
N	10.538086	0.746285	29.008960
N	12.060738	4.260379	27.130569
C	12.170879	4.945320	28.334255
C	11.217145	5.278056	30.570009
C	11.348847	3.404854	23.739909
C	9.928210	2.859510	23.713331
C	6.098829	2.188878	26.601070
C	8.050087	2.502818	25.143419
C	12.368747	1.327593	24.631422
C	12.579116	0.648595	25.975169
C	11.410760	0.321057	28.049138
C	10.236875	-0.064697	30.172937
C	13.342867	3.524137	25.203832
C	12.989056	4.713752	26.081510
H	11.871750	3.237725	22.771784
H	11.330084	4.495807	23.933443
H	9.295281	3.519073	23.082389
H	9.890376	1.858246	23.223689
H	5.911637	1.984696	27.672254
H	5.678310	1.352230	26.005439
H	5.542766	3.111203	26.316215
H	8.182184	2.554291	27.176214
H	13.243558	1.193288	23.957880
H	11.482468	0.894673	24.132067
H	12.538864	-0.451967	25.842236
H	13.592627	0.871881	26.384506
H	10.005686	1.611199	28.790011
H	9.579578	0.515419	30.847546
H	11.160068	-0.333951	30.727823
H	9.717838	-1.013943	29.909579
H	13.880000	3.828666	24.278826
H	13.998678	2.837422	25.771242
H	13.911254	5.141994	26.523837
H	12.529489	5.529026	25.473690
H	10.582369	3.888573	29.024454
H	10.575476	4.716204	31.275271
H	10.756479	6.277686	30.394753
H	12.201575	5.446556	31.051617

Table A.5.25. Cartesian Coordinates for DFT-optimized Model of [Mn^{V}(O)(H_3buea)].

Atom	x	y	z
Mn	0.108963	-0.182819	-0.058754
O	0.222547	-0.344549	1.625949
O	2.413010	3.219440	0.383132
O	1.963254	-3.869253	-0.270104
O	-3.979672	0.012775	0.502568
N	-2.388732	-0.372325	2.099659
N	-0.033565	0.020932	-2.177324
N	-1.754383	0.085137	-0.153249
N	0.793669	-1.879207	-0.513574
N	1.566454	1.903965	2.051366
N	1.544054	-2.646236	1.616248
N	1.239287	1.315034	-0.236406
C	1.782044	2.213536	0.751149
C	2.102077	2.743628	3.106769
C	-1.248282	0.839585	-2.414120
C	-2.342415	0.357887	-1.479295
C	-3.366653	-0.553752	3.156352
C	-2.786815	-0.093560	0.836107
C	-0.150126	-1.362960	-2.699880
C	0.824472	-2.246216	-1.942798
C	1.474706	-2.868629	0.282650
C	2.200769	-3.601937	2.488663
C	1.218582	0.699410	-2.594124
C	1.519821	1.805654	-1.599947
H	-1.368625	-0.440211	2.264246
H	1.036966	1.034865	2.243057
H	1.102662	-1.778358	1.968899
H	1.778339	2.336891	4.082477
H	1.737307	3.787662	3.011619
H	3.212183	2.775846	3.079319
H	-1.561969	0.789287	-3.481184
H	-0.991329	1.890359	-2.181422
H	-3.142702	1.119627	-1.390987
H	-2.850513	-0.554302	-1.866451
H	-2.833120	-0.772212	4.099650
H	-4.055676	-1.394248	2.928540
H	-3.987728	0.356383	3.294563
H	0.030561	-1.391535	-3.798107
H	-1.186774	-1.702242	-2.514065
H	0.558628	-3.315056	-2.066911
H	1.861915	-2.156676	-2.337640
H	2.148425	-3.227930	3.527690
H	3.266311	-3.738547	2.207658
H	1.713725	-4.598682	2.438169
H	1.135022	1.087494	-3.634298
H	2.028023	-0.054662	-2.573478
H	2.578631	2.123397	-1.679483
H	0.924141	2.724100	-1.804733

Appendix A.6.

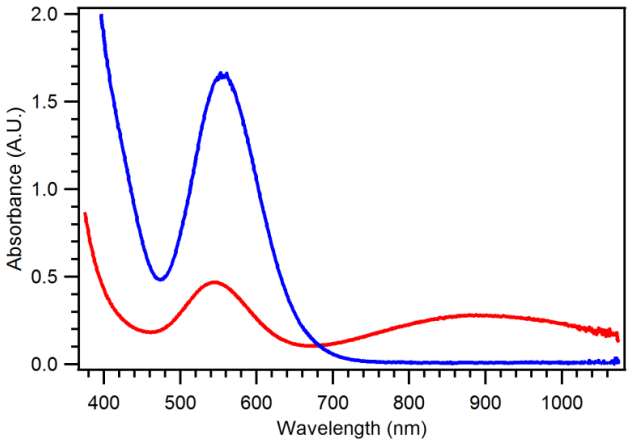

Figure A.6.1. 298 K electronic absorption spectra of 2.0 mM $[Mn^{IV}(OH)_2(Me_2EBC)]^{2+}$ (blue) in (4:1) acetone:water (pH = 5.1) showing the conversion to $[Mn^{IV}(O)(OH)(Me_2EBC)]^{+}$ (red) as the pH was increased to 8.7 upon addition of 0.3 M NaOH.

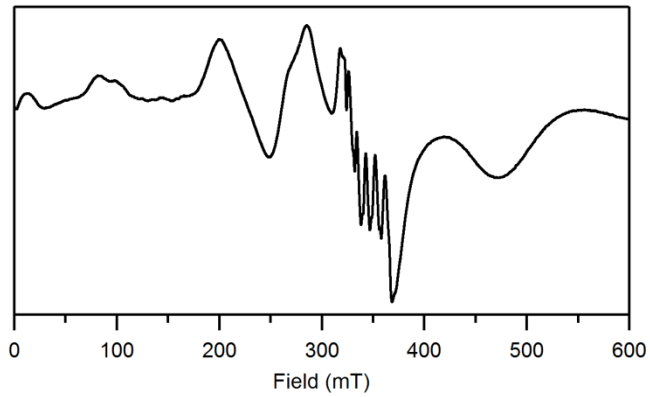

Figure A.2. X-band, perpendicular-mode EPR spectrum of a frozen 2.45 mM acetone:water (4:1) solution of $[Mn^{II}(Cl)_2(Me_2EBC)]$ (average of 5 scans). Recording conditions: T = 6.8 K, 9.6369 GHz microwave frequency, 2.000 mW microwave power, 0.6 mT modulation amplitude, 100 kHz modulation frequency, and 163.84 ms time constant.

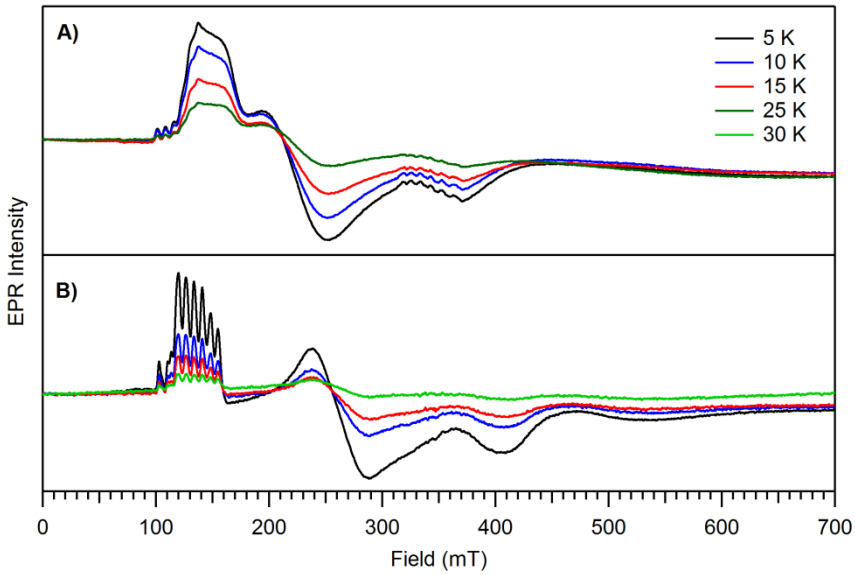

Figure A.6.3. X-band, perpendicular-mode EPR spectra of a frozen 1.9 mM acetone:water (4:1) solution of $[Mn^{IV}(OH)_2(Me_2EBC)]^{2+}$ collected at T = 5, 10, 15, and 25 K. Each spectrum represents the average of 5 scans. **(B)** X-band, perpendicular-mode EPR spectra of a frozen 1.9 mM acetone:water (4:1) solution of $[Mn^{IV}(O)(OH)(Me_2EBC)]^{+}$ collected at T = 5, 10, 15, and 30 K. Each spectrum represents the average of 5 scans. Experimental recording conditions: 9.6378 and 9.6375 GHz microwave frequencies for $[Mn^{IV}(OH)_2(Me_2EBC)]^{2+}$ (**A**) and $[Mn^{IV}(O)(OH)(Me_2EBC)]^{+}$ (**B**), respectively, T = 5 K, 2.000 mW microwave power, 0.6 mT modulation amplitude, 100 kHz modulation frequency, and 163.84 ms time constant.

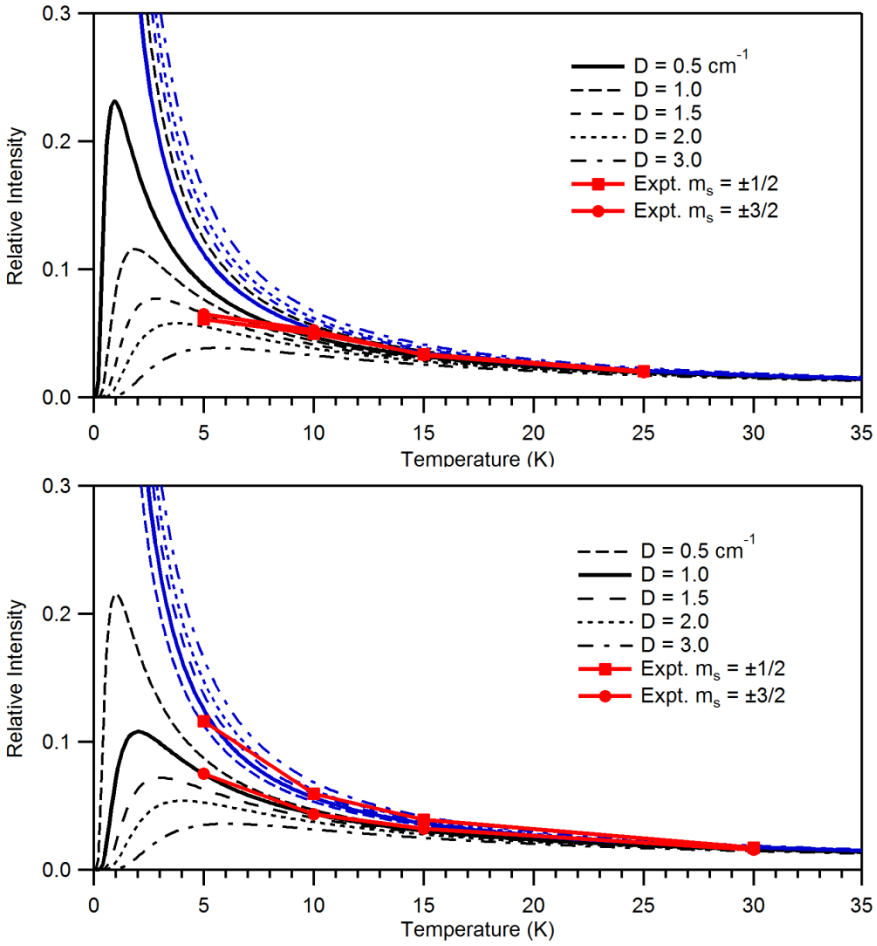

Figure A.6.4. (Top) Relative signal intensity of resonances at g_{eff} = 5.95 (m_s = 3/2; red trace with square marker) and 4.59 (m_s = 1/2; red trace with circle marker) for $[Mn^{IV}(OH)_2(Me_2EBC)]^{2+}$ collected at T = 5, 10, 15, and 25 K. **(Bottom)** Relative signal intensity of resonances at g_{eff} = 6.05 (m_s = 3/2; red trace with square marker) and 4.99 (m_s = 1/2; red trace with circle marker) for $[Mn^{IV}(O)(OH)(Me_2EBC)]^{+}$ collected at T = 5, 10, 15, and 30 K. Black and blue traces denote simulated temperature-dependent profiles as a function of D-value (D = 0.5, 1.0, 1.5, 2.0, and 3.0 cm^{-1}) for resonances within the m_s = ±3/2 and ±1/2 doublets, respectively, with E/D = 0.15 for $[Mn^{IV}(OH)_2(Me_2EBC)]^{2+}$ (top) and E/D = 0.223 for $[Mn^{IV}(O)(OH)(Me_2EBC)]^{+}$ (*bottom*). The solid black and blue traces denote D-values used in the X-band EPR simulations shown in Figure 6.3.